Strongly Coupled Theories in Lattice Coulomb Gauge

Dissertation

der Mathematisch-Naturwissenschaftlichen Fakultät
der Eberhard Karls Universität Tübingen
zur Erlangung des Grades eines
Doktors der Naturwissenschaften
(Dr. rer. nat.)

vorgelegt von
Hannes Andreas Vogt
aus Friedrichshafen

Tübingen
2017

Gedruckt mit Genehmigung der Mathematisch-Naturwissenschaftlichen Fakultät der Eberhard Karls Universität Tübingen.

Tag der mündlichen Qualifikation:	03.07.2017
Dekan:	Prof. Dr. Wolfgang Rosenstiel
1. Berichterstatter:	Prof. Dr. Hugo Reinhardt
2. Berichterstatter:	Prof. Dr. Dr. h.c. mult. Amand Fäßler

Zusammenfassung

Obwohl die Quantenchromodynamik durch eine einfache und elegante Lagrangedichte beschrieben wird und auch experimentell sehr gut bestätigt ist, sind einige interessante Fragen, im Energiebereich, der nicht-störungstheoretisch zugänglich ist, noch immer unbeantwortet. Insbesondere die Frage nach dem Ursprung des Farbeinschlusses (Confinement) beschäftigt die theoretische Teilchenphysik seit mehreren Jahrzehnten. Analytische Zugänge, basierend auf Dyson–Schwinger-Gleichungen oder dem Variationsprinzip, sind wichtige Hilfsmittel, um die nicht-störungstheoretischen Eigenschaften von Feldtheorien zu untersuchen. Aus der zweiten Kategorie bietet insbesondere der Hamiltonzugang in Coulombeichung eine schlüssige physikalische Interpretation der Zweipunktfunktionen der Theorie. Auch beflügelt durch die enorme Leistungssteigerung der Computer sowie Fortschritte in numerischen Algorithmen hat sich die Gitterfeldtheorie zur bedeutendsten Technik zur Erforschung des nicht-störungtheoretischen Sektors von Feldtheorien entwickelt. Eine Überprüfung der Resultate aus den verschiedenen Zugängen ist von großem Interesse, um etwaige Beschränkungen der Methoden zu verstehen.

Im ersten Teil dieser Arbeit beschäftigen wir uns mit den Korrelationsfunktionen der reinen SU(2) Yang–Mills-Theorie bei Nulltemperatur und bei endlichen Temperaturen. Nach einer Einführung zur QCD und der Gitterfeldtheorie werden wir uns zuerst mit dem Gribovproblem beschäftigen, sowie einem neuen Vorschlag dieses zu beheben. Anschließend werden wir die Theorie bei endlicher Temperatur betrachten, um den Deconfinementphasenübergang zu untersuchen. Basierend auf dem Bild der Zentrumsvortices, einem Modell zur Beschreibung des Confinements, werden wir eine Erklärung finden wieso, der Phasenübergang in Korrelatoren in Coulombeichung auf dem Gitter nicht sichtbar ist. Dann werden wir die reine Eichtheorie verlassen und die sogenannte Minimal Walking Technicolor Theorie betrachten, die eine mögliche Erweiterung des Standardmodells darstellt. Abschließen werden wir diese Arbeit mit einem Kapitel über die effiziente Implementierung von Algorithmen der Gitterfeldtheorie auf Grafikkarten, welche heutzutage als Rechenbeschleuniger im High Performance Computing zur Anwendung kommen.

Abstract

Quantum chromodynamics, despite its simple and elegant formulation at the Lagrangian level and numerous experimental verifications, still poses many interesting questions to particle physicists in the region where perturbation theory breaks down. The origin of confinement of quarks and gluons is one of these big puzzles. Analytic techniques, based on Dyson–Schwinger equations or the variational approach have proven to be useful tools to study the non-perturbative aspects of field theories. Of the latter, the Hamiltonian approach in Coulomb gauge offers an appealing physical interpretation of two-point functions of the theory. In recent years, as numerical algorithms improved and more and more compute power became available to the physics community, lattice gauge theory, a fully numerical approach, has become established as the main tool for studies in the non-perturbative sector of field theories. A verification of these different approaches against each other is of great interest to learn about their limitations.

In the first part of this work we will study the correlation functions of pure SU(2) Yang–Mills theory at zero and finite temperature. After an introduction to QCD and lattice gauge theory, we will discuss the Gribov problem and investigate a recent proposal to resolve it. Then we will turn on temperature to study the deconfinement phase transition. Based on the center vortex picture of confinement, we will propose an answer to the question why the correlators from lattice gauge theory in Coulomb gauge fail to detect the phase transition. Afterwards we will leave pure Yang–Mills theory and apply our knowledge to the so-called Minimal Walking Technicolor theory, a possible extension to the Standard Model. Finally we discuss how lattice gauge theory applications can be implemented efficiently on graphics processing units used nowadays in high performance computing.

Contents

1. Introduction

One of the most interesting and challenging goals of modern physics is a comprehensive understanding of the elementary particles of nature and their interactions. The ultimate goal would be the unification of all known forces into a single *theory of everything*. The known forces of nature are gravity, electromagnetism, the weak force and the strong force. For three of them, the electromagnetic, the weak and the strong interactions, the accepted theory is the *Standard Model* of particle physics. Only gravity does not yet fit in the picture. The Standard Model is very successful in describing most of the experimental observations and predicted successfully many experimental results, like the existence of the top quark which was found in 1995 [1, 2]. In recent years, the most prominent prediction was the existence of a Higgs boson, since it was the last undiscovered particle of the Standard Model. Finally, it was discovered in 2012 [3, 4] and F. Englert and P. Higgs were awarded with the physics Nobel Prize a year thereafter "for the theoretical discovery of a mechanism that contributes to our understanding of the origin of mass of subatomic particles [...]". Despite its celebrated success, the Standard Model is not complete as it falls short in explaining some observations. In 2015 the Physics Nobel Prize was awarded "for the discovery of *neutrino oscillations*, which shows that neutrinos have mass" [5, 6]. In the Standard Model, however, the neutrino is described as a massless particle. Secondly, the Standard Model does not provide a particle that explains *dark matter*, a hypothetical form of matter that is believed to amount for approximately 85% of the total matter content of the universe [7]. Thus it is clear that theories *beyond the Standard Model* will be needed to satisfy the theoretical desire for a unified theory and to describe the physical implications dictated by experiments.

The mathematical framework of the Standard Model are gauge theories. The first such theory was quantum electrodynamics (QED) which combined quantum mechanical principles with special relativity to describe (electrically) charged particles: the interaction of electrons mediated by photons. The building principle for such a gauge theory is to promote a global symmetry on the Lagrangian level to a local symmetry. The symmetry of the QED Lagrangian is described by the Abelian group U(1). The gauge theories of the Standard Model built upon the framework developed for QED. The Standard Model contains the Glashow–Salam–Weinberg theory, which unifies the description of electromagnetism and the weak force into the *electroweak* interaction, and *quantum chromodynamics* (QCD), the theory of strong interactions.

In this work we will be concerned with QCD and QCD-like gauge theories. QCD describes hadronic matter, like protons, neutrons and mesons, as composite particles made of *quarks*. The force carriers, which mediate the strong interaction, are the *gluons*. Similar to the electrical charge in QED, the fermionic particles carry a charge, the so-called *color charge*, which occurs in three different types related to the symmetry group SU(3). However, in contrast to QED, the gauge bosons itself carry charge which leads to interesting new phenomena, since the gluons can interact with themselves. The mathematical manifestation of this fact is that, while the QED gauge group U(1) is an Abelian group, SU(3) is non-Abelian. Due to the self-interaction of gluons, a theory without fermionic fields is still a non-trivial theory and already contains interesting phenomena of the full theory with quarks. Because of the groundbreaking work of Yang and Mills to describe

these pure gauge theories [8], they are called *Yang–Mills theories*. As extensions for the Standard Model many different kinds of theories are discussed in the literature. One of these is the *technicolor* family, where another strong sector with *techniquarks* and *technigluons* is proposed at the TeV scale to replace the Higgs mechanism of the Standard Model. Technicolor theories are SU(N) gauge theories coupling to fermions in different representations of the gauge group. We will discuss the properties which qualify a gauge theory as a technicolor theory in more detail later.

QCD, and already the pure SU(N) gauge theories, contains two important phenomena which makes it substantially different to QED. At high energies or small distances the coupling constant becomes small: the interaction between quarks and gluons becomes weak. In 2004, this important feature was awarded the physics Nobel Prize "for the discovery of *asymptotic freedom* in the theory of the strong interaction". The importance of this feature is that it enables *perturbation theory* to be applicable for high energy processes and thus provides a systematic tool to compute cross sections of these processes. The energy scale for processes that are relevant in every day life is well below the scale Λ_{QCD} where perturbation theory becomes applicable. In this low-energy regime, the important phenomenon of the strong dynamics is the absence of free quarks and gluons. Quarks are only observed in color-neutral bound states as hadrons, like the proton and the neutron. This so-called *color confinement* is found to be realized in QCD, though an unambiguous description of its underlying mechanism and a rigorous proof is still lacking. Since perturbation theory is not applicable to study confinement and other low energy phenomena, so-called non-perturbative techniques are required.

One way to approach the non-perturbative regime is by solving the *Dyson–Schwinger equations* of the theory. The Dyson–Schwinger equations are an infinite set of coupled integral equations which can be regarded as the equations of motion for the Green functions of the theory. Full knowledge of the infinitely many Green functions, which are the correlation functions of the fields, would solve the theory in the whole perturbative and non-perturbative regime. Of course, this approach requires a truncation of the infinite tower of equations, though there is no systematic theory to estimate the errors which are introduced by these approximations. The gauge symmetry induces unphysical degrees of freedom. While physical observables are not affected by the gauge degrees of freedom, the Green functions change under *gauge transformations*. Therefore, in the Dyson–Schwinger approach one has to restrict the fields by imposing a gauge condition. Besides Coulomb gauge [9–13] which will be the subject of this work, a popular choice is the covariant Landau gauge [14–16].

Another appealing analytical approach for studying correlation functions in Coulomb gauge is the *Hamiltonian variational approach* [17–23] . There, starting from a trial wave functional for the ground state of the Yang–Mills Schrödinger equation, the best approximation within this parameterization is sought with the variational principle by minimizing the energy density. Thus, in this approach, the quality of the solution depends on the quality of the trial wave functional. As in the case of the Dyson–Schwinger approach, after truncation, one finds a finite set of coupled integral equations. While the asymptotic behavior of these equations can be studied analytically, one has to rely on numerical techniques to solve the equation on a computer in the whole momentum regime.

Lattice QCD, a numerical approach in which the continuous 3+1 dimensional space-time is discretized on a hypercubic lattice, is the only ab initio approach to non-perturbative QCD. The lattice approach is the subject of this work. Although gauge fixing is not necessary in principle in lattice field theory, we will investigate gauge variant Green functions in Coulomb gauge. The so-called continuum approaches and the lattice approach are mutu-

ally stimulating each other. While on the lattice, as opposed to the continuum, the effects which lead to a certain result cannot be disentangled easily, the continuum approach needs the lattice input to introduce the physical scale and to justify the necessary approximation. The errors which are introduced by the discrete lattice spacing and the finite volume can be improved systematically by reducing the lattice spacing and increasing the lattice size. However with increasing lattice size, the numerical work also increases with the number of lattice points. After K. G. Wilson's seminal paper in 1974 [24], the first numerical results in pure Yang–Mills theory where presented in simulations of tiny lattices of size 4^4 [25] which can be reproduced today in seconds on a desktop computer. However the state of the art simulations on large lattices and with fermion masses close to their physical values are still tasks for supercomputers, e.g. [26].

Starting around 2001, graphic processing units (GPUs) were more and more used outside their original field as *general-purpose computing* platforms (GPGPU). These energy-efficient devices are nicely suited to accelerate highly parallel algorithms, like the ones which appear in lattice field theory [27–29]. Most of the results of this work were produced with a CUDA C++ code executed on GPUs.

The outline of this work is as follows. Starting from the continuum theory we will introduce the basic concepts of lattice QCD and discuss the relevant observables and Coulomb gauge correlation functions in Chapter 2. It is a well-known fact that the Coulomb gauge condition is not enough to select a unique gauge field on the *gauge orbit*, the set of fields which are related by a gauge transformation. This gives rise to the so-called *Gribov problem* and requires an additional condition on the gauge fields. In Chapter 3 we will discuss the Gribov problem in detail and we will compare two attempts to resolve it. With increasing temperature, QCD will undergo a phase transition from the confined to the deconfined phase which is also found in lattice calculations. The *deconfinement phase transition*, which was expected to be visible in the Coulomb gauge correlation functions, will be investigated in Chapter 4. We will find that the lattice Coulomb gauge correlation functions do not sense the deconfinement phase transition, in contrast to the continuum approach. In Chapter 5 we will propose an explanation which is based on the *center vortex picture* of confinement. In Chapter 6, we will study a strongly coupled theory, which is significantly different to the QCD-like theories we discussed so far: we will analyze a possible technicolor candidate, the *minimal walking technicolor* theory, an SU(2) gauge theory coupled to two fermions in the adjoint representation. Finally, in Chapter 7, we will show the steps to port a lattice application to GPUs at the example of the gauge fixing code. We will discuss performance optimizations and compare the result to a CPU application.

2. From Continuum QCD to Lattice Field Theory in Coulomb Gauge

In this chapter we will first give an introduction to quantum chromodynamics (QCD), the theory that describes the strong interaction. Before we introduce lattice field theory we will give an overview of the Hamiltonian variational approach in Section 2.3, a non-perturbative (semi-) analytical approach in Coulomb gauge to which we will compare the lattice results. In Section 2.4 we explain the lattice approach. Then we discuss how confinement can be measured on the lattice and discuss different confinement mechanisms in Section 2.5. In Section 2.6 we will finally introduce the Coulomb gauge propagators which we will investigate in different setups in the following chapters. There we will also summarize related work in Coulomb gauge and discuss some open issues between results from the Hamiltonian approach and the lattice.

2.1. Quantum Chromodynamics

The fundamental equation of QCD, which describes the interaction of quarks and gluons, is the Lagrangian density [30, 31]

$$\mathcal{L} = -\frac{1}{4} F^a_{\mu\nu} F^{a,\mu\nu} + \sum_f \bar{q}_f \left(\mathrm{i}\gamma_\mu D^\mu - m_f \right) q_f. \tag{2.1}$$

The first term describes the gluons and, in contrast to an Abelian gauge theory, like QED, their self-interaction. The difference shows up in the Yang–Mills field strength tensor

$$F^a_{\mu\nu} = \partial_\mu A^a_\nu - \partial_\nu A^a_\mu - g f_{abc} A^b_\mu A^c_\nu, \tag{2.2}$$

where a term quadratic in the gauge fields A appears which is not present in electrodynamics. The quadratic contribution is the reason why gluons, unlike photons, interact with each other. Therefore, the theory without fermionic fields, i.e. without quarks, is already nontrivial and contains many interesting features like confinement. The Lagrangian contains $N_c^2 - 1$ real-valued fields A^a_μ, the color components, which can be combined in the gauge field

$$A_\mu = \sum_a A^a_\mu T_a \tag{2.3}$$

which is an element of the Lie algebra of the gauge group. Here N_c denotes the number of colors, where $N_c = 3$ for QCD[1]. The constants T_a are $N_c \times N_c$ traceless Hermitian matrices, the generators of the gauge group $\mathrm{SU}(N_c)$ which are related to each other by the structure constants f^{abc}

$$\left[T^a, T^b \right] = \sum_c f^{abc} T^c, \tag{2.4}$$

and normalized such that

$$\mathrm{tr} T^a T^b = \frac{1}{2} \delta^{ab}. \tag{2.5}$$

[1] In practice it is often convenient to study the simpler theory with $N_c = 2$.

The second term in (2.1) describes the interaction of the quarks mediated by the gluons. It is a sum of the interactions of the different quark flavors q_f, which do not mix in the strong dynamics. The only difference is their bare mass m_f. Similar to QED the covariant derivative

$$D_\mu = \partial_\mu + \mathrm{i}gA_\mu \tag{2.6}$$

is introduced which makes the Lagrangian invariant under the *local* gauge transformation $g(x) \in \mathrm{SU}(N)$ [32, Chapter 15]

$$q_f(x) \to g(x) q_f(x), \tag{2.7}$$

$$A_\mu(x) \to g(x) \left(A_\mu(x) - \frac{\mathrm{i}}{g} \partial_\mu \right) g^\dagger(x). \tag{2.8}$$

The gauge transformations $g(x)$, as elements of the gauge group $\mathrm{SU}(N)$, can be parameterized as

$$g(x) = \exp\left[\mathrm{i}T^a \phi^a(x)\right] \tag{2.9}$$

with the generators T^a and real-valued functions $\phi^a(x)$.

In this work we will be interested in the lattice approach to gauge theories. The standard lattice approach is based on the path integral formulation, where we evaluate the expectation value of a quantity $O[q, \bar{q}, A_\mu]$ as

$$\langle O \rangle = \frac{1}{Z} \int \mathcal{D}\bar{q}\mathcal{D}q\mathcal{D}A_\mu \; O[\bar{q}, q, A] \; \mathrm{e}^{\mathrm{i}\int \mathrm{d}^4x \; \mathcal{L}[\bar{q}, q, A_\mu]} \tag{2.10}$$

$$Z = \int \mathcal{D}\bar{q}\mathcal{D}q\mathcal{D}A_\mu \; \mathrm{e}^{\mathrm{i}\int \mathrm{d}^4x \; \mathcal{L}[\bar{q}, q, A_\mu]}. \tag{2.11}$$

The partition function Z normalizes the expectation value such that $\langle 1 \rangle = 1$. The exponential factor weights the field contributions with the QCD action

$$S_{\mathrm{QCD}} = \int \mathrm{d}^4x \; \mathcal{L}[\bar{q}, q, A_\mu] = \int \mathrm{d}^4x \; \mathcal{L}_{\mathrm{YM}}[A_\mu] + \int \mathrm{d}^4x \; \mathcal{L}_f[\bar{q}, q, A_\mu], \tag{2.12}$$

where we introduced the subscript YM for the Yang–Mills part of the Lagrangian and the subscript f for the fermionic contribution. The functional integration measure $\int \mathcal{D}\bar{q}\mathcal{D}q\mathcal{D}A_\mu$ cannot be used as it stands since it introduces double-counting of gauge-equivalent fields. In the next chapter we will resolve this issue by gauge fixing via the Faddeev–Popov technique.

2.2. Gauge Fixing

The QCD action as given in (2.12) is not yet complete. In the path integral formulation of the expectation value (2.10) the integral $\int \mathcal{D}A_\mu$ is formally defined as an integration over the group at each (continuous) space-time point. However, for each gauge field A_μ there exist infinitely many gauge-equivalent fields. The set of these fields forms an equivalence class, called the gauge orbit of A_μ

$$\mathrm{orb}[A_\mu] = \left\{ A^g_\mu \mid A^g_\mu = gA_\mu g^\dagger - \frac{i}{g_0} \left(\partial_\mu g\right) g^\dagger; g \in \mathrm{SU}(N) \right\}. \tag{2.13}$$

Formally we can factorize a divergent integral over the group space in the partition function

$$Z = \int \mathcal{D}A_\mu \, \mathrm{e}^{\mathrm{i}S_{\mathrm{YM}}[A_\mu]} = \int \mathcal{D}g\mathcal{D}\bar{A}_\mu \, \mathrm{e}^{\mathrm{i}S_{\mathrm{YM}}[\bar{A}_\mu]} = \int \mathcal{D}\bar{A}_\mu \, \mathrm{e}^{\mathrm{i}S_{\mathrm{YM}}[\bar{A}_\mu]} \int \mathcal{D}g \tag{2.14}$$

where $\bar{A}_\mu$ represents one selected gauge field of each gauge orbit. Since $S_{\mathrm{YM}}[A_\mu]$ is gauge invariant, the divergent factor $\int \mathcal{D}g$ can be separated and demonstrates the overcounting of gauge-equivalent fields.

To resolve the double counting of gauge-equivalent fields, Faddeev and Popov [33] developed a technique to single-out one representative of each gauge orbit. We formulate the gauge condition in the form

$$F[A_\mu] \stackrel{!}{=} 0, \tag{2.15}$$

where F is a functional of the gauge fields. In this work we will discuss Coulomb gauge, i.e. $F[A_\mu] = \partial_i A_i$, however the technique described here is valid for other gauge conditions in the form (2.15). For the following we introduce the so-called Faddeev–Popov determinant $\mathcal{J}_F[A_\mu]$ by the identity

$$\mathbb{1} = \mathcal{J}_F[A_\mu] \int \mathcal{D}g \delta[F[A^g_\mu]], \tag{2.16}$$

where $\delta[F[A^g_\mu]]$ is a delta-functional which restricts the integration to gauge fields satisfying (2.15). Thus, the Faddeev–Popov determinant $\mathcal{J}_F[A_\mu]$ depends only on a single configuration from each gauge orbit. The measure in the integration (2.16) over the group space $\mathrm{SU}(N)$ is the functional measure

$$\mathcal{D}g = \prod_x \mathrm{d}g(x) \ , \tag{2.17}$$

a product of the Haar measure $\mathrm{d}g(x)$ at each continuous space-time point. The Haar measure of a group G is invariant under left and right multiplication by a group element

$$\mathrm{d}g \ = \mathrm{d}gg' \ = \mathrm{d}g'g \tag{2.18}$$

and normalized such that

$$\int \mathrm{d}g \ = 1. \tag{2.19}$$

By inserting the identity (2.16) in the path integral (2.11) we get the gauge fixed partition function

$$Z_{\mathrm{gf}} = \int \mathcal{D}A_\mu \ \mathcal{J}_F[A_\mu] \int \mathcal{D}g \delta[F[A^g_\mu]] \, \mathrm{e}^{\mathrm{i}S_{\mathrm{YM}}[A_\mu]} \tag{2.20}$$

$$= \int \mathcal{D}g \int \mathcal{D}A_\mu \ \mathcal{J}_F[A_\mu] \delta[F[A^g_\mu]] \, \mathrm{e}^{\mathrm{i}S_{\mathrm{YM}}[A_\mu]}, \tag{2.21}$$

where in the second line we applied a gauge transformation $A^g_\mu \to A_\mu$ and used that $\mathcal{J}_F[A_\mu]$ and $S_{\mathrm{YM}}[A_\mu]$ are gauge invariant. The integral over A_μ is now independent of the integral over g and thus $\int \mathcal{D}g$ contributes only as an irrelevant normalization with the volume in group space, which cancels in expectation values.

The Faddeev–Popov determinant introduced in (2.16)

$$\mathcal{J}_F[A_\mu] = \det M = \det \left[\frac{\delta F[A^g_\mu]}{\delta g} \right] \tag{2.22}$$

can be regarded as the Jacobian of a coordinate transformation from Cartesian coordinates to curvilinear coordinates [34]. In Coulomb gauge the Faddeev–Popov operator M is given by

$$M^{ab}[A^g_\mu] = -\partial_i D^{ab}_i[A^g_\mu], \tag{2.23}$$

where $D_i^{ab}[A_\mu^g]$ is the covariant derivative in the adjoint representation. It is convenient to include the Faddeev–Popov determinant directly in the action by introducing anti-commuting (Grassmann valued) fields, the so-called ghosts c, $\bar{c}$

$$\mathcal{J}_F[A_\mu] = \int \mathcal{D}\bar{c}\mathcal{D}c\, \mathrm{e}^{-\mathrm{i}\int \mathrm{d}^4x\, \bar{c}^a M^{ab} c^b}. \tag{2.24}$$

Although the ghost fields do not represent physical particles their structure gives insight in physical phenomena, as for example in the Gribov–Zwanziger scenario of confinement, Section 2.5.5.

Again, for convenience we can rewrite the δ-function in (2.16) by

$$\delta[F[A_\mu^g]] = \mathrm{e}^{-\frac{\mathrm{i}}{2\alpha}F[A_\mu^g]^2} \tag{2.25}$$

which, for small α, is highly peaked at the gauge field which satisfies the gauge condition. This allows to include the δ-function in the Lagrangian

$$\mathcal{L} = \mathcal{L}_{\mathrm{YM}} - \frac{1}{2\alpha}F[A_\mu^g]^2 - \bar{c}^a M^{ab} c^b. \tag{2.26}$$

With Eq. (2.26) we arrived at the gauge fixed Lagrangian for pure Yang–Mills theory.

2.2.1. Gribov Copies

The original idea of Faddeev and Popov is based on the assumption that a gauge condition as in (2.15) is enough to single out one representative of each gauge orbit. However, in non-Abelian gauge theories this is no longer true. Gribov [35] found that there exist configurations which are non-equivalent but obey the gauge condition. These configurations are the so-called *gauge copies* or *Gribov copies*.

To select only a single gauge copy from the gauge orbit, Gribov proposed to restrict the path integral to the region where the Faddeev–Popov operator is strictly positive definite, the so-called *first Gribov region*

$$\Omega = \{A_\mu \mid \partial_i A_i = 0, M(A_\mu) > 0\}\,. \tag{2.27}$$

For Coulomb gauge the restriction to the first Gribov region can be implemented by minimizing the functional

$$F_A[g] = \int \mathrm{d}^3x\; A_i^g(x) A_i^g(x). \tag{2.28}$$

By expansion of the functional around small gauge transformation one finds that indeed all *local minima* fulfill the Coulomb gauge condition $\partial_i A_i(x) = 0$.

However the restriction to the first Gribov region is still not enough to select only gauge-inequivalent configurations, see e.g. Ref. [36]. A further restriction can be achieved by choosing the absolute minimum of (2.28) which defines the *fundamental modular region* (FMR)

$$\Lambda = \{A_\mu \mid F_A[1] < F_A[g]\ \forall g \in \mathrm{SU}(N)\} \tag{2.29}$$

which is by construction contained in the first Gribov region Ω.

For the first Gribov region and the fundamental modular region one can find several properties of which we will summarize the most important ones for further discussion in Chapter 3.

One can easily show that the vacuum configuration $A_i = 0$ is contained in Λ and in Ω. For $A_i = 0$ the covariant derivative in (2.23) reduces to the partial derivative ∂_i and thus

the Faddeev–Popov operator is given by the (negative) Laplacian $M^{ab} = -\delta^{ab}\Delta$. Since the eigenvalues of the negative Laplacian are strictly positive, the configuration $A_i = 0$ satisfies all conditions of the Gribov region (2.27). Additionally, since the functional (2.28) is positive and takes its smallest value $F_{A_i=0}[1] = 0$, the vacuum is also inside of the FMR.

A very important property is that both the Gribov region and the FMR are intersected by every gauge orbit at least once [37]. Thus, with the restriction to the FMR (exactly) one representative of each gauge orbit still enters the path integral.

The Gribov region is bound by the (first) Gribov Horizon $\partial\Omega$ where the lowest non-trivial eigenvalue of the Faddeev–Popov operator is zero. It has common points with the border of the FMR $\partial\Lambda$ when the gauge fixing functional has degenerate absolute minima [38].

Whereas the identification of configurations in the FMR is highly non-trivial in the lattice theory, see Chapter 3, Zwanziger showed that the Gribov copies inside the Gribov region have no influence on expectation values calculated from Dyson–Schwinger equations in the continuum theory [39].

In Section 2.5.5 we will discuss the importance of configurations close to the Gribov horizon for the infrared physics and the confinement phenomenon.

2.3. The Hamiltonian Approach

In this section we will give a brief overview of the canonical quantization of Yang–Mills theory in Coulomb gauge which is the basis for the Hamiltonian variational approach. For a more detailed discussion see the recent review [34] and references therein.

2.3.1. Canonical Quantization of Yang–Mills Theory

In the following we will explain the approach for pure Yang-Mills theory, i.e. the theory without dynamical quark fields. The action for pure Yang-Mills theory is given by (2.1) as

$$S_{\mathrm{YM}} = \int \mathrm{d}^4x\ \mathcal{L}_{\mathrm{YM}}(x) = -\frac{1}{4}\int \mathrm{d}^4x\ F^a_{\mu\nu}(x)F^{a,\mu\nu}(x) \tag{2.30}$$

with the non-Abelian field strength tensor (2.2). The canonical quantization builds upon the classical Hamiltonian density $\mathcal{H}$. To obtain the Hamiltonian from the Lagrangian density we interpret the gauge fields $A_\mu(x)$ as coordinates. The conjugate momenta are given by the derivatives of the Lagrangian $\mathcal{L}$ with respect to the time derivative of the gauge field $\dot{A}^a_\mu(x) = \partial_0 A^a_\mu(x)$

$$\Pi^a_\mu(x) = \frac{\partial\mathcal{L}(x)}{\partial\dot{A}^a_\mu(x)}. \tag{2.31}$$

In the canonical quantization the quantized theory is obtained by imposing equal-time commutation relations

$$\left[\hat{A}^a_\mu(\boldsymbol{x},t), \hat{\Pi}^b_\nu(\boldsymbol{x}',t)\right] = -\mathrm{i}\delta^{ab}g_{\mu\nu}\delta(\boldsymbol{x}-\boldsymbol{x}') \tag{2.32}$$

$$\left[\hat{A}^a_\nu(\boldsymbol{x},t), \hat{A}^b_\nu(\boldsymbol{x}',t)\right] = 0 \tag{2.33}$$

$$\left[\hat{\Pi}^a_\nu(\boldsymbol{x},t), \hat{\Pi}^b_\nu(\boldsymbol{x}',t)\right] = 0 \tag{2.34}$$

However, without further requirements one runs into a problem. Since the temporal momentum operator vanishes

$$\Pi^a_0(x) = 0, \tag{2.35}$$

the corresponding equal time commutation relations cannot be satisfied. A way to avoid this problem is to impose the Weyl gauge $A_0^a = 0$ before quantization. Then the canonical momenta, associated with the remaining spatial fields $A_i^a(x)$, are

$$\Pi_i^a(x) = \partial_0 A_i^a = -E_i^a(x), \tag{2.36}$$

where we introduced the color electric field $E_i^a(x)$. The Hamiltonian is then found to be

$$\mathcal{H}(x) = \Pi_i^a(x)\dot{A}_\mu^a(x) - \mathcal{L}_{YM}(x) \tag{2.37}$$

$$= \frac{1}{2}\left(E_i^a(x)E_i^a(x) + B_i^a(x)B_i^a(x)\right), \tag{2.38}$$

with the color magnet field $B_i^a(x) = \frac{1}{2}\varepsilon_{ijk}F_{jk}$ which is defined in analogy to the Maxwell theory. The non-vanishing commutation relations take the form[2]

$$\left[\hat{A}_i^a(\boldsymbol{x}), -\hat{E}_j^b(\boldsymbol{x}')\right] = \mathrm{i}\delta^{ab}\delta_{ij}\delta(\boldsymbol{x}-\boldsymbol{x}'). \tag{2.39}$$

In the coordinate (or field representation) of the functional Schrödinger picture [40] the wave functionals are functions of the gauge field

$$\Psi[A] = \langle A|\Psi\rangle, \tag{2.40}$$

where the states $|A\rangle$ are the eigenvectors of the field operators $\hat{A}$ with eigenvalue A,

$$\hat{A}_i^a(\boldsymbol{x})\,|A\rangle = A_i^a(\boldsymbol{x})\,|A\rangle\,. \tag{2.41}$$

The momentum operator (electric field operator) is the functional differential operator with respect to the gauge fields $A_i^a(\boldsymbol{x})$

$$\langle A|\,\hat{\Pi}_i^a(\boldsymbol{x}) = -\mathrm{i}\frac{\delta}{\delta A_i(\boldsymbol{x})}\,\langle A|\,. \tag{2.42}$$

Thus, the functional Schrödinger equation takes the form

$$H\Psi[A] = \int \mathrm{d}^3x\ \mathcal{H}(\boldsymbol{x})\Psi[A] = E\Psi[A] \tag{2.43}$$

$$\int \mathrm{d}^3x\ \left[\frac{1}{2}\frac{\delta}{\delta A_i(\boldsymbol{x})}\frac{\delta}{\delta A_i(\boldsymbol{x})} + \frac{1}{4}F_{ij}^a(\boldsymbol{x})F_{ij}^a(\boldsymbol{x})\right] = E\Psi[A]. \tag{2.44}$$

Due to the Weyl gauge, the equations of motion no longer contain Gauß's law. Therefore, the Schrödinger equation allows for a larger set of solutions which are not physical. The states have to be restricted to the physical Hilbert space by enforcing Gauß's law, as an auxiliary condition, on the wave functionals $\Psi[A]$. In the presence of a an external color charge density ρ_{ext}^a Gauß's law reads

$$D_i^{ab}(\boldsymbol{x})\Pi_i^b(\boldsymbol{x})\Psi[A] = -g\rho_{\text{ext}}^a\Psi[A], \tag{2.45}$$

with the covariant derivative in the adjoint representation of the gauge group

$$D_i^{ab}(\boldsymbol{x}) = \delta^{ab}\partial_i - gf^{abc}A_i^c(x). \tag{2.46}$$

[2] We use the non-covariant notation in the following as Lorentz invariance is broken by the Hamiltonian formulation.

The expectation value of an operator, which is a functional of the gauge field and the conjugate momentum in the canonical formalism, with respect to the state $|\Psi\rangle$ is given by

$$\langle O[A,\Pi]\rangle_\Psi = \langle\Psi|\, O[A,\Pi]\,|\Psi\rangle \tag{2.47}$$

with the scalar product defined as the path integral

$$\langle\phi|\ldots|\psi\rangle = \int \mathcal{D}\boldsymbol{A}\phi^*[\boldsymbol{A}]\ldots\psi[\boldsymbol{A}] \tag{2.48}$$

In the variational approach it turns out that working with gauge invariant states is not practical and therefore it is advantageous to fix the gauge completely. The choice of Weyl gauge, which is necessary for the canonical quantization, does still allow for time-independent gauge transformations $g(\boldsymbol{x})$. To fix the residual gauge freedom it is convenient to choose Coulomb gauge implemented by the Faddeev–Popov technique which was introduced in Section 2.2.

2.3.2. The Coulomb Gauge Hamiltonian

In Coulomb gauge $\partial_i A_i = 0$, only the transverse field components

$$A_i^\perp(\boldsymbol{x}) = t_{ij}(\boldsymbol{x})A_j(\boldsymbol{x}) \tag{2.49}$$

survive, with the transverse projector defined as

$$t_{ij}(\boldsymbol{x}) = \delta_{ij} - \frac{\partial_i\partial_j}{\partial^2}. \tag{2.50}$$

After Faddeev–Popov gauge fixing to Coulomb gauge, the scalar product (2.48) now contains the Coulomb gauge Faddeev–Popov determinant, compare (2.23),

$$\mathcal{J}_F = \det\left(-D_i^{ab}[\boldsymbol{A}^\perp]\partial_i\right), \tag{2.51}$$

and the integration is over the transverse fields

$$\langle\phi|\ldots|\psi\rangle = \int \mathcal{D}\boldsymbol{A}^\perp\mathcal{J}_F[\boldsymbol{A}^\perp]\phi^*[\boldsymbol{A}^\perp]\ldots\psi[\boldsymbol{A}^\perp]. \tag{2.52}$$

While the longitudinal gauge field components $\boldsymbol{A}^\parallel$ were eliminated by the gauge condition, the longitudinal conjugate momenta $\boldsymbol{\Pi}^\parallel$ are still present. However, from Gauß's law (2.45) one finds

$$\boldsymbol{\Pi}^{\parallel,a}\Psi[\boldsymbol{A}] = -\boldsymbol{\nabla}\left(-D_i\partial_i\right)^{-1}\rho^a\Psi[\boldsymbol{A}] \tag{2.53}$$

which can be used to eliminate $\boldsymbol{\Pi}^\parallel$, see e.g. Refs. [41, 42]. The non-Abelian color charge density ρ^a contains the external charge from Gauß's law ρ^a_{ext} and the dynamical charge density from the gluon fields

$$\rho^a = \rho^a_{\text{ext}} - f^{abc}\boldsymbol{A}^b\boldsymbol{\Pi}^{\perp,c}. \tag{2.54}$$

Finally one finds the Hamiltonian in Coulomb gauge, which was first derived in Ref. [43]

$$H = H_{\text{YM}} + H_C \tag{2.55}$$

with

$$H_{\text{YM}} = \frac{1}{2}\int \mathrm{d}^3x\ \left[\mathcal{J}_F[\boldsymbol{A}]^{-1}\Pi_i^a(\boldsymbol{x})\mathcal{J}_F[\boldsymbol{A}]\Pi_i^a(\boldsymbol{x}) + \frac{1}{2}F_{ij}^a(\boldsymbol{x})F_{ij}^a(\boldsymbol{x})\right] \tag{2.56}$$

and

$$H_C = \frac{g^2}{2} \int \mathrm{d}^3x \int \mathrm{d}^3y \; \mathcal{J}_F[\boldsymbol{A}]^{-1} \rho^a(\boldsymbol{x}) \mathcal{J}_F[\boldsymbol{A}] F_A^{ab}(\boldsymbol{x}, \boldsymbol{y}) \rho^a(\boldsymbol{y}). \tag{2.57}$$

The second contribution H_C is called the Coulomb term, where we introduced the non-Abelian Coulomb kernel

$$F_A^{ab}(\boldsymbol{x}, \boldsymbol{y}) = \int \mathrm{d}^3z \; G_A^{ac}(\boldsymbol{x}, \boldsymbol{z})(-\Delta_z) G_A^{cb}(\boldsymbol{z}, \boldsymbol{y}) \tag{2.58}$$

with the ghost operator, which is the inverse of the Faddeev–Popov operator

$$G_A^{bc} = (-D_i^{ab}\partial_i)^{-1} \delta^{ac} \delta(\boldsymbol{x} - \boldsymbol{y}). \tag{2.59}$$

The vacuum expectation value of (2.58) defines the non-Abelian Coulomb potential

$$V(\boldsymbol{x} - \boldsymbol{y}) = g^2 \left\langle F_A(\boldsymbol{x}, \boldsymbol{y}) \right\rangle \tag{2.60}$$

In the Abelian theory, where the Faddeev–Popov operator reduces to the (negative) Laplacian, the Coulomb kernel is just the Green function of the Laplacian

$$F_A^{ab}(\boldsymbol{x}, \boldsymbol{y}) = \frac{\delta^{ab}}{4\pi |\boldsymbol{x} - \boldsymbol{y}|} \tag{2.61}$$

and thus the Coulomb term reduces to the potential energy of an electromagnetic field in the presence of external charges

$$H_C = \frac{g^2}{2} \int \mathrm{d}^3x \int \mathrm{d}^3y \; \frac{\rho_{\mathrm{ext}}(\boldsymbol{x}) \rho_{\mathrm{ext}}(\boldsymbol{y})}{4\pi |\boldsymbol{x} - \boldsymbol{y}|}. \tag{2.62}$$

The Coulomb gauge Hamiltonian (2.55) is substantially more complicated than the Hamiltonian in Weyl gauge (2.37), however the solutions of the functional Schrödinger equation with the Coulomb Hamiltonian have the advantage that they automatically fulfill Gauß's law.

2.3.3. The Variational Approach

Before we discuss the lattice approach in the next section, we will give a basic overview of the variational approach to Coulomb gauge. In later chapters we will compare the lattice solutions to continuum results of the Hamiltonian variational approach.

In the variational approach, which can also be used in ordinary quantum mechanics, one seeks the best approximation of the ground state by minimizing the energy. For this purpose one chooses an ansatz for the wave functional which contains free parameters. The values at which energy is minimal describes the best approximation for the wave functional within the space spanned by the trial wave functional. The energy to be minimized is the expectation value of the Hamilton operator

$$E[\Psi] = \langle \Psi | \, H \, | \Psi \rangle = \int \mathcal{D}A \mathcal{J}_F[A_\mu] \Psi^*[A] H \Psi[A]. \tag{2.63}$$

A first choice for the trial wave functional is the Gaussian ansatz of Ref. [17]

$$\Psi[A] = \frac{1}{\sqrt{\mathcal{J}_F[A_\mu]}} \exp\left[-\frac{1}{2} \int \mathrm{d}^3x \int \mathrm{d}^3y \; A_i^a(\boldsymbol{x}) \omega(\boldsymbol{x}, \boldsymbol{y}) A_i^a(\boldsymbol{y}) \right]. \tag{2.64}$$

with the variational kernel $\omega(\boldsymbol{x}, \boldsymbol{y})$. With this ansatz the gluon propagator $D(\boldsymbol{p})$ is the inverse of the variational kernel. From the so-called gap equation for ω one finds two possible solutions [17, 18]. The one which leads to a linear rising Coulomb potential, is described by the Gribov formula [35]

$$2D(\boldsymbol{p}) = \omega(\boldsymbol{p})^{-1} = \frac{1}{\sqrt{\boldsymbol{p}^2 + \frac{M^4}{\boldsymbol{p}^2}}}. \tag{2.65}$$

The propagator has the correct perturbative UV behavior and approaches zero in the infrared which signals the confinement of gluons. The result is in very good agreement with the lattice results of [44]. Further results which are relevant for this work will be discussed in Section 2.6 where the lattice quantities are introduced.

Since this first result, the Hamiltonian variational approach was further refined by investigating ansätze beyond the pure Gaussian functional [19], by including quark interactions [21–23] and by extension to finite temperatures [20].

2.4. Introduction to Lattice Field Theory

In lattice gauge theory the continuous space-time is discretized on a hyper-cubic lattice. After discretization, the space-time integrals of the continuum theory are finite sums and can be calculated on a computer. Additionally the finite lattice spacing serves as a ultraviolet regulator for the theory. Since there is a close connection between an Euclidean field theory and statistical mechanics one can apply many well-known techniques to lattice field theory which were originally developed in the context of statistical mechanics.

In the following we will summarize the most important basics of the lattice approach. For a detailed introduction many textbooks are available, see e.g. [31, 45–47]. We will introduce the lattice framework along the lines of [31]. In (2.10) we introduced the Minkowskian path integral formulation where the partition function (2.11) reads for the pure Yang–Mills part

$$Z = \int \mathcal{D}A_\mu \ \mathrm{e}^{\mathrm{i}S[A]} \tag{2.66}$$

which has a similar structure as the partition function of a statistical system

$$Z = \sum_s \mathrm{e}^{-\beta H[s]} \tag{2.67}$$

where the summation is over all possible realizations of the system and $\beta = \frac{1}{k_B T}$ is the inverse temperature. A simple example for the classical Hamiltonian $H[s]$ would be the Ising model which describes a system of spins with nearest neighbor couplings. The connection of (2.66) to the statistical system becomes even more obvious after a Wick rotation to imaginary time $x_0 \to -\mathrm{i}x_0$. After Wick rotation we obtain the Euclidean partition function

$$Z = \int \mathcal{D}A_\mu \ \mathrm{e}^{-S_E[A]}, \quad S_E = \frac{1}{4}\int \mathrm{d}^4x \ F^a_{\mu\nu}(x)F^a_{\mu\nu}(x). \tag{2.68}$$

In partition function of the Euclidean field theory, the factor $\mathrm{e}^{-S_E[A]}$ plays the role of the Boltzmann weight $\mathrm{e}^{-\beta H[s]}$ of statistical mechanics and the sum over all possible states is replaced by an integral over infinitely many *continuous* field configurations. This connection allows us to solve expectation values of the form (2.10) by means of Monte Carlo integration, Section 2.4.1. However, for this approach we need to restrict the continuous fields to discrete ones.

From the Euclidean formulation of (2.10) we proceed to the discrete lattice version by restricting the space-time points to $x_\mu = a_\mu n_\mu$, where a_μ is the lattice spacing in μ direction and n_μ is a four dimensional vector of integers. Each component is restricted to a finite number $n_\mu = 0, \ldots, N_\mu - 1$, where we usually use the same lattice structure in all spatial directions, i.e. we define the spatial lattice extent $N_s \equiv N_1 = N_2 = N_3$ and the spatial lattice spacing a_s accordingly. The temporal lattice dimension will be defined by $N_t \equiv N_0$ and the lattice spacing in time direction a_t.[3] We will use periodic boundary conditions for the lattice such that the lattice sites n_μ and $n_\mu + N_\mu$ are identified. While the fermionic fields are defined on the lattice sites

$$q(n), \quad \bar{q}(n) \tag{2.69}$$

the lattice version of the gauge fields live on the connection between neighboring lattice sites along coordinate axes, the so-called links.

The *link variables* are introduced for the same reason as in the continuum theory, where the gauge fields enter the covariant derivative to formulate gauge invariant derivative terms in the Lagrangian. A straightforward translation of the continuum derivative, using a symmetric discretization, yields

$$\partial_\mu q(x) = \frac{q(n+\hat{\mu}) - q(n-\hat{\mu})}{2a}, \tag{2.70}$$

where $\hat{\mu}$ is the (lattice) unit vector in μ direction. A gauge transformation of the form

$$q(n) \to q'(n) = g(n)q(n), \quad \bar{q}(n) \to \bar{q}'(n) = \bar{q}(n)g^\dagger(n), \tag{2.71}$$

with $g(n) \in \mathrm{SU}(N)$, violates gauge invariance in products of quark fields $\bar{q}(n), q(n+\hat{\mu})$ at different lattice points. Connecting these terms by a link variable $U_\mu(n) \in \mathrm{SU}(N)$ from n to $n+\hat{\mu}$ which transforms like

$$U_\mu(n) \to U'_\mu(n) = g(n)U_\mu(n)g^\dagger(n+\hat{\mu}) \tag{2.72}$$

yields a gauge invariant object

$$\bar{q}(n)U_\mu(n)q(n+\hat{\mu}) \to \bar{q}'(n)U'_\mu(n)q'(n+\hat{\mu}) \tag{2.73}$$

$$= q(n)g^\dagger(n)g(n)U_\mu(n)g^\dagger(n+\hat{\mu})g(n+\hat{\mu})q(n+\hat{\mu}), \tag{2.74}$$

The expressions $gg^\dagger$ at the same lattice point cancel as they are unitary matrices. The link $U_\mu(n)$ is directed from site n to $n+\hat{\mu}$. The link of opposite direction $U_{-\mu}(n+\mu)$ is the inverse $U^\dagger(n)$, as illustrated in Fig. 2.1.

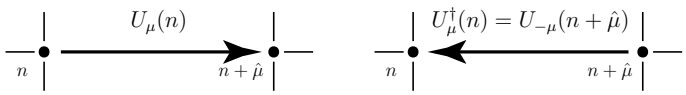

Figure 2.1.: A link $U_\mu(n)$ connecting the lattice points n and $n+\hat{\mu}$ and the link in the opposite direction $U^\dagger(n)$.

[3] Although we are working in the Euclidean formulation, we will use the index 0 for the time direction.

A first *naive fermion gauge action* would then be

$$S_f^{\text{lat}} = a^4 \sum_{n\in\Lambda} \sum_{\mu=0}^{3} \frac{1}{2a} \left[\bar{q}(n)\gamma_\mu U_\mu(n) q(n+\hat{\mu}) - \bar{q}(n)\gamma_\mu U_\mu^\dagger(n-\hat{\mu}) q(n-\hat{\mu}) \right] + m\bar{q}(n)q(n) \tag{2.75}$$

$$= a^4 \sum_{n,m\in\Lambda} \bar{q}(n) D(n,m) q(m), \tag{2.76}$$

where we introduced the lattice Dirac operator which is given by

$$D(n,m) = \sum_{\mu=0}^{3} \frac{1}{2a} \gamma_\mu \left[\delta_{m,n+\hat{\mu}} U_\mu(n) - \delta_{m,n-\hat{\mu}} U_\mu^\dagger(n-\hat{\mu}) \right] + m\delta_{n,m}. \tag{2.77}$$

However, this action suffers from the so-called fermion doubling problem: After Fourier transformation and inversion of the naive lattice Dirac operator we obtain the quark propagator[4]

$$\langle \bar{q}(x) q(y) \rangle = \lim_{a\to 0} \int_{-\pi/a}^{\pi/a} \frac{\mathrm{d}^4 p}{(2\pi)^4} \frac{-\frac{\mathrm{i}}{a} \sum_{\mu=0}^{3} \gamma_\mu \sin(a p_\mu) + m}{\frac{1}{a^2} \sum_{\mu=0}^{3} \sin^2(a p_\mu) + m^2} \tag{2.78}$$

which is of the same form as the continuum propagator after identification of the lattice momentum

$$\tilde{p}_\mu = \frac{1}{a} \sin(a p_\mu). \tag{2.79}$$

Equation (2.78), indeed, has the correct pole at $p = (0,0,0,0)$ in the continuum limit (for massless fermions). However, there appear additional poles at the edges of the Brillouin zone, i.e. whenever the components of p are either 0 or π/a. Thus, in $d = 4$ dimensions 15 unwanted poles are introduced which are pure lattice artifacts. Wilson proposed to decouple the doublers from the theory by giving them an extra mass proportional to $1/a$ which makes the doublers infinitely heavy in the continuum limit. The Dirac operator in momentum space then reads

$$D(p) = m + \frac{\mathrm{i}}{a} \sum_{\mu=0}^{3} \gamma_\mu \sin(a p_\mu) + \frac{1}{a} \sum_{\mu=0}^{3} (1 - \cos(a p_\mu)). \tag{2.80}$$

Though Wilson's fermion action solves the doubling problem, it explicitly breaks chiral symmetry. Actually, a theorem by Nielsen and Ninomiya [48–50] gives strong bounds on constructing actions which overcome the doubling problem and preserve chiral symmetry. In Appendix D.1, where we use the Wilson Dirac operator, we will discuss more problems which arise due to the Wilson term.

The continuum analog of a link variable is the parallel transporter (along a lattice axis)

$$U_\mu(n) = U(x, x + a\hat{\mu}) = P \exp\left\{ \mathrm{i} \int_x^{x+a\hat{\mu}} A_\mu(y) \mathrm{d}y \right\}, \tag{2.81}$$

where P denotes path-ordering. This relation allows to interpret the link variables $U_\mu(n)$ as the lattice version of the gauge fields

$$U_\mu(n) = \exp\left\{ \mathrm{i} a A_\mu \left(n + \frac{1}{2}\hat{\mu} \right) \right\}, \tag{2.82}$$

[4] See for example Ref. [46, Chapter 4] and Ref. [31, Chapter 5.2].

where the lattice gauge fields are usually defined at the mid-point between lattice sites. To describe the gauge dynamics we need a lattice gauge action for link variables which is gauge invariant and reproduces the correct continuum action in the limit $a \to 0$. The simplest form is the plaquette action of Wilson [24]. To obtain a gauge invariant object of link variables we can take the trace of a closed loop of links. The smallest loop, the so-called *plaquette*

$$U_{\mu\nu}(n) = U_\mu(n) U_\nu(n+\hat{\mu}) U_\mu^\dagger(x+\hat{\nu}) U_\nu^\dagger(n) \tag{2.83}$$

is illustrated in Fig. 2.2. Summing over all plaquettes and taking the trace thereof consti-

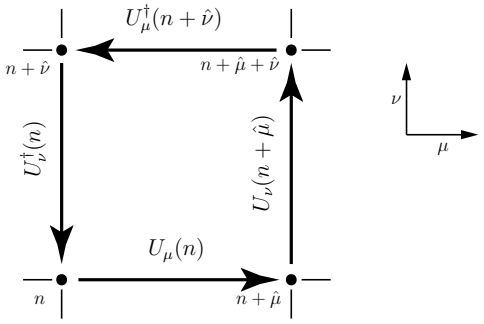

Figure 2.2.: Illustration of a plaquette, the smallest loop on the lattice.

tutes Wilson's gauge action

$$S_g^{\text{lat}} = \frac{\beta}{N} \sum_{n\in\Lambda} \sum_{\mu=0}^{3} \sum_{\nu=\mu+1}^{3} \operatorname{Re}\operatorname{tr}\left[\mathbb{1} - U_{\mu\nu}(n)\right], \tag{2.84}$$

where the free parameter

$$\beta = \frac{2N}{g^2} \tag{2.85}$$

is the usual (inverse) coupling parameter for lattice simulations and g is the (continuum) coupling constant from (2.2). The sum over μ and ν is taken such that each plaquette is counted only once. The normalization is chosen such that it corresponds to the continuum action (2.68) in the limit $a \to 0$. Thus, the lattice analog of the continuum expectation value (2.10) for the pure Yang–Mills action is given by

$$\langle O \rangle = \frac{1}{Z} \int \mathcal{D}[U] O[U] \, \mathrm{e}^{-S_g^{\text{lat}}[U]} \tag{2.86}$$

where the functional measure is given by the product Haar measure at each discrete space-time point

$$\mathcal{D}[U] = \prod_{n\in\Lambda} \prod_{\mu} \mathrm{d}U_\mu(n) \,. \tag{2.87}$$

In this work we will sometimes use a modification of (2.84), the anisotropic Wilson gauge action [51], with different coupling constants for the temporal β_t and spatial directions β_s. A convenient choice is a parameterization by $\beta = \frac{2N}{g^2}$ as in the isotropic case and the bare anisotropy ξ_0 such that

$$\beta_s = \frac{\beta}{\xi_0}, \quad \beta_t = \beta \xi_0. \tag{2.88}$$

Then the anisotropic Wilson gauge action takes the form [52]

$$S_g^{\text{ani}} = \frac{\beta}{N} \sum_{n\in\Lambda} \sum_{j=i+1}^{3} \left\{ \sum_{i=1}^{3} \frac{1}{\xi_0} \operatorname{Re}\operatorname{tr}\left[\mathbb{1} - U_{ij}(n)\right] + \xi_0 \operatorname{Re}\operatorname{tr}\left[\mathbb{1} - U_{0i}(n)\right] \right\}. \tag{2.89}$$

This choice allows to have different lattice spacings a_t and a_s which is necessary to approach the Hamiltonian limit $a_t \to 0$, see the discussion in Section 2.6, and is a convenient choice in the finite temperature setup of Chapter 4. For a fixed inverse coupling β, the parameter ξ_0 has to be adjusted such that the renormalized anisotropy

$$\xi = \frac{a_s}{a_t} \tag{2.90}$$

takes the desired value.

2.4.1. The Monte Carlo Technique

The lattice expectation value (2.86) contains an integration in group space at each lattice point which makes the path integral impossible to solve analytically. A viable technique to solve the path integral is a so-called Monte Carlo simulation. In a Monte Carlo simulation the integration is approximated by choosing a finite number N of statistically independent field configurations $U^{(n)}$ which are chosen randomly in the integration region, the set of all possible configurations $\{U\}$. The expectation value is then approximated by

$$\langle O \rangle \approx \frac{1}{N} \frac{1}{Z} \sum_{n}^{N} O[U^{(n)}]\, \mathrm{e}^{-S[U^{(n)}]}. \tag{2.91}$$

However, in such a naive Monte Carlo approach one will include many field configurations which give only a negligible contribution if the action has a sharp peak which is to be expected for large lattices [47]. A solution to that problem is *importance sampling*. Instead of choosing the configurations uniformly we would like to generate the configurations directly with the probability density

$$p[U] = \frac{\mathrm{e}^{-S[U]}}{Z}. \tag{2.92}$$

Then the number of configurations to properly sample the integration region can be chosen much smaller and the expectation value is given by

$$\langle O \rangle \approx \frac{1}{N} \sum_{n}^{N} O[\tilde{U}^{(n)}], \tag{2.93}$$

with the important difference to (2.91) that the configurations $\tilde{U}$ have to be chosen with the weight (2.92). Unfortunately there is no algorithm which directly produces configurations with the measure (2.92) but one can produce configurations in a so-called Markov chain which has the desired probability distribution $p[U]$ in its equilibrium. The Markov chain is defined by a transition probability P which describes how a configuration $U^{(n+1)}$ is obtained from a configuration $U^{(n)}$. A transition probability P which is *irreducible*

$$P[U \leftarrow U'] > 0 \qquad \forall U, U' \in \{U\}, \tag{2.94}$$

i.e. every state (configuration) can be reached, and fulfills *detailed balance*

$$P[U \leftarrow U']p[U'] = P[U' \leftarrow U]p[U] \qquad \forall U, U' \in \{U\} \tag{2.95}$$

is guaranteed to converge to the equilibrium distribution

$$\lim_{n\to\infty} P^n p_0[U] = p[U], \tag{2.96}$$

where $p_0[U]$ is an arbitrary initial distribution, e.g. $p_0[U] = \delta(U - U_0)$ with an arbitrary configuration U_0. Then, by the strong law of large numbers the average of the quantity O in (2.93) (the sample average) will converge with probability one to the desired ensemble average. The central limit theorem states that the error on the sample average will falloff like $1/\sqrt{N}$ [53]. The detailed balance condition (2.95) is actually more strict than necessary, however, this condition is already fulfilled for many relevant algorithms like the ones in lattice gauge theory, see [47, 53] for details.

According to (2.96) we can start from any configuration and will get configurations which are distributed by $p[U]$ after some *equilibrating* steps. A practical choice for the initial configuration is either a *cold lattice* where all links are set to the identity or a *hot lattice* where all links are chosen randomly. The configurations in the equilibration phase are discarded from the Monte Carlo sample. When the equilibrium is reached the configurations in the Markov chain are still correlated as they are produced by a deterministic algorithm. This so-called *autocorrelation* has to be included in the calculation of the variance of the observable. One finds that a Markov chain Monte Carlo run of N steps is equivalent to a Monte Carlo measurement with $N/(2\tau_{\text{int}})$ independent configurations, where τ_{int} is the integrated autocorrelation time [53]. Thus, to get an expectation value which is free of the autocorrelation effect one should discard $N_{\text{disc}} \gtrsim \tau_{\text{int}}$ configurations in the Markov chain. Note that the autocorrelation time may be different between lattice observables and therefore N_{disc} should be defined from the one with the largest autocorrelation time. For error estimates in this work we use the Wolff routine [54] which incorporates the integrated autocorrelation time in the error estimates.

A crucial point for the performance of the Monte Carlo method is to choose an algorithm where the autocorrelation time is small. The most famous and very general algorithm is the *Metropolis algorithm* [55] which relies only on the detailed balance condition. For the Wilson gauge action in SU(2) the more efficient *heat bath algorithm* exists [25]. Especially the combination of heat bath steps with overrelaxation steps [56, 57] provides a very efficient algorithm for the SU(2) gauge theory. A generalization to SU(N) is possible by means of the Cabibbo–Marinari technique where the SU(2) algorithms are employed in the $N^2 - 1$ SU(2) subgroups of the SU(N) links [58].

With these algorithms for the pure gauge Wilson action one can produce a reasonable Monte Carlo ensemble for large lattices on single node computers or small clusters. The simulation of the action including the fermionic part is substantially more difficult from the technical as well as from the computational aspect. While the comparably cheap pure gauge configurations in this work are produced by us, the configurations including *dynamical* fermions in Chapter 6 were provided by the authors of Refs. [59–62]. In the expectation value of a quantity $O[U, \bar{q}, q]$ including the fermionic contribution

$$\langle O \rangle = \frac{1}{Z} \int \mathcal{D}[U]\, \mathrm{e}^{-S_g^{\text{lat}}[U]} \frac{1}{Z_f[U]} \int \mathcal{D}[\bar{q}]\mathcal{D}[q]\, \mathrm{e}^{-S_f^{\text{lat}}[U,\bar{q},q]} O[U, \bar{q}, q], \tag{2.97}$$

the functional measure $\mathcal{D}[q]$ is a product of Grassmann integrals which accounts for the antisymmetric nature of fermions. For a quantity which depends only on the gauge field $O[U]$, but with the fermionic interactions still turned on, the Grassmann integration can

be carried out explicitly and yields, see e.g. Ref. [47],

$$\langle O \rangle = \frac{1}{Z} \int \mathcal{D}[U] \, \mathrm{e}^{-S_g^{\mathrm{lat}}[U]} \det(D[U]) O[U] \tag{2.98}$$

$$Z = \int \mathcal{D}[U] \, \mathrm{e}^{-S_g^{\mathrm{lat}}[U]} \det D[U], \tag{2.99}$$

where $\det D[U]$ is the determinant of the Dirac operator, e.g. the Wilson Dirac operator (2.80). The fermion determinant can then be absorbed in an effective action

$$Z = \int \mathcal{D}[U] \, \mathrm{e}^{-S_{\mathrm{eff}}[U]}, \tag{2.100}$$

$$S_{\mathrm{eff}}[U] = S_g^{\mathrm{lat}}[U] - \mathrm{tr} \log D[U]. \tag{2.101}$$

Since the full fermion action of (2.1) is a sum over the individual quark flavors we get a fermion determinant for each of these. If we want to include the fermion determinant in the probability density, it has to be a real and positive quantity. The Wilson Dirac operator and many other discretizations of the Dirac operator obey γ_5-Hermiticity

$$\gamma_5 D \gamma_5 = D^\dagger. \tag{2.102}$$

For these operators one can show that the determinant is indeed real [31]. A problem arises in calculations at finite temperature and density because γ_5-Hermiticity is lost when a chemical potential is introduced. This complication is known as the *sign problem* and is a subject of active research, see e.g. Ref. [63] for a recent review. To guarantee the positivity of the fermion determinant one can use two mass-degenerate quark flavors, e.g. a simulation with up and down quarks with $m_u = m_d$, then

$$\det D_u \det D_d = (\det D)^2 \geq 0. \tag{2.103}$$

is positive [31].

Besides these technical obstacles also the computational work for generating these configurations with dynamical fermions is high because basically the fermion determinant has to be calculated (at least approximately) in each Monte Carlo step. For more details we refer to Ref. [31].

2.4.2. Renormalization and Continuum Limit

In quantum field theories one often finds integrals which are divergent. To get finite values for these quantities one needs to regularize the integrals. One possible regularization is via a momentum cutoff Λ. However, the result will now depend on the cutoff. Therefore, to obtain a physical value one has to get rid of the cutoff-dependence. This is done by imposing *renormalization* conditions between the bare quantities and the physical (renormalized) quantities.

In the lattice formulation a cutoff is already introduced by the finite lattice spacing a. The Fourier transformation of a one dimensional function [46]

$$f(x) = \int_{-\infty}^{\infty} \frac{\mathrm{d}p}{2\pi} \tilde{f}(p) \, \mathrm{e}^{-\mathrm{i}px} \tag{2.104}$$

restricted on a discrete but infinite lattice with lattice points $x_n = an$, $n \in \mathbb{N}$ is limited to

momenta in the Brillouin zone[5] $p \in [-\frac{\pi}{a}, \frac{\pi}{a}]$

$$f(na) = \int_{-\frac{\pi}{a}}^{\frac{\pi}{a}} \frac{\mathrm{d}p}{2\pi} \tilde{f}(p)\, \mathrm{e}^{-\mathrm{i}pan}. \tag{2.106}$$

Thus, the integral gets a momentum cutoff of the order of the inverse lattice spacing $\Lambda \sim \frac{1}{a}$.

Now, we need to remove the lattice cutoff $a \to 0$ to obtain continuum physics. The bare parameters of the theory, the bare coupling g and the bare masses m_f which appear in the action, will change with the cutoff. Therefore these parameters are called running coupling $g(a)$ and running masses $m_f(a)$. Again we will for simplicity discuss only the pure gauge part where the only bare parameter in the action is the coupling $g(a)$. By construction of the lattice formalism, all lattice observables are dimensionless and we have to introduce a scale to relate them to their physical values.[6]

As an example we will discuss the string tension σ which describes how the potential of a static quark-antiquark pair increases with distance $V(r) = \sigma r$. A non-zero value value for the string tension implies confinement, as will be explained in Section 2.5.1. Its experimental value is $\sigma_{\text{phys}} = (440\,\text{MeV})^2$. We will denote the dimensionless string tension in lattice units as $\hat{\sigma}$ and the string tension in physical units, but for a finite lattice spacing, with σ. Since σ has mass dimension 2, the relation between them is

$$\sigma(g(a), a) = \frac{1}{a^2}\hat{\sigma}(g). \tag{2.107}$$

This relation shows that $\hat{\sigma}$ is divergent in the limit $a \to 0$ at a fixed value of the coupling constant. To obtain the continuum value the running of the coupling $g(a)$ has to be such that

$$\lim_{a\to 0} \sigma(g(a), a) = \sigma_{\text{phys}}. \tag{2.108}$$

From this equation one can find the functional form of $g(a)$ which should be independent of the choice of observable for small enough lattice spacing. Then, $g(a)$ will compensate the divergent part of any observable O when performing the continuum limit. The relations (2.107) and (2.108) are covered in form of a differential equation by the *renormalization group equation* [46, Chapter 9]

$$\left[a\frac{\partial}{\partial a} - \beta(g)\frac{\partial}{\partial g}\right] O(g(a), a) = 0. \tag{2.109}$$

where we introduced the β-function

$$\beta(g) = -a\frac{\partial g}{\partial a}. \tag{2.110}$$

If the β-function is known we can calculate, by integrating (2.109), how the observable O changes with g. If one expands the β-function in powers of g around $g = 0$ and applies perturbation theory to determine the coefficients one finds [31, Chapter 3]

$$\beta(g) = -\beta_0 g^3 + \mathcal{O}(g^5) \tag{2.111}$$

[5] On a finite lattice with periodic boundary conditions $x_n = an$, $n \in [0, N-1]$, $f(x_n + aN) = f(x_n)$, the momentum variable is further restricted to the Matsubara frequencies [31, Appendix A] $p_n = \frac{2\pi}{aN} k_n$, $k_n \in [-N/2+1, \ldots, N/2]$ and the Fourier integral becomes a finite sum

$$f(na) = \frac{1}{N}\sum_{p_n} \tilde{f}(p_n) \exp(\mathrm{i}p_n na). \tag{2.105}$$

[6] The following description is along the lines of Ref. [46].

with

$$\beta_0 = \frac{1}{16\pi^2}\left(\frac{11}{3}N_c - \frac{2}{3}n_f\right) \tag{2.112}$$

for n_f massless fermions. For $n_f < \frac{11}{2}N_c$ the β-function is negative in the vicinity of $g = 0$ and therefore the coupling will decrease when a decreases. Thus the zero of the β-function at $g = 0$ is attractive, i.e. the coupling has a fixed point at small length scales. This ultraviolet fixed point describes asymptotic freedom.

From the leading order expansion of the β-function (2.111) and the differential equation (2.110) we can compute the lattice spacing as a function of the coupling

$$a(g) = \frac{1}{\Lambda}\,\mathrm{e}^{-\frac{1}{2\beta_0 g^2}}. \tag{2.113}$$

The integration constant Λ can be determined by identifying a lattice observable at fixed $\tilde{g}$ with its physical value, as for example the string tension

$$a^2(\tilde{g}) = \frac{\hat{\sigma}(\tilde{g})}{\sigma_{\text{phys}}}. \tag{2.114}$$

Note that in practice one usually does not rely on such a simple relation to determine the lattice spacing. Instead one determines the string tension (or other observables) at many values of the coupling and interpolates between them.

To sum up, the continuum limit of lattice QCD $a \to 0$ is approached by decreasing the coupling constant, i.e. increasing the inverse coupling β. However in any practical simulation the number of lattice points is limited by the computational resources: increasing the number of lattice points roughly means increasing the computational work. If we decrease the lattice spacing a at a fixed number of lattice points the physical lattice volume will shrink. Then at a certain point the volume will be so small that the correlation length of an observable does not fit on the lattice anymore. On the other hand, the coupling constant has to be much smaller than the characteristic scale of the quantity to be able to resolve the fluctuations of the observable. These limits define a small range of feasible values for the coupling constant, the so-called *scaling window*. A possible way to analyze the scaling window is by comparing the lattice results at different coupling constants to the scaling according to the perturbative result (2.113)[7].

2.5. Lattice Observables and Confinement

In this section we will describe two (lattice) observables which are important for confinement: the Wilson loop and the correlation of Polyakov loops can be used to describe the potential between a (static) quark-antiquark pair. In the second part we will discuss mechanisms which try to explain the origin of the confining force in QCD. The first two scenarios attribute confinement to the formation of topological defects in the field configurations: magnetic monopoles and center vortices. A different approach is the Gribov–Zwanziger scenario of confinement. There, confinement emerges by a restriction of configurations to the fundamental modular region which imply conditions on the IR properties of the gluon and the ghost propagator in Coulomb and Landau gauge.

The static quark potential provides a very intuitive picture for confinement. If the potential energy between a quark and an antiquark rises linearly with distance, more

[7] Usually one uses the two loop result for a scaling analysis, see e.g. Ref. [46, Chapter 9].

and more energy is needed to separate the particles. Thus it is impossible to completely separate the quark from the antiquark: they are bound in a meson. The emergence of the linear rising term in a non-Abelian theory is attributed to the formation of a string-like flux tube, in contrast to the Abelian theory where the field lines spread out. However, in the interacting theory this picture is too simple. There a quark-antiquark pair can be generated from the vacuum. Thus at a certain distance the creation of such a pair is energetically favorable and the confining string breaks. In the following we will discuss only the case where no quark-antiquark creation or annihilation is allowed and the potential will be linear rising for large separations. This is the limit of infinitely heavy quarks which in lattice formulation can be implemented by neglecting the fermion determinant, the so-called *quenched approximation*. In the region of asymptotic freedom, i.e. at small distances, one expects a Coulomb-like potential as in QED. For the quenched theory we therefore describe the static quark potential by

$$V(R) = \frac{\alpha(R)}{R} + \sigma R + c, \tag{2.115}$$

where $\alpha(R)$ is the running coupling in the perturbative regime and a universal constant, the so-called Lüscher-term [64], in the strong-coupling regime, σ is the string tension, and c is an irrelevant normalization which can be used to define the zero point energy.

2.5.1. The Wilson Loop

A possible way to measure the static quark potential is via Wilson loops. On the lattice, a Wilson loop is the trace of a product of links along a closed contour. We already encountered the smallest Wilson loop, the plaquette (2.83), when we introduced the lattice gauge action and found that it is gauge invariant. We will denote a space-time Wilson loop along a rectangular contour $\mathcal{C} = R \times T$ by

$$W(R,T) = \operatorname{tr} \prod_{(n,\mu)\in\mathcal{C}} U_\mu(n), \tag{2.116}$$

where R is the extension in space and T the extension in time. One finds the relation

$$\langle W(R,T)\rangle \overset{T\to\infty}{=} c\,\mathrm{e}^{-V(R)T} \tag{2.117}$$

where $V(R)$ is the static quark potential[8] and thus

$$V(R) = -\lim_{T\to\infty} \frac{1}{T} \log \langle W(R,T)\rangle\,. \tag{2.118}$$

In the strong coupling expansion one can show [47, Chapter 3.5] that the leading contribution to the expectation value of Wilson loops are of the form

$$\langle W(R,T)\rangle = c\,\mathrm{e}^{-\sigma RT + \mu(R+T) + \dots}. \tag{2.119}$$

Therefore one expects that the Wilson loop falls-off with an *area law* in a confining theory, while the fall-off is described by a *perimeter law* if the linear rising term is not present. This categorization by the Wilson loop fall-off is known as the *Wilson criterion* for confinement.

For a measurement of the string tension on a finite lattice one has to consider a large loop in the temporal direction and perform a fit in the large R region where the area law

[8] For a derivation see e.g. Ref. [65] or textbooks e.g. Ref. [47, Chapter 3.5].

dominates. *Creutz ratios* [66] are a convenient way to directly access the string tension already from smaller Wilson loops. With the ratio

$$\chi(R+0.5,T+0.5) = -\log \frac{\langle W(T+1,R+1)\rangle \langle W(R,T)\rangle}{\langle W(R+1,T)\rangle \langle W(R,T+1)\rangle} \tag{2.120}$$

the perimeter law and a constant is already canceled and yields the string tension (in lattice units)[9]. In Chapter 5 we will use Creutz ratios to determine if confinement is present in our theory.

2.5.2. The Polyakov Loop

The Polyakov loop is a special kind of Wilson loop which winds once around the periodic lattice in time direction

$$P(\boldsymbol{x}) = \operatorname{tr} \prod_{t=0}^{N_t-1} U_t(t,\boldsymbol{x}). \tag{2.121}$$

The correlation of two oppositely-oriented Polyakov loops at spatial distance $R = |\boldsymbol{x}-\boldsymbol{y}|$ gives another definition for the static quark potential. The relation to the former definition can be obtained by using a Wilson loop of temporal extend $T = N_t$. With gauge transformations it is possible to set all links in spatial direction to the identity and one ends up with just the two Polyakov loops of opposite orientation. Since the Polyakov loop is gauge invariant the interpretation in this special gauge is valid independent of the choice of gauge. Therefore,

$$\left\langle P(\boldsymbol{x})P^\dagger(\boldsymbol{y})\right\rangle = c\,\mathrm{e}^{-aN_tV(R)}. \tag{2.122}$$

With both definitions (2.117) and (2.122) we can measure the string tension and therefore conclude if we are in the confined or in the deconfined phase. However the expectation value of a Polyakov loop alone is already an order parameter for confinement. In the pure gauge theory the deconfinement phase transition is related to *center symmetry*. The pure gauge action is invariant under a *center transformation*

$$U_t(\tilde{t},\boldsymbol{x}) \to zU_t(\tilde{t},\boldsymbol{x}), \quad \forall \boldsymbol{x} \tag{2.123}$$

where all temporal links of a time slice $\tilde{t}$ are multiplied with the same element z from the center of the gauge group. The center of a group is the set of all elements which commute with every other element of the group. For $\mathrm{SU}(N)$ the center is given by the cyclic group

$$\mathbb{Z}_N = \{\exp(2\pi \mathrm{i} n/N)\,\mathbb{1} \mid n \in [0,\ldots,N-1]\} \in \mathrm{SU}(N). \tag{2.124}$$

One can easily verify that for any (trivially) closed loop the center phase just drops out and therefore the gauge action which is built from such loops is invariant under a center transformation. However, the Polyakov loop winds around the lattice and is not invariant under z

$$P(x) \to zP(x). \tag{2.125}$$

Thus, the Polyakov loop is an order parameter for the center symmetry. In the center symmetric phase the expectation value of a Polyakov loop vanishes, if center symmetry is broken the expectation value will acquire a finite value. The expectation value of a Polyakov loop can also be interpreted as a free energy of a color charge F_q, see Ref. [31, Chapter 12],

$$|\langle P\rangle| = c\,\mathrm{e}^{-aN_tF_q}. \tag{2.126}$$

[9] We use the notation of Ref. [67].

In the center-symmetric phase the free energy diverges $F_q \to \infty$, thus the quark is confined whereas in the broken phase the free energy is finite. In Chapter 4 we will see that the finite temporal extent aN_t plays the role of the inverse temperature of the system.

2.5.3. The Dual Superconductor and Abelian Monopoles

The dual superconductor picture of confinement is based on an analogy to ordinary superconductors in electrodynamics. These superconductors are classified into two categories by the Ginzburg–Landau parameter $\kappa = \frac{\lambda}{\xi}$, where λ is the penetration depth of the magnetic field and ξ the correlation length of Cooper pairs. Type I superconductors are characterized by $\kappa < 1$.[10] The phenomenological observation is the Meißner–Ochsenfeld effect: the magnetic field is expelled from the interior of the medium to a layer of thickness $\sim \lambda$ around the surface. For a magnetic field above some critical value superconductivity will break down. On the other hand in type II superconductors ($\kappa > 1$), superconductivity does not break down immediately, but it is energetically favorable to form quantized magnetic flux lines in the interior of the material, the so-called Abrikosov vortices. Thus, type II superconductors exhibit three different phases characterized by the critical fields B_{c_1} and B_{c_2}: the normal phase ($B > B_{c_2}$), the so-called Shubnikov phase ($B_{c_1} < B < B_{c_2}$) where vortices penetrate the material and the superconducting phase ($B < B_{c_1}$).

Though no magnetic monopoles are observed in nature, it is instructive, for the discussion of the dual superconductor picture, to consider a hypothetical magnetic monopole. If one places such a magnetic monopole and an anti-monopole in a non-superconducting material, the magnet field will spread out in the same way as the electric field for electric charges, with a potential $V(r)$ which falls-off like $1/r$. However in a superconducting material, the magnetic flux cannot spread out, due to the Meißner–Ochsenfeld effect. Since the magnetic charges are placed in the superconductor, the magnetic field cannot be expelled completely due to the (magnetic) Gauß's law[11]. It is squeezed in a flux tube which joins the monopole and the anti-monopole. Since the energy density along the flux tube is constant, the energy will rise linearly with the distance of the monopole and anti-monopole. If the monopole and the anti-monopole existed, they would be confined by this mechanism.

In the dual superconductor, the roles of the electric and the magnetic field is exchanged: in QCD the confinement of a color-electric quark-antiquark pair can be explained by the formation of electric flux tubes [69, 70]. The mechanism builds upon an Abelian $U(1)$ theory. Thus, in the context of non-Abelian SU(N) gauge theories one needs to choose an Abelian subgroup [71]. Such a subgroup can be generated from the Cartan subalgebra and is given by the group $U(1)^{N-1}$. The most prominent choice to single out an Abelian subgroup of SU(N) is the maximally Abelian gauge where one tries to make the gauge field as diagonal as possible. Then, the Abelian part of the gauge field is obtained by eliminating the components along the non-diagonal generators from the gauge field.

The authors of Ref. [72] conjectured that if the Abelian monopoles are relevant for confinement, then the Abelian part alone will dominate the long-range physics. In fact, many results from lattice gauge theory [73–80] and continuum calculations [81–86] support the Abelian dominance hypothesis, see also Appendix F.

[10] In the notation of Ref. [68, Chapter 21.6].

[11] Gauß law for the magnetic field $\nabla B = m$ is obtained after symmetrization of the Maxwell equations, where m is the magnetic charge

2.5.4. The Center Vortex Picture

In this section we give a very brief overview of the center vortex picture. A more detailed introduction is postponed to Chapter 5 were we use the center vortex picture as a tool to eliminate the confining properties from lattice configurations.

The center vortex model was first proposed by 't Hooft [87] and Mack and Petkova [88]. The idea is that sufficiently random vortices produce an area law for the Wilson loop. A center vortex in 3 dimensions is a closed loop in the dual lattice, carrying quantized flux of a non-trivial center element of the gauge group. A Wilson loop will detect a center vortex if they are non-trivially linked, i.e. if the area of the Wilson loop is pierced by the vortex. Then, the Wilson loop measures the flux associated with the non-trivial center element. However, center vortices, as they appear in SU(N) gauge theories, are objects of a finite width (*thick vortices*) and cannot be detected directly. To detect the center vortices on the lattice, the thick vortices are squeezed by a center gauge to the SU(N) element which is closest to a center element. To extract so-called *thin vortices* of the width of one lattice spacing, the links, after center gauge fixing, are then projected to its closest center element. In the literature, these projected vortices are often called *P-vortices*. Many lattice results confirm that center vortices are the relevant physical objects for confinement, see Chapter 5.

The center vortex picture originates from the lattice approach and is formulated in terms of the group valued link variables. Still a continuum analog of center gauge fixing and center projection could be derived [89] which allows the interpretation of a center vortex as the half of a Dirac string [90].

2.5.5. Confinement in Coulomb Gauge

Gribov and Zwanziger developed an explanation of confinement based on an entropic argument [35, 91, 92]. The argument is that, as the volume of a high-dimensional sphere

$$\mathrm{d}V_N = r^{N-1}\mathrm{d}r\ \mathrm{d}\Omega\ , \tag{2.127}$$

is located in a small region around around the surface of the sphere, the relevant configurations in the high-dimensional path integral will be concentrated around the Gribov horizon.

Since close to the Gribov horizon the Faddeev–Popov operator develops a small eigenvalue, the momentum space ghost propagator will diverge very fast in the IR, which is seen from the spectral decomposition in momentum space

$$G(\boldsymbol{p}) = \sum_n \frac{\phi_n(\boldsymbol{p})\phi_n(-\boldsymbol{p})}{\lambda_n}, \tag{2.128}$$

where λ_n are the eigenvalues and ϕ_n the eigenfunctions of the Faddeev–Popov operator. Since the ghost propagator enters the Coulomb operator twice

$$V_C \sim M^{-1}(-\nabla)M^{-1} \tag{2.129}$$

it is argued that the reason for a long-range Coulomb potential is due to the diverging ghost propagator. Additionally, the restriction to the FMR implies a vanishing gluon propagator [91]. Finally, it was shown that the Coulomb potential is an upper bound for the physical potential from Wilson loops at large distances [93]

$$V_W(r) \leq V_C(r), \quad r \to \infty. \tag{2.130}$$

Thus a confining Coulomb potential is a necessary condition for confinement.

2.6. The Coulomb Gauge Propagators

In the following we will introduce the lattice Coulomb gauge correlation functions which are relevant for this work. We will also summarize related work in Coulomb gauge and discuss discrepancies between lattice and continuum results. The discussion of related work at finite temperature is postponed to Chapter 4.

2.6.1. Gauge Fixing on the Lattice

In Section 2.2 we have seen that gauge fixing is necessary in continuum calculations. In the lattice theory gauge fixing is not per se necessary as long as one is only interested in gauge invariant observables. Since the integration is only over a finite number of variables with the compact Haar measure the lattice path integral is well-defined. However, gauge fixing is of course necessary if one is interested in gauge variant quantities in a particular gauge. Though the gauge variant quantities do not have a direct physical meaning one can still draw physical conclusions from them. One example is the Gribov–Zwanziger scenario where one derives the (gauge independent) observation of confinement from gauge-variant correlation functions.

We have already seen how we can implement gauge fixing in the continuum path integral with the Faddeev–Popov technique in Section 2.2. In the lattice approach it is (numerically) inconvenient to incorporate the gauge condition in the path integral directly (2.86) by generating the Monte Carlo ensemble with the action

$$S = S_{\mathrm{YM}} + S_{\mathrm{GF}} + S_{\mathrm{FP}}. \tag{2.131}$$

This approach would involve the calculation of the Faddeev–Popov determinant in each Monte Carlo step. The standard technique is to produce the gauge configuration with the Yang–Mills action alone and then transform these configurations to a particular gauge [94].

To implement Coulomb gauge the task is to find the minimum of the lattice version of (2.28) for a given Monte Carlo configuration U which reads

$$F^U[g] = \frac{1}{3N_c N_s^3} \sum_{x,i} \mathrm{Re}\,\mathrm{tr}\,[\mathbb{1} - U_i^g(x)] \tag{2.132}$$

In later chapters we will usually drop the "1−" term and talk about maximizing the functional, see (7.2). From (2.132) it is apparent that lattice Coulomb gauge is the gauge which brings the spatial links as close as possible to unity.

More details on lattice gauge fixing, including the numerical algorithms and an efficient implementation for GPUs, will be discussed in Chapter 7.

2.6.2. The Gluon Propagator

The gluon propagator is the two-point function of the gauge fields

$$D_{ij}^{ab}(x-y) = \left\langle A_i^a(x) A_j^b(y) \right\rangle. \tag{2.133}$$

For the gauge fields on the lattice we use the linear mid-point definition in terms of the link variables

$$A_\mu(x + \hat{\mu}/2) = \frac{1}{2\mathrm{i}ag} \left[U_\mu(x) - U_\mu^\dagger(x) \right]_{\mathrm{traceless}}. \tag{2.134}$$

The momentum space gluon propagator

$$D_{ij}^{ab}(k) = \left\langle A_i^a(k) A_j^b(-k) \right\rangle, \tag{2.135}$$

with $A^a_\mu(k) = \sum_x A_\mu \, \mathrm{e}^{ik\cdot(x+\hat{\mu}/2)}$ obtained by Fourier transformation, is transverse and diagonal in color-space

$$D^{ab}_{ij}(\boldsymbol{p}) = \delta^{ab}\left(\delta_{ij} - \frac{p_i p_j}{|\boldsymbol{p}|^2}\right) D(\boldsymbol{p}). \tag{2.136}$$

Equation (2.136) defines the scalar propagator $D(\boldsymbol{p})$, where $p_\mu(k_\mu) = \frac{2}{a}\sin(ak_\mu/2)$ and $k_\mu = \frac{2\pi}{aL_\mu}n_\mu$ are the discrete lattice momenta in the first Brillouin zone, see Appendix A. The transversality is a consequence of the Coulomb gauge condition in momentum space

$$\boldsymbol{p}\cdot\boldsymbol{A}(\boldsymbol{p}) = 0. \tag{2.137}$$

Related Work

The Coulomb gauge gluon propagator was first studied in [95, 96] on various lattice sizes but only at a fixed coupling $\beta = 2.2$ for the gauge group SU(2). The authors found that the propagator fits well to Gribov's formula (2.65). The static propagator can be interpreted as the (inverse) energy dispersion relation for the gluons $\omega^{-1}(\boldsymbol{p}) = 2D(\boldsymbol{p})$. If we compare the Gribov form to the dispersion relation of a massive particle $\omega^2 = \boldsymbol{p}^2 + m^2$, we see that the term $m^2(\boldsymbol{p}) = M^4/\boldsymbol{p}^2$ in Gribov's formula can be interpreted as a momentum dependent mass which diverges in the IR limit. This describes infinitely heavy gluons at small momenta which cannot propagate and thus signals confinement.[12]

While in a first study at different couplings [98] the propagator shows proper multiplicative renormalization, scaling violations were observed in later studies both for the gauge groups SU(2) [99] and SU(3) [100, 101]. In these works, a conclusive statement about the IR behavior was not possible.

Since these violations were observed, several solutions were proposed. In Ref. [102] the scaling violations were resolved by introducing a momentum cut in addition to the established cone and cylinder cut (Appendix A.2.2). The authors see a tendency for an infrared finite gluon propagator which would be in contrast to continuum calculations, see Section 2.6.6.

A different solution was proposed by authors of our group [44]. They found that when calculating the static propagator from the full propagator with the lattice cutoff π/a_t

$$D(\boldsymbol{p}) = \int_{-\frac{\pi}{a_t}}^{\frac{\pi}{a_t}} \frac{\mathrm{d}p_0}{2\pi} D(p_0, \boldsymbol{p}), \tag{2.138}$$

the propagator gets a spurious extra momentum dependence. This can be seen already for the free propagator [97]. We will will briefly sketch this simpler calculation from Ref. [97] here. The free propagator is given by $D_0(p_0, \boldsymbol{p}) = \frac{1}{p_0^2 + \boldsymbol{p}^2}$. Integrating the propagator on the finite lattice interval yields

$$D_0(\boldsymbol{p}) = \int_{-\frac{\pi}{a_t}}^{\frac{\pi}{a_t}} \frac{\mathrm{d}p_0}{2\pi} \frac{1}{p_0^2 + \boldsymbol{p}^2} = \frac{1}{2\,|\boldsymbol{p}|}\frac{2}{\pi}\arctan\left(\frac{\pi}{a_t\,|\boldsymbol{p}|}\right). \tag{2.139}$$

Thus on the finite lattice there will always be an extra factor

$$\arctan\left(\frac{\pi}{a_t\,|\boldsymbol{p}|}\right) = \arctan\left(\frac{\pi\xi}{a_s\,|\boldsymbol{p}|}\right). \tag{2.140}$$

[12] A more rigorous interpretation would be that such a momentum space propagator corresponds to a propagator which violates reflection positivity and thus cannot describe a physical particle. In Ref. [97] the gluon propagator was calculated in position space.

compared to the continuum result

$$D_0(\boldsymbol{p}) = \frac{1}{2\boldsymbol{p}}. \tag{2.141}$$

This factor will only vanish in the Hamiltonian limit $a_t \to 0$ which can be approached by lattices with high anisotropy $\xi \to \infty$. Such a spurious $\boldsymbol{p}$ dependence, which was also found for the interacting lattice propagator in Ref. [44], prevents the static propagator from being multiplicatively renormalizable. Additionally, earlier studies did not take into account that the static propagator might be influenced by fixing the residual gauge of the links in time direction, see Appendix B. For the full bare propagator after residual gauge fixing with the integrated Polyakov gauge they found a factorization in a function of $|\boldsymbol{p}|$ and a function of $z = \frac{p_0}{|\boldsymbol{p}|}$

$$D_\beta(p_0, |\boldsymbol{p}|) = f_\beta(\boldsymbol{p}) g_\beta(z), \tag{2.142}$$

where we use the subscript β to indicate that the functions depend on the coupling. Since $g_\beta(z)$ depends on the coupling they conclude that the full propagator cannot be multiplicatively renormalizable and therefore the same holds for the static propagator. However they find that the propagator at fixed energy shows proper scaling and can be used as the static propagator $D(\boldsymbol{p}) = D(p_0 = 0, \boldsymbol{p})$. To improve the statistics they propose to divide out the z dependency and then take the p_0 average. In this work we will use this latter approach which is explained in more detail in the next section. With this technique they find again the Gribov formula from the first studies at fixed β. This is not surprising since at the stronger coupling (in the low β region of the scaling window) of the first study, the correction in [44] is small.

From the calculation (2.140) for the free propagator and especially from the general calculation in Ref. [44] it is apparent that the spurious $\boldsymbol{p}$ dependence can be corrected for by using anisotropic lattices with a smaller lattice spacing in the time direction. This approach was followed in Refs. [97, 103]. Indeed the authors find that with increasing anisotropy the scaling violations are clearly reduced and the gluon propagator is again found to vanish in the IR. Additionally, the power law in the UV approaches the perturbative $\frac{1}{|\boldsymbol{p}|}$ of the Hamiltonian approach.

Calculating the Propagator

To resolve the scaling violations on an isotropic lattice the authors of Ref. [44] proposed to use the functional form of $g_\beta(z)$ to match the propagator at different energies p_0. Their strategy, which we will adopt in this work also for anisotropic lattices, is as follows. We obtain the functional form of $g_\beta(z)$ by calculating the ratios (2.142) between p_0 and a fixed $\tilde{p}_0$ which we chose to be $\tilde{p}_0 = 0$. With the choice $\tilde{p}_0 = 0$ the resulting data points are closest to a single curve. If we set $g_\beta(0) = 1$ (other choices would only change the normalization) we get

$$g_\beta(z) = \frac{D_\beta(p_0, |\boldsymbol{p}|)}{D_\beta(0, |\boldsymbol{p}|)}. \tag{2.143}$$

To the lattice data $g_\beta(z)$ we fit a function of the form

$$\hat{g}_\beta(z) = (1 + z^2)^\alpha \sum_{p=0}^{p_{\max}} c_p z^p \tag{2.144}$$

where $p_{\max} \leq 4$ in the polynomial factor. Then we remove the z-dependence from the bare propagator by dividing with $\hat{g}_\beta(z)$ and thus get a energy-independent quantity which

we average over p_0 to reduce the statistical fluctuations

$$f_\beta(|\boldsymbol{p}|) = \frac{1}{N_t} \sum_{p_0} \frac{D_\beta(p_0, |\boldsymbol{p}|)}{\hat{g}_\beta(z)}. \tag{2.145}$$

From (2.145) we define the bare static propagator

$$D_\beta(|\boldsymbol{p}|) = \frac{f_\beta(|\boldsymbol{p}|)}{|\boldsymbol{p}|}. \tag{2.146}$$

As already noted the propagator is then found to be multiplicatively renormalizable

$$D_\mu(|\boldsymbol{p}|) = Z(\beta, \mu) D_\beta(|\boldsymbol{p}|). \tag{2.147}$$

Since with the Gribov formula we have a functional form for all momenta which matches the propagator well, we will use a fit to Gribov's formula to define the renormalization constant Z. This procedure from Ref. [44] corresponds to the renormalization condition

$$D_\mu(|\boldsymbol{p}|)|_{\mu\to\infty} = \frac{1}{2\mu}, \tag{2.148}$$

i.e. we renormalize that propagator such that it takes its tree-level value for some (large) fixed value of $\boldsymbol{p}$.

2.6.3. The Ghost Propagator

From (2.24) we can read off that the ghost propagator, i.e. the two-point function of the ghost fields. It is given by the inverse Faddeev–Popov matrix M

$$G^{ab}(\boldsymbol{x} - \boldsymbol{y}) = \langle \bar{c}(\boldsymbol{x}) c(\boldsymbol{y}) \rangle = \left\langle (M^{-1})^{ab}_{\boldsymbol{xy}} \right\rangle. \tag{2.149}$$

Since the propagator is diagonal in color space

$$G^{ab}(\boldsymbol{p}) = \delta^{ab} G(\boldsymbol{p}) \tag{2.150}$$

we can define the scalar propagator (in momentum space) as

$$G(\boldsymbol{p}) = \frac{d(\boldsymbol{p})}{\boldsymbol{p}^2} = \frac{1}{N_c^2 - 1} \frac{1}{N_s^3} \left\langle \sum_a \sum_{\boldsymbol{x},\boldsymbol{y}} \mathrm{e}^{\mathrm{i}\boldsymbol{k}(\boldsymbol{x}-\boldsymbol{y})} (M^{-1})^{aa}_{\boldsymbol{xy}} \right\rangle, \tag{2.151}$$

where $d(\boldsymbol{p})$ is the ghost form factor which describes the deviation from the Abelian case. In the Abelian theory the Faddeev–Popov operator is the inverse Laplacian and therefore the ghost propagator is $G(\boldsymbol{p}) = 1/\boldsymbol{p}^2$. The Coulomb gauge Faddeev–Popov matrix on the lattice for the linear definition of the gauge field (2.134) is given by

$$M^{ab}_{\boldsymbol{xy}} = \sum_i \Big\{ \delta(\boldsymbol{x} - \boldsymbol{y}) \operatorname{Re}\operatorname{tr} \left\{ T^a, T^b \right\} (U_i(\boldsymbol{x}) + U_i(\boldsymbol{x} - \hat{\boldsymbol{\imath}})) \tag{2.152}$$

$$-2\delta(\boldsymbol{x} + \hat{\boldsymbol{\imath}} - \boldsymbol{y}) \operatorname{Re}\operatorname{tr} T^b T^a U_i(\boldsymbol{x}) \tag{2.153}$$

$$-2\delta(\boldsymbol{x} - \hat{\boldsymbol{\imath}} - \boldsymbol{y}) \operatorname{Re}\operatorname{tr} T^a T^b U_i(\boldsymbol{x} - \hat{\boldsymbol{\imath}}) \Big\}, \tag{2.154}$$

where we used the notation of Ref. [104]. For a derivation we refer to [36]. The Faddeev–Popov operator has $N_c^2 - 1$ zero modes which belong to the constant eigenfunctions $\Psi^a(\boldsymbol{x}) = 1/\sqrt{N_s^3}\delta^{ab}$. In the vector space orthogonal to these trivial zero modes the

Faddeev–Popov operator is positive-definite and the conjugate gradient algorithm can be used to invert the operator

$$M^{ab}_{\boldsymbol{xy}}\phi^b(\boldsymbol{y}) = \Psi^a(\boldsymbol{x}). \tag{2.155}$$

We use momentum space sources [105]

$$\Psi^a_{(c,\boldsymbol{k})}(\boldsymbol{x}) = \delta^{ac}\,\mathrm{e}^{-\mathrm{i}\boldsymbol{k}\boldsymbol{x}} \tag{2.156}$$

with fixed c and $\boldsymbol{k}$ which has the advantage that for $\boldsymbol{k} \neq 0$ the r.h.s. of (2.155) as well as the conjugate gradient iterates are orthogonal to the eigenspace of the zero modes. The ghost propagator in momentum space is then given by $G(\boldsymbol{p}) = \left\langle \Psi_{(c,\boldsymbol{k})} \middle| \phi_{(c,\boldsymbol{k})} \right\rangle$.

In the Gribov–Zwanziger confinement scenario, Section 2.5.5, one expects a divergent ghost form factor in the IR limit, the so-called horizon condition,

$$\lim_{|\boldsymbol{p}|\to 0} d^{-1}(|\boldsymbol{p}|) = 0. \tag{2.157}$$

Such a ghost form factor allows another intuitive physical interpretation. The ghost form factor in Coulomb gauge can be interpreted as the dielectric function of the QCD vacuum [106]

$$\epsilon(\boldsymbol{p}) = d^{-1}(\boldsymbol{p}). \tag{2.158}$$

This implies that the QCD vacuum is a perfect dielectric medium since $\epsilon(0) = 0$ and thus implies dual superconductivity.

Related Work

As already discussed for the gluon propagator, taking the lattice Hamiltonian limit is non-trivial and induces scaling violations. Such scaling violations were also found for the ghost propagator on isotropic lattices for SU(2) [107] and SU(3) [102]. Since the ghost propagator is by definition equal-time and only involves links in spatial direction it is independent of the residual gauge freedom and one cannot expect a prescription to resolve the scaling violations as in the case of the gluon propagator. However, the analysis of anisotropic lattices [108] revealed that the scaling violations are resolved by increasing the anisotropy. While all studies agree on a infrared divergent form factor, the precise value for the infrared exponent is open for debate since the ghost propagator is rather sensitive on the prescription of how the Gribov ambiguity is resolved. This will be discussed in detail in Chapter 3. With the standard prescription, where one tries to find the global minimum of (2.132), the best estimate is $d(|\boldsymbol{p}|) \sim 1/|\boldsymbol{p}|^{0.55}$ for $|\boldsymbol{p}| \to 0$ [108]. In Section 2.6.6 we will discuss this result in more detail in relation to findings in continuum calculations.

Related to the ghost propagator is the eigenvalue spectrum of the Faddeev–Popov operator which was investigated in Refs. [109, 110]. They find that the eigenvalues on large lattices accumulate near zero which is the Gribov–Zwanziger entropy argument that leads to a divergent ghost form factor.

2.6.4. The Coulomb Potential

An important quantity to study confinement in Coulomb gauge is the Coulomb potential (2.60). As the Coulomb potential provides an upper bound for the physical quark-antiquark potential at large distances, one expects that it is also linear rising $V_C(R) = \sigma_C R$ for $R \to \infty$. Then one is interested in verifying the relation

$$\sigma \leq \sigma_C \tag{2.159}$$

where σ is the physical string tension and σ_C the string tension of the Coulomb potential. A linear rising potential for large R in position space corresponds to a potential $V(p) = (8\pi\sigma)/p^4$ for small momenta $|\boldsymbol{p}| \to 0$ in momentum space. Thus to verify Zwanziger's inequality (2.159) we will study the ratio $(p^4 V_C(|\boldsymbol{p}|))/(8\pi\sigma)$ which yields σ_C/σ for $|\boldsymbol{p}| \to 0$.

In the literature several ways were proposed on how to define the continuum Coulomb potential from lattice quantities. Of course all definitions should agree in the continuum limit, however on a finite lattice they might differ.

The Coulomb Kernel: A straightforward one is to use directly the Coulomb kernel (2.58). Then the Coulomb potential (in momentum space) is obtained from the Monte Carlo expectation value

$$V_C(\boldsymbol{p}) = \frac{1}{N_c^2 - 1} \frac{1}{N_s^3} \left\langle \sum_a \sum_{\boldsymbol{x},\boldsymbol{y}} \mathrm{e}^{\mathrm{i}\boldsymbol{k}(\boldsymbol{x}-\boldsymbol{y})} \left(M^{-1}(-\Delta)M^{-1} \right)^{aa}_{\boldsymbol{x}\boldsymbol{y}} \right\rangle . \tag{2.160}$$

With this definition we can use the same technique as for the ghost propagator (2.155) by just replacing $M \to M(-\Delta)^{-1}M$.

The Temporal Gluon Propagator: In Ref. [111] the authors derived the relation

$$D_{00}(x-y) = V_C(\boldsymbol{x}-\boldsymbol{y})\delta(x_0 - y_0) + P(x-y), \tag{2.161}$$

where D_{00} is the time-time component of the gluon propagator and $P(x-y)$ is a non-instantaneous vacuum polarization term. They suggest [95] to calculate the Coulomb potential from the temporal equal-time propagator

$$V_C(\boldsymbol{x}) = \lim_{\epsilon \to 0} \int_{-\epsilon}^{\epsilon} \mathrm{d}x_0 \; D_{00}(x_0, \boldsymbol{x}) \tag{2.162}$$

$$= D_{00}(\boldsymbol{x}). \tag{2.163}$$

The $U_0 U_0^\dagger$-Correlator: A third definition originates from Ref. [112] and was put forward by Greensite and Olejník [113]. We will shortly summarize their reasoning following Ref. [114]. Consider the vacuum state Ψ_0 of the theory in Coulomb gauge (2.55) and denote the operator which creates a quark-antiquark pair at distance R with $\bar{q}(0)q(R)$. Then,

$$|\Psi_{q\bar{q}}\rangle = \bar{q}(0)q(R)\,|\Psi_0\rangle \tag{2.164}$$

is the state of a quark-antiquark pair in Coulomb gauge. The Coulomb energy can then be defined as

$$E_C(R) = \langle \Psi_{q\bar{q}} | H | \Psi_{q\bar{q}} \rangle - \langle \Psi_0 | H | \Psi_0 \rangle \tag{2.165}$$

$$= V_C(R) + \text{const.}, \tag{2.166}$$

which defines the Coulomb potential up to an R-independent constant. With $E_0 = \langle \Psi_0 | H | \Psi_0 \rangle$ we can introduce

$$G(R,T) = \left\langle \Psi_{q\bar{q}} \middle| \mathrm{e}^{-(H-E_0)T} \middle| \Psi_{q\bar{q}} \right\rangle \tag{2.167}$$

$$= \sum_n |\langle \Psi_n | \Psi_{q\bar{q}} \rangle|^2 \, \mathrm{e}^{-(E_n - E_0)T}, \tag{2.168}$$

where Ψ_n are the normalized energy eigenstates

$$H\left|\Psi_n\right\rangle = E_n\left|\Psi_n\right\rangle, \quad \left\langle\Psi_n|\Psi_m\right\rangle = \delta_{nm}. \tag{2.169}$$

By taking the time derivative and the limit $T \to 0$ of (2.168) and by using (2.169) we obtain the Coulomb potential

$$\lim_{T\to 0}\left[-\frac{\mathrm{d}}{\mathrm{d}T}\log G(R,T)\right] = V_C(R) + \text{const.} \tag{2.170}$$

On the lattice, the operator $G(R,T)$ can be built from Polyakov line correlators

$$G(R,T) = \left\langle \mathrm{tr} P_t^\dagger(\boldsymbol{x}) P_t(\boldsymbol{y})\right\rangle, \tag{2.171}$$

where in contrast to (2.121) the product of links in time-direction is of finite length $T < N_t$

$$P_T(\boldsymbol{x}) = U_0(0,\boldsymbol{x})U_0(\hat{t},\boldsymbol{x})U_0(2\hat{t},\boldsymbol{x})\ldots U_0((T-1)\hat{t},\boldsymbol{x}). \tag{2.172}$$

Thus, we find the third definition [113, 115]

$$V_C(R) = -\frac{1}{a_t}\log\left\langle \mathrm{tr} U_0^\dagger(\boldsymbol{x})U_0(\boldsymbol{y})\right\rangle, \tag{2.173}$$

where the time derivative was replaced by the discrete lattice derivative $\frac{\mathrm{d}f}{\mathrm{d}T} = \frac{f(t+a_t)-f(t)}{a_t}$.

Related Work

The Coulomb potential from the Coulomb kernel (2.160) was numerically investigated in Ref. [98, 108, 116]. In Ref. [116] their best estimate for the Coulomb string tension is $\sigma_C = 1.6\sigma$ (SU(3)) and $\sigma_C = 2.2\sigma$ (SU(2)) in Ref. [108]. However the authors give reasons why the results has to be taken with care. First of all there is a strong Gribov copy effect whose origin is found in Chapter 3 to be related to the low lying eigenvalues of the Faddeev–Popov operator. Secondly, the numerical data for $p^4V_C(|\boldsymbol{p}|)$ shows a peak around $0.5\text{GeV} \lesssim 1\text{GeV}$ which is not expected from theoretical considerations. This introduces an ambiguity in defining a fit function and in defining an appropriate IR range for the fit. Additionally, the fits are based on only a few data points in the IR.

The $\langle A_0A_0\rangle$ propagator (2.162) was studied in [95, 97, 102]. As for the transverse (spatial) gluon propagator the temporal propagator shows scaling violations which can be improved by going to anisotropic lattices [97]. Only there, and only in position space, an estimate for the Coulomb string tension could be obtained with $\sigma_C \approx (1.4\ldots1.6)\sigma$. The authors attribute this rather small value, compared estimates from the other definitions, to the presence of the polarization term in Eq. (2.161).

Finally the $U_0U_0^\dagger$-correlator (2.173) was used in various studies with different focus. The technique was first used in Refs. [113, 115] for SU(2) where the Coulomb string tension was found to be significantly larger than the physical string tension $\sigma_C \gtrsim 3\sigma$. There the authors also studied the relation between Coulomb confinement and the center vortex picture. They find that the Coulomb string tension vanishes if center vortices are removed, see also Chapter 5. The first study of SU(3) was done in Ref. [117] and again a confining Coulomb potential is found, though they do not compare the Coulomb string tension to the physical string tension. They also did not compare their finite temperature results to $T = 0$. In the range $T = 1.5\ldots5T_c$ they find that the string tension rises linearly with temperature. In Ref. [118] the authors use an interpolation gauge between Landau and

Coulomb gauge, where in the Coulomb gauge limit they obtain a string tension $\sigma_C \simeq 2.6\sigma$. The same authors also show [119] that the confining nature of the potential is due to the low momentum components of the link variable. In Ref. [120] a value of $\sigma_C \gtrsim 4\sigma$ was reported for SU(3). In the appendix of Ref. [121] the author argues that $\langle A_0 A_0 \rangle$ should not be used to define the Coulomb potential, since it is not clear which branch of the logarithm should be used when A_0 is defined from the relation $U_0 = \exp(\mathrm{i}A_0)$.

2.6.5. The Quark Propagator

The quark propagator will be discussed only briefly in Appendix D in the context of a technicolor model. For QCD the Coulomb gauge quark propagator was studied in Ref. [122] and in the quenched approximation for an improved discretization of the Dirac operator in Ref. [123].

2.6.6. Discussion of Continuum and Lattice Results

In Section 2.3 we already mentioned that within the Hamiltonian approach one finds different solutions for the gap equation which lead to a different behavior of the propagators. These solutions are classified in two categories: the critical solutions [17, 18] are classified by a infrared divergent ghost form factor and the subcritical solutions [124] by a ghost form factor which is infrared finite. From our discussion of confinement in Coulomb gauge it is obvious that the critical solutions are expected to be the physical solutions. The critical solutions can be classified by their asymptotic behavior. We will use the notation of [108] to describe the asymptotic of the gluon propagator and the ghost form factor. In the IR the propagator can be described by a power law

$$D(|\boldsymbol{p}|) = \frac{1}{|\boldsymbol{p}|^{\kappa_{\mathrm{gl}}}}, \quad d(|\boldsymbol{p}|) = \frac{1}{|\boldsymbol{p}|^{\kappa_{\mathrm{gh}}}}, \quad |\boldsymbol{p}| \to 0. \tag{2.174}$$

In the UV we assume that the propagators are described by their tree-level value with possibly logarithmic corrections

$$D(|\boldsymbol{p}|) = \frac{1}{|\boldsymbol{p}| \log^{\gamma_{\mathrm{gl}}}\left(\frac{|\boldsymbol{p}|}{m}\right)}, \quad d(|\boldsymbol{p}|) = \frac{1}{\log^{\gamma_{\mathrm{gh}}}\left(\frac{|\boldsymbol{p}|}{m}\right)} \quad |\boldsymbol{p}| \to \infty. \tag{2.175}$$

The anomalous dimensions are found to be $\gamma_{\mathrm{gl}} = 0$ and $\gamma_{\mathrm{gh}} = \frac{1}{2}$. One finds two critical solutions which differ by their IR exponents

$$\kappa_{\mathrm{gl}} = -1, \quad \kappa_{\mathrm{gh}} = 1, \tag{2.176}$$

$$\kappa_{\mathrm{gl}} \approx -0.6, \quad \kappa_{\mathrm{gh}} \approx 0.8. \tag{2.177}$$

The first solution (2.176) is also called confining solution since it leads to a linear rising Coulomb potential [18]. Both solutions are found by an analytical IR analysis and by numerically solving the integral equations. From the IR analysis [125] one finds that the critical solutions have to obey the sum rule

$$\kappa_{\mathrm{gl}} + 2\kappa_{\mathrm{gh}} = 1. \tag{2.178}$$

The sum rule was derived under the assumptions that the ghost-gluon vertex does not need renormalization. In Landau gauge the validity of this assumption was verified on the lattice for SU(2) [126] and SU(3) [127]. In Coulomb gauge it was found that a finite

dressing of the vertex does not influence the numerical solutions [125]. Therefore one usually assumes that the sum rule is valid in Coulomb gauge.

In an approach derived from functional renormalization group equations, the sum rule is also found but with different values for the IR exponents [128]

$$\kappa_{\mathrm{gl}} \approx -0.28, \quad \kappa_{\mathrm{gh}} \approx 0.64. \tag{2.179}$$

In comparison to lattice results a big discrepancy shows up. While the gluon IR exponent of the solution (2.176) from the Hamiltonian approach perfectly fits to the lattice results [44], the exponent of the ghost form factor of all lattice studies is found to be around or below $\kappa_{\mathrm{gh}} \lesssim 0.5$ [101, 102, 108]. These results clearly violate the sum rule (2.178). In Ref. [108] the authors report that from time to time configurations which are very close to the Gribov horizon, indicated by a close to zero eigenvalue of the Faddeev–Popov operator, enter the Monte Carlo ensemble. They argue that these configurations, which contribute significantly to the IR enhancement, maybe underrepresented in the ensemble. In Chapter 3 we will investigate this question in detail. One might also question if the assumption that lead to the sum rule, i.e. a bare ghost-gluon vertex, is fulfilled in Coulomb gauge, though this question is not addressed in this work.

3. The problem of Gribov copies

In this chapter we will discuss the effect of Gribov copies on the Coulomb gauge propagators. As opposed to earlier approaches to resolve the Gribov ambiguity we choose a different strategy which was recently proposed by the authors of Ref. [129]: we select a configuration by the value of the smallest non-trivial Faddeev–Popov eigenvalue. After an introduction on the lattice Gribov problem and its common solutions, Section 3.1, we will first compare gauge fixing to the best-functional value to the new approach in Section 3.3. Then we discuss its implications on the Coulomb gauge propagators in Section 3.4. The results of this chapter were published in Ref. [130].

3.1. Introduction

The Gribov problem, see Section 2.2.1, arises because Coulomb gauge, $\partial_i A_i = 0$, is not sufficient to select a single configuration from the gauge orbit. On the lattice, as will be discussed in detail in Chapter 7, Coulomb gauge fixing is achieved by maximization of the functional

$$F_t^U[g] = \frac{1}{N_c N_d V} \sum_{\boldsymbol{x},i} \mathrm{Re}\,\mathrm{tr}\,[U_i^g(t,\boldsymbol{x})] \tag{3.1}$$

for each time slice t. Yet, a local maximum of (3.1) locates only a, more or less random, configuration in the first Gribov region, which is known to contain many more Gribov copies all satisfying the same gauge condition. Only the global maximum of (3.1), i.e. a configuration in the FMR, resolves the Gribov problem completely. Finding the global maximum of such a functional, however, is analogous to finding the ground state of an SU(N) spin glass [131], a problem which is known to be NP-hard even for the simpler $\mathbb{Z}_2$ theory [132].

There are two widely used approaches to the problem of Gribov copies in lattice gauge theory. The first one is to plainly neglect the problem which can be seen as taking the average over all Gribov copies (in a large ensemble). Essentially, the argument is that the Gribov copy effect should be negligible in (gauge invariant) physical observables, even if they are calculated from combinations of gauge variant correlation functions which are affected by the Gribov problem. This approach, in which one takes the first local maximum found by the algorithm, is called the "minimal gauge" in the literature [133].

The second approach is to locate the global maximum as well as possible, in the hope that the biggest local maximum one can find is a good approximation of the true global maximum. In order to clarify this statement, let $\{U_{\mathrm{FMR}}\}$ be the ensemble of gauge configurations which are in the FMR, i.e. $F[U_{\mathrm{FMR}}] = \max.$, and let $\{U_{\mathrm{bc}}\}$ be the ensemble with gauge configurations such that they are close to the maximum

$$F[U_{\mathrm{FMR}}] \gtrsim F[U_{\mathrm{bc}}], \tag{3.2}$$

i.e. the set of configurations which correspond to the best maximum one could find numerically. One assumes then that the configuration $\{U_{\mathrm{bc}}\}$ is in some sense close to the one in the FMR $\{U_{\mathrm{FMR}}\}$ and that this carries over to the expectation values of gauge variant

quantities O

$$\langle O(U_{\mathrm{bc}})\rangle \approx \langle O(U_{\mathrm{FMR}})\rangle \equiv \langle O\rangle_{\mathrm{phys}}\,, \tag{3.3}$$

i.e. that the expectation value calculated from $\{U_{\mathrm{bc}}\}$ is a good approximation for the physical relevant one which is in the FMR. For historical reasons, we will call the ensemble $\{U_{\mathrm{bc}}\}$ the *best copy* (bc) ensemble. Unfortunately, it is not possible to verify this assumption numerically on large lattices, since that would imply to solve the global maximization problem. Additionally, there is no mathematical proof that the assumption holds. In a simple toy model, a U(1) lattice theory on a 2-dimensional sphere [134], there is actually numerical evidence against this hypothesis.

Recently a third approach for resolving the Gribov problem has been discussed in Landau gauge [135, 136]: instead of choosing the copy with the best functional-value one chooses the copy for which the first non-trivial eigenvalue of the Faddeev–Popov operator is smallest, the *lowest copy* (lc). We will borrow this notation from the aforementioned papers. The idea behind the lowest copy approach is that this should locate configurations which are close to the Gribov horizon. These are, according to Gribov and Zwanziger's entropic reasoning, the relevant configurations in the thermodynamic limit. The authors of Ref. [135, 136] found that both the ghost dressing function and the gluon propagator are enhanced in the IR for the lowest copy when compared to the best-copy approach, while they become flatter for the Gribov copy with a large smallest eigenvalue. While this effect is significant for the ghost dressing function, the effect on the gluon propagator is mild. Similar attempts to improve Landau gauge fixing to explain the IR properties of the decoupling solutions continuum calculation from Dyson–Schwinger and Functional Renormalization Group equations were put forward in [137, 138] with mixed results.

In Coulomb gauge a discrepancy exists between the IR exponent of the ghost dressing function in the Hamiltonian variational approach and lattice results [108, 139, 140]. On the other hand the behavior of the gluon propagator agrees very well [44], see Section 2.6.6. The IR exponents of the ghost form factor and gluon propagator are related by a sum rule, which is a direct consequence of a bare ghost-gluon vertex. The assumption that the ghost-gluon vertex is finite was verified for Landau gauge on the lattice and is usually assumed to be valid for Coulomb gauge as well. A possible explanation for the disagreement between continuum and lattice results might be that the lattice data is biased by artifacts related to the Gribov problem. In a recent paper [129], the authors propose that indeed the gauge copy with the smallest first non-trivial eigenvalue should provide better agreement with the continuum calculations, since it is the copy which is closest to the Gribov horizon. To test this conjecture we will apply this approach in the following. We will find, that it is numerically much easier to find a high value of the functional, i.e. a best copy, compared to a configuration with a very small eigenvalue of the Faddeev–Popov operator. Therefore we need to compute many gauge copies in order to find the Gribov copies with small eigenvalues. As a by-product we get the best-functional copy with a high number of trials which allows us to review the best copy strategy as well.

3.2. Lattice setup

For this study we used isotropic lattices of three different sizes and discretizations. Since the ghost propagator is known to suffer from strong scaling violations on isotropic lattices we include an anisotropic lattice. Our setup is summarized in Table 3.1. To fix the lattice spacing, we used an interpolation formula based on data of Ref. [108] and references therein. We use $\sqrt{\sigma} = 0.44\mathrm{GeV}$ as the physical value for the string tension.

Label	Size	ξ	β	a_s [GeV^{-1}]	L [fm]
A1	16^4	1	2.2	1.07	3.4
A2	16^4	1	2.3	0.84	2.6
A3	16^4	1	2.4	0.61	1.9
B1	24^4	1	2.2	1.07	5.0
B2	24^4	1	2.3	0.84	4.0
B3	24^4	1	2.4	0.61	2.9
C1	32^4	1	2.2	1.07	6.7
C2	32^4	1	2.3	0.84	5.3
C3	32^4	1	2.4	0.61	3.8
D1	128×32^3	4	2.25	1.11	7.0

Table 3.1.: Lattice setup.

3.3. Gauge fixing and Gribov copies

Both for the lowest copy and the best copy strategy, we us the over-relaxation technique as will be discussed in Chapter 7. There, we also explain simulated annealing as a technique to increase the probability to find the absolute maximum of the gauge fixing functional, i.e. to find a better best-functional copy. Usually a combination of repeated gauge fixing and a preconditioning with simulated annealing is used to find the (best approximation of the) global maximum. Repeated gauge fixing means to start gauge fixing multiple times from a random gauge transformation (gauge copies) and select the one which best satisfies the best-functional (or lowest-eigenvalue) condition. In Fig. 3.1 we show an illustrative plot of the evolution of the gauge fixing precision $\theta_{\max}$ (7.7) over the number of gauge fixing steps. In the figure on the left hand side four runs with over-relaxation parameter

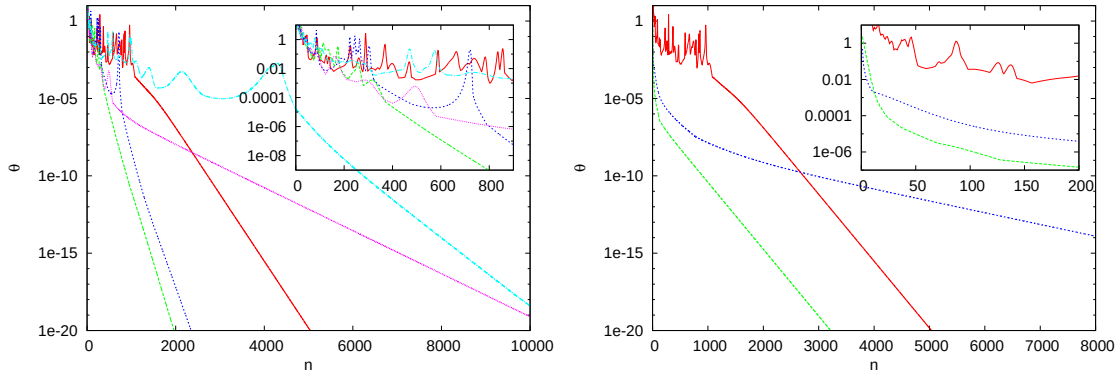

Figure 3.1.: Gauge precision θ over the number of over-relaxation steps. L.h.s.: 5 gauge copies of the same configuration, the light blue line is with simple relaxation, the other lines with $\omega = 1.7$, the pink line corresponds to a significantly smaller value of the first non-trivial eigenvalue of the Faddeev–Popov operator λ_1 compared to the other copies; r.h.s.: the green ($\omega = 1.7$) and blue line ($\omega = 1.0$) are preconditioned with simulated annealing which reduces/removes the first phase where the algorithm tries to locate a maximum, the slope of the second phase does not change (compare the red and green lines with $\omega = 1.7$); all three lines correspond to the same Gribov copy, identified by the functional value and the first non-trivial eigenvalue.

$\omega = 1.7$ and one run with $\omega = 1$ (pure relaxation) are shown. The gauge fixing has two characteristic stages. In the first stage the precision is fluctuating strongly at a rather high value until a maximum is located with a precision of about 10^{-4}. Then, in the second stage, the precision monotonically approaches zero. As shown on the right hand side, if simulated annealing preconditioning is used, the first stage is already overcome in the simulated annealing phase (which is not shown in the plot).

As we focus in this study on the lowest-copy gauge fixing, we don't want to precondition our algorithm to find an absolute maximum and therefore we cannot use simulated annealing. Since the best copy results are mostly a byproduct of the search for the lowest copy, they are also not preconditioned with simulated annealing, if not explicitly stated otherwise. Unfortunately, no algorithm is known that would precondition the gauge fixing to a low eigenvalue of the Faddeev–Popov operator and we have to rely on pure over-relaxation with a high number of gauge copies N_r.

In a first run we calculated the lowest eigenvalue λ_1 on $N_r = \mathcal{O}(10^3)$ copies of the small lattices. In Ref. [109] it was already noticed that the size of the smallest eigenvalue is correlated with the number of gauge fixing iterations N_{it} that are necessary to achieve a given accuracy $\theta_{\max}$, as indicated in Fig. 3.1. The reason for this behavior is that a low eigenvalue means an almost flat direction in the gauge fixing functional and an ill-conditioned Faddeev–Popov operator, which leads to a slow convergence in the iteration process. In Fig. 3.2 we investigate this behavior in more detail. We find a perfect correlation of λ_1 and N_{it} which is independent of the coupling β. Additionally, the slope does only depend very weakly on the over-relaxation parameter ω. We find the data described perfectly by a simple power law

$$\lambda_1 \left(N_{\text{it}}\right) = \frac{c}{N_{\text{it}}^{\gamma}}. \tag{3.4}$$

with an exponent of $\gamma \approx 1.1$. The proportionality factor c depends strongly on ω. To rule out that the over-relaxation parameter ω conditions the algorithm to find a gauge copy with a certain value of λ_1, we verified that in average ω has no influence on how often a configuration with small eigenvalue is found. This is also indicated in Fig. 3.2, though in the plot it is obfuscated by the bulk around the minimal number of iterations.

The correlation of the number of iterations and the smallness of the Faddeev–Popov eigenvalue allows us to tweak our algorithm: since the calculation of eigenvalues is computationally the most demanding part in our gauge fixing program, we implemented a (self-adjusting) threshold. We calculate the eigenvalues only for "promising" gauge copies, where the number of iterations exceeds a certain threshold $N_{\min}$. Since the smallest eigenvalue (which we are able to find) differs from configuration to configuration, we usually start with a small threshold, e.g. $N_{\min} = 0$. When a smaller eigenvalue is found, the threshold is increased to a multiple $\alpha < 1$ of the number of iterations N_{it} that where needed to find this eigenvalue (or left unchanged if αN_{it} is smaller than the current threshold). We find that $\alpha = 0.8$ provides a suitable update strategy. In a typical run with this setting, eigenvalues are calculated for all gauge copies up to a point where a small eigenvalue is found and the threshold is substantially increased. Since usually the Gribov copy with the so-far smallest eigenvalue is well separated from the one with the next-to-smallest eigenvalue in terms of N_{it}, this procedure eventually constrains the program to only evaluate the eigenvalues for configurations with this smallest λ_1.

Since the first Gribov region and the FMR have a common boundary, one may wonder if the best-copy approach, which can be seen as an approximation of the configuration in the FMR and the lowest-copy approach, as an approximation for the configuration closest to the Gribov horizon, eventually converge to the same configuration. However, from the

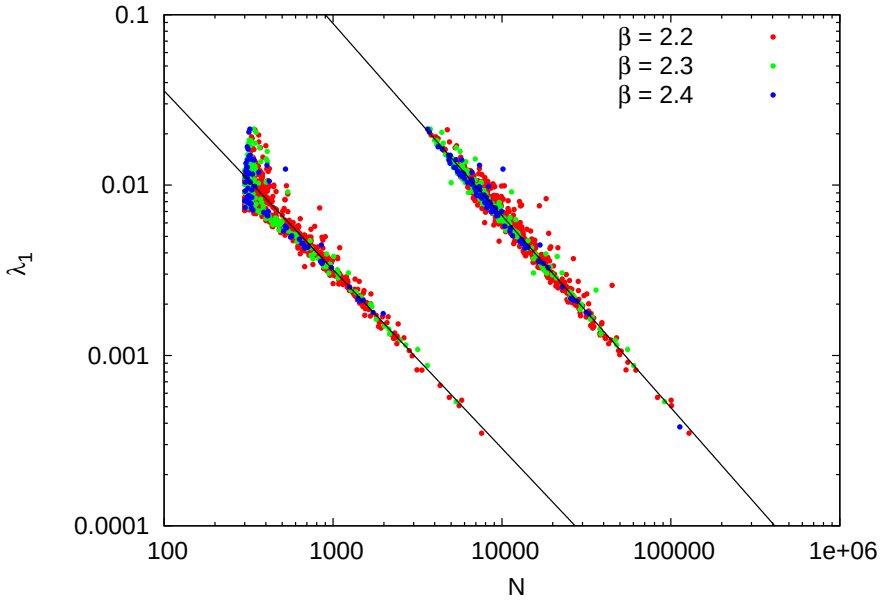

Figure 3.2.: Smallest eigenvalue λ_1 as a function of the number of gauge-fixing iterations. From each set A1, A2 and A3, we used 10 configurations and calculated 1,000 gauge-copies. The data points which correspond to fewer iterations (left) are from runs with $\omega = 1.9$, for the points with more iterations (right) we used $\omega = 1$.

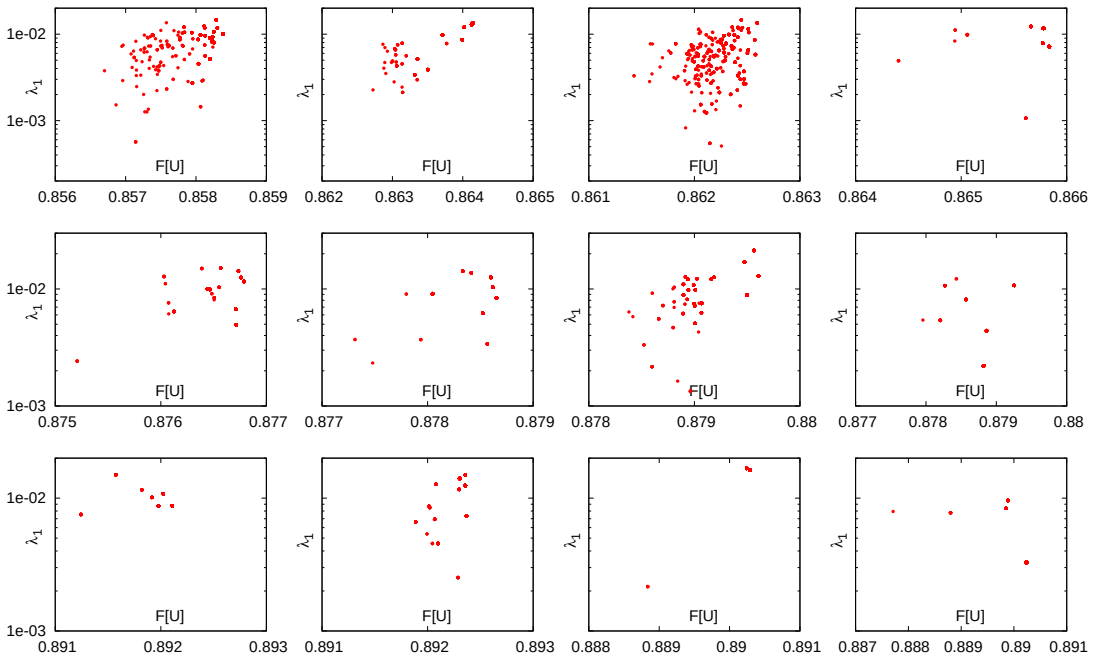

Figure 3.3.: Smallest eigenvalue vs. functional value for 1,000 copies from 4 arbitrary configurations of the 16^4 lattices A1, A2, A3 (from top to bottom). The number of distinct Gribov copies decreases with finer lattices.

Landau gauge data of Ref. [135] there is no such indication. Also for our Coulomb gauge data there is no evidence that they may coincide. In Fig. 3.3 we show scatter plots for four arbitrarily selected configurations of each of the 16^4 lattices (A1, A2, A3 from top to bottom). The data points are from 1,000 different gauge copies. Often, however, the same Gribov copy is found multiple times. The number of unique Gribov copies (we could find) varies strongly between configurations, as can be seen in the third and fourth configuration of the A1 lattice (top right). As expected the number of Gribov copies decreases with finer lattice spacing.

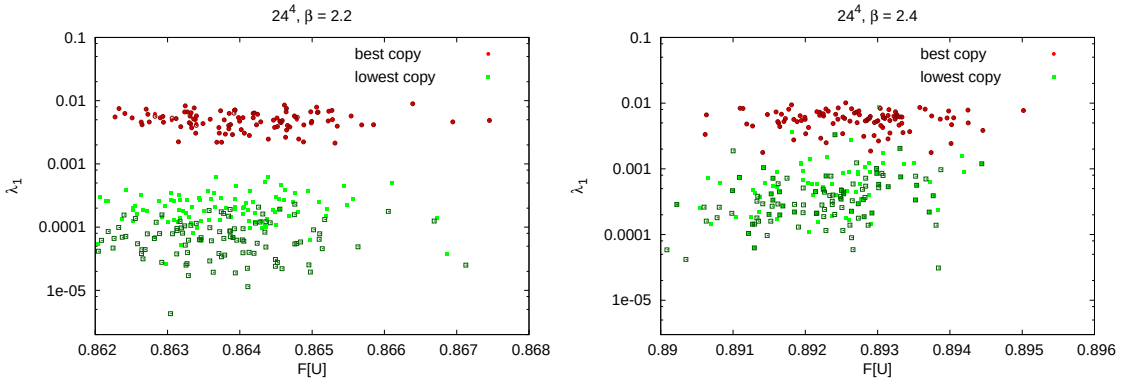

Figure 3.4.: Best approximation of the FMR, i.e. the best copy, and the Gribov horizon, i.e. the lowest copy for the B1 (left) and B3 (right) lattices. Full light-colored symbols denote 1,000 trials; the empty, dark-colored symbols denote 10,000 gauge copies. There is no configuration where the best-copy and the lowest-copy configuration are same.

Another indication is the result of Fig. 3.4. There we compare the best approximation of the FMR and the Gribov horizon for all 100 configurations of the 24^4 sets B1 and B3 after 1,000 and 10,000 gauge copies. Neither on the coarse lattice (B1) nor on the fine lattice (B3) a configuration is found where the best copy and the lowest copy coincide. For the coarse lattice, after 10,000 copies, the smallest eigenvalues are well separated by one order of magnitude in a first region with the best copies and a second region with the lowest copies. While only very few (B1) or no configurations (B3) see improvement in the best copy from 1,000 to 10,000 copies, the lowest copy is still significantly improved. In Ref. [138] a similar comparison was done for Landau gauge. There, the authors used the smallest non-zero value of the ghost propagator as an estimate of the smallness of the lowest eigenvalue. While they used a much larger ensemble of $\mathcal{O}(10^3)$, they used much less gauge fixing repetitions $N_r \approx \mathcal{O}(10)$. With their setup they found configurations that are both closest to the FMR and the Gribov horizon. However, it is clear that their setup (many configurations, small N_r) is biased towards finding such configurations while our setup is biased in the opposite direction (fewer configurations, large N_r). For a detailed study of this effect, which is not our focus, we would have to significantly increase statistics.

Finally, we try to estimate the number of Gribov copies by counting how many distinct Gribov copies we are able to find for a given number of trials, illustrated in Fig. 3.5. For this study, we use only the functional value to discriminate the Gribov copy, since we do not have the smallest eigenvalue available for all copies due to the threshold strategy. Note that for an unambiguous definition of a Gribov copy we would of have to ensure that all gauge dependent quantities are preserved. The identification of the Gribov copy by only a single parameter thus introduces a bias towards finding too few Gribov copies, as distinct

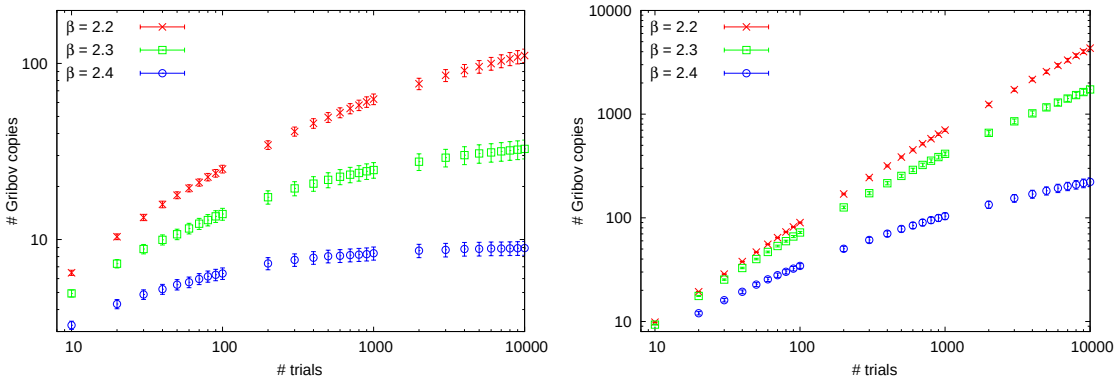

Figure 3.5.: Number of distinct Gribov copies vs. the number of gauge copies for the 16^4 (left) and the 24^4 (right) lattices. Only for the finest 16^4 lattice a saturation is observed. The Gribov copy is identified only by the value of the gauge fixing functional.

copies might erroneously be identified as being the same[1]. An unambiguous estimate would further require that each Gribov copy is found with equal probability, however very likely there are local maxima which are easier to locate by the algorithm than others. This effect will lead to an underestimation of the number of Gribov copies. Thus our estimate has to be treated very carefully. More comprehensive studies of the number of Gribov copies in lattice gauge theory can be found for example in Refs. [141, 142].

Since the number of Gribov copies varies a lot between different configurations, the error bars are rather larger. Only on the smallest and finest lattice a saturation of the number of Gribov copies is observed within 10,000 trials. The main conclusion we can draw from Fig. 3.5 is that we are far from having investigated the whole Gribov region, which would be essential if the (absolute) lowest-eigenvalue copy still differs substantially from the lowest-eigenvalue copy in our limited search space.

3.4. Results

While there is no obvious reason why the lowest-copy approach should have a large effect on the gluon propagator we expect a clear impact on the ghost propagator, given its spectral representation

$$G(\boldsymbol{p}) = \sum_n \frac{\phi_n(\boldsymbol{p})\phi_n(-\boldsymbol{p})}{\lambda_n}, \tag{3.5}$$

where λ_n are the eigenvalues and $\phi_n(\boldsymbol{p})$ the momentum space eigenfunctions of the Faddeev–Popov operator. For the Coulomb potential we expect a strong effect as well.

Gluon propagator

In Landau gauge [135] a small Gribov copy dependence was observed for the gluon propagator on a large 54^4 lattice in the deep IR. With our lattice setup we are not able to reach that far in the IR and do not see a significant effect on the gluon propagator in Fig. 3.6. The static gluon propagator is calculated with the technique discussed in Section 2.6.2 and therefore the gauge has to be fixed for all time slices. The ghost propagator and the

[1] Actually, the authors of Ref. [138] found that there are gauge copies with same functional value but different value for the ghost propagator at smallest non-zero momentum.

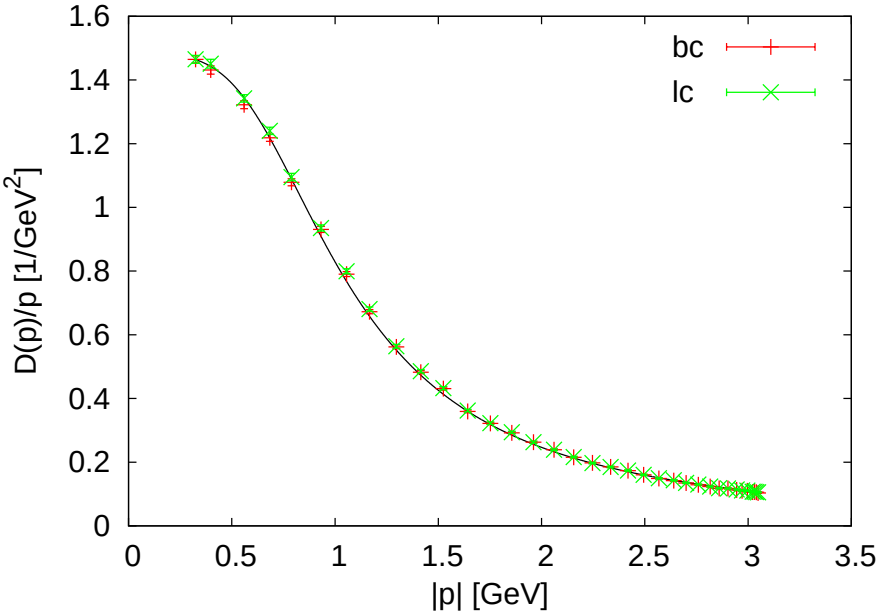

Figure 3.6.: The gluon propagator for the B1 lattice with the best and the lowest copy from 1,000 trials. The solid line is a fit to the Gribov formula [35]. No signal of the Gribov copy effect is visible.

Coulomb potential are calculated only on a single time slice, which allows us to put more computer time in a high number of repetitions. Much larger lattices would be needed to clarify the details of the gluon propagator in IR which is not subject of this study.

Ghost propagator

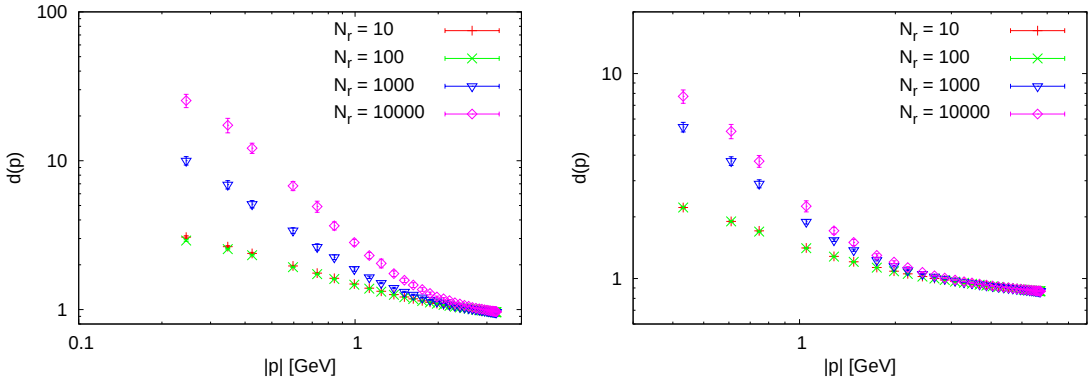

Figure 3.7.: The ghost form factor after gauge fixing to the lowest copy with increasing number of trials from 10 to 10,000 on 24^4 lattices at $\beta = 2.2$ (B1, l.h.s.) and $\beta = 2.4$ (B3, r.h.s.).

As expected from (3.5) the Gribov copy effect has a huge impact on the ghost propagator. In Fig. 3.7 we see that for the 24^4 lattice, the ghost form factor is drastically enhanced in the IR with the number of lowest-copy gauge fixing repetitions. For both lattice spacings, the coarse and the fine lattice, the effect becomes visible only for more than 100 repetitions. However, even for 10,000 iterations a saturation is not yet observed. While the IR exponent

of the form factor is clearly increased from 100 to 1,000 copies, the effect is much less pronounced between 1,000 and 10,000 copies. The huge difference in the IR is mainly due to a sharper bending in the region between 1 and 3 GeV. The data for different β was presented in separate plots on purpose: the ghost form factor is known to suffer from scaling violations on isotropic lattices [108], so that the data points for different coupling do not fall on top of each other over the whole momentum range (after multiplicative renormalization). Moreover, since the lowest copy curves have not yet converged it is not possible to match data points at different β, because the quality of how well the absolute lowest-eigenvalue copy is found for given N_r most likely depends on β.

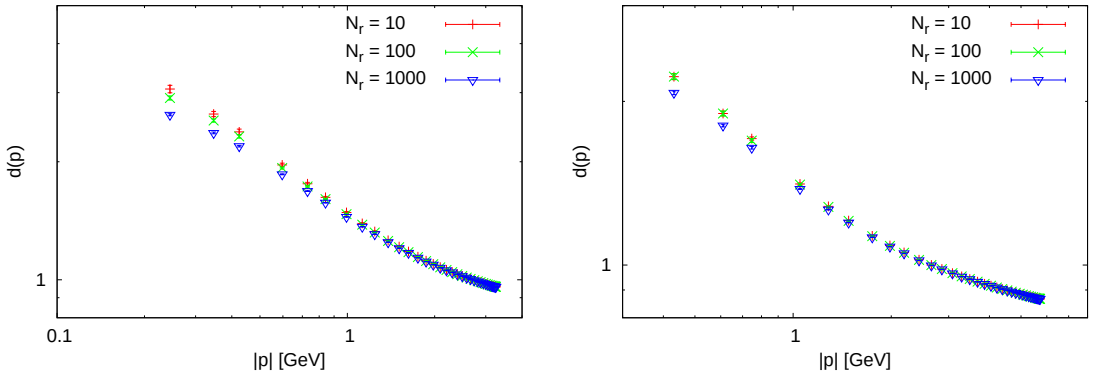

Figure 3.8.: The ghost form factor after gauge fixing to the best copy with increasing number of trials from 10 to 1,000 on 24^4 lattices at $\beta = 2.2$ (B1, l.h.s.) and $\beta = 2.4$ (B3, r.h.s.). The data points for 10,000 copies are omitted since no better copy is found, compare Fig. 3.4.

In Fig. 3.8 we compare the ghost form factor with best-functional gauge fixing for the same lattices. First of all, the effect is much less pronounced compared to the lowest copy results of Fig. 3.7. Secondly, the effect goes in the opposite direction. While for lowest copy the IR was enhanced, with more best-copy trials the IR is slightly suppressed. The effect on the IR behavior is small between 10 and 100 repetitions, but becomes significant between 100 and 1,000 trials.

In Fig. 3.9 we compare the results for lowest and best copy gauge fixing at 10,000 copies, our best values at this lattice size. We renormalized the form factor to

$$d(p = 3\text{GeV}) = 1. \tag{3.6}$$

The best-copy data at different β fit quite well to each other, especially when considering the scaling violations. Compared to the lowest-copy data the error bars for the best-copy approach are much smaller.

Finally, we employ the anisotropic D1 lattice in Fig. 3.10 to estimate the infrared exponent of the form factor. We use a power-law $p^{-\kappa}$ corrected by the ratio of two polynomials as a fit function [108]. For the best-copy strategy we find $\kappa \simeq 0.5$ in agreement with Refs. [108, 139, 140]. For the lowest-copy configurations we find $\kappa \simeq 0.9$ already for $N_r = 50$ and the exponent keeps growing up to $\kappa \simeq 1.6$ for $N_r = 5000$. The quality of the fit χ^2/d.o.f. was in the range between 0.9 and 1.4. Again, a saturation with respect to N_r could not be observed and the IR exponent of the Hamiltonian approach is clearly overshot.

If we focus on the last data points in the infrared we might conclude that the fitting function does not account for these and therefore overestimates the IR exponent κ. Although

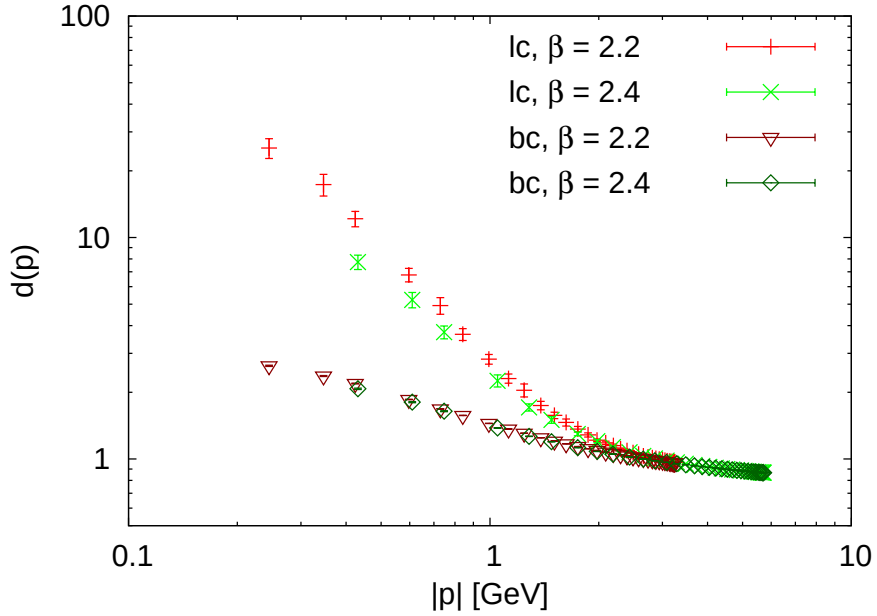

Figure 3.9.: The ghost from factor from the lattices B1 and B3 after 10,000 copies of best and lowest copy gauge fixing.

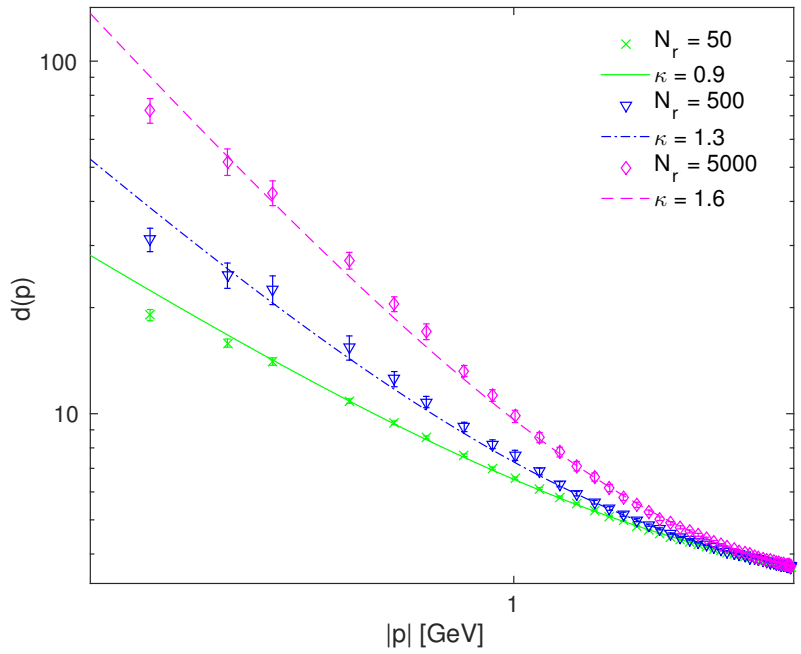

Figure 3.10.: Fit to the ghost form factor of the anisotropic lattice (D1).

these data points are affected by finite volume effects one might argue that a better fitting function could produce the value $\kappa \simeq 1$ expected in the Hamiltonian approach. We did not include such fits for two reasons. First, there is no theoretical motivation for a different functional form than a power-law. Second, the result for the Coulomb potential, which will be presented in the next section, rises doubt that the lowest-eigenvalue procedure, as implemented here, is promising at all.

Coulomb potential

The most important quantity for Coulomb gauge confinement is the Coulomb potential since it provides direct access to the Coulomb string tension. However, the estimation of the string tensions from the momentum space Coulomb kernel (2.160) is affected by large uncertainties, as was discussed in Section 2.6.4. A linear rising potential for large distances corresponds to a momentum space potential which diverges like $1/p^4$ in the IR. Thus, it is convenient to plot the potential such that the intersection with the vertical axis yields the Coulomb string tension in units of the physical string tension

$$\frac{p^4 V_C(p)}{8\pi\sigma} \xrightarrow{p\to 0} \frac{\sigma_C}{\sigma}, \tag{3.7}$$

where σ is the physical string tension as calculated from Wilson loops, Section 2.5.1.

In Fig. 3.11 we show the Coulomb potential calculated from the Coulomb kernel (2.160) for the same configurations as were used in Fig. 3.8 for the ghost propagator. On the left hand side of the plot, the data for $N_r = 10$ is omitted since it contained a configuration with a small eigenvalue leading to very big error bars. We will discuss the issue when we come to the lowest copy results.

In earlier studies of the Coulomb potential a bump in $p^4 V_C(p)$ was observed at around 0.5 to 1 GeV, affecting extrapolations to the intersection with the vertical axis, see the discussion in Section 2.6.4. As Fig. 3.11 shows, this bump vanishes when the number of gauge copies is increased and at the same time the Monte Carlo errors decrease. This might indicate that the fluctuations between individual configurations are suppressed and a region free of Gribov copies has been reached. We already found such a behavior in Ref. [143] in a slightly different context. If we are indeed close to the FMR with the best-copy approach, we would expect that the Coulomb potential in the lowest-copy approach is not substantially different, since according to Gribov–Zwanziger we would expect that the path integral would be dominated by the configurations at the common boundary of the FMR and the first Gribov region (in the thermodynamic limit).

Unfortunately, the lowest copy gauge fixing does not provide such a result. In Fig. 3.12 the data for the best-copy and the lowest-copy approach are compared for the B1 and B3 lattices. While for the ghost propagator the different gauge fixing strategies provided a nice overlap in the UV regime, compare Fig. 3.9, the Coulomb potential, over the whole momentum range, is increased by several orders of magnitude. The same behavior is observed on all lattices that we investigated.

Since this result is quite surprising, we repeated the calculation with a different solver. Usually, we use a conjugate gradient algorithm with Laplace preconditioning. To ensure the validity of our solver we compared the results of our conjugate gradient to a publicly available C++ implementation [144] of the MINRES algorithm [145]. Both algorithms yield the same solution up to numerical precision.

Although the Coulomb potential from the kernel (2.160) does not provide physically meaningful results in the lowest-copy approach, the alternative definition (2.173) works well, as shown in Fig. 3.13, with a modest Gribov copy effect. To extract the Coulomb

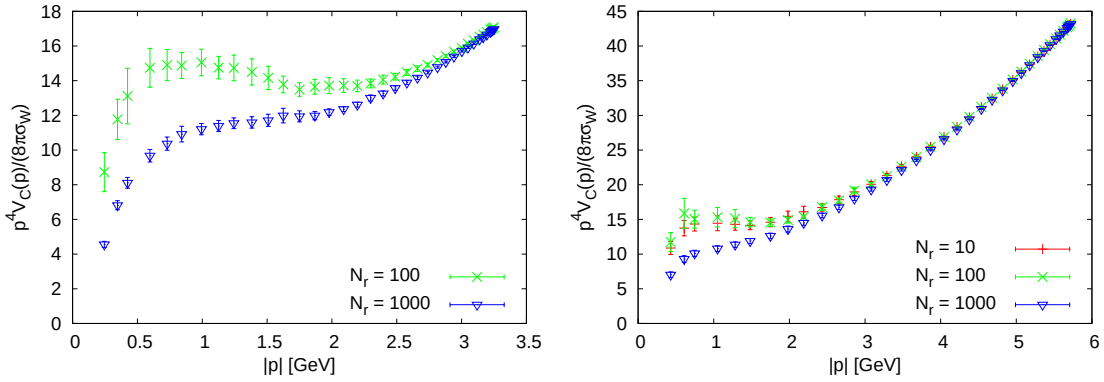

Figure 3.11.: The Coulomb potential according to (2.160) for the lattices B1 (l.h.s.) and B3 (r.h.s.). The $N_r = 10'000$ data shows no difference, compare Fig. 3.4. For the B1 lattice we omitted the $N_r = 10$ data which contained a small Faddeev–Popov eigenvalue, see the discussion in the text.

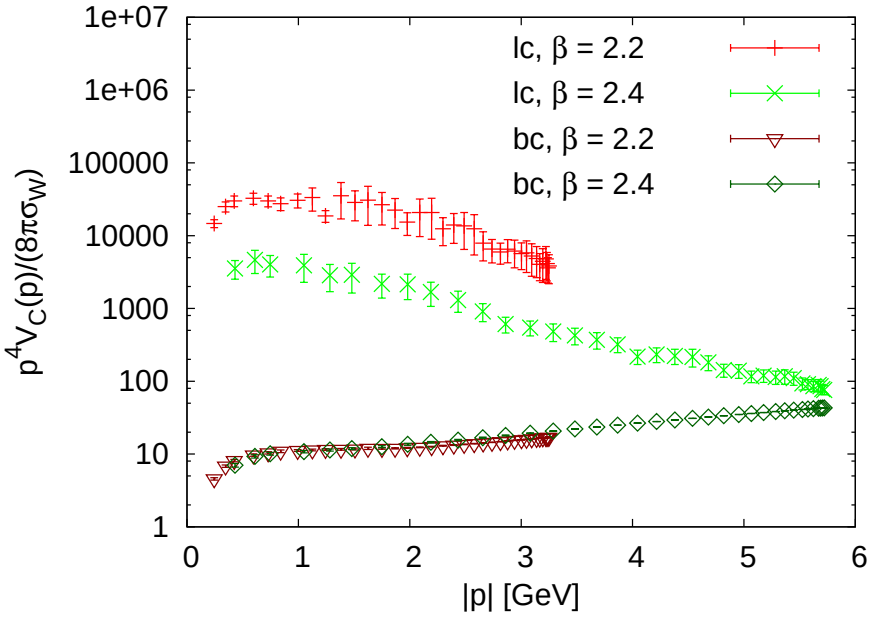

Figure 3.12.: The Coulomb potential calculated from the Coulomb kernel (2.160) after 10'000 copies for the lattices B1 and B3.

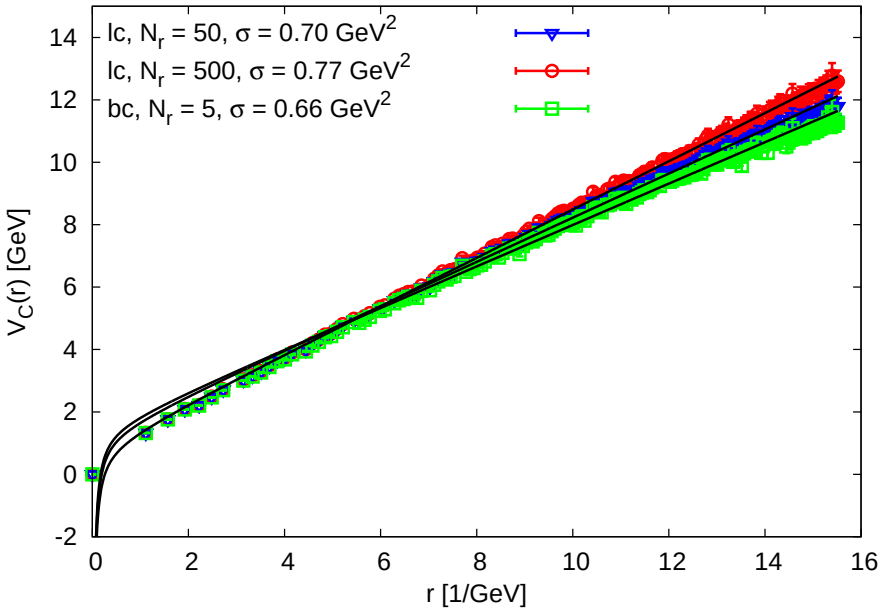

Figure 3.13.: Coulomb potential in position space from the $\left\langle U_0 U_0^\dagger \right\rangle$ correlator (2.173) (D1 lattice). The bc configurations where gauge fixed with simulated annealing preconditioning.

string tension we fitted the potential to

$$V(r) = \frac{\alpha}{r} + \sigma r + \text{const.}, \tag{3.8}$$

where we kept the Lüscher-coefficient $\alpha = -\frac{\pi}{12}$ fixed. In the fit range $[6/a, 14/a]$ we find a Coulomb string tension between $\sigma = 0.66\text{GeV}^2$ (bc, $N_r = 5$) and $\sigma = 0.77\text{GeV}^2$ (lc, $N_r = 500$) with χ^2/d.o.f. between 0.58 (lc, $N_r = 500$) and 0.95 (bc, $N_r = 5$).

3.5. Summary

In this chapter we investigated the Gribov copy effect on the Coulomb gauge propagators. We focused on the novel idea to choose the gauge copy with the smallest eigenvalue of the Faddeev–Popov operator which was put forward in Ref. [129]. Our main result is that the size of the smallest eigenvalue saturates only very slowly to a smallest one when increasing the number of gauge fixing repetitions, if it converges at all. A lower-bound for the smallest eigenvalue, however, would be expected from an effective IR-cutoff on a finite lattice, especially in the context of the entropic argument of the Gribov–Zwanziger scenario. From our study we cannot claim that such a lower bound exists, though it must be noted that we are far from having investigated the whole Gribov region, as Fig. 3.5 indicates.

The small eigenvalues have a drastic effect on the IR behavior of the propagators: the ghost propagator is enhanced compared to the best-copy approach and comes closer to the result of the Hamiltonian approach. However it actually overshoots the expected value of $\kappa = 1$ for the IR exponent of the form factor from continuum calculations and convergence of the exponent is not observed within the data accessible in this work. While the results for the ghost propagator are therefore to some extent positive, the Coulomb potential

calculated from (2.160) is at odds with all expectations and does not allow a physical meaningful interpretation, as an estimate for the Coulomb string tension would be orders of magnitude too large. This effect is expected to become even worse if we would better explore the Gribov region by increasing N_r.

These results allow different interpretations and demand further research for clarification.

First, it might be that the constraint on the lowest eigenvalue is not enough to find the physical relevant configurations which are expected to be on the common boundary of the first Gribov region and the FMR. There, the absolute maxima of (3.1) become degenerate and the eigenvalue density is expected to be shifted towards zero. A straightforward extension of our study would be to choose the gauge copy where the two (or more) lowest eigenvalues are small and (nearly) degenerate.

A second possible explanation for our result could be that the Faddeev–Popov operator, and therefore especially the Coulomb potential from (2.160), suffers from a yet unknown discretization effect. It might be that such an artifact becomes apparent only when the operator is very ill-conditioned, as is the case in the lowest-copy approach. This would make definitions based on the inversion of the Faddeev–Popov operator impractical on the lattice. This hypothesis is supported by the fact that the definition of the Coulomb potential from time-like links (2.173), where no inversion of the operator is needed, provides reasonable results. Additionally, the lack of saturation in the smallest eigenvalues might indicate spurious artifacts in the spectrum of the lattice Faddeev–Popov operator. If one could overcome such an issue and eventually a saturation could be observed, one could still expect to find meaningful results for the Coulomb potential (2.160) and the continuum predictions for the ghost propagator.

Finally, such a lattice artifact could well be related to artifacts which are known to exist in fundamental discretizations of the gauge action and affect gauge-invariant topological observables [146–149]. It might be that these also influence the gauge-variant Coulomb gauge propagators. The discretization might introduce spurious quasi-zero modes of the Faddeev–Popov operator. If such an effect is at work it would require a study of the Coulomb gauge quantities with alternative, numerically more demanding, discretizations of the gauge action [147, 148, 150, 151].

As a by-product in the search for the lowest eigenvalue we generated configurations in the best-functional approach with a high number of gauge copies. For the gluon and ghost propagator we found results in line with previous results, compare Section 2.6, while for the Coulomb potential we observed that the “bump” in the low momentum region vanishes when increasing the number of gauge copies. This result might help to improve the estimates for the Coulomb string tension if one wants to ignore possible lattice artifacts as discussed previously. However for a precision measurement of σ_C much larger lattices and a systematical finite-size analysis would be needed which was not the focus of this chapter.

4. Finite Temperature

So far we solely discussed QCD and Yang–Mills theory at low temperatures were quarks and gluons are confined. The low temperature limit describes the hadronic world where we are living in. However, shortly after the big bang, before the formation of hadrons, the universe was in very hot, dense state, the *quark gluon plasma*. Today neutron stars are the only natural sources which are expected to have a high enough temperature and density that matter is in the state of a quark gluon plasma. The only way to study quarks and gluons under such extreme conditions experimentally is in heavy ion collisions at the high energy particle colliders: at the RHIC (relativistic heavy ion collider), which was specifically built to study the quark gluon plasma, and the LHC, where some measurement time is devoted to heavy ion collisions [152]. For a better understanding of these processes in colliders and in the early universe it is therefore important to understand QCD at high temperatures around and above the *deconfinement phase transition*, the point at which the hadronic matter dissolves into the quark gluon plasma.

In this chapter we will extend the zero temperature studies of lattice Yang–Mills theory in Coulomb gauge to finite temperature. In Section 4.1 we will see how finite temperature is introduced by using the relation between an Euclidean field theory and statistical mechanics. Then we will shortly summarize related work in continuum Coulomb gauge in Section 4.2. Finally, we will discuss the results of our simulations at finite temperature in Section 4.3. The results were already published in Ref. [143].

4.1. Finite Temperature on the Lattice

In Section 2.4 we already discussed the close relationship of Euclidean field theory and statistical mechanics. This analogy allows a straightforward implementation of finite temperature in lattice field theory.

For simplicity we will limit the discussion to a scalar field theory. The central object for a statistical ensemble is its partition function Z from which the thermodynamical variables can be derived. It is given by the trace of the density matrix $\mathscr{D}$, which for a canonical ensemble is a function of the inverse temperature $\beta_T = \frac{1}{k_B T}$[1] and the Hamiltonian of the system

$$\begin{aligned} Z &= \mathrm{tr}\mathscr{D} = \mathrm{tr}\left[\mathrm{e}^{-\beta_T H}\right] \\ &= \sum_a \int \mathrm{d}\phi_a \, \left\langle \phi_a \middle| \mathrm{e}^{-\beta_T H} \middle| \phi_a \right\rangle , \end{aligned} \tag{4.1}$$

where the trace goes over a complete set of (infinitely many) states, as indicated in the second line. For the right hand side of (4.1) we will now find the path integral representation. There the transition from a state ϕ_1 at $t = 0$ to a state ϕ_2 at $t = T$ is given by, see e.g. [32, 153],

$$\left\langle \phi_1 \middle| \mathrm{e}^{-\mathrm{i}HT} \middle| \phi_2 \right\rangle = \int \mathcal{D}\phi \, \mathrm{e}^{\mathrm{i}S}, \tag{4.2}$$

[1] In the literature, the inverse temperature is usually denoted as just β. Here we will use β_T for the inverse temperature to avoid confusion with the inverse coupling. In the following we will set $k_B = 1$.

with the action

$$S = \int_0^T \mathrm{d}t \int \mathrm{d}^3x \, \mathcal{L} \tag{4.3}$$

and $\mathcal{L}$ being the Lagrangian density[2]. The path integral in (4.2) has to be taken such that the states at $t = 0$ and $t = T$ are held fixed to their values ϕ_1 and ϕ_2 respectively. After a Wick rotation to imaginary time $t \to -\mathrm{i}\tau$ and by introducing $T = -\mathrm{i}\beta_T$ we get

$$\left\langle \phi_1 \middle| \mathrm{e}^{-\beta_T H} \middle| \phi_2 \right\rangle = \int \mathcal{D}\phi \, \mathrm{e}^{-S_E} = \int \mathcal{D}\phi \, \mathrm{e}^{-\int_0^{\beta_T} \int \mathrm{d}^3x \, \mathcal{L}_E}, \tag{4.4}$$

where we introduced the Euclidean action S_E and the Euclidean Lagrangian density $\mathcal{L}_E$. If we compare we (4.1) and (4.4) we see that we can express the partition function by the path integral

$$Z = \mathrm{tr}\left[\mathrm{e}^{-\beta_T H}\right] = \int \mathcal{D}\phi \, \mathrm{e}^{-S_E}, \tag{4.5}$$

where the path integration is now over all states with the periodic boundary conditions[3]

$$\phi(\beta_T, \boldsymbol{x}) = \phi(0, \boldsymbol{x}). \tag{4.6}$$

Thus we can describe a quantum field theory at finite temperature by compactifying the temporal direction in the Euclidean theory.

In the lattice setup we already encountered a similar situation. There the lattice is finite in all directions and the fields are introduced with periodic boundary conditions. In that sense any lattice calculation is by construction always a simulation at finite temperature. When we where interested in zero temperature we extracted continuum physics by taking the limit of an infinite space-time, i.e. by increasing the physical volume until the quantities of interest are no longer sensitive to the finite extent of the lattice in space and time. Now, for the calculations at non-zero temperature we want to keep the time extent $a_t N_t$ finite to identify its inverse with temperature

$$T = \frac{1}{\beta_T} = \frac{1}{a_t N_t}. \tag{4.7}$$

Thus, for the continuum limit we have to take $a_t, a_s \to 0$ with the spatial volume approaching infinity $a_s N_s \to \infty$ but with a fixed physical extent in time $a_t N_t = \text{const}$.

Summing up, for finite-temperature studies on the lattice we can use exactly the same setup as in the zero temperature case. The only difference is that we have to adjust the lattice spacing a_t and the size of the lattice N_t in time direction to the temperature of interest. While we can adjust the temperature via N_t only in discrete steps, with the help of the anisotropic action (2.89) we can adjust the temperature continuously while still keeping the physical spatial volume fixed.

4.2. Finite Temperature in Coulomb Gauge

In the continuum, finite-temperature Yang–Mills theory in Coulomb gauge was studied with two complementary methods within the framework of the Hamiltonian approach. In the first method the grand canonical ensemble was investigated [20]. However, the full Hamiltonian density matrix of the grand canonical ensemble cannot be handled analytically and is therefore approximated by a single-particle operator [155]. In Ref. [20]

[2] By taking the limit $T \to \infty$ one would obtain the vacuum amplitude, i.e. the analogous expression to (2.11).

[3] For fermionic fields one needs to impose antiperiodic boundary conditions, see e.g.[154, Chapter 2.5].

the finite temperature equations are solved numerically with the same techniques which were developed for zero temperature, see the references in Section 2.3 and Section 2.6.6. As opposed to Ref. [155] where the finite-temperature propagators were studied for the subcritical solution, the authors of Ref. [20] implement the horizon condition (2.157) for all temperatures. There, the solutions $\kappa_{\mathrm{gh}} \approx 0.8$ and $\kappa_{\mathrm{gh}} = 1$ merge to a single solution $\kappa_{\mathrm{gh}} = 0.5$ above the deconfinement temperature T_C. At the same time the gluon propagator becomes finite, $\kappa_{\mathrm{gl}} = 0$. Thus, the sum rule (2.178) is fulfilled at any temperature. The transition temperature is found to be close to the one obtained in lattice calculations.

In the second approach finite temperature is introduced by compactifying a spatial dimension instead of the temporal one. This reinterpretation of a spatial direction as the time direction is justified because of the Euclidean invariance of the action. In the Hamiltonian approach where Weyl gauge $A_0 = 0$ is implied on the gauge field, this change is necessary if one wants to study for example the Polyakov loop as the order parameter of confinement. With Weyl gauge applied to the compactified direction, the temperature information would be lost as the Polyakov loop[4]

$$P = \frac{1}{N_c} \operatorname{tr} \mathcal{P}\, \mathrm{e}^{-\int_0^{\beta_T} \mathrm{d}t\, A_0(t,\boldsymbol{x})} \overset{A_0=0}{=} 1, \tag{4.8}$$

becomes trivial, independent of temperature. The advantage of this approach compared to the previous one is that one does not need an approximation of the density matrix. In Ref. [156] the effective potential of the Polyakov loop is derived. There the authors find the critical temperature of the deconfinement phase transition to be in good agreement with the grand canonical ensemble calculations [155]. In Ref. [157] the finite-temperature propagators are calculated, though a direct comparison with lattice results is not straightforward.

On the lattice, so far, only a few studies of Coulomb gauge propagators are available. In Ref. [115] the SU(2) Coulomb potential was found to be linearly rising even above T_C, though it was only calculated at a fixed temperature. The Coulomb string tension was also calculated for SU(3) in the temperature range $T = 1.5T_c \ldots 5.0T_c$ [117]. In this range the Coulomb string tension increases linearly with temperature. A direct comparison of the zero temperature with the finite temperature value was not provided, though by comparing their numbers we find that between $T = 0$ and $T = 1.5T_c$ the string tension does not change a lot.

In Ref. [109] these findings are interpreted in the following way. In the Gribov–Zwanziger confinement scenario the near-horizon configurations lead to a diverging ghost propagator and a linear rising Coulomb potential. In Landau and Coulomb gauge we find these near horizon configurations by gauge fixing to the fundamental modular region. Since Coulomb gauge on the lattice is implemented in each timeslice separately the gauge condition locates the three dimensional gauge fields which lie close to the Gribov horizon of a three dimensional theory. The authors of Ref. [109] conclude that this statement is not influenced by introducing temperature via compactification of the time dimension, i.e. the dimension which is not included in the gauge fixing prescription. Therefore the Gribov–Zwanziger confinement scenario might fail to give an explanation for the deconfined phase.

4.3. Results

In the following we present our results for the lattice Coulomb gauge propagators at finite temperature for pure Yang–Mills theory to fill the gap in the literature. We use the SU(2)

[4] $\mathcal{P}$ denotes path-ordering.

anisotropic Wilson gauge action (2.89) with a renormalized anisotropy $\xi = a_s/a_t = 4$. This setup allows us to reach higher temperatures (up to $6T_c$) while still having a reasonable number of lattice points in time direction. In addition, as discussed in Section 2.6, a higher anisotropy reduces the scaling violations which were observed on isotropic lattices.

We found in Chapter 3 that Gribov copies are problematic, especially for the ghost propagator and the Coulomb potential, and discussed two ways to solve it. In this chapter we will use the standard way to resolve the ambiguity: we will try to locate the FMR by searching the global maximum of the gauge fixing functional with the help of the simulated annealing algorithm (7.2.2) and five restarts of the gauge fixing procedure. For the calculation of the gluon propagator we will fix the residual gauge freedom with the integrated Polyakov gauge, see Appendix B.1. The ghost propagator and the Coulomb potential are not influenced by residual gauge fixing.

T/T_c	Size	ξ_0	β	a_s [GeV^{-1}]	L_s [fm]
0	128×32^3	3.20	2.25	1.11	7.0
		3.33	2.40	0.74	4.7
		3.40	2.49	0.56	3.5
		3.46	2.59	0.37	2.3
		3.49	2.64	0.28	1.8
1.5	8×32^3	3.20	2.25	*	*
	12×32^3	3.33	2.40	*	*
	16×32^3	3.40	2.49	*	*
	24×32^3	3.46	2.59	*	*
	32×32^3	3.49	2.64	*	*
3.0	4×32^3	3.20	2.25	*	*
	6×32^3	3.33	2.40	*	*
	8×32^3	3.40	2.49	*	*
	16×32^3	3.49	2.64	*	*
4.0	6×32^3	3.40	2.49	*	*
	9×32^3	3.46	2.59	*	*
	12×32^3	3.49	2.64	*	*
6.0	4×32^3	3.40	2.49	*	*
	6×32^3	3.46	2.59	*	*
	8×32^3	3.49	2.64	*	*

Table 4.1.: Lattice setup with anisotropy $\xi = 4$ and spatial volume 32^3. The lattice spacing marked by "*" for the finite temperature setup is equal to the zero temperature lattice spacing at the corresponding coupling (ξ_0, β).

The phase transition temperature for pure SU(2) Yang–Mills theory was found in Ref. [158] to be $T_c/\sqrt{\sigma} = 0.69$. For the physical value of the string tension we use $\sqrt{\sigma} = 440\,\text{MeV}$. With these values we set the phase transition temperature $T_c = 300\,\text{MeV}$. With an interpolation formula from the data of Ref. [108] we determine the lattice spacing at coupling (ξ_0, β) as given in Table 4.1. We verified that the definition for the critical temperature is consistent with our lattice setup from the expectation value of Polyakov loops. As an example we show the Polyakov loop expectation value over temperature in Fig. 4.1 for a fixed coupling $\xi_0 = 3.40$, $\beta = 2.49$ by varying the lattice extent in time direction $N_t = 4 \ldots 128$. For small temperatures the expectation value is zero, then starting to rise at T_c which corresponds to $N_t \approx 24$. For high temperatures the Polyakov loop will

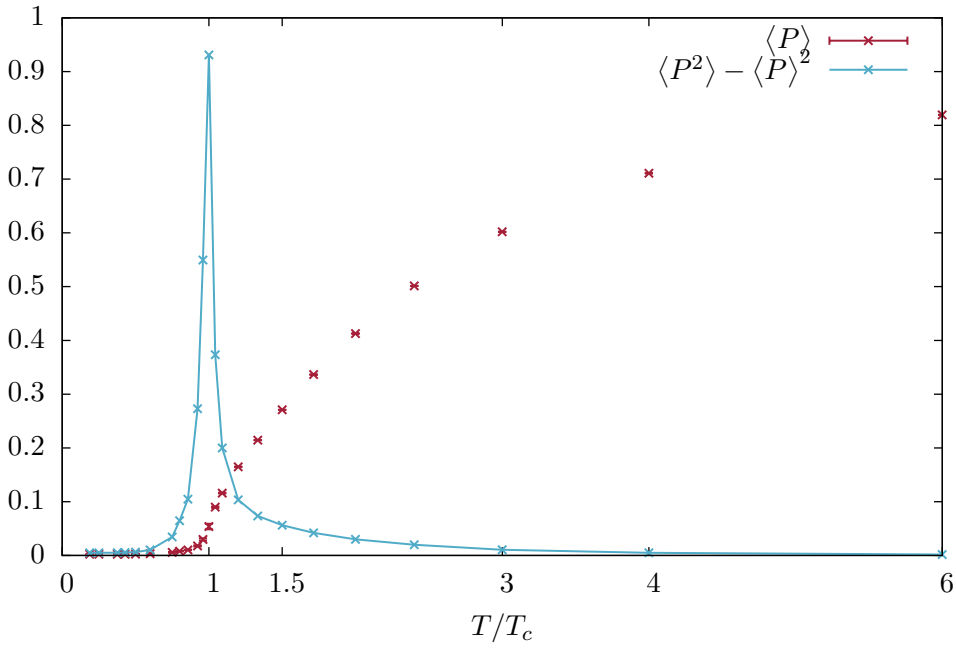

Figure 4.1.: Expectation value of the Polyakov loop $\langle P \rangle$ and susceptibility $\langle P^2 \rangle - \langle P \rangle^2$ for fixed $\xi_0 = 3.40$, $\beta = 2.49$ and varying $N_t = 4 \ldots 128$.

approach unity. We also plotted the quantity $\langle P^2 \rangle - \langle P \rangle^2$ (in arbitrary units) which peaks at the phase transition, see [31, Chapter 12]. Another indication of the phase transition is that the integrated autocorrelation time diverges as expected for an order parameter. This effect is reflected in larger errors around the transition.

4.3.1. The Gluon Propagator

To calculate the static gluon propagator we will use the technique described in Section 2.6.2. This technique was developed for an isotropic lattice setup in [44]. A factorization of the propagator in an energy-independent part and a function of the ratio $|\boldsymbol{p}|/p_0$ was used to eliminate the energy dependence of the full propagator. For our anisotropic setup we find that the factorization is still valid, though small deviations become apparent in the fit of $g(|\boldsymbol{p}|/p_0)$. Nevertheless, we think the technique can be justified. At any rate, as we will see, the choice of technique does not spoil the conclusion of this chapter.

In the following, we plot the propagator divided by the momentum to highlight on the infrared properties of the propagator: a finite value at $|\boldsymbol{p}| \to 0$ indicates a vanishing propagator. In Ref. [44] a very good agreement of their results with Gribov's formula

$$\frac{D(|\boldsymbol{p}|)}{|\boldsymbol{p}|} = \frac{1}{\sqrt{|\boldsymbol{p}|^4 + M^4}} \tag{4.9}$$

was found. In that case the $p = 0$ value will yield the (squared inverse) Gribov mass $\lim_{|\boldsymbol{p}|\to 0} D(|\boldsymbol{p}|)/|\boldsymbol{p}| = 1/M^2$.

For the gluon propagator calculated on the anisotropic lattice we find that the simple form (4.9) does not provide a reasonable fit. We get a good fit for the zero temperature

propagator by modifying Gribov's formula with two additional parameters α, γ

$$\frac{D(|\boldsymbol{p}|)}{|\boldsymbol{p}|} = \frac{Z}{\sqrt{|\boldsymbol{p}|^4 + \gamma M^2 / |\boldsymbol{p}|^2 + \alpha M^3 |\boldsymbol{p}| + M^4}}. \tag{4.10}$$

The parameter Z is the renormalization constant. We renormalize the bare propagator by a fit to (4.10) and choose $Z = 1$ for the renormalized propagator. This choice corresponds to a renormalization point in the far ultraviolet regime

$$D_\mu(|\boldsymbol{p}|)|_{\mu\to\infty} = \frac{1}{\mu}. \tag{4.11}$$

In order to reduce spurious effects of the fitting procedure, i.e. different renormalization parameters for the same coupling at different temperatures, we apply a combined fit of the bare data of all lattices. For each temperature we have the three parameters α_T, γ_T and M_T. Additionally, we have the renormalization parameters $Z_{(\beta,\gamma_0)}$ which we chose to be independent of the temperature.

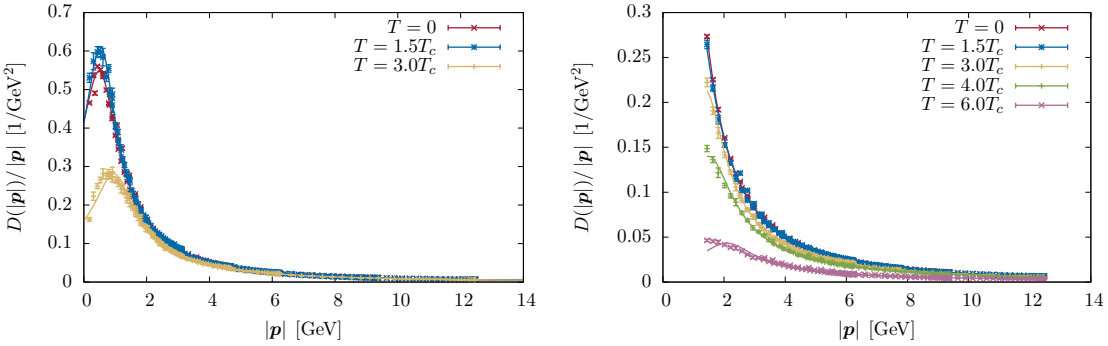

Figure 4.2.: The gluon propagator at zero and finite temperature up to $6T_c$.

In Fig. 4.2 we show our result. On the l.h.s. the propagator is shown in the deep infrared for temperatures up to $3T_c$. At higher temperatures we are restricted to lattices with a smaller physical volume which limits the available momentum range in the IR. Therefore, on the r.h.s. of Fig. 4.2, we decided to show only data where the momentum range is available for all temperatures up to $6T_c$. In both plots we find that the propagator does not change clearly when increasing the temperature from zero to $1.5T_c$. Only around the peak we see a small increase from zero to $1.5T_c$, though the data is a bit noisy in that region. Additionally the data points are from the lattice at the strongest coupling where discretization effects might set in. Therefore we expect that this difference will vanish at weaker coupling and/or with higher statistics. More computer time for larger lattices and a larger Monte Carlo ensemble would be needed for a precise measurement. Another indication that the increase from zero to $1.5T_c$ is not a physical effect is that the propagator at higher temperatures tends in the opposite direction. With increasing temperature the gluon propagator is further suppressed in the IR. This result is surprising as it would indicate that gluons might be even more confined at higher temperatures.

4.3.2. The Ghost Propagator

For the ghost propagator we need the anisotropic setup to soften the scaling violations. Since for $\xi = 4$ the scaling violations are not completely resolved we show the ghost dressing function only at a fixed coupling (β, ξ_0). We chose the lattices at the largest

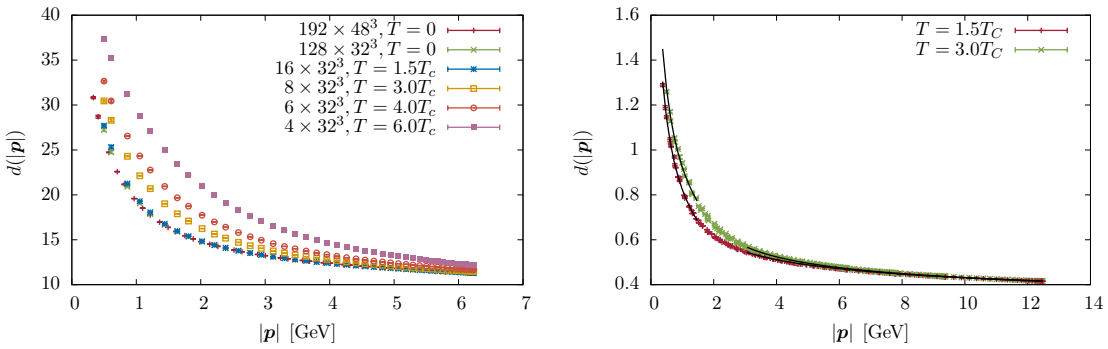

Figure 4.3.: The ghost form factor at fixed coupling $\xi_0 = 3.40$, $\beta = 2.49$. On the r.h.s. a IR and UV fit is shown with the asymptotic behavior of (2.174) and (2.175).

physical volume which is available at all temperatures. Similar to the gluon propagator, the ghost dressing function does not show a signal of deconfinement close to the transition temperature in Fig. 4.3. We verified that we obtain an IR exponent (2.174) of $\kappa_{\text{gh}} \approx 0.5$ as in [108] by a fit to the low momentum regime. Again deviations from the zero temperature propagator are only observed at temperatures above $1.5T_c$. The deviations affect mostly the slope in the mid-momentum range which is indicated by a fit to the IR in the r.h.s. of Fig. 4.3. We find $\kappa_{\text{gh}} = 0.47$ at $1.5T_c$ and still $\kappa_{\text{gh}} = 0.46$ at $3T_c$. Only at $6T_c$ the IR slope tends to a smaller IR exponent, though we cannot rule out that this is a lattice artifact of the small number of lattice points in the compactified dimension.

For the anomalous dimension in the UV (2.175) we find $\gamma = 0.63$ with $m = 0.22\,\text{GeV}$ at $1.5T_c$. We also tried the constraint fit with the anomalous dimension of the Hamiltonian approach $\gamma = 0.5$ [17] and found the same quality of the fit with $m = 0.44\,\text{GeV}$. At $3T_c$ we find $\gamma = 0.42$ with $m = 0.83\,\text{GeV}$. The constrained fit did not work well at $3T_c$, indicated by a doubling in $\chi^2/\text{d.o.f.}$

4.3.3. The Coulomb Potential

In Fig. 4.4 we show the Coulomb potential (2.160) at three temperatures for two physical volumes. With the results of the gluon and ghost propagator in mind the outcome is not surprising: the potential at zero temperature and $1.5T_c$ is indistinguishable. However several effects, which we will discuss in the following, inhibit to give more precise statements.

In Chapter 3 we saw that the Coulomb potential from the Coulomb kernel is strongly affected by which Gribov copy is chosen. Especially configurations with a very small eigenvalue, i.e. close to the Gribov horizon, give a large contribution in the Monte Carlo average. Such Gribov copies can appear in the best copy gauge fixing scheme and are indicated by a slow convergence in the inversion of the operator. This effect is seen in the data at $3T_c$, where the Monte Carlo errors are much larger for one data set. On the l.h.s. of Fig. 4.5 we show the raw data for the problematic ensemble at $3T_c$. A single configuration, plotted in red, is significantly enhanced over the (green) bulk of the other configurations. The average from Fig. 4.4 is shown in blue. On the r.h.s. we show the same data as in Fig. 4.4 but the singular configuration is removed from the Monte Carlo ensemble.

Secondly, the potential, even at $\xi = 4$, shows still severe scaling problems. The Coulomb potential is a renormalization group invariant and therefore should not depend on the coupling constant. In the IR the data matches quite well (at the same temperature), however towards larger $|\boldsymbol{p}|$ the data for different couplings drift apart. This indicates that

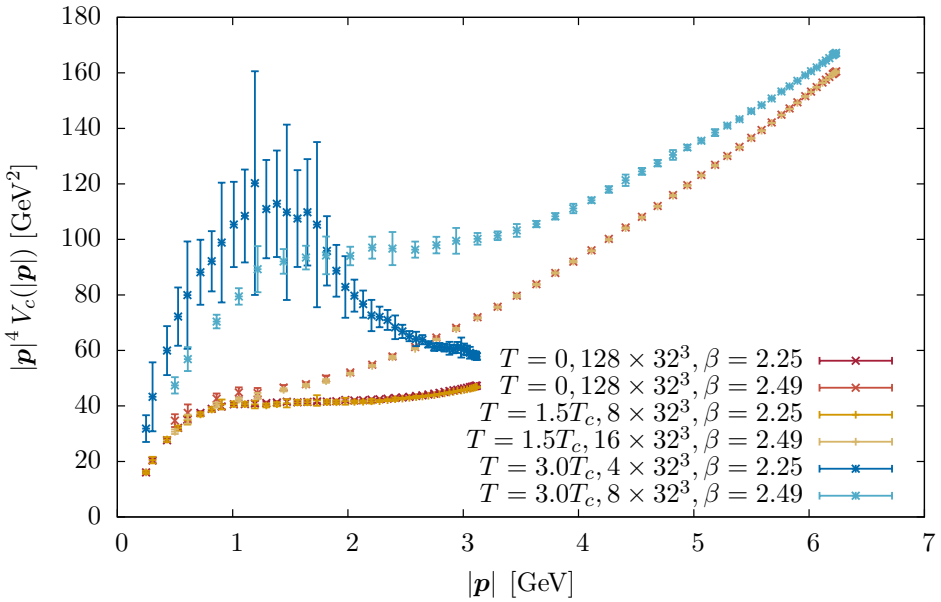

Figure 4.4.: The Coulomb potential up to $3T_c$.

we are outside of the scaling window for the Coulomb potential.

Finally, fitting a string tension from the limited data points in the IR, in the presence of the scaling and Gribov problem, seems unsatisfactory, though these problems are also present in earlier studies [108, 116]. With an optimistic estimate we may conclude that the Coulomb potential in Fig. 4.4 indicates an increase in the Coulomb string tension.

In Fig. 4.6 we show the Coulomb potential obtained from the definition (2.173) at fixed coupling in position space. The lines show a nice linear behavior at large distances. As before the difference between $T = 0$ and $1.5T_c$ is merely visible. When we further increase the temperature the large distance slope, i.e. the Coulomb string tension, increases as already found in Ref. [117]. We fitted the data again with (3.8) in the range $r = 4 \ldots 7.5\,\mathrm{GeV}^{-1}$ with $\alpha = -\pi/12$. The string tension is given in Table 4.2. A linear behavior of the Coulomb string tension $\sigma_C(T)$ with temperature, above $1.5T_c$, as reported in Ref. [117] is possible, though we would need a better sampling to give a quantitative

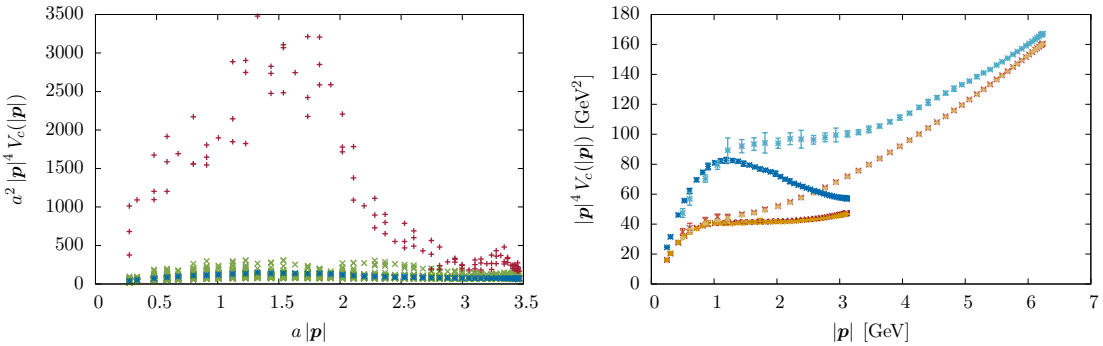

Figure 4.5.: Raw data for the Coulomb potential (l.h.s.): the singular configuration shown in red, the other configurations in green, the Monte Carlo average of Fig. 4.4 in blue. On the r.h.s. the singular configuration is removed compared to Fig. 4.4.

T/T_c	0	1.5	3.0	4.0	6.0
$\sigma_C[\mathrm{GeV}^2]$	0.81(1)	0.80(1)	1.36(2)	2.11(2)	2.97(1)

Table 4.2.: Coulomb string tension σ_C obtained from a fit to the data shown in Fig. 4.6.

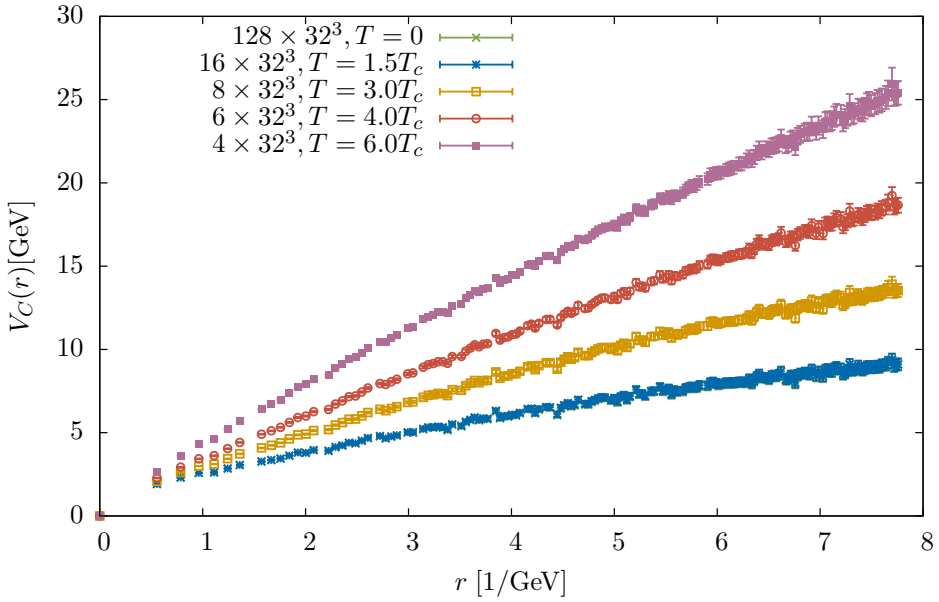

Figure 4.6.: The Coulomb potential from $\left\langle U_0^\dagger U_0 \right\rangle$ in position space up to $6T_c$ for $\xi_0 = 3.40$, $\beta = 2.49$.

statement.

4.4. Summary

In this chapter we investigated the effect of finite temperature on the gluon and ghost propagator as well as the Coulomb potential. Whereas in continuum studies a clear signal of deconfinement shows up, the lattice results do not show such a signal. We compared the zero temperature results with the propagators at finite temperature up to $6T_C$. Between $T = 0$ and $1.5T_C$ we found no significant change in the propagators. Only at higher temperatures the propagators differ compared to zero temperature. A possible explanation would be that the propagators under study, which are all based on links of only one timeslice do not sense the finiteness of the temporal lattice dimension. As we will see in Chapter 5, the Coulomb gauge propagators indeed do not couple to the physical string tension which triggers the deconfinement phase transition, but are related to the spatial string tension σ_s which is known to persist and even rise above T_C [159, 160]. For future studies it would be interesting to adopt the idea of a compactified spatial dimension to lattice field theory, which was developed for the Hamiltonian approach as mentioned in Section 4.2. The idea is to incorporate the compactification in a spatial direction which enters the gauge fixing procedure and the definition of the propagators. Even though the technical implementation of this approach is straightforward, a reliable study would require a comprehensive investigation of discretization effects which are introduced by such an asymmetric lattice.

5. Center Vortices and the Coulomb String Tension

In Chapter 2.6 we discussed that the calculation of static Coulomb gauge propagators is not straight forward due to the problem of how to reach the Hamiltonian limit on a finite space-time lattice. Highly anisotropic lattices are needed at zero temperature. Due to the limited temporal extend of the finite temperature lattice this problem becomes even more pronounced. At finite temperature we found, in Chapter 4, that none of the investigated Coulomb gauge quantities are sensitive to the deconfinement phase transition. In Section 5.2, we will argue that this is a result of the Coulomb gauge propagators coupling to the *spatial* string tension and not to the physical *temporal* string tension which triggers deconfinement. For our reasoning we make use of the center vortex picture of confinement which was already mentioned in Section 2.5.4 and will be summarized in Section 5.1. The results of this chapter are published in Ref. [140].

5.1. Introduction to the Center Vortex Picture of Confinement

To introduce the center vortex picture of confinement we will first consider a $\mathbb{Z}_2$ gauge theory [161], i.e. a gauge theory where the links take only values $Z(x) = \pm 1$. The plaquettes $P_{\mu\nu}(x)$ in (2.83) are just products of these ± 1 links and thus $P_{\mu\nu}(x) = 1$ for an even number of nontrivial (negative) links and $P_{\mu\nu}(x) = -1$ for an odd number. These negative plaquettes form closed loops (in 3 dimensions) on the dual lattice, i.e. they pierce the midpoint of the plaquette perpendicular to the plane of the plaquette. These loops are called *center vortices* as they carry flux of a non-trivial center element. Analogous, in 4 dimensions the center vortices form closed surfaces.

Random Vortex Model In the following we will discuss the so-called random vortex model (RVM), a simple model [162, 163] in which one can relate *percolating* $\mathbb{Z}_2$-vortices to an area law of the Wilson loop and thus to confinement. We will follow the pedagogical introduction of Ref. [164]. Consider a Wilson loop with contour $\mathcal{C}$ surrounding an area $\mathcal{A}$. The value of the Wilson loop is given by the product of links $U(l)$ along $\mathcal{C}$

$$W[\mathcal{C}] = \prod_{U(l)\in\mathcal{C}} U(l). \tag{5.1}$$

With the help of Stokes' law we can divide the loop $\mathcal{C}$ in a product of smaller loops. If we choose to divide our Wilson loop into a product of plaquettes, the smallest possible loops, we find

$$W[\mathcal{C}] = \prod_{P(k)\in\mathcal{A}} P(k) = (-1)^n, \tag{5.2}$$

where n is the number of vortices piercing the surface $\mathcal{A}$ of the loop for a particular $\mathbb{Z}_2$ lattice configuration. The expectation value of the Wilson loop (5.2) is calculated by

$$\langle W[\mathcal{C}]\rangle = \sum_{n=0}^{\infty} (-1)^n p(n), \tag{5.3}$$

given the probability $p(n)$ that n vortices pierce the surface $\mathcal{A}$. We will now calculate this expectation value in the random vortex model where the percolation of vortices is modeled by describing them as uncorrelated objects. For simplicity we will assume that the Wilson loop $\mathcal{C}$ is embedded in a plane spanned by two axes of the lattice, which we choose to be the $x-y$-plane with volume L^2. If the location of a vortex piercing the $x-y$-plane is completely random, then the probability that this vortex also pierces the surface of the Wilson loop is given by $p = \frac{\mathcal{A}}{L^2}$, i.e. by the fraction of the area of the Wilson loop over the total area. The probability of finding n vortices in $\mathcal{A}$ if there are N vortices piercing the $x-y$ plane it then given by the binomial distribution

$$P_N^{\mathrm{RVM}}(n \leq N) = \binom{N}{n} p^n (1-p)^{N-n}. \tag{5.4}$$

Using this expression for the probability in the expectation value (5.3) yields

$$\left\langle W^{\mathrm{RVM}} \right\rangle = \sum_{n=0}^{N} (-1)^n P_N^{\mathrm{RVM}}(n) = (1-2p)^N. \tag{5.5}$$

Introducing the vortex density $\rho = \frac{N}{L^2}$ in the $x-y$-plane, one takes the infinite volume limit, $L \to \infty$, $N \to \infty$ with $\rho = \text{const.}$ and finds

$$\left\langle W^{\mathrm{RVM}} \right\rangle = \lim_{N\to\infty} \left(1 - \frac{2\rho\mathcal{A}}{N}\right)^N = \mathrm{e}^{-2\rho\mathcal{A}}. \tag{5.6}$$

Thus, in the random vortex model we find an area law fall-off of the Wilson loop with the string tension $\sigma^{\mathrm{RVM}} = 2\rho$. The value in this simple model somewhat overestimates the measured value of $\sigma \approx 1.4\rho$ for the SU(2) theory which will be discussed in the next paragraph [165]. This result might indicating that the center vortices in the SU(2) theory are not completely random.

The important assumption in this model which led to the confining behavior was that the vortices percolate over the whole lattice and therefore pierces the plane randomly. In a similar model one can also understand the deconfined phase in the center vortex picture. This model was developed in Ref. [163]. Instead of assuming vortices which percolate over the lattice, the authors assume that the vortices are of finite length. Then, Wilson loops which are large compared to the vortex size are pierced twice by the same vortex. With the assumption that Wilson loops are always pierced twice in a given distance they find that the Wilson loop develops a perimeter law which signals the deconfined phase. Thus the deconfinement phase transition can be regarded as a transition from a phase with percolating center vortices to a phase where they cease to percolate and become short-range. For details we refer to Refs. [163, 164].

Center Vortices in SU(N) Gauge Theory In the $\mathbb{Z}_2$ theory, which we discussed so far, the appearance of center vortices as clusters of "-1" plaquettes is straightforward. The important question is how the center vortex picture can be found in the physical relevant SU(N) theories. The basic assumption to extend the center vortex picture to SU(N) theories is that any SU(N) configurations can be decomposed into center vortices and a non-confining part. Then the randomly fluctuating center vortices will contribute to an area law for the Wilson loop in the way described above, while the non-confining background will only contribute to a perimeter law [114].

While the thickness of a center vortex in the discrete $\mathbb{Z}_2$ theory is only one lattice spacing by definition, the vortices in the SU(N) theory, built from continuous links, can smear out

over several lattice sites. Therefore the $\mathbb{Z}_2$ vortices are called *thin vortices* as opposed to the *thick vortices* of the SU(N) gauge theory. How the thick vortices can be located and separated from the background will be discussed in the next paragraph.

Direct Maximal Center Gauge The general idea to locate center vortices is to concentrate the smeared out thick vortices as much as possible. In this work we will use the direct maximal center gauge for this purpose [166] in which the links are transformed as close as possible to center elements. In SU(2) this is achieved by maximizing the functional

$$F[U] = \sum_{x,\mu} \left[\operatorname{tr} U_\mu(x)\right]^2 . \tag{5.7}$$

Subsequently we extract thin center vortices by a center projection: we project the links in the maximal center gauge to their closest center elements

$$Z_\mu(x) = \text{sign } \operatorname{tr}\left[U_\mu(x)\right] \mathbb{1}. \tag{5.8}$$

The projected center vortices are often called *P-vortices* in the literature. The assumption in this approach is that P-vortices properly locate the actual thick center vortices of the SU(2) theory, though there is no direct proof. In Section 5.1.1 we will summarize the main findings that indicate that the assumption is valid.

The idea behind center projection is that a link can be decomposed in

$$U_\mu(x) = Z_\mu(x) V_\mu(x), \tag{5.9}$$

where the $Z_\mu(x)$ links carry the whole information about the center vortices and $V_\mu(x)$ is the non-confining background. This decomposition describes how we can get a vortex-free configuration by eliminating the center vortices as described in Ref. [167]

$$V_\mu(x) = Z_\mu(x) U_\mu(x). \tag{5.10}$$

This procedure is called vortex removal.

5.1.1. Review of Results of the Center Vortex Picture

In the preceding section we gave a short summary of the center vortex picture for confinement and how center vortices can be found on the lattice by center gauge fixing and center projection. The important assumption for the validity of the center vortex picture is that the P-vortices locate the thick center vortices and carry all the information about confinement. In the following we will summarize the main arguments that support this conjecture. For a deeper overview we refer to Ref. [114, Chapter 6].

P-vortices reproduce the string tension, vortex-free configurations lose the area law The most striking observation in favor of the center vortex picture is that the string tension measured from Wilson loops on the projected configurations reproduce the full string tension of the unprojected configuration in the SU(2) gauge theory. This was verified in many studies, see e.g. Ref. [168] and Section 5.3. We explained that the string tension is measured from large Wilson loops, Section 2.5.1. In center projected configurations the asymptotic string tension is already reached for small loops [168]. The interpretation is that in the full configurations one measures only parts of the thick vortex (for small loops) whereas in the center projected configurations one measures always a complete thin vortex [114].

Unfortunately, the center vortex picture in the SU(3) theory is not that clear. The string tension measured from center projected configurations is only about 60% of the unprojected value [169], indicating the the procedure of center gauge fixing and center projection fails to find all vortices.

Besides the direct measurement of the center projected string tension there are other signals that confinement is due to center vortices: if only Wilson loops in the unprojected configurations $U_\mu(x)$ are measured which are not pierced by P-vortices or pierced by an even number of P-vortices, the string tension vanishes [166].

Additionally, if vortices are removed by (5.10) the string tension again vanishes both in SU(2) [167] and SU(3) [169].

The density of vortices scales If center vortices are physical objects and the P-vortices locate the center vortices, the P-vortex density should be a physical quantity, i.e. renormalization group invariant. That means that the vortex density in physical units, i.e. the number of vortices N_v which pierce a plane $L = a^2N^2$,

$$\rho = \frac{N_v}{a^2N^2} \tag{5.11}$$

should be invariant under a change of the coupling. Indeed the vortex density scales properly in SU(2) [166, 170] and SU(3) [169].

P-vortices locate thick center vortices In Ref. [166] the authors measured Wilson loops in the unprojected configurations whose area is pierced by a fixed number of P-vortices. They find that large Wilson loops obey

$$W_n/W_0 = (-1)^n, \tag{5.12}$$

where W_n is the expectation value of Wilson loops which are pierced exactly n times. This behavior is expected since each vortex will contribute with a factor of "-1" to the Wilson loop and the (short range) non-confining background W_0 will average out for large loops. Again this was found also for SU(3) [169].

Since these studies imply that P-vortices locate the thick center vortices we will not make this distinction any more and will just speak about center vortices in the following.

Problems and open questions While there are a lot of reasons to believe in the center vortex picture as a description for confinement, we should also summarize the shortcomings of center gauge fixing and center projection. We already mentioned that the string tension is not fully reproduced after center projection in SU(3), which might be due to a cancellation of the two types of vortices associated with the two non-trivial center elements.

Additionally, and this is not limited to SU(3), center gauge fixing has a Gribov problem: if the maximal center gauge fixing algorithm is improved to better locate the global maximum of (5.7), the string tension of the center projected ensemble is lowered. This was shown by using simulated annealing in addition to the usual overrelaxation technique[1] [171]. Another point is that if one uses Landau gauge as a precondition before center gauge fixing [172] one finds again a higher global maximum of the gauge fixing functional (5.7) but the resulting string tension is compatible with zero. Of course, Landau gauge can be seen as the opposite of maximal center gauge as it smears out the vortices as much as possible, however it rises doubts on the procedure if maximal center gauge cannot locate the vortices which are expected to be a gauge invariant feature. For further discussion see also Ref. [173].

[1] See Section 7.2.2 for an introduction to simulated annealing in the context of Coulomb gauge fixing.

Relation to the confinement scenario of Gribov and Zwanziger In Section 2.5 we discussed different methods to describe the origin of the confining force. Of course an interesting question is whether these mechanisms are related and are compatible with each other. The relation between the center vortex picture and confinement in Coulomb gauge was first studied in Ref. [113]. It was found that the Coulomb potential (2.173) becomes flat at large distances when vortices are removed. This demonstrates that confinement in the center vortex picture and the idea of Gribov and Zwanziger are indeed compatible. Additionally, in Ref. [115] the authors showed that center projected configurations (5.8) which are subsequently transformed to Coulomb gauge are not only close to the Gribov horizon, which would be the statement of Gribov–Zwanziger confinement, but lie exactly on the Gribov horizon. These configurations lie at points where the Gribov horizon touches the boundary of the FMR. In Ref. [109] the same authors investigated the connection between center vortices and the density of near-zero eigenvalues of the Faddeev–Popov operator in more detail. They found that the enhancement of the eigenvalue density near zero can be attributed to the presence of center vortices, since this enhancement is not observed in the vortex-free configurations. In Ref. [174] the Landau gauge gluon and ghost propagators in three space-time dimension were studied upon center vortex removal and compared to Coulomb gauge in four dimensions. After center vortex removal the ghost form factor becomes infrared finite signaling that confinement is lost.

5.2. Coulomb versus Physical String Tension

In Chapter 4 we found that finite-temperature propagators in Coulomb gauge are not sensitive to deconfinement. These propagators are built of spatial links only and are restricted to a fixed timeslice. We argue that because of this limitation the Coulomb gauge propagators only sense space-space correlations and therefore they do not detect the deconfinement phase transition. Because of the unbroken $O(4)$ symmetry at zero temperature the distinction of space-space and space-time correlations is irrelevant and therefore lattice investigations of zero temperatures are fully valid. It is well-known that the spatial string tension, i.e. the string tension calculated from spatial Wilson loops, persists above T_c and even increases for higher temperatures as shown in the Creutz ratio plots of Fig. 5.1. We will explain this figure in more detail in Section 5.3. A qualitatively similar increase was also found for the Coulomb string tension in Chapter 4, see Fig. 4.6.

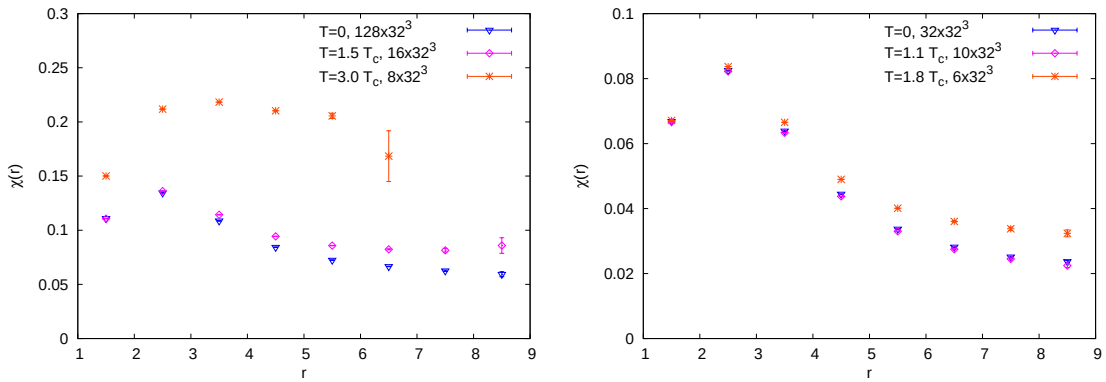

Figure 5.1.: Creutz ratios of spatial Wilson loops (a) $\xi = 4$ anisotropic lattice at $\beta = 2.49$, data points for $r > 7$ are omitted due to a poor signal-to-noise ratio, (b) isotropic lattice at $\beta = 2.6$.

This observation leads us to the assumption that the Coulomb string tension σ_C is strongly correlated with the spatial Wilson string. Therefore the relationship between the Gribov-Zwanziger scenario and Wilson confinement is not realized on the lattice at finite temperature.

Before we go into detail we will summarize the reasoning behind our idea for testing this assumption. Since we want to study the effect of the spatial and temporal string tension separately, we need a technique to change one without changing the other. For this purpose, we use the technique of vortex removal. We will either remove all center vortices, we call this procedure *full vortex removal*, or only vortices piercing space-space Wilson loops, the *spatial vortex removal*, as will be explained in the next section.

By full vortex removal, we disable confinement as discussed in the previous section. Thus Coulomb gauge observables are expected to show a non-confining behavior. This was already found in the references mentioned in the preceding section. On the other hand, by spatial vortex removal, the quark-antiquark potential should not be affected. Especially, the Polyakov loop potential, which is built of time-like links $U_0(x)$ only, is not changed by spatial vortex removal, since the time-like links are not touched at all. Therefore the Wilson string tension calculated from Polyakov loops is unaffected by spatial vortex removal and Wilson confinement is still realized. That means, if the Coulomb gauge propagators lose their confining behavior it cannot be because of physical deconfinement, but can be only due to their coupling to the spatial string tension.

5.2.1. Center Vortex Removal

In this work we identify thick center vortices in the Monte-Carlo ensemble by fixing the configurations to the direct maximal center gauge, as already explained, by maximizing the functional (5.7). The difference to earlier studies is that in addition to ordinary (full) maximal center gauge where $\mu = 0, 1, 2, 3$, we also do *spatial center gauge fixing* where $\mu = 1, 2, 3$ for locating vortices piercing space-like Wilson loops only.

The gauge fixing is done with an iterated overrelaxation algorithm as explained in more detail in Appendix C. The gauge fixing iteration is stopped when the change in functional (5.7) is less then a given precision ϵ within 100 steps. Center gauge fixing is performed in double precision with $\epsilon = 10^{-12}$ for configurations on which we calculate Coulomb gauge quantities. Computation of the spatial and temporal Wilson string tension via Creutz ratios need a much bigger Monte-Carlo ensemble to guarantee an acceptable signal-to-noise ratio. There, we use single precision configurations and stop center gauge fixing at $\epsilon = 10^{-7}$.

Center projection is done either on all links or only on spatial links

$$Z_\mu^{s/f}(x) = \text{sign tr}\left[U_\mu(x)\right] \mathbb{1} \in \{\pm\mathbb{1}\}\,. \tag{5.13}$$

The indices f and s label the configurations after full ($\mu = 0, 1, 2, 3$) or spatial ($\mu = 1, 2, 3$) center projection. Note that in the latter case, the temporal links $U_0(x)$ are not changed and therefore remain elements of the SU(N) gauge group. After full center projection all links are elements of the center, i.e. $\pm\mathbb{1}$ for SU(2).

Accordingly, full or spatial center vortex free configurations are obtained by the d'Elia-Forcrand technique [167]

$$V_\mu^{s/f}(x) = Z_\mu^{s/f}(x) \cdot U_\mu(x). \tag{5.14}$$

Thus we obtain the five ensembles: the original (unprojected) SU(2) ensemble U, the spatial (sCP) and full (CP) center projected ensembles Z^s, Z^f and the spatial (sVR) and

full (VR) vortex free configurations V^s, V^f. In a subsequent step these ensembles are then transformed to Coulomb gauge by the usual procedure, i.e. a combination of simulated annealing and overrelaxation, see Chapter 3 and Chapter 7. Note that after Coulomb gauge fixing the links $Z_\mu^{s/f}(x)$ are not anymore elements of the center.

5.3. Results

Our lattice setup for this chapter is summarized in Table 5.1. We chose a coarse and a fine isotropic lattice at $T = 0$ and two lattices at non-zero temperature for the coarser setup. Additionally we used three temperature values on anisotropic lattices from Chapter 4 to calculate the spatial string tension in Fig. 5.1.

Size	ξ	β	a_s^{-1} [GeV]	T/T_c
32^4	1	2.15	1.20	0
32^4	1	2.60	0.30	0
10×32^3	1	2.60	0.30	1.1
6×32^3	1	2.60	0.30	1.8
128×32^3	4	2.49	0.56	0
16×32^3	4	2.49	0.56	1.5
8×32^3	4	2.49	0.56	3.0

Table 5.1.: Simulation parameters used in this chapter.

5.3.1. The String Tension

In a first step we will compare the spatial Wilson string tension to the finite temperature behavior of Coulomb gauge propagators. We calculate the string tension from Creutz ratios as defined in Section 2.5.1. For large loops the Creutz ratios will approach the asymptotic string tension. The spatial string tension σ_s is calculated from pure spatial Wilson loops, i.e. loops of type $W(R_1, R_2)$ with R_1, R_2 along spatial dimensions. For the temporal string tension the time direction is included $W(R, T)$. To improve on the signal-to-noise ratio it is common to use smearing steps which soften short-range fluctuations. We applied 5 steps of APE smearing [175]

$$U_\mu(x) \to (1-\alpha)U_\mu(x) + \frac{\alpha}{6}\sum_{\mu>\nu} C_{\mu\nu} \tag{5.15}$$

with

$$C_{\mu\nu} = U_\nu(x)U_\mu(x+\hat{\nu})U_\nu^\dagger(x+\hat{\mu}) + U_\nu^\dagger(x-\hat{\nu})U_\mu(x-\hat{\nu})U_\nu(x-\hat{\nu}+\hat{\mu}) \tag{5.16}$$

on the links which are affected by vortex removal, i.e. on all links for full vortex removal or on spatial links for the case of spatial vortex removal, respectively.[2] In both cases we used a smearing parameter $\alpha = 0.5$. For center projection we did not use smearing which would be contradictory to the idea of squeezing the vortices into thin objects. Actually, full center projected configurations do not need a signal-to-noise improvement since they are already very stable at short distances as explained before, see Ref. [168].

In the motivation of our procedure we already compared the qualitative behavior of the spatial Wilson string tension to the Coulomb potential at finite temperature. In the plot on

[2] We used the notation of Ref. [31].

the l.h.s. of Fig. 5.1 we used exactly the same simulation setup as in Fig. 4.6. We fixed the inverse coupling β and the bare anisotropy ξ_0 to values that correspond to a renormalized anisotropy $\xi = 4$. Then, we varied the temporal lattice extent to simulate at three different temperatures $T = 0$, $1.5T_c$ and $3T_c$. As in Chapter 4 we give the temperature in units of T_c, see Table 5.1. For the highest temperature, $T = 3T_c$, the signal-to-noise ratio for this data set becomes very poor for large Wilson loops. Therefore, we do not show the data points for Creutz ratios with $r > 7$. The change in the extrapolated string tension is small when going from zero temperature to $1.5T_c$. At $3T_c$, for the values shown, the spatial Creutz ratios are significantly higher.

On the r.h.s. of Fig. 5.1 we compare the temperature dependence of spatial Creutz ratios on an isotropic lattice at $\beta = 2.6$. There, the signal-to-noise ratio is much better under control, however the relatively small lattice spacing $a = a_t = a_s$ limits our temperature range to below $2T_c$. The data at zero temperature and $T = 1.1T_c$ are indistinguishable within the error bars. At $1.8T_c$ the Creutz ratios saturate at a significantly higher value for the string tension.

This effect qualitatively agrees with the results for the Coulomb gauge propagators at finite temperature found in Section 4 and summarized in the beginning of this chapter. It is exactly this observation that led us to the assumption that the Coulomb string tension on the lattice originates from the spatial string tension. To check our assumption we will investigate the effect on the Coulomb string tension when the degrees of freedom which are related to confinement are removed from the lattice configuration, i.e. by removing the center vortices.

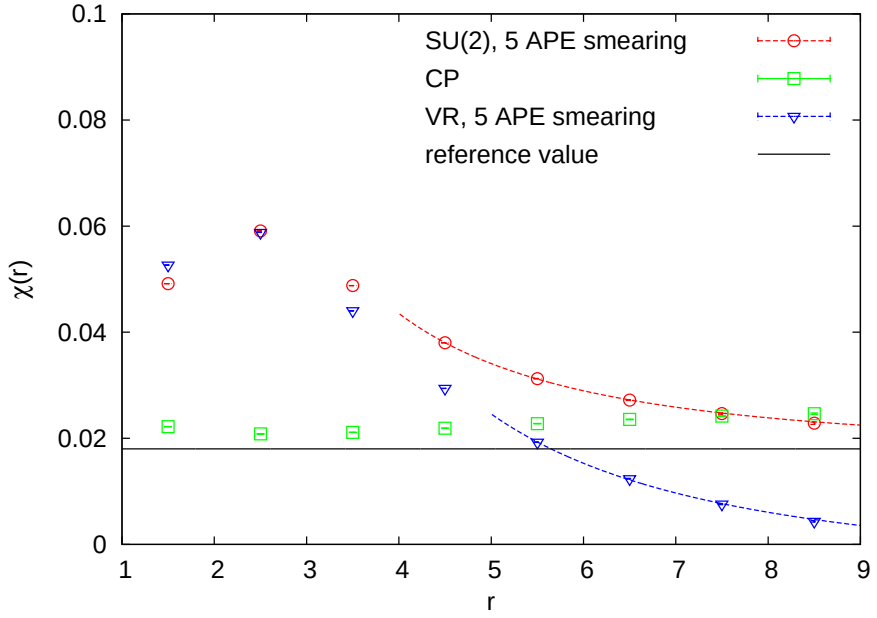

Figure 5.2.: Creutz ratios for the unmodified SU(2) configurations, full center vortex projection (CP) and removal (VR) at $\beta = 2.6$. The reference value $\chi = 0.01915$ was taken from [176].

In Fig. 5.2 we verify the well-established results that under center projection the Wilson string tension is approximately preserved while after removing (full) center vortices the string tension is zero, i.e. Wilson confinement is lost.

Our final goal is to remove confinement associated with the spatial Wilson string tension.

Therefore, in a next step we repeat the procedure with spatial center projection and spatial vortex removal as defined in Section 5.2.1. Due to the 4-dimensional Euclidean invariance in the case of full vortex removal (at $T = 0$) it was not necessary to distinguish the temporal and the spatial string tension. Our procedure breaks this invariance since spatial and temporal links are now treated differently. Thus, the string tension from space-space Creutz ratios $\chi(R_1, R_2)$ and space-time Creutz ratios $\chi(R, T)$ are expected to be different. On the l.h.s of Fig. 5.3 we show the result. As in the case of full vortex removal, the spatial string tension drops to zero. However, it turned out that the temporal string tension σ_T is impossible to measure directly via Creutz ratios. Space-time Wilson loops after vortex removal suffer from a huge signal-to-noise problem. The source of this issue is explained by the histogram on the r.h.s. of Fig. 5.3. The histogram shows the distribution of values for the plaquettes (Wilson loops with size of one lattice spacing in both dimensions) in the unmodified SU(2) case and for the space-space and space-time plaquettes after spatial vortex removal. Apparently, the center projected link in the spatial directions introduce (nearly) random flips in the space-time Wilson loops. Extracting a stable average with reasonable errors is therefore impossible.

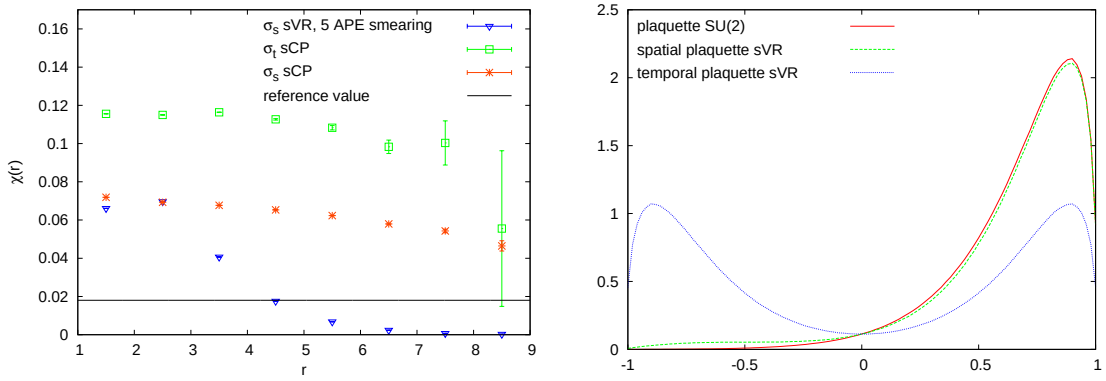

Figure 5.3.: (a) Creutz ratios for spatial center projection (sCP) and removal (sVR) at $\beta = 2.6$. The symbols refer to the temporal (σ_t) and spatial (σ_s) string tension; (b) Histogram of plaquettes before and after spatial vortex removal.

Nevertheless, we can still compute the temporal string tension σ_t from Polyakov loops as described in Section 2.5.2. Since Polyakov loops are built from temporal links U_t only, Polyakov loops do not change in the vortex removal procedure, which acts only on spatial links. Therefore, we conclude that the gauge configurations after spatial vortex removal still contain (temporal) confinement since they possess exactly the same physical string tension σ_t as the original SU(2) configurations.

Both, the temporal and spatial Creutz ratios, after spatial center projection, do not reach a plateau in the accessible region $r < 9$ where the errors are under control. We are lacking a conclusive explanation for why the convergence to the string tension, i.e. to a plateau in the Creutz ratio, is much slower, compared to the case of full center projection.[3]

In the following, we will investigate the effect of spatial center projection on Coulomb gauge propagators.

[3]Note that the Creutz ratios from space-time loops mixes center projected $\mathbb{Z}_2$ links ($U_s \equiv Z_s$) with the unprojected temporal SU(2) links U_t.

5.3.2. The Ghost Form Factor

The ghost form factor for the original SU(2) in Fig. 5.4 shows the well-known power law in the infrared with an exponent of about 0.5. After removing full *or* spatial vortices we

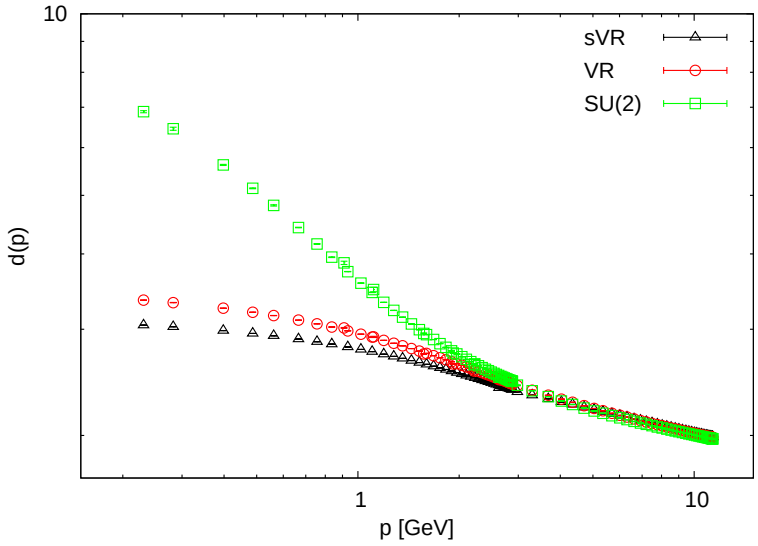

Figure 5.4.: The ghost form factor at $\beta = 2.15$ and $\beta = 2.60$, renormalized at a reference scale $\mu = 3\,\mathrm{GeV}$, before and after vortex removal.

cannot find a power law anymore. A similar results was also found for the Landau gauge ghost form factor in Ref. [177]. For our investigation the crucial point is the second result: in the gauge configurations where "spatial confinement" is removed, the Coulomb gauge confinement behavior, a infrared divergent ghost form factor, is lost.

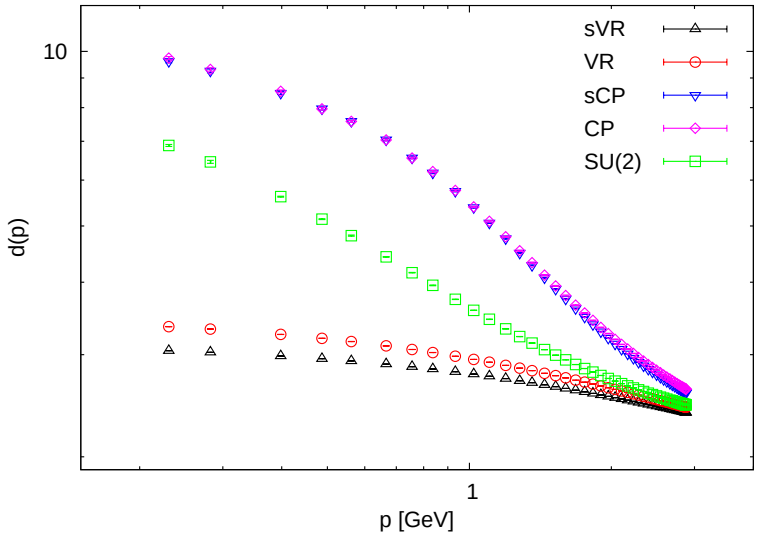

Figure 5.5.: The ghost form factor after center projection (restricted to the subspace orthogonal to the zero-modes) at $\beta = 2.15$.

After center projection the Faddeev–Popov operator acquires additional zero modes from vortices sitting on the Gribov horizon [115]. With these zero modes a direct inversion

of the Faddeev–Popov operator is impossible since these zero modes, unlike the $N_c^2 - 1$ constant zero modes with momentum $\boldsymbol{p} = 0$, cannot be excluded without the loss of information. However, we can still invert the Faddeev–Popov operator on a subspace orthogonal to the additional zero modes. The thus obtained propagator, Fig. 5.5, is enhanced for intermediate momenta compared to the original propagator. In the infrared the ghost form factor is suppressed, a result that is also found if one removes contributions from modes with small eigenvalues [178]. Thus, we conclude that this suppression is due to the excluded zero modes.

5.3.3. The Coulomb Potential

We already discussed in Section 2.6.4 that the extrapolation of the Coulomb string tension σ_C suffers from large uncertainties. As usual we plot the ratio $p^4 V_C(p)/(8\pi\sigma_W)$, since the

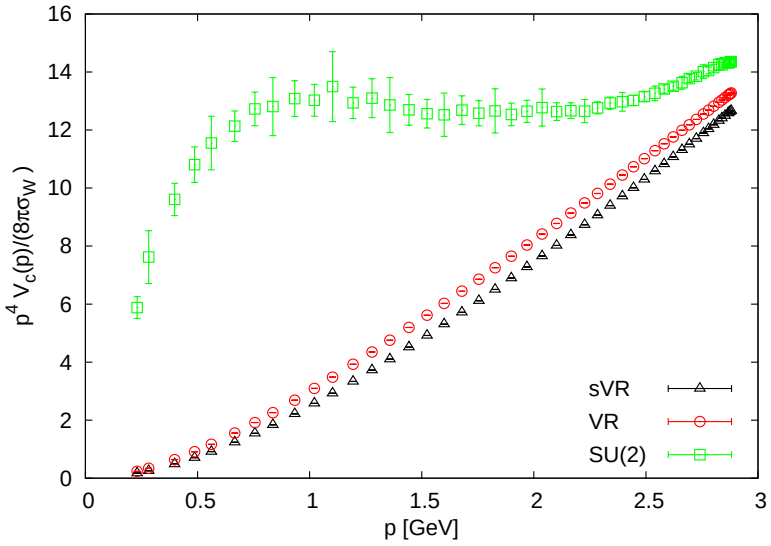

Figure 5.6.: The Coulomb potential in momentum space computed from (2.160). The data is normalized such that the intercept at $\boldsymbol{p} \to 0$ yields the ratio σ_C/σ_W.

infrared limit yields directly the Coulomb string tension σ_C in units of σ_W. In contrast to the original SU(2) ensemble, the data for the configurations free of center vortices (full and spatial) nicely extrapolate to a string tension of zero as shown in Fig. 5.6. As already emphasized many times, the configurations after spatial center vortex removal still have the unchanged temporal string tension σ_t from the original SU(2) configurations. This result clearly demonstrates that the Coulomb string tension is directly related to the spatial string tension and not to the temporal one.

We also show the result for the Coulomb potential from the alternative definition (2.173). This definition has the advantage that a fit of a linear rising potential to extract the string tension performs much better as we already saw in earlier chapters. In agreement with the results of [113] we find a Coulomb string tension close to zero after full vortex removal, illustrated on the l.h.s of Fig. 5.7. After center projection σ_C is slightly higher than in the original SU(2) configurations. This agrees well with Fig. 5.2 where the Wilson string tension is slightly larger for the same setup ($\beta = 2.6$ on a 32^4 isotropic lattice). On the r.h.s of Fig. 5.7, again in qualitative agreement with the results for the Wilson string tension, Fig. 5.3, we find for the spatial center projected $U_0 U_0^\dagger$-correlator a Coulomb string tension that is much higher compared to the SU(2) result.

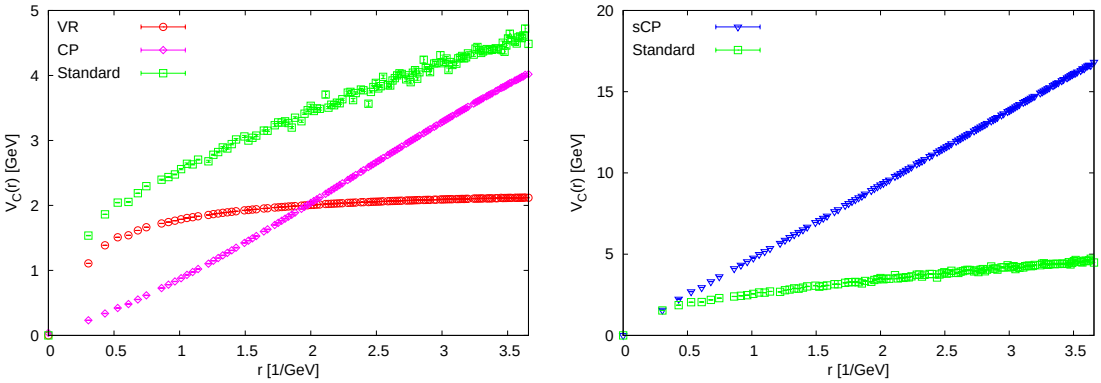

Figure 5.7.: The Coulomb potential in position space from (2.173): (a) for full center vortex projection and removal. A linear behavior sets in at moderate distances, so that we could afford a large coupling $\beta = 2.60$ to minimize discretization effects. (b) for spatial center projection. With spatial center projection, the string tension is overestimated by a large factor.

For the $U_0U_0^\dagger$-correlator from spatial vortex removed configurations we are faced with the same problem as in the case of the temporal string tension. By fixing to Coulomb gauge we introduce noise in the temporal links which makes a reliable measurement of the potential impossible.

5.4. Summary

In this chapter we found a relationship between the spatial string tension and Coulomb gauge propagators. We conclude that the lattice Coulomb gauge propagators which are built only from spatial links on a fixed timeslice cannot be used to describe confinement beyond $T = 0$. Since the Coulomb string tension is coupled to the spatial string tension the Coulomb gauge propagators fail to resolve the phase transition. Even the $U_0U_0^\dagger$-correlator, which is a quantity built from temporal links, does not show a clear signal of deconfinement as we saw in Chapter 4.3. We expect that only on longer Polyakov lines a correlator would be able to sense the phase transition. However, the physical interpretation of such a correlator is unclear.

6. Minimal Walking Technicolor

In this chapter we will discuss the SU(2) gauge theory coupled to two fermions in the adjoint representation. This theory is expected to be quite different from the QCD-like pure SU(2) gauge theory which was discussed in the preceding chapters: its features make it a possible candidate for walking technicolor. Technicolor theories are a proposal to explain the dynamical mass generation of the Standard Model without a Higgs field and its accompanying fundamental scalar boson. In the first section we will motivate and introduce the concept of technicolor and its constraints from electroweak measurements which will lead to so-called *walking technicolor* theories. In Section 6.2 we will summarize our setup of lattice configurations for this study and discuss some general problems. Finally we will present and discuss our results for the gluonic observables in Section 6.3. A conclusive result for the quark sector could not be obtained within this work because of several technical problems with the Wilson quark propagator which are discussed in Appendix D.

6.1. Introduction

In this introduction we will sketch only the common aspects of field theories which fall in the class of technicolor. We will describe the reason why the original idea of technicolor should be extended and we will finally arrive at the so-called walking technicolor theories without going into too many details of the phenomenological constraints. The introduction is oriented at Refs. [179–181]. The first one is a general text book introduction, where the later two are recommended as a detailed introduction with several specific realizations of (extended) technicolor theories and a discussion of phenomenological constraints.

6.1.1. Motivation

In the Standard Model the gauge bosons acquire their mass when the electroweak symmetry is broken down to the low energy electromagnetic $U(1)$ symmetry by the Higgs mechanism. The fermion masses are introduced by Yukawa couplings to the Higgs field. The Higgs mechanism, or to be more general, a mechanism for electroweak symmetry breaking (EWSB), is necessary since explicit mass terms on the Lagrangian level for gauge fields are gauge-dependent and lead to non-renormalizable theories, see e.g. [179].

In the following, we will shortly summarize the Higgs mechanism at the simple example of a complex scalar U(1) gauge theory, the *Abelian Higgs model*. The Lagrangian density for this theory is given by

$$\mathcal{L} = (D_\mu \phi)^\dagger (D_\mu \phi) - V(\phi^\dagger \phi) - \frac{1}{4} F_{\mu\nu} F^{\mu\nu} \tag{6.1}$$

with the potential

$$V(\phi^\dagger \phi) = -\mu^2 \phi^\dagger \phi + \lambda (\phi^\dagger \phi)^2 \tag{6.2}$$

and the Abelian covariant derivative D_μ and the Abelian field strength tensor $F_{\mu\nu}$

$$D_\mu = \partial_\mu - \mathrm{i} g A_\mu, \quad F_{\mu\nu} = \partial_\mu A_\nu - \partial_\nu A_\mu. \tag{6.3}$$

The Lagrangian of (6.1) is invariant under local U(1) gauge transformations of the form

$$\phi(x) \to \phi'(x) = \mathrm{e}^{-\mathrm{i}\alpha(x)}\phi(x) \tag{6.4}$$
$$A_\mu(x) \to A'_\mu(x) = A_\mu(x) - \frac{1}{g}\partial_\mu\alpha(x).$$

If $\mu^2 > 0$ the potential has the famous shape of a Mexican hat and develops a minimum at a non-zero value of the scalar field

$$|\phi| = v/\sqrt{2}, \quad v = \sqrt{\mu^2/\lambda}. \tag{6.5}$$

Thus, the vacuum expectation value of the field is given by[1]

$$\langle\phi\rangle = v/\sqrt{2}. \tag{6.6}$$

A convenient parameterization of the scalar field are (shifted) radial coordinates

$$\phi(x) = \frac{1}{\sqrt{2}}\left[v + \eta(x)\right]\mathrm{e}^{\mathrm{i}\xi(x)/v}. \tag{6.7}$$

which allow to get rid of one field component: with the gauge transformation $\alpha(x) = \xi(x)/v$ the ξ field vanishes. With this choice the transformation (6.4) for the scalar and vector field reads

$$\phi'(x) = \frac{1}{\sqrt{2}}(v + \eta(x)) \tag{6.8}$$
$$B_\mu(x) = A_\mu(x) - \frac{1}{gv}\partial_\mu\xi(x) \tag{6.9}$$

and one finds the Lagrangian density

$$\mathcal{L} = \frac{1}{2}\partial_\mu\eta\partial^\mu\eta - \mu^2\eta^2 - \frac{1}{4}F^B_{\mu\nu}F^{B,\mu\nu} + \frac{1}{2}(gv)^2 B_\mu B^\mu + \mathcal{L}_I, \tag{6.10}$$

where the letter B in $F^B_{\mu\nu}$ indicates the field strength tensor for the transformed field and $\mathcal{L}_I$ contains coupling terms between the scalar field and the gauge field. The first two terms describe a massive (real) scalar field with $m_\eta = \sqrt{2}\mu$ and the third and fourth term describe a massive vector field with mass $m_B = gv$. Instead of a complex scalar field ϕ with two degrees of freedom, we now have a real scalar field η which is the Higgs boson of this model. One says that the missing degree of freedom was "eaten" to become the additional longitudinal degree of freedom for the now massive vector field. The parameter μ^2 triggers the symmetry breaking from the massless phase ($\mu^2 \leq 0$) to the Higgs phase ($\mu^2 > 0$). In the Standard Model the scalar field ϕ is replaced by a doublet of complex fields, where three components give mass to the $W^\pm$ and Z bosons and the remaining component is the massive Higgs boson, while the photon remains massless. The masses for the Standard Model fermions can be introduced in a gauge-invariant way by Yukawa couplings to the Higgs field. The coupling coefficients for the different fermions are free parameters to be adjusted to the masses found in experiments.

[1] We follow the pedagogical introduction which is found in many textbooks, e.g. [179], though we want to emphasize that this semi-classical formulation has a severe drawback: Elitzur's theorem states that a local gauge symmetry cannot be broken spontaneously and especially the vacuum expectation value of any gauge variant quantity is zero, i.e. $\langle\phi\rangle = 0$. The unambiguous treatment was developed by t'Hooft who showed the renormalizability of the theory with a Higgs fields [182, 183].

While the Higgs mechanism offers a simple way to describe the dynamical mass generation of gauge bosons and fermions, there are still reasons why physicists are searching for alternatives, even though the long missing Higgs boson was finally detected in 2012 [3, 4]. The existence of dark matter, the non-zero neutrino masses or the origin of the baryon asymmetry are experimental facts that are not explained within the Standard Model. Theories "Beyond the Standard Model" (BSM) are needed to describe these features of nature. But even if we leave aside these experimental findings, the Standard Model with the Higgs mechanism has severe theoretical shortcomings [184]: it does not offer a dynamical explanation for electroweak symmetry breaking; it is "unnatural" and therefore requires fine-tuning; it suffers from the hierarchy problem.

The first point boils down to the problem that the mass parameter $-\mu^2$ is introduced in (6.1) "by hand" and set to its specific value just to trigger electroweak symmetry breaking. There is no explanation why the parameter is negative and why $v = 246\,\text{GeV}$ in the Standard Model [184, 185].

A theory is said to be unnatural if it contains sensitive correlations between well separated energy scales [186]. This happens for a theory with an elementary scalar particle, like the Higgs boson: the Higgs boson mass gets additive radiative corrections which are quadratic in the cut-off Λ. For the Higgs mass to be natural we would therefore expect it to be of the order of the cut-off, e.g. the Planck scale $\Lambda = M_P \approx 10^{18}$ GeV. Thus, in order to obtain the small value of the Higgs mass $m_H \approx 125\,\text{GeV}$ the radiative corrections have to be canceled by a delicate *fine-tuning* of the Standard Model parameters to a precision of $M_P^2/m_H^2 \sim 10^{32}$ [184].

The tiny ratio of the weak scale to the Planck scale of $M_W/M_P \approx 10^{-16}$ to which the Standard Model does not offer an explanation is also known as the *gauge hierarchy problem*. In contrast, the smallness of the QCD scale relative to the Planck scale $\Lambda_{\text{QCD}}/M_P \approx 10^{-20}$ is well understood as a consequence of asymptotic freedom [180].

Various solutions to resolve these theoretical shortcomings are discussed among theorists and are sought for in experiments, see e.g. Ref. [180, 187].

The most famous models are supersymmetric theories (SUSY) where the naturalness problem is resolved by introducing a symmetry that protects that Higgs mass from radiative corrections. Each Standard Model particle get a superpartner with the same quantum numbers except spin: each fermion gets a bosonic partner and each boson gets a fermionic partner. In the phase where SUSY is intact the mass of the scalar Higgs is equal to the mass of its fermionic superpartner which in turn is protected by chiral symmetry [180]. Since these superpartners are not found with the same mass as the Standard Model particles, the SUSY symmetry itself must be broken below the electroweak scale.

Other solutions are theories with *extra space-time dimensions*, the so-called *little Higgs models*, where a Higgs boson appears as a pseudo Nambu-Goldstone boson with a light mass, or theories with a *composite* scalar operator, see e.g. Ref. [187] and references therein. The chiral condensate of QCD is such an operator and is the basis of technicolor as will be explained in the following.

6.1.2. Technicolor and Extended Technicolor

The original idea of technicolor [188, 189] borrows the concept of chiral symmetry breaking from QCD to explain the masses of the Standard Model gauge bosons.

For simplicity we will discuss QCD with only two quarks u, d following Ref. [179, Chapter 13]. If we assume that these quarks are exactly massless, the Lagrangian possesses an

$\mathrm{SU}(2)_L \times \mathrm{SU}(2)_R$ symmetry. It can be written as

$$\mathcal{L} = \bar{q}\gamma_\mu D^\mu q = \bar{q}_L \gamma_\mu D^\mu q_L + \bar{q}_R \gamma_\mu D^\mu q_R \tag{6.11}$$

where the left- and right-handed components

$$q_L = P_L q = P_L \begin{pmatrix} u \\ d \end{pmatrix}, \quad q_R = P_R q \tag{6.12}$$

are obtained by the projectors $P_L = \frac{1}{2}(\mathbb{1} - \gamma_5)$ and $P_R = \frac{1}{2}(\mathbb{1} + \gamma_5)$. At the QCD scale this symmetry is spontaneously broken by the chiral condensate

$$\langle \bar{q}_L q_R + \bar{q}_R q_L \rangle \neq 0 \tag{6.13}$$

which is only symmetric with respect to simultaneous transformations of left- and right-handed fields, i.e. the symmetry is broken down to $\mathrm{SU}(2)_{L+R}$. According to Goldstone's theorem one obtains three massless Goldstone bosons, the pions $\pi^\pm, \pi^0$ of QCD.[2]

If we now include the electroweak interactions, the $\mathrm{SU}(2)_L \times U(1)_Y$ will be broken by the chiral condensate to $U(1)_{\mathrm{em}}$ and the pions are eaten by $W^\pm$ and Z bosons, like in the Higgs mechanism. However the contribution to their masses by this mechanism is orders of magnitude too small compared to the experimental values. The contribution from chiral symmetry breaking to the W boson mass is given by

$$M_W = \frac{g f_\pi}{2} \approx 30\,\mathrm{MeV}, \tag{6.14}$$

where f_π is the pion decay constant, while the experimental value is $M_W^{\mathrm{exp}} = 80\,\mathrm{GeV}$ [179, Chapter 13]. Otherwise, the relation between the $W^\pm$ and Z boson masses, with the Weinberg angle θ_W, is obtained correctly

$$M_W / M_Z = \cos\theta_W. \tag{6.15}$$

Thus, a mechanism for EWSB is already included in QCD and generates a dynamical boson mass, only the mass scale is completely wrong.

A possible solution is to postulate a new strong interaction, *technicolor*, with new *techniquarks* and *technigluons* which break the electroweak symmetry at the right scale. The gauge group of the Standard Model $G_{\mathrm{SM}} = \mathrm{SU}(3)_c \times \mathrm{SU}(2)_L \times U(1)_Y$ would then be extended by a yet undefined technicolor gauge group G_{TC}

$$G = G_{\mathrm{SM}} \times G_{\mathrm{TC}}. \tag{6.16}$$

From the W boson mass, the technicolor scale is estimated to be around $\Lambda_{\mathrm{TC}} = 1\,\mathrm{TeV}$ where the new particles should be observable. Since technicolor is an asymptotically free theory, the hierarchy of scales would be naturally explained by the running of the technicolor coupling. Thus technicolor could be able to produce the correct gauge boson masses without the need for a fundamental scalar field. However technicolor, and the Standard Model as well, does not explain the fermion masses. In the Standard Model they are just introduced as free parameters. A complete, fundamental theory should not only explain the gauge boson masses but also provide a mechanism for the fermion masses.

[2] Since up and down quarks have a small mass, chiral symmetry is not exact and the pions acquire their (small) mass.

So-called *Extended Technicolor* models (ETC) [190, 191] try to implement the fermion masses. There one postulates additional gauge bosons at a scale Λ_{ETC} above the technicolor scale which couple to technicolor and Standard Model fermions [187]. The masses of the Standard Model fermions are then generated by effective Yukawa couplings originating from four-fermion operators. Again, as already technicolor, ETC is not a specific theory, but a whole class of theories with the aforementioned property. A subclass of ETC are the *one family models* [192] which additionally offer a dynamical explanation for the different mass scales of the Standard Model generations: a ETC gauge group, e.g. $\mathrm{SU}(N_{\mathrm{ETC}}) = \mathrm{SU}(N_{\mathrm{TC}} + 3)$, spontaneously breaks in three steps to $\mathrm{SU}(N_{\mathrm{TC}})$, where at each symmetry breaking scale Λ_g one generation of Standard Model fermions acquire their masses[3] [181]

$$m_g \sim 4\pi \frac{F_\pi^3}{\Lambda_g^2}, \tag{6.17}$$

where F_π is the technipion decay constant.

In Ref. [180] the most relevant low-energy (below the ETC scale) terms originating from four-fermion operators for a generic ETC theory are described by[4]

$$\alpha_{ab} \frac{\bar{Q} T^a Q \bar{q} T^b q}{\Lambda_{\mathrm{ETC}}^2} + \beta_{ab} \frac{\bar{Q} T^a Q \bar{Q} T^b Q}{\Lambda_{\mathrm{ETC}}^2} + \gamma_{ab} \frac{\bar{q} T^a q \bar{q} T^b q}{\Lambda_{\mathrm{ETC}}^2} + \ldots, \tag{6.18}$$

where the capital Q's denote techniquarks and the lower case q's denote ordinary Standard Model fermions, the T^a are the generators of the unspecified ETC gauge group and α, β, γ are parameters depending on the specific ETC theory, too. The terms proportional to α are the ones generating the Standard Model fermion masses

$$m_q \sim \left(\frac{g_{\mathrm{ETC}}}{M_{\mathrm{ETC}}} \right)^2 \left\langle \bar{Q} Q \right\rangle_{\mathrm{ETC}}, \tag{6.19}$$

where g_{ETC} is the ETC coupling constant and $\langle \bar{Q} Q \rangle_{\mathrm{ETC}}$ the technicolor condensate, both evaluated at the ETC scale; M_{ETC} is the ETC gauge boson mass. The second contribution in (6.18) is not relevant for this introduction. It will generate masses for pseudo Goldstone bosons and techniaxions. A problematic aspect of ETC comes from the γ term: it will induce flavor-changing neutral currents (FCNCs) between quarks and leptons which are highly suppressed in the Standard Model. From the experimental constraints the authors of Ref. [180] estimated that if the specific ETC theory is QCD-like, i.e. has a QCD-like running coupling, the scale would have to be $\Lambda_{\mathrm{ETC}} \gtrsim 10^3$ TeV to suppress the FCNCs down to experimental data. However, with such a high scale one could only explain Standard Model quark masses of less than 100 MeV, the top quark mass $m_t \approx 170$ GeV [193] is far above this limit.

The problem to explain the masses of the heavy quarks while at the same time suppressing the FCNCs is addressed by the so-called *Walking Technicolor* theories. Since the Standard Model quark masses (6.19) are proportional to the techniquark condensate at the ETC scale it is instructive to investigate its renormalization effect when going from the technicolor scale to the ETC scale [180]

$$\left\langle \bar{Q} Q \right\rangle_{\mathrm{ETC}} = \exp\left(\int_{\Lambda_{\mathrm{TC}}}^{\Lambda_{\mathrm{ETC}}} \mathrm{dlog}(\mu)\, \gamma_m(\alpha(\mu)) \right) \left\langle \bar{Q} Q \right\rangle_{\mathrm{TC}}, \tag{6.20}$$

[3] The origin of the different masses within a generation is not explained.

[4] We use the convention of Ref. [181].

with the anomalous dimension of the mass γ_m. If one assume a QCD-like running coupling with a logarithmic fall-off above Λ_{TC}

$$\alpha(\mu) \propto \frac{1}{\log(\mu)} \tag{6.21}$$

and $\gamma_m \propto \alpha(\mu)$ one finds

$$\left\langle \bar{Q}Q \right\rangle_{\mathrm{ETC}} = \log\left(\frac{\Lambda_{\mathrm{ETC}}}{\Lambda_{\mathrm{TC}}}\right)^{\gamma_m} \left\langle \bar{Q}Q \right\rangle_{\mathrm{TC}}. \tag{6.22}$$

Thus the renormalization effect is logarithmically small and therefore $\left\langle \bar{Q}Q \right\rangle_{\mathrm{ETC}} \approx \left\langle \bar{Q}Q \right\rangle_{\mathrm{TC}}$ which would yield with $\langle \bar{Q}Q \rangle_{\mathrm{TC}} \sim \Lambda_{\mathrm{TC}}^3$ [181]

$$m_q \approx \left(\frac{g_{\mathrm{ETC}}}{M_{\mathrm{ETC}}}\right)^2 \Lambda_{\mathrm{TC}}^3. \tag{6.23}$$

If we assume, instead of the QCD-like running, a theory where the running coupling is approximately constant between the scales Λ_{TC} and Λ_{ETC}, i.e. a theory with a nearly conformal fixed point $\alpha(\mu) \approx \alpha^*$ one obtains a power law correction

$$\left\langle \bar{Q}Q \right\rangle_{\mathrm{ETC}} = \left(\frac{\Lambda_{\mathrm{ETC}}}{\Lambda_{\mathrm{TC}}}\right)^{\gamma_m} \left\langle \bar{Q}Q \right\rangle_{\mathrm{TC}}. \tag{6.24}$$

Thus the techniquark condensate at Λ_{ETC} is significantly enhanced if the mass anomalous dimension is of order 1. This in turn implies that the quark mass (6.19) is enhanced. At the same time, the FCNCs are not enhanced since the γ-term, from which they originate, do not couple to the condensate. Such a mechanism with a "walking" (slowly running) coupling might allow the heavy quark masses in the technicolor framework. For model building it is therefore of prime interest to discriminate between conformal, near-conformal (walking) or QCD-like theories. Additionally, a large mass anomalous dimension would be necessary for a Walking Technicolor theory to be a viable candidate to replace the Higgs sector of the Standard Model. Of course, a theory possessing these features has still to pass the tests of the electroweak precision measurements, however this aspect will not be the subject of our work. In recent years a lot of effort has been put into the analysis of gauge theories with different gauge groups and fermions in different representations to locate the conformal window, i.e. the region where the theory, for a given number of colors and fermions, develops a non-trivial fixed point of the running coupling. Around that point one is investigating if the theory is really conformal or only quasi-conformal (walking).

For a first estimate, the two-loop beta function for SU(N)

$$\beta(g) = -\frac{\beta_0}{(4\pi)^2} g^3 - \frac{\beta_1}{(4\pi)^4} g^5 \tag{6.25}$$

can be used to find bounds on the so-called *conformal window* introduced below [194]. The coefficients β_0 and β_1 are given by

$$\beta_0 = \frac{11}{3} C_2(G) - \frac{4}{3} T(r) N_f \tag{6.26}$$

$$\beta_1 = \frac{34}{3} C_2^2(G) - \frac{20}{3} C_2(G) T(r) N_f - 4 C_2(r) T(r) N_f \tag{6.27}$$

for a representation r with the quadratic Casimir defined by $C_2(r)\mathbb{1} = T_r^a T_r^a$ and the normalization of the generators $\mathrm{tr}[T_r^a T_r^b] = T(r)\delta_{ab}$, adopting the notation of Ref. [194]. G denotes the adjoint representation with the coefficients $T(G) = N$, $C_2(g) = N$ and dimension $N^2 - 1$.[5]

As an upper bound for the number of fermions N_f for a given representation r one obtains [194]

$$N_f^{\mathrm{I}} = \frac{11}{4}\frac{C_2(G)}{T(r)}. \tag{6.28}$$

At this point the first coefficient β_0 becomes negative (then also $\beta_1 < 0$) which implies that asymptotic freedom is lost. For SU(3) and fermions in the fundamental representation the upper bound is $N_f^{\mathrm{fund}} \leq 16$. For any SU($N$) theory with adjoint fermions the bound is $N_f^{\mathrm{adj}} \leq 2$. A lower limit can be derived by the point where β_1 becomes negative, while β_0 is still positive [195]

$$N_f^{\mathrm{III}} = \frac{C_2(G)}{T(r)}\frac{17C_2(G)}{10C_2(G) + 6C_2(r)}. \tag{6.29}$$

There the running coupling of the theory develops a fixed point. At the fixed point the theory is conformal. The region between the point were a fixed point appears and the point were asymptotic freedom is lost defines the conformal window. For the bound of (6.29) one finds for SU(3) $N_f^{\mathrm{fund}} \geq 8$ and for any SU(N) $N_f^{\mathrm{adj}} \geq 2$. As these bounds are derived from a perturbative expansion, they are only estimates and the true conformal window has to be sought for by means of non-perturbative methods, e.g. Dyson–Schwinger calculations, see the summary in Ref. [181] and references therein, or the lattice approach.

From (6.28) and (6.29) we conclude that the only fermion number for the adjoint representation is $N_f = 2$. In the following we will investigate the Coulomb gauge correlators of the theory with gauge group SU(2). The theory is called *Minimal Walking Technicolor* (MWT) since it is the theory with minimal matter content and number of colors for which a walking behavior is anticipated.[6] This makes the theory a perfect candidate for first lattice studies as with more fermion flavors and colors the numerical work would also increase.

6.1.3. SU(2) with Two Adjoint Fermions

A first lattice investigation of the theory was done in Refs. [196, 197]. There also a summary of appealing phenomenological results for MWT is provided: it passes electroweak precision tests, offers possible dark matter candidates and allows unification of the Standard Model couplings. Since these results were published before the Higgs boson was found experimentally, a possible composite Higgs with a specific mass was not discussed. In this first works the phase diagram of the theory is analyzed with respect to the bare coupling and the fermion masses. By inspecting meson masses the authors find a behavior which is consistent with a conformal theory or possibly a walking behavior when the bare masses are tuned towards zero: the meson masses tend to zero as expected in a theory with no intrinsic scale. However, the authors also note that finite volume effects might not be fully understood.

[5] Note that the one-loop approximation in (2.111) is recovered with $T = 1/2$ for the fundamental representation.

[6] Note that for SU(2) the two-index symmetric representation and the adjoint representation coincide. Therefore the MWT theory can also be regarded as one representative of the theories with fermions in the two-index symmetric representation which have less strict bounds on the conformal window for SU(N) with $N > 2$.

Later the MWT theory was studied independently by other groups [59–62] and [198–200]. The former used the Wilson Dirac discretization in all their studies, while the latter began using improved fermion actions for their studies. In their most recent analysis they agree that the theory develops an IR fixed point, i.e. it describes a conformal (not a walking) theory, and they estimate a mass anomalous dimension at the fixed point between $\gamma^* \approx 0.2$ [199, 200] and $\gamma^* \approx 0.37$ [61]. These results would rule out that MWT is a viable candidate for BSM physics in the context discussed above. However it might still be interesting for other scenarios where an exact conformal theory is needed, as e.g. in *unparticle* models [201, 202].

A viable candidate theory for BSM physics of course needs to explain the Higgs excitation. A possible candidate for a Higgs-like particle, a so-called Higgs impostor, is the scalar 0^{++} glueball [203] which turned out to be the lightest excitation of the MWT theory.

6.2. Configurations

In this work we use configurations which were kindly provided by the authors of [59–62]. The configurations were created using the (isotropic) Wilson gauge action (2.84) and the Wilson fermion action

$$S_f = a^4 \sum_{x,y} \bar{q}(x) D(x,y) q(y) \tag{6.30}$$

where the Wilson Dirac operator is given by

$$\begin{aligned} D(x,y) = &\left(m + \frac{4}{a}\right) \delta_{xy} \\ &- \frac{1}{2a} \sum_{\mu=0}^{3} \left\{ (1-\gamma_\mu)\, U_\mu^r(x) \delta_{x+\mu,y} + (1+\gamma_\mu)\, U_\mu^{\dagger r}(x-\hat{\mu}) \delta_{x-\mu,y} \right\} \end{aligned} \tag{6.31}$$

with the links U^r in the representation r. In the adjoint representation the SU(2) links are given by

$$U_{ab}^A = \frac{1}{2} \operatorname{tr}\left[t^a U t^b U^\dagger \right] \tag{6.32}$$

where t^a are the generators of the fundamental representation of SU(2) and U are the usual links in the fundamental representation, see Section 2.4.

For details of the implementation to generate the configurations we refer to the original literature [204]. For convenience we use the same labels as in the original works as given in Table 6.1. The parameters and masses are taken from the papers mentioned in the table. The lattices Qx are quenched configurations generated by us. Compared to the Yang–Mills studies of the earlier chapters the lattices sizes of the MWT configurations are rather small with the exception of the F1 lattice. The authors of Ref. [62] found that on larger lattice sizes the autocorrelation times increase dramatically and the computer time has to be increased accordingly to achieve reliable studies. In Ref. [62] the authors successfully softened the problem by implementing open boundary conditions instead of the commonly used (anti-) periodic boundaries which allowed them to simulate on lattices of sizes up to 80×48^3. These lattices are not included in our study as it would involve an extensive and careful examination of the corresponding Yang–Mills propagators to be able to distinguish effects of the MWT theory from effects of the open boundary conditions.

On the lattice it is not possible to simulate exactly massless quarks. Therefore all simulation have to be done with a finite quark mass. The massless limit is then approached by decreasing the bare quark mass towards the critical point where the renormalized quark

masses vanish. In principle every choice of bare mass corresponds to a different theory. If we assume that the transition from the massive to the massless theory is smooth we can extrapolate to the massless limit, see also the discussion in Ref. [205]. All configurations in this study are for a fixed coupling $\beta = 2.25$, where the critical bare mass is found to be around $m_c \approx -1.20$ [59].

	V	N_{conf}	$-am_0$	am_{PCAC}	$aM_{0^{++}}$	a^{-1} [GeV]
B0	24×12^3	317	0.95	0.3931(38)	0.793(41)[a]	172
B1	24×12^3	266	1.00	0.3368(40)	0.658(56)[a]	193
B2	24×12^3	222	1.05	0.2765(40)	0.510(33)[a]	228
B3	24×12^3	201	1.075	0.2410(38)	0.4901[b]	255
B4	24×12^3	174	1.10	0.2025(40)	0.4260[b]	293
B5	24×12^3	168	1.125	0.1604(34)	0.3527[b]	354
B6	24×12^3	92	1.15	0.1198(52)	0.256(18)[c]	468
B10	24×12^3	145	1.19	0.0302(16)	0.0794[b]	1573
C0	32×16^3	140	1.15	0.1175(30)	0.256(18)[c]	468
C4	32×16^3	95	1.19	0.0308(10)	0.0794[b]	1573
F1	64×32^3	206	1.15	0.1175(30)[d]	0.256(18)[c]	468
Q0	24×12^3	300	-	-	-	-
Q1	32×16^3	300	-	-	-	-
Q2	64×32^3	100	-	-	-	-

Table 6.1.: Summary of configurations; PCAC masses are taken from Ref. [59]. The lattice spacing is obtained from the interpolation of the 0^{++} glueball mass.

6.2.1. Setting the Scale

In Section 2.4.2 we discussed how to find the physical scale of the lattice theory for QCD: a physical observable, like the string tension or a hadron mass, is measured in the lattice setup and identified with its physical value. The SU(2) Yang–Mills theory in the absence of quarks which was subject of the previous chapters is, of course, not realized in nature and therefore the scale setting is rather arbitrary. However, the SU(2) theory resembles full QCD in many aspects and therefore one may use an observable which can be measured in full QCD to define the scale of the (unphysical) SU(2) Yang–Mills theory.

For the SU(2) theory with two adjoint fermions there is no (known) corresponding realization in nature as long as the proposed technicolor candidate is not verified experimentally. In the Landau gauge studies [205, 206] the authors proposed a way to set the scale which we will adopt in our work. They chose the scalar 0^{++} glueball to set the physical scale. The 0^{++} glueball has the same properties as the Standard Model Higgs particle and is the lightest bound state in the theory under study. In the would-be technicolor theory the Higgs particle might be this glueball [203] or at least mix with this state as was argued in Ref. [206]. Therefore they identify the mass of the 0^{++} glueball

[a] The value is taken from Ref. [60].

[b] Interpolated and extrapolated ($-am = 1.19$) values were obtained from a four parameter fit to the available masses of Refs. [60, 62].

[c] The value is taken from Ref. [62]. We will use that value even the data has large systematic uncertainties because of long autocorrelation times.

[d] We use the value of the C0 lattice.

with 125GeV, the physical mass of the Higgs boson[7]. For some of the configurations the glueball masses were reported in Refs. [60, 62]. We used a four parameter fit to that data to interpolate the masses for the other lattices and to extrapolate to $-am_0 = 1.19$. In the fit we excluded the set at $-am_0 = 0.9$ as this is a distinct outlier. The lattice spacing as reported in Table 6.1 is then obtained from the interpolation formula.

Not that this scale can only be meaningful if the theory is not conformal, but only quasi-conformal. For this reason we will also show the results in lattice units.

6.3. Results

In the following we will discuss the Coulomb gauge correlation functions we already investigated for the pure SU(2) gauge theory in the preceding chapters: the gluon propagator and the ghost propagator in momentum space and the Coulomb potential in position space, from (2.173), and in momentum space, from (2.160). First we will have a look at finite volume effects and discuss possible effects of the Gribov ambiguity. Then we investigate how the quantities behave when the mass is changed towards the critical value at fixed lattices size. We will find that the data points for different masses are quite well described by a single curve when we use the physical scale given by the mass of the 0^{++} glueball. Therefore we will finally compare configurations at different mass and volume and will again find a surprisingly good overlap.

6.3.1. Finite Volume Effect and Gribov Ambiguity

To study the finite volume effects we use the sets B6, C0 and F1 where configurations are available with the same bare mass $am_0 = -1.15$ of the adjoint quarks. The spatial volume of these configurations is 12^3, 16^3 and 32^3 respectively. In the plots Fig. 6.1 we present the results in lattice units. In addition to the data from the simulation with adjoint quarks (l.h.s.) we show for comparison the data of the quenched configurations (r.h.s.) at the same lattice sizes. These are provided to give an estimate of the size of the finite volume effects in the pure gauge theory, however the comparison has to be taken with care since we compare two very different theories. We find a very consistent behavior from the plots of the different quantities on the lattices with adjoint fermions: the curves from the two smaller lattices are identical within error bars while the largest lattice shows a clear deviation in the infrared. A possible explanation could be that the difference in size of the B6 and C0 lattice is too small to see significant effects, while the F1 lattice is twice the size of the C0 lattice in each direction. For the quenched configurations the finite volume effect is considerably smaller or even negligible in the case of the Coulomb potential. When we compare the quenched to the unquenched correlation function we find a very different form in the IR. However the form of the curves suggest that the propagators from the adjoint theory might be closer to the quenched case at much weaker coupling. This assumption is further backed up by the value of the gauge fixing functional (3.1) which is higher for the configurations with adjoint quarks. Furthermore, the adjoint configurations do not show a Gribov copy effect even on the largest lattice which points to very smooth configurations as we have seen at higher values of β in Chapter 3.

In the plot of the gluon propagator (topmost plots of Fig. 6.1) we included two extra curves to accommodate for a possible ambiguity in our two-step procedure to calculate the static gluon propagator. The lighter red and green curves are calculated with the

[7] At the time of the earlier study [205] the Higgs boson was not yet detected, there the author arbitrarily set the scalar glueball mass to 2TeV.

standard procedure where we calculate the function $g(p_0/|\boldsymbol{p}|)$ in (2.143) and $D(|\boldsymbol{p}|)$ in (2.146) from the same data set. The darker symbols denote the case where we used the fit to $g(p_0/|\boldsymbol{p}|)$ from the largest lattice F1 to compute the propagator (2.146). We see that in this second case the data points from all three lattices sizes fall on the same curve, telling us that the finite volume effect is completely encoded in the function $g(p_0/|\boldsymbol{p}|)$, i.e. in the energy-dependent part. It seems that the pure spatial part of the correlator is less sensitive to a "contamination" from exited states which are always present on a finite lattice. This effect is also seen in the Yang–Mills correlator.

For completeness we should mention that the authors of Ref. [60] found that for the small lattice the spatial center phase is broken close to the critical mass. We cannot completely exclude that this feature is the origin of the gap between the smaller lattices and the big one, however from the results in the next section there is no hint that this effect might be play a role for the Coulomb gauge quantities.

6.3.2. Mass Dependency

In Fig. 6.2 we show the correlation functions as they change with varying the bare mass. The configurations are of the smallest lattice size in our set, where we have 8 different masses available from $-am_0 = 0.95$ to $-am_0 = 1.19$. The results on the l.h.s. are in lattice units while on the r.h.s. we used the scale as explained in Section 6.2.1.

We will first discuss the results in lattice units. The gluon propagator only shows a small variation with different masses. It is very close to the tree-level propagator at all masses as a fit to a pure power-law

$$D(|\boldsymbol{p}|) = \frac{\text{const.}}{|\boldsymbol{p}|^{\kappa}} \tag{6.33}$$

shows. The exponent ranges between $\kappa = 1.06(1)$ (largest mass) and $\kappa = 0.98(2)$ (smallest mass) with $\chi^2/\text{n.d.f.} \approx 5$. We consider this a very good fit regarding the fact that we use a simple power-law without logarithmic corrections and the potential finite volume artifacts.

The ghost form factor $d(p)$ shows a clear separation of the lines for different masses. As in the pure Yang–Mills case we find two different functional forms in the IR and the UV. In the IR fit we included only the first four data points in a power-law fit. We find an exponent smaller than 0.5 which is decreasing down to 0.33(2) at the smallest mass. In the UV the data is well described by the logarithmic fall-off, as described in (2.175),

$$d(|\boldsymbol{p}|) = \frac{1}{\log^{\gamma_{\text{gh}}}\left(\frac{|\boldsymbol{p}|}{m}\right)}, \tag{6.34}$$

however the data is not sensitive enough to the logarithm to fit γ and m precisely: in an unconstrained fit the reduced χ^2 is far below 1. If we constrain $\gamma = 0.5$ (as expected for the UV sum-rule, see Ref. [108]) the fit improves with decreasing mass, from $\chi^2/\text{n.d.f.} \approx 15$ on the B0 lattice to ≈ 0.4 on B10.

The Coulomb potential in momentum space from the Coulomb kernel (2.160) (third row of Fig. 6.2) and in position space from the $U_0 U_0^\dagger$-correlator (fourth row) agree qualitatively very well. The Coulomb string tension, which is found as the intersection with the vertical axis in the momentum space plot and the slope at large distances in position space, decreases when going to smaller bare masses. In both plots the factor between the string tension at the largest and the smallest mass is approximately 0.5, when we use a linear fit at large distances in the position space plot and compare the values at the smallest momentum accessible in the IR in the momentum space plot.

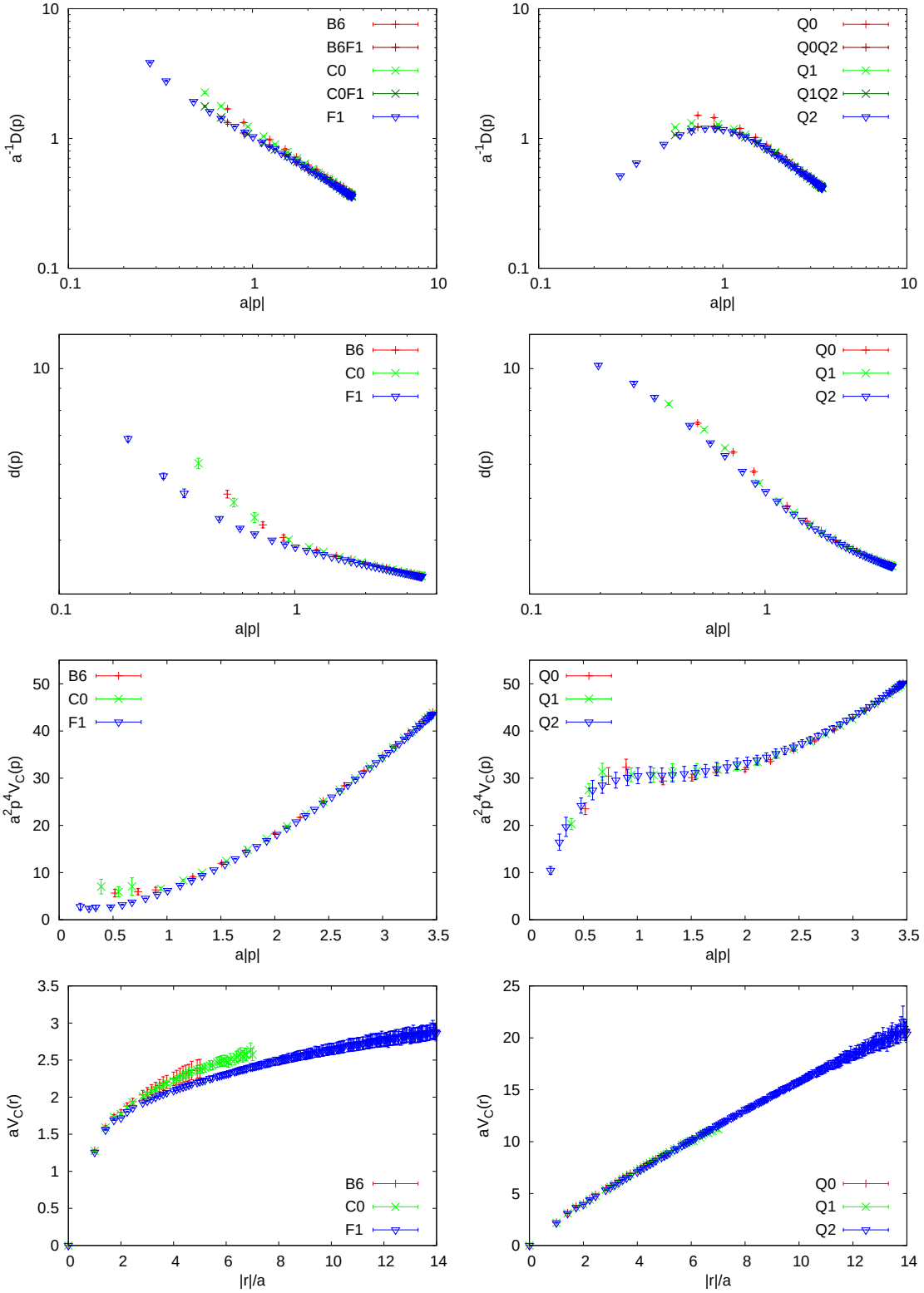

Figure 6.1.: The Coulomb gauge correlation functions in lattice units at $-am_0 = 1.15$ (l.h.s.) and in the quenched approximation (r.h.s.). From top to bottom: the gluon propagator, the ghost form factor and the Coulomb potential in momentum and position space. The difference between the light and dark colored points in the gluon propagator plots is explained in the text.

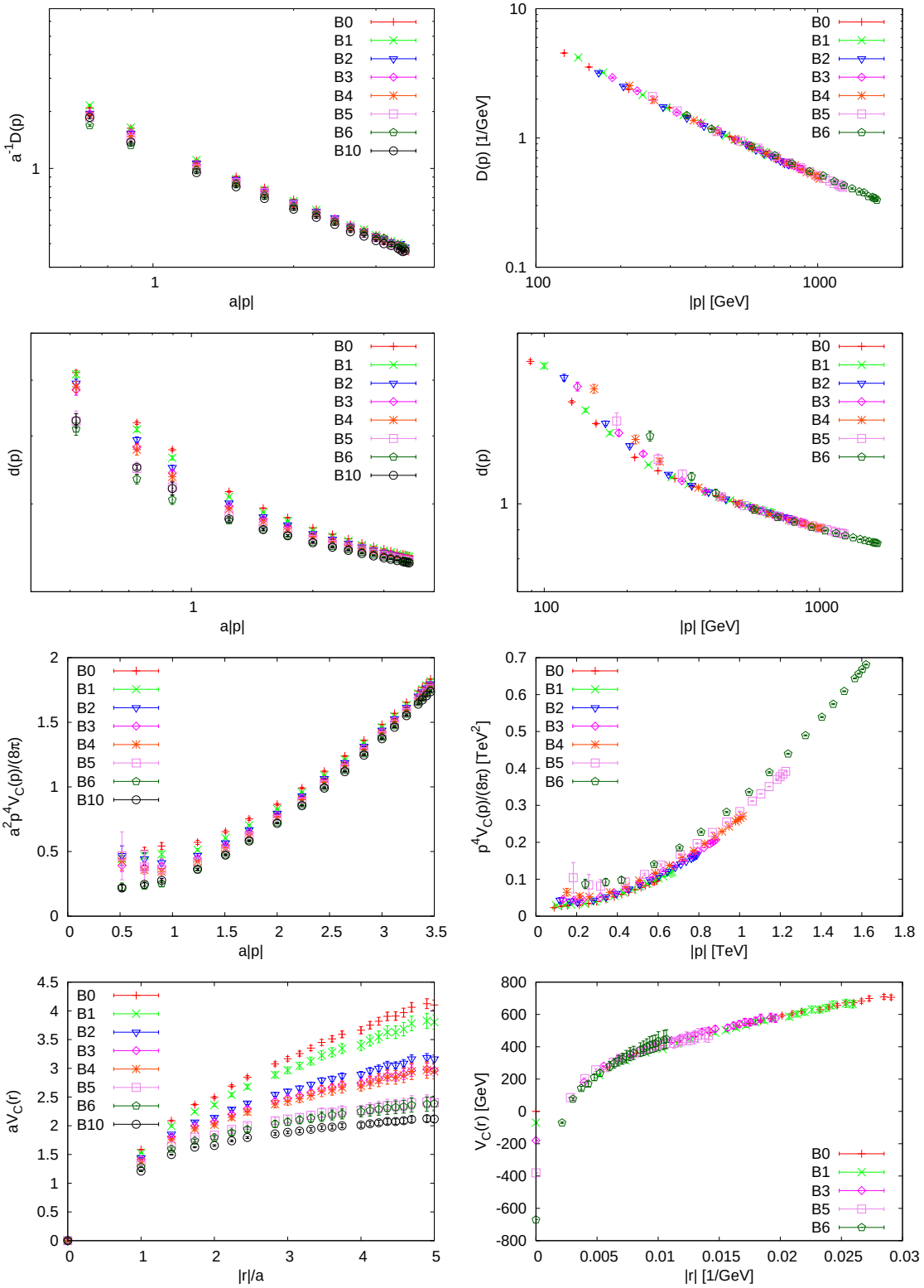

Figure 6.2.: The Coulomb gauge correlation functions at fixed lattice size 24×12^3 for various bare masses in lattice units (l.h.s.) and with the scale set (r.h.s.) as explained in Section 6.2.1. From top to bottom: the gluon propagator, the ghost form factor and the Coulomb potential in momentum and position space.

Next we will turn to the results in the r.h.s. of Fig. 6.2, where we set the scale assuming the 0^{++} technigliueball is a Higgs impostor. In this plot we excluded the B10 lattice, i.e. the lattice with the smallest bare mass. For this lattice the 0^{++} glueball mass was not available and an extrapolation with our fit function failed: the data from this lattice, for all quantities, was in disagreement with the other lattices.

After multiplicative renormalization the data points for the gluon propagator from all masses fall perfectly on a single line over the whole momentum range. Note that applying a renormalization in the plot with lattice units would not yield such a result. This effect is truly an effect of the scale setting.

Although not as clearly, the ghost form factor shows the same nice agreement with a single line. The deviations in the IR could be explained by finite volume effects as we saw in the previous section. The plot in Fig. 6.1 suggests that for the B6 lattice at least the two last data points should be excluded from the plot. The B6 lattice is the one with the smallest lattice spacing and therefore is expected to show the strongest finite volume effects. These outliers could be treated by a cone-cut [207]. Since we don't have the configurations for a more detailed finite volume study at the bare masses we decided to keep all points in the IR.

Finally for the Coulomb potential we find again good agreement with a unique function for all masses. In position space we normalized the data to overlap at large distances. This shift is allowed since it just defines the zero-point energy. Since the Coulomb potential is a renormalization group invariant no multiplicative renormalization is allowed in momentum space. If we would shift the data points for the smallest masses B5 and B6 towards higher momenta we would get an even better overlap. This would indicate that our scale setting is not perfect, provided that the unique line is the physical result.

In Fig. 6.3 we compare the the largest bare mass on the smallest lattice with the smallest mass available on the biggest lattice. The rationale for this choice is that the smallest bare mass corresponds to the largest physical volume when we use the scale from the 0^{++} technigliueball mass. Thus finite volume effects should be minimal with this mass compared to the other lattices of same size. The result is remarkable: all quantities show very good agreement with a single line. Again the momentum space Coulomb potential might suggest that the scale setting is not perfect. In position space we did a fit to the data of the smaller lattice. As can be seen this fit agrees very well with the data up to very short distances. Quantitatively the string tension from the Coulomb kernel plot (l.h.s.) and the $U_0U_0^\dagger$-correlator (r.h.s.) seem compatible. The fit in position space yields $\sigma_C \approx 0.013\text{TeV}^2$ while in momentum space anything in the range $\sigma_C = 0.01 \ldots 0.04\text{TeV}^2$ seems reasonable. The large uncertainty stems from the discrepancy between the two lattices: on the larger lattice the potential looks already constant below $p = 0.2\text{TeV}$, while on the smaller lattice it is still decreasing in that range. Additionally, as mentioned before, they do not agree perfectly which might be a problem in the scale setting.

6.4. Discussion and Summary

In the preceding section we presented our results in two different ways: first in lattice units, then with the scale set by the mass of the 0^{++} technigliueball. A similar analysis was performed in Ref. [205] for Landau gauge based on the same lattice configurations[8]. Our results essentially show a similar behavior and therefore we will borrow the interpretation from this study.

[8]The largest lattice was not available to this study.

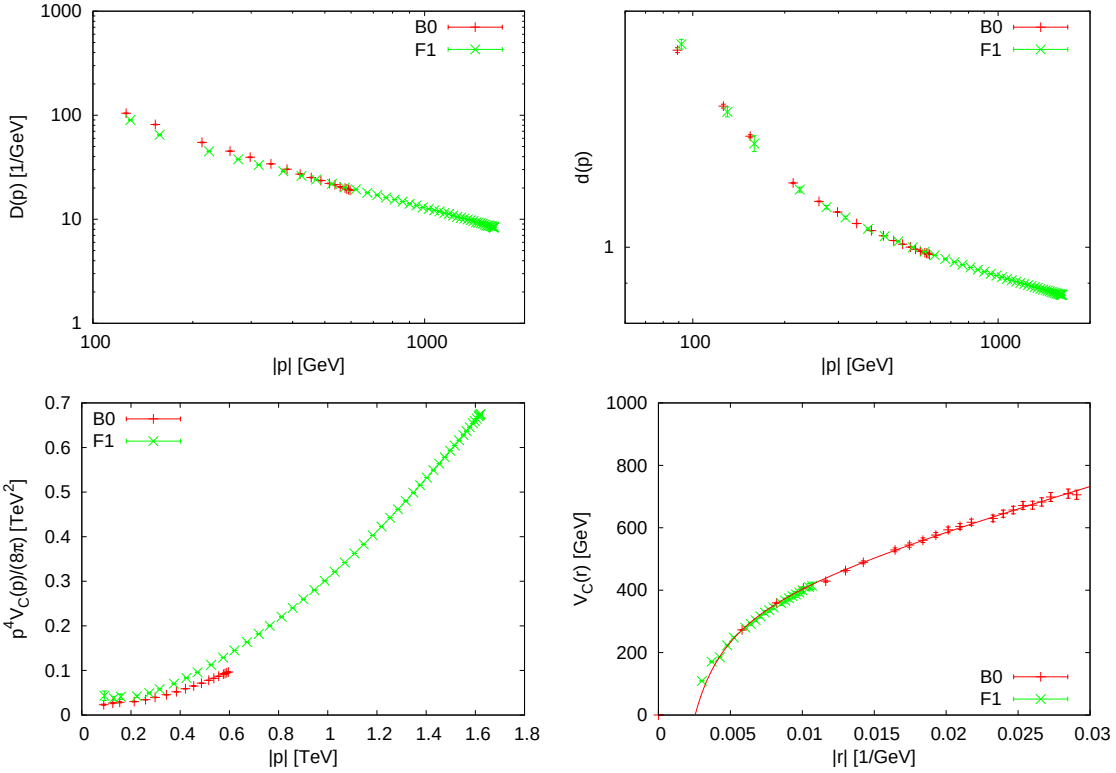

Figure 6.3.: The Coulomb gauge correlation functions from the smallest lattice at the largest bare mass and the largest lattice in physical units. The data points lie remarkably well on a single line. The line in the position space Coulomb potential plot is a fit to the B0 data only.

The first case where we showed the results in lattice units is the physical correct one if the influence of the bare mass on the scale is assumed to be small. This result is not unreasonable since it is found for QCD, as was pointed out in Ref. [205]. We found that the gluon propagator is well described by a single power-law over the whole momentum range and is very close to its tree-level value (without an anomalous dimension). The ghost form factor becomes flatter in the IR if the bare mass is tuned towards the massless limit, i.e. approaches the tree-level behavior, although according to the current data most likely with a non-zero anomalous dimension. Since also the bend softens, that separates the IR and UV regions, the ghost form factor might eventually show a universal power-law in the limit of zero techniquark mass. As the author of Ref. [205] argues this is expected for a conformal theory. Additionally, the Coulomb string tension decreases towards smaller masses and might even vanish in the chiral theory as would be expected for a conformal theory, since a non-zero string tension would imply a scale in the theory.

The 0^{++} glueball has the same quantum numbers as the Standard Model Higgs boson. Additionally in the MWT theory it is the lightest particle in the spectrum [59–62], in contrast to QCD where the pseudoscalar (the pion) is the lightest excitation. This makes the 0^{++} glueball a perfect candidate for non-elementary Higgs particle. Therefore we investigated the behavior of the propagators if we introduce the scale by setting the 0^{++} mass to the value of the Higgs boson. With this scale, we found that the Coulomb gauge quantities at different masses agree very well with a single line which supports the hypothesis of the 0^{++} glueball as a Higgs impostor. If this scale is meaningful, the

behavior would be different to the QCD case, where the scale mainly depends on the running coupling and not on the fermion masses. The Coulomb gauge propagators indicate a confining in the massless limit at the fixed gauge coupling of this study.

As already pointed out, our results in Coulomb gauge are in line with the findings in Landau gauge and we could not refine the conclusions of Ref. [205]. Essentially, the data allows two different interpretations, one signaling a quasi-(conformal) theory, the other describes the Higgs boson as a technicolor glueball. Only a refined analysis of finite volume effects can clarify if the very good agreement of the data at different bare mass and lattice size in the second interpretation is accidental or physical. A larger set of bare masses at the largest lattice size would be needed. To clarify the relevance of the gauge coupling on the scale we would also need configurations at different β.

7. cuLGT: Lattice Gauge Fixing on GPUs

As mentioned before, several computational intensive tasks have to be performed in lattice gauge theory. Fortunately, most of these algorithms are well-suited for highly parallel architectures, like graphic processing units (GPUs). Using GPUs beyond its original application for computer graphics (general-purpose computation on graphics processing units, GPGPU), is a comparatively new field in high performance computing. Only very few lattice QCD applications were using this new technique when cuLGT and its prior versions were developed. Therefore, the main technical tasks for the results of this thesis was the implementation and optimization of algorithms for the use on graphic processing units. cuLGT is a library for lattice gauge theory written in C++ using NVIDIA's CUDA platform with a focus on flexible memory usage for the gauge fields. In this chapter, we will discuss only the gauge fixing part of cuLGT, which is publicly available and in which most optimization effort was put. This chapter is mainly based on the articles [29, 208–210] and extended by unpublished material.

7.1. GPU Computing in Lattice Field Theory

Modern graphic processing units are optimized to calculate many pixels of an image (shading) in parallel. Already in 2001, a first attempt [211] was made to use these devices outside of its original field. At that time, the authors concluded that their matrix multiplication on a GPU using a 8-bit fixed-point format would not be competitive to a CPU program when using 32-bit floating point operations[1]. According to Ref. [212], one of the first algorithms that ran faster on a GPU was a LU factorization with partial pivoting compared to well-established CPU libraries [213]. In lattice gauge theory, GPU programming was first used for multiplication with Wilson and staggered Dirac operators [214].

The introduction of NVIDIA's CUDA platform in 2007 significantly simplified GPGPU programming led to an adoption by a larger community. Nowadays, GPGPU is well established in high performance computing and co-processors solely for general purpose computation but equipped with GPU-chips are produced by the market leaders NVIDIA and AMD. Later, Intel joined the market with the Intel MIC[2] architecture in the Xeon Phi co-processors. In the Top 500 list of supercomputers [215], as of November 2015, 104 systems are equipped with coprocessors, 66 of them with NVIDIA GPUs and 27 with Intel Xeon Phis. The second place is occupied by a system which uses NVIDIA Tesla K20x GPUs.

An alternative to CUDA, which does not tie the user to NVIDIA GPUs, is the OpenCL framework used in the lattice code [216]. Recently, the parallelization framework OpenACC was introduced which simplifies parallelization by defining OpenMP-like pragmas, see Ref. [217] for an application to lattice field theory.

The first CUDA application for lattice gauge theory is the QUDA library [27, 28] which is still under active development. In Ref. [218] a first gauge fixing code for GPUs using the overrelaxation algorithm was presented by one of the authors of cuLGT. Later the authors

[1] At the time, floating point operations were not supported by GPUs.
[2] Many Integrated Core Architecture

who used CUDA for the first time to generate pure gauge configurations [219, 220], implemented a gauge fixing for GPUs using a Fourier accelerated steepest descent algorithm [221] and later implemented overrelaxation, adopting our 8-threads-per-site strategy, see Section 7.4.2, in Ref. [222].

The first stable version of cuLGT was presented in Ref. [29] (cuLGT1) and in most parts rewritten for Ref. [210] (cuLGT2). In Fig. 7.1, the optimizations by a factor of four from the first (unpublished) attempt to the most recent version is summarized. With the most recent version the implementation runs at 80% of the theoretical peak performance, given by the memory throughput. The performance will be discussed in more detail in Section 7.5.

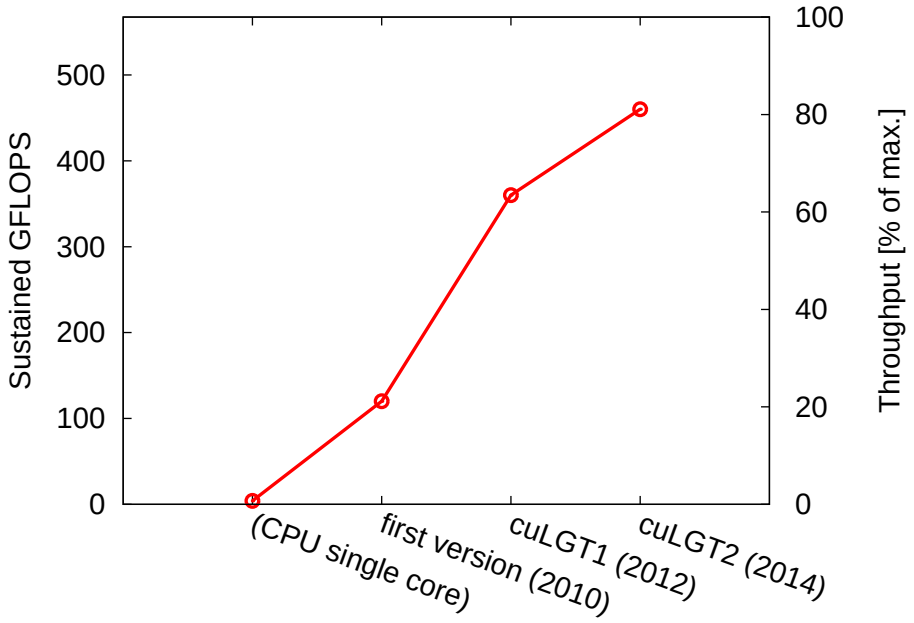

Figure 7.1.: Performance history of the cuLGT Landau gauge fixing code on a 32^4 lattice with a GTX 580. Details are explained in Section 7.5.

7.2. Lattice Gauge Fixing as an Optimization Problem

Lattice Landau and Coulomb gauge is formulated as an optimization problem as a discretization of the continuum functional (2.28). Every minimum of (2.28) satisfies the local gauge condition

$$\partial_\mu A_\mu(x) = 0, \tag{7.1}$$

where $\mu = 0, 1, 2, 3$ for Landau gauge and $\mu = 1, 2, 3$ for Coulomb gauge.

7.2.1. Gauge functionals for Landau and Coulomb gauge

A possible choice for the lattice functional is given by

$$F^U[g] = \frac{1}{N_c N_d V} \sum_{x,\mu} \mathrm{Re}\,\mathrm{tr}\left[U^g_\mu(x)\right] \tag{7.2}$$

where U^g denotes the gauge transformed link variables

$$U^g_\mu(x) = g(x)U_\mu(x)g^\dagger(x+\hat{\mu}). \tag{7.3}$$

Eq. (7.2) is a translation of the continuum functional (2.28) which corresponds to the common linear definition of the gauge field

$$A^{\text{lat}}_\mu(x+\hat{\mu}/2) = \frac{1}{2\text{i}}\left[U_\mu(x) - U^\dagger_\mu(x)\right]_{\text{traceless}} \tag{7.4}$$

which is accurate up to $\mathcal{O}(a^2)$. A measure for convergence of the algorithm is how well the Landau/Coulomb gauge condition (7.1) is satisfied numerically. The lattice divergence is given by the difference approximation

$$\Delta(x) = [\partial_\mu A_\mu(x)]^{\text{lat}} = \sum_\mu \left[A^{\text{lat}}_\mu(x) - A^{\text{lat}}_\mu(x-\hat{\mu})\right]. \tag{7.5}$$

We take either the lattice average of the L^2-norm of Δ

$$\theta^{\text{avg}} = \frac{1}{N_c V}\sum_x \text{tr}\left[\Delta(x)\Delta^\dagger(x)\right] \tag{7.6}$$

or, the more strict condition, the maximum thereof

$$\theta^{\text{max}} = \frac{1}{N_c}\max_x \text{tr}\left[\Delta(x)\Delta^\dagger(x)\right] \tag{7.7}$$

as a criterion for terminating our algorithm.

7.2.2. The Algorithms

After having formulated lattice gauge fixing as an optimization problem we will explain the algorithms which we use for solving the problem in the next sections. A detailed study of various updating algorithms is presented in Ref. [223]. The algorithms are well-established in the lattice community, only their optimization for GPUs is the novel contribution in this chapter.

All algorithms are based on a localized version of the functional (7.2). We rewrite the functional as a sum of local functions which depend only on the lattice site in the form

$$F^U[g] = \frac{1}{2N_c N_d V}\sum_x f_x[g] \tag{7.8}$$

with

$$f_x[g] = \text{Re}\,\text{tr}\,[g(x)K(x)] \tag{7.9}$$

where we made the dependence on $g(x)$ explicit. The function $K(x)$ is given by

$$K(x) = \sum_\mu \left[U_\mu(x)g^\dagger(x+\hat{\mu}) + U^\dagger_\mu(x-\hat{\mu})g^\dagger(x-\hat{\mu})\right]. \tag{7.10}$$

Function (7.9) is then optimized *locally*, i.e. with respect to $g(x)$ for all lattice points x, one after the other. Updating all lattice points once is called a (gauge fixing) sweep. To achieve global convergence of (7.2), many sweeps are necessary until a given precision ϵ is reached, i.e. $\theta < \epsilon$ in (7.6) or (7.7).

Relaxation

For the gauge group SU(2) the local maximum of (7.9) is given by the gauge transformation

$$g(x) = \frac{K^\dagger(x)}{\sqrt{\det K^\dagger(x)}} \tag{7.11}$$

which defines the relaxation algorithm. For gauge groups SU(N_c) with $N_c > 2$ the maximization is done iteratively for the $N_c^2 - 1$ SU(2) subgroups by the Cabibbo-Marinari technique [58].

Overrelaxation

The authors of [224] proposed to replace the optimal gauge transformation $g(x)$ in (7.11) by the transformation

$$g \to g^\omega \tag{7.12}$$

with $\omega \in [1, 2]$. This updating procedure defines the overrelaxation algorithm, which reduces critical slowing down compared to the relaxation algorithm. The lower limit $\omega = 1$ is, of course, the standard relaxation. The upper limit $\omega = 2$ is a so-called microcanonical update. It does not change the value of the functional but helps to speed up thermalization in the simulated annealing algorithm (Section 7.2.2). The optimal value for ω is determined experimentally and is found to be between $\omega = 1.7 - 1.9$ for SU(2) and slightly lower for SU(3).

Stochastic Relaxation

Stochastic relaxation is another algorithm to reduce the critical slowing down. The relaxation update $g(x)$ is replaced by a microcanonical gauge transformation with a given probability p. Again the parameter $p \in (0, 1)$ has to be tuned by benchmarking.

Simulated Annealing

In the past algorithms inspired by nature have been applied successfully to numerical optimization problems: genetic algorithms [225], particle swarm optimization [226] and many more. These algorithms are especially helpful for finding global extrema in a rough optimization landscape. For lattice gauge fixing, simulated annealing [227, 228] has proven to be a very useful tool. It was first adopted to gauge fixing in Ref. [229]. Simulated annealing is inspired by the field of metallurgy: to get a solid with few defects in the crystal structure, the material is heated up above the melting point and then slowly cooled down to the ground state.

In our application the ground state corresponds to the global maximum of the gauge fixing functional (7.2). In contrast to the other algorithms discussed so far, which increase the local functional (7.9) in each (local) update step, the simulated annealing algorithm allows for worsening of the functional with a probability given by a Boltzmannian weight.

The simulated annealing update can be described by a Metropolis step where random gauge transformation is accepted according to the probability distribution

$$P[g(x)] = \begin{cases} 1 & \text{if} \quad f^g(x) \geq f(x) \\ \exp\left(\frac{f^g(x) - f(x)}{T}\right) & \text{else,} \end{cases} \tag{7.13}$$

That means the random update is always accepted if it increases the functional value and accepted with the given Boltzmann distribution if it decreases the value. The parameter T plays the role of the temperature of the system. In practice, the simple Metropolis algorithm will be replaced by a heat bath step where the random gauge transformations are already generated with the correct probability distribution. It has exactly the same structure as the updates in the Monte-Carlo chain for generating the gauge configurations, see Section 2.4.1. The heat bath update is favorable for performance because the acceptance/rejection step is avoided.

A crucial factor for the success of the algorithm is how the annealing schedule is defined. In order to surely converge to the global maximum the system has to be in equilibrium at all times. That means the temperature should be decreased in infinitely small steps to $T = 0$. In practice, of course, a trade-off between the time to spend in the algorithm and the quality of the optimization has to be made. In our algorithm we use linear temperature steps, which are described by three parameters: the starting Temperature $T_{\max}$, the final temperature $T_{\min}$ and the total number of simulated annealing sweeps N_{SA}. These parameters have to be determined experimentally, see Section 7.5.3.

As already mentioned, applying microcanonical updates between the simulated annealing heat bath sweeps helps to thermalize the system. Note that repeated heat bath steps for a fixed temperature would as well thermalize the system but they are numerically much more expensive compared to the microcanonical updates. Usually, we use 3 to 5 microcanonical steps per heat bath step.

The simulated annealing algorithm alone (with a finite number of temperature steps) will not satisfy (7.6) with high precision. Therefore, after the gauge configuration is brought close to a maximum by the simulated annealing algorithm, we perform (over-)relaxation updates until the desired precision is reached. These final updates can be thought of as simulated annealing in the limit of zero temperature.

7.2.3. Logarithmic Gauge Field Definition

An alternative to the linear $\mathcal{O}(a^2)$ approximation of the gauge field (7.4), the so-called logarithmic definition is used sometimes, see for example Refs. [77, 230, 231]. There the lattice gauge-field is extracted from the logarithm of the $N \times N$ matrix U by diagonalization

$$A_\mu(x + \hat{\mu}/2) = \frac{1}{\mathrm{i}ag} \Omega_\mu^\dagger(x) \log U_\mu^d(x) \Omega_\mu(x), \tag{7.14}$$

with the diagonal matrix

$$U_\mu^d = \Omega_\mu(x) U_\mu(x) \Omega_\mu^\dagger(x) \tag{7.15}$$

in the notation of Ref. [77]. For the logarithm definition the algorithms discussed here are not suitable, since they are based on the linear approximation. A widely used algorithm which is suitable for the linear and the logarithmic definition is Fourier accelerated steepest decent, as for example in the CUDA implementation of Refs. [221, 222].

7.2.4. Parallelization

Due to the strict locality of the algorithms based on (7.10), a generalization to parallel architectures is straightforward. For the computation of the gauge transformation $g(x)$ at site x, only the links $U_\mu(x)$ and $U_\mu(x - \hat{\mu})$ contribute. Therefore, every second sites are completely independent of each other. That allows to update the sites in parallel in a 4-D checkerboard fashion as illustrated in Fig. 7.2. This will be the starting point for the CUDA implementation. The Fourier accelerated steepest decent algorithm as

mentioned in Section 7.2.3 does not allow for such a simple parallelization due to the non-local nature of the Fourier transform. For pure MPI or pure CUDA codes an efficient fast Fourier transform is available, while to our knowledge a heterogeneous MPI-CUDA implementation is not available. Therefore, a multi-GPU implementation of the Fourier accelerated steepest decent is still lacking.

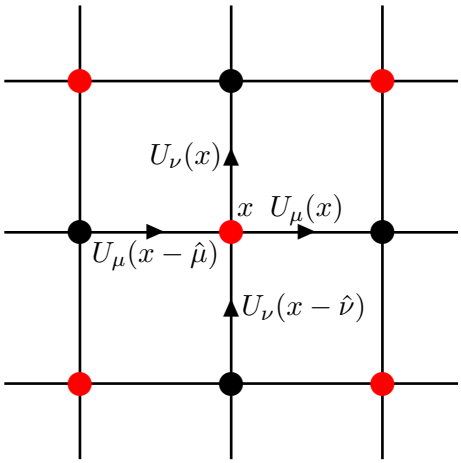

Figure 7.2.: Two-dimensional checkerboard layout for the parallel update of gauge transformations. Red and black sites are independent of each other and allow an update in parallel.

7.3. The CUDA Programming Model

In this section we will give a short introduction to GPU computing with CUDA. We focus on the peculiarities that are needed to understand the design of our implementation. A more detailed introduction can be found in the official CUDA programming guide [232] and in various textbooks, e.g. Refs. [233, 234].

7.3.1. The Thread Hierarchy

The CUDA programming model provides two levels of parallelism: a fine-grained parallelism were threads can communicate in a so-called *block* and a coarse-grained parallelism of blocks within a *grid*. The grid structure provides scalability to devices with different number of multiprocessors. For a problem with a fixed number of blocks, these blocks are divided to the available number of multiprocessors. If more multiprocessors are available, less blocks are scheduled to each multiprocessor. Since blocks cannot communicate with each other, the problem has to be formulated such that individual blocks are completely independent of each other and can run in any order. For communication within blocks a *shared memory* and barrier synchronization is available.

The development of code with such a thread hierarchy is introduced in the C++ language by the `__global__` specifier to denote a special kind of function, the so-called *kernel*. A kernel is invoked by specifying the grid size (the number of blocks) and the block size (the number of threads per block). CUDA, with the background of 3D computer graphics, offers a 3 dimensional grid and block structure, a 4 dimensional structure as needed for

the 3+1 dimensional space-time of lattice QCD is not available. Therefore, we use the linear, one dimensional structure and calculate 4 dimensional coordinates from the one dimensional index if needed.

Of special importance is, that threads within a block are executed in groups, the so-called *warps*. A warp consists of 32 threads on all present architectures. All threads of a warp should execute the same instruction for highest efficiency. If branching occurs within a warp, i.e. if the threads follow a different code path in an `if`- or `switch`-statement, the execution is serialized for each of the branches (*warp divergence*).

7.3.2. Hardware and Memory Layout

The CUDA thread hierarchy of the preceding section is reflected in the hardware of the GPUs. The CUDA cores are organized in so-called streaming multiprocessors (SM for Fermi, SMX for Kepler). Each Fermi SM features 32 CUDA cores (units for arithmetic operations), while the SMX of the Kepler generation features 192 cores. The number of streaming multiprocessors differs between chips of the same architecture. All threads of a thread block are assigned to one of the streaming multiprocessors. This allows on-chip data exchange within blocks via shared memory, see below.

In the CUDA terminology the CPU is called *host* and the GPU is called *device*. Both host and device have their separate physical memory, called host and device memory. Memory transfers between host and device are limited by the bandwidth of the PCIe bus. The bandwidth between host and device is considerably lower compared to on-device memory transactions. However, for our single GPU implementation, we only need to copy the data (the gauge field) once to the device and once back, after gauge fixing is done. In this case host-device transactions are completely negligible. In the multi-GPU implementation, Section 7.4.4, care has to be taken to hide the host-device transfer times by computation.

On the device, several types of memory are available. *Global memory* is the part of device memory that is accessible from the host and all device threads. For devices of the Fermi architecture it is cached in L1 and L2 caches[3]. In the Kepler architecture a L1 cache is available, however L1 caching is disabled by default and can be activated only for some devices. The L1 cache is then solely reserved for caching local memory, see below. For our application bandwidth to global memory is the limiting factor for performance and needs special attention, see Section 7.4.1. Additionally to the bandwidth limitations, reads from global memory have a very high latency of about 500 cycles. To hide the latency it is desirable to have much more active threads than CUDA cores on a multiprocessor. *Shared memory* is a fast on-chip memory which is accessible by all threads within a block and resides in the same hardware as the L1 cache. Each thread can use its own private memory, the so-called *local memory*. Local memory is automatically used for all variables within a kernel that cannot be placed in registers. Variables are put in local memory, for example, if more registers are needed than available or for arrays where the elements are not addressable at compile time. Local memory uses the same hardware as global memory and therefore suffers from the same bandwidth and latency limitations.

Detailed characteristics of the devices (latencies of the memory types/caches, caching strategies, etc.) are usually not officially documented. However, there are several studies which try to track down the characteristics by microbenchmarking. These benchmarks

[3]These caches are much smaller compared to CPU caches and additionally shared by more cores. Therefore they should in general not be thought of caches to reuse data that was previously loaded, but more to improve imperfect memory access patterns, see Section 7.4.1. Cache-blocking, which is a standard optimization technique for CPUs, is therefore not applicable in GPU programming.

try to disentangle the different performance-relevant factors. For a recent review see [235] and references therein.

7.4. Optimizations for GPUs

At the time of the development of the first version of cuLGT the most recent generation of CUDA-capable GPUs was the so-called Fermi architecture. Therefore, the theoretical considerations in this chapter are mainly based on the properties of Fermi GPUs as listed in Table 7.1.

architecture	Fermi	Kepler	
compute capability	2.0	3.0	3.5
cores / SM	32 per SM	192 per SMX	
warp size	32		
L1 cache / SM	16 KiB or 48 KiB		
shared memory / SM	16 KiB or 48 KiB		
32-bit registers / SM	32768 (32Ki)	65536 (64Ki)	
max. registers / thread	63		255

Table 7.1.: Specifications of the Fermi and Kepler architectures.

7.4.1. Memory Transfer

Before we start with the optimization we will do a theoretical analysis of the gauge fixing algorithm. For the sake of simplicity we will concentrate on the overrelaxation implementation for the gauge group SU(3) in single precision.

The *arithmetic intensity* or *compute to global memory access (CGMA) ratio* [234]

$$I = \frac{N_{\text{ops}}}{T_{\text{mem}}} \tag{7.16}$$

of an algorithm is a measure of how many (floating-point) arithmetic operations N_{ops} are executed per memory transfer T_{mem}. It can be used as a measure of how well a certain algorithm fits to the hardware. To fully utilize a device the arithmetic intensity should be as close as possible to the FLOPS[4] to bandwidth ratio I_{dev} of the device. In the case of $I > I_{\text{dev}}$ we say the algorithm is *compute bound*. That means the performance is limited by the floating point operations per second. On the other hand, we say a program is *memory bandwidth bound* if $I < I_{\text{dev}}$, i.e. if the algorithm is limited by the memory bandwidth. The ideal CGMA ratio is listed in Table 7.2 for several devices. For all devices the

	GTX 580	GTX 680	GTX Titan	Tesla K20
$I_{\text{dev}}^{\text{SP}}[\text{byte}^{-1}]$	8.2	16.1	15.6	16.9
$I_{\text{dev}}^{\text{DP}}[\text{byte}^{-1}]$	1.0	0.7	5.2	5.6

Table 7.2.: Optimal CGMA ratio for single and double precision.

value is around 10 for single precision and significantly lower for double precision, due

[4] We use FLOPS (with capital "S") for floating point operations per second and FLOPs (small "s") for the plural of floating point operation.

to the reduced number of double precision units per streaming multiprocessor[5]. The overrelaxation algorithm allows an easy calculation of the arithmetic intensity as it is fully deterministic[6].

Updating a single site with the overrelaxation algorithm costs 2274 FLOPs. See Appendix E for a detailed description about how we counted FLOPs. For the computation of the new gauge transformation the $2N_d$ surrounding links have to be loaded from (global) memory and stored after the update. For SU(3) we are dealing with 3×3 complex matrices, and thus with a size of 72 bytes in single precision or 144 bytes in double precision. For $N_d = 4$ space-time dimensions, this amounts to 576 bytes or 1152 bytes for single and double precision respectively for reading and the same amount for writing the updated matrices back to memory, per lattice site. This result in an arithmetic intensity of

$$I_{\text{over}}^{\text{SP}} \approx 2.0/\text{byte}, \tag{7.17}$$

$$I_{\text{over}}^{\text{DP}} \approx 1.0/\text{byte} \tag{7.18}$$

for the overrelaxation Landau gauge algorithm. From these theoretical considerations it is clear that our algorithm is limited by memory bandwidth in single precision and also in double precision for most of the devices.

Reduce Memory Transfer

To reduce the memory usage in the gauge fixing algorithms we can make use of the symmetry of the SU(3) matrices. Instead of keeping the full 3×3 complex matrices (18 parameters) in memory we keep only the first two rows u and v (12 parameters) and reconstruct the third row by the cross product of the complex conjugates of u and v when needed:

$$U = \begin{pmatrix} u \\ v \\ u^* \times v^* \end{pmatrix}. \tag{7.19}$$

With this optimization we reduce the memory load for one site by a factor of 1/3 to 384 bytes (by the exchange for more arithmetic operations). The increase in floating point operations is expected to be hidden since the kernel is memory bound as discussed in the previous section. This technique was proposed long ago in [236] and first applied to GPU computing in [214]. Note that a minimal 8 parameter representation $U = u_a T^a$, with T^a the generators of SU(3), would be possible. However the reconstruction would drastically increase the computation and numerical inaccuracies are expected to accumulate faster. Compared to the application in Ref. [27] this effect is even more pronounced in our setup, since we need to compress and reconstruct the matrices in every iteration, where they only need to reconstruct. Therefore, we did not try this approach.

Optimize Memory Access: the Memory Patterns

The most important aspect for memory bound kernels is to read data efficiently. On GPUs one has to deal with a special design of the memory controller. Memory transactions of the same warp are coalesced into a single load/store operation if the data resides in the

[5] In the gaming GPU GTX 580 some of the double precision floating point units are disabled.

[6] The simulated annealing algorithm, which is based on a probabilistic evaluation with random numbers, only allows to determine a lower bound with simple calculation. A precise calculation (based on averaging multiple runs) would be a function of the gauge coupling, since the roughness of the gauge field influences the behavior of the algorithm.

same 128-byte aligned memory segment.
Simplified that means that neighboring threads should access neighboring memory location in each load/store operation. In practice that means for our algorithm that instead of using a natural memory layout where matrix elements of the same matrix are adjacent in memory (*array of structures*) one has to reorder the gauge configuration in a *structure of array* form as illustrated in Fig. 7.3, i.e. all the first entries of all matrices are adjacent in memory.

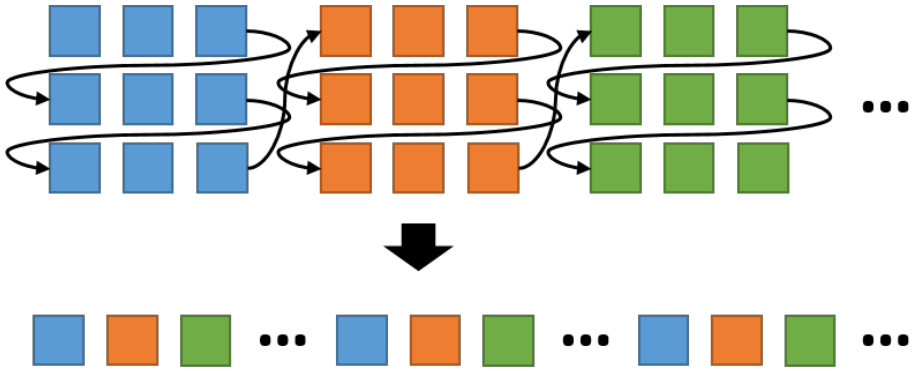

Figure 7.3.: Illustration of the memory layout. In the standard layout (top) the matrices are stored (in a row-major order) one after the other. In the GPU-optimized patterns (bottom) the first elements are the first entries of all matrices, then the second elements of all matrices and so on.

Parity ordering: As already explained, we use a checkerboard layout to do the parallel updates. For coalesced memory transactions it is necessary to order the lattice sites by parity

$$p = (t + x + y + z) \mod 2 \tag{7.20}$$

as illustrated in Fig. 7.4. All sites of the same parity are adjacent in memory.

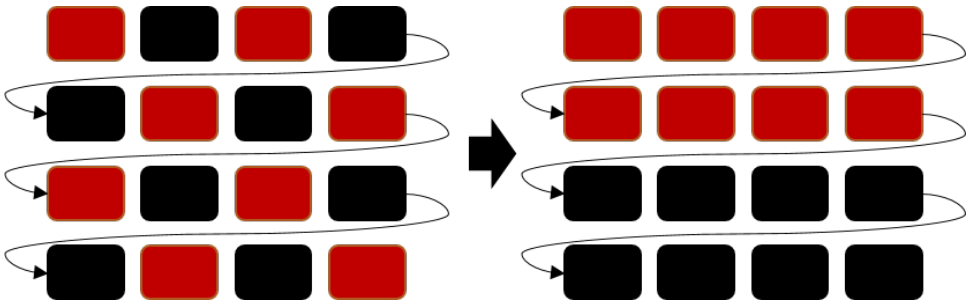

Figure 7.4.: Starting from the checkerboard layout (l.h.s) the sites are rearranged according to their parity (r.h.s).

Using CUDA vector datatypes: In the first version of cuLGT (cuLGT1) the individual matrices where represented as scalar `float` or `double` variables. In an improved version (cuLGT2) this restriction was relaxed, allowing to use the native CUDA vector datatypes `float4` and `double2` to represent a matrix. A reason to prefer vector datatypes over the

scalar datatypes is the following: For a given site $x^{(a)}$ 8 links are loaded from memory. Four of these start from the site $x^{(a)}$, the links $U_\mu(x^{(a)})$. As described above, it is now possible to reorder the lattice in a way that the next lattice site $x^{(a+1)}$ is adjacent to $x^{(a)}$ in memory. However it is not possible to arrange the lattice in a way that at the same time the four neighbors $U_\mu(x^{(a)} - \hat{\mu})$ fulfill the same condition, i.e. that elements of $U_\mu(x^{(a+1)} - \hat{\mu})$ are adjacent to $U_\mu(x^{(a)} - \hat{\mu})$ for all μ. In this case coalesced loads are not possible. For a representation with scalar datatypes that means that, in the worst case, each thread in the warp needs a full 128-byte memory load for a single float (4 byte) or double (8 byte) variable. For the vector datatypes (16 byte) the utilization of the memory is improved by a factor of 4 (float) or 2 (double).

Summary of memory patterns: While a full 4 dimensional checkerboard layout is the natural choice for Landau gauge, Coulomb gauge operates only on a 3 dimensional timeslice. Therefore, we have an additional memory pattern where the timeslice index is running slowest, i.e. a whole timeslice is a block in memory. This layout is also convenient for the multi-GPU Landau gauge application, Chapter 7.4.4, where we distribute timeslices over the nodes. Finally, for the CPU implementation, Section 7.5.2, we use a layout where matrices are continuous in memory, but the lattices sites are ordered by parity. The memory patterns for gauge configurations in cuLGT are

- `StandardPattern` (natural layout): t, x, y, z, μ, M_i
- `StandardPatternParityPriority`: $p, [t, x, y, z]_p, \mu, M_i$
- `GPUPatternParityPriority`: $p, \mu, M_i, [t, x, y, z]_p$
- `GPUPatternTimesliceParityPriority`: $t, p, \mu, M_i, [x, y, z]_p$.

The slowest running index is given first, space-time indices are denoted by t, x, y, z. M_i denotes the index of the matrix elements. In the previous sections we discussed the 12 parameter representation of SU(3) matrices and the use of the CUDA vector types. In the case of the 12 parameter representation we need three `float4` or `double4` variables, then M_i would be $0 \dots 2$. For a *full* matrix representation with `float`s or `double`s we would have $M_i = 0 \dots 17$.

Using the Texture Cache

In addition to the L1- and L2-caches, Section 7.3.2, the GPUs have a read-only *texture*-cache. The texture cache is designed for reads with a 2D spatial locality [237]. The requirement for coalescing are not as strict as for reads from global memory. Non-optimal memory reads as mentioned in the previous section may benefit from the use of the texture cache for link loading. Additionally, local memory is displaced from the L1-cache to the slow device memory with a lower probability. In [27] texture loading was already successfully applied to link loading. Also, in the context of gauge-fixing, this technique proved very useful [221]. In cuLGT, using the texture cache is implemented as a template switch in the `GlobalLink` class.

7.4.2. Multiple Threads per Lattice Site

The straight-forward parallelization is to update one site per thread. Such a strategy, however, is not ideal. To update a single site we need to keep $8 \times 18 = 144$ real variables available (all 8 links are loaded and then all these links are updated with the gauge

transformation). However, in the Fermi architecture only 63 32-bit registers are available per thread[7]. Thus, a lot of variables are spilled to local memory increasing the pressure on the memory bus, which is already the main limitation for the bandwidth-limited algorithm.

With this naive approach we do not use the two levels of parallelization (grids and blocks) that are available in CUDA. To relax the register pressure we therefore use a finer level of parallelization. In cuLGT1 we used 8 threads for a site update. Then, each thread deals with only one of the eight links. In cuLGT2 we added the option to use 4 threads per site. Both strategies considerably improve performance compared to the naive single thread per site technique. On most GPUs the 4-thread-per-site strategy is the favored one. With this improved parallelization the number of registers per thread, to store the links, is reduced to 18 (SP) or 36 (DP). In practice, of course, more registers are needed for intermediate results in the computation (reconstruction, calculation of the gauge transformation, application of the transformation).

For both strategies it is essential to invoke the kernel with a block size that is a multiple of N times the warp size (32 threads) to prevent warp divergence, where $N = 4$ or 8 is the number of threads per site. For the 8-threads-per-site strategy the order of threads to avoid warp divergence is illustrated in Fig. 7.5. The first 32 threads in the block deal with the time-links $U_t(x)$ for 32 different sites x, the next 32 threads take care of the neighbors in time $U_t(x - \hat{t})$ and so on.

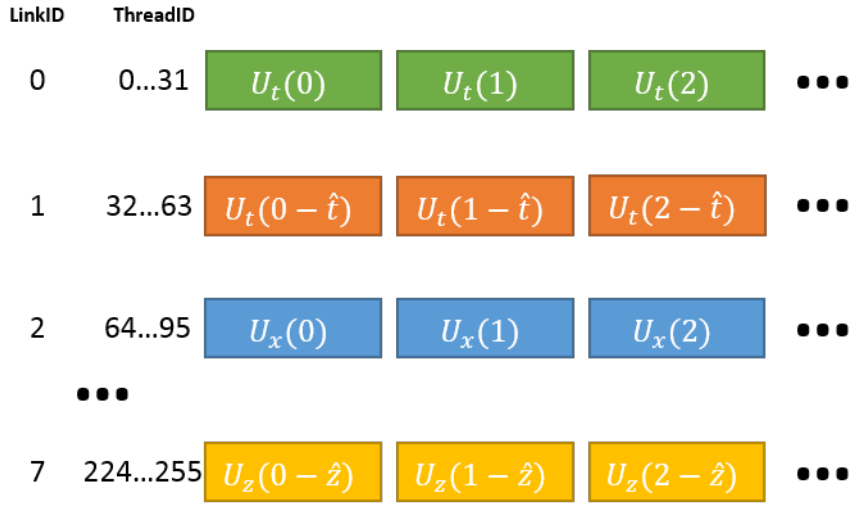

Figure 7.5.: Structure of a thread block for the 8-threads-per-site strategy.

In contrast to the naive parallelization, the multiple-threads-per-site strategies need to communicate with each other. As already mentioned, for inter-thread communication within a block we can use the fast on-chip shared memory to accumulate the sum of links in (7.10). To avoid a race condition on the summation variables we use *atomic* operations (`atomic_add()`) for single precision. For double precision, due to the lack of a corresponding double precision atomic operation, we are forced to serialize the memory access using *barriers* (`__syncthreads()`)[8]. With the 8-threads-per-site strategy no register

[7] Note that on the Kepler (for compute capability > 3.0) and Maxwell architecture the register limitation is relaxed to 255. Still, for double precision we would need 288 32-bit registers, exceeding again the register limitation.

[8] Emulating double precision atomic adds with the `atomicCAS` (compare and swap) operation as proposed

spilling occurs at all, if no further restrictions are manually applied to the kernel (see the discussion of launch bounds in Section 7.4.3). On the other hand, the total number of registers in a streaming multiprocessor is limited, too. As a result, the number of simultaneous active sites in the multiprocessor is reduced because the total amount of registers per site is increased. As it turned out, the multiple-threads-per-site strategy still gives a huge performance improvement, see Fig. 7.6 for a comparison of the single thread and the 8 threads code. However, the balance between relaxing register pressure (by more

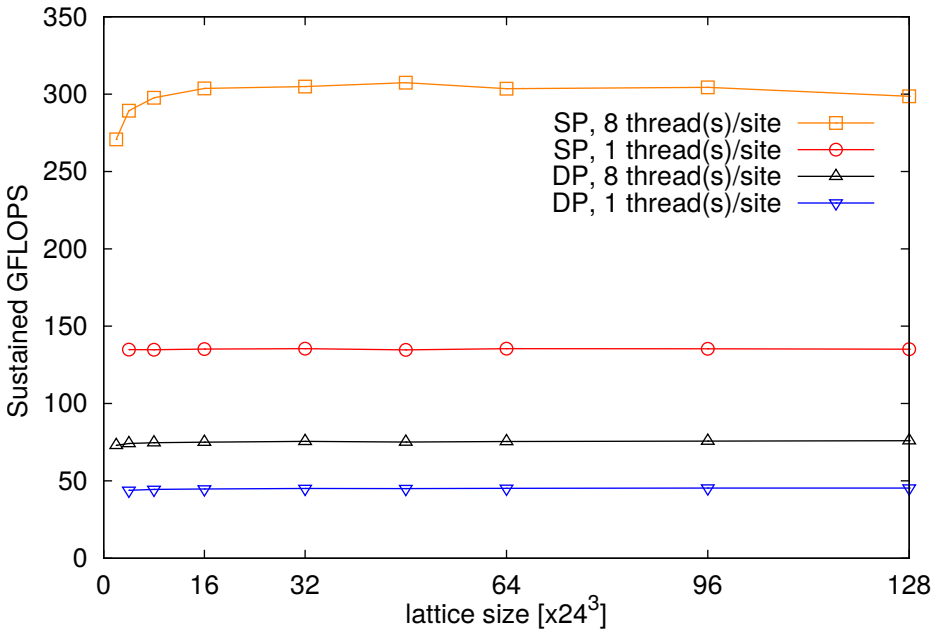

Figure 7.6.: Performance of 8 threads per site vs. 1 thread per site (cuLGT1) for various lattice sizes in single and double precision.

threads per site) and increasing the number of simultaneous active threads (by less threads per site) cannot easily be estimated and depends on the specific hardware.

7.4.3. Automatic Tuning for Optimal Performance

Another optimization one may consider is manually restricting the number of registers by forcing *launch bounds* on the kernel. By specifying the *maximum number of threads per block* and the *minimum number of blocks per multiprocessor* one can manually influence the default heuristic of the compiler which tries to balance between register spilling and instruction count [232]. The concept for optimization is the same as discussed in the preceding section (less registers may increase performance by a higher occupancy) and for the same reason a theoretical estimate for optimal settings is hardly feasible.

Therefore, in cuLGT2 we introduced a automatic tuning of the gauge fixing kernels, which allows for a detection of the optimal setup for each individual hardware. Before the actual gauge fixing we run a stage where the kernels are probed with all combinations of different options. In cuLGT2 the options are:

- various launch bounds
- enable or disable link loading via the texture cache

in Ref. [232] turned out to be less performant than our approach.

- use 4 or 8 threads per site.

These options are combined at compile-time via template meta-programming using boost's MPL [238]. The optimal setting is then selected in the first program launch at run-time and saved for the next run.

7.4.4. Multi-GPU

The memory that is available on a GPU is limited and, in contrast to the CPU memory, it is not extendable. At the time of writing, the devices with the largest memory are the Tesla K40 and Tesla K80 with 12 GiB memory. This gives an upper limit of around 64^4 on the size of SU(3) lattices that can be kept on a GPU. Thus, for large lattice sizes it is essential to split the computation among multiple GPUs. The common and most general approach is to use a MPI-based parallelization for the communication between the hosts of different GPUs. On a smaller scale it would be possible to use CUDA streams to run kernels on multiple GPUs assembled in one host system. We will discuss the MPI-based approach. The data presented in this section is based on the implementation of Ref. [29] (cuLGT1).

In the following, we will assume that one MPI host process is associated with one GPU. Thus, the number of processes N_{procs} is equal to the number of GPUs. We use a domain decomposition of the $N_t \times N_s^3$ lattice in only the time direction. Then, each GPU works on a partition of N_t/N_{procs} timeslices. In the following, we will skip the spatial argument $\boldsymbol{x}$ for a lattice point $x = (t, \boldsymbol{x})$, whenever only the timeslice index t is important. Since the gauge update at a partition boundary involves the links $U_t(x - \hat{t}) \equiv U_t(t-1)$ of the partition to the left, we need to exchange these boundary layers between devices.

Data Exchange

We will label the first timeslice of device i with t^i_{min} and the last timeslice with t^i_{max}. Then, only the gauge transformation at the first timeslice $g(t^i_{\text{min}})$ depends on data of a different node, since it involves the links $U_t(t^i_{\text{min}} - 1) = U_t(t^{i-1}_{\text{max}})$. These links need to be exchanged. Since we operate on the red and black sublattices separately, the calculation of the gauge transformations $g(t^i_{\text{max}})$ of the active parity are independent of the data exchange of the passive links $U_t(t^i_{\text{max}})$. Thus, all timeslices except the t^i_{min} can be updated independently (without data exchange), while for the update of t^i_{min} we need to perform communication steps. The setup is depicted schematically in Fig. 7.7. In the following listing we use CUDA and MPI language to name the communication steps: `cudaMemcpyXToX` for communication between host and device and `MPI_Send`/`MPI_Recv` for inter-node communication.

1. `cudaMemcpyDeviceToHost` of $U_t(t^i_{\text{max}})$
2. - `MPI_Send` of $U_t(t^i_{\text{max}})$ to device $i+1$
   - `MPI_Recv` of $U_t(t^i_{\text{min}} - 1)$ from device $i-1$
3. `cudaMemcpyHostToDevice` of $U_t(t^i_{\text{min}} - 1)$
4. update timeslice t_{min} (affects $U_t(t^i_{\text{min}} - 1)$)
5. `cudaMemcpyDeviceToHost` of $U_t(t^i_{\text{min}} - 1)$
6. - `MPI_Send` of $U_t(t^i_{\text{min}} - 1)$ to device $i-1$
   - `MPI_Recv` of $U_t(t^i_{\text{max}})$ from device $i+1$

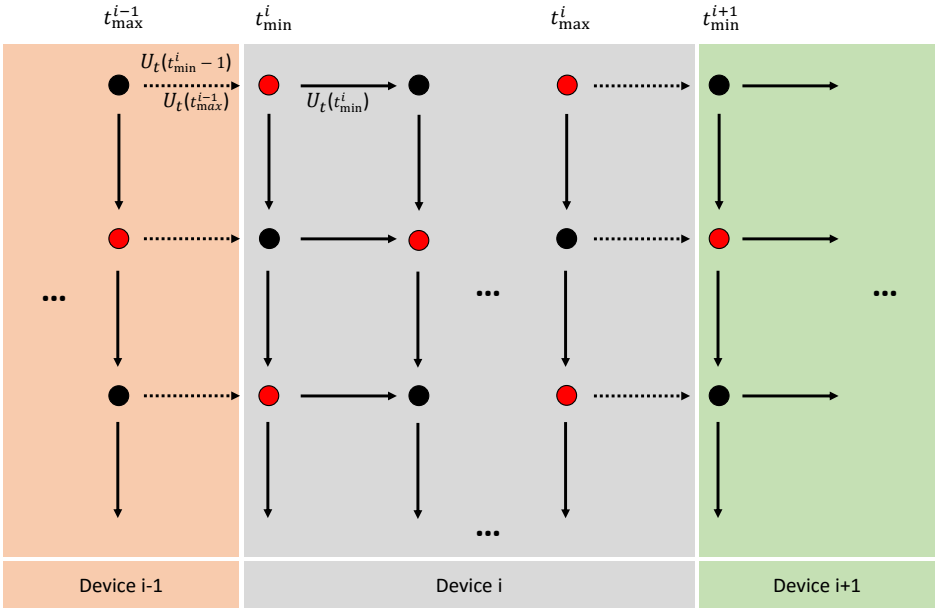

Figure 7.7.: Distribution of the timeslices in the multi-GPU setup. The doted arrows denote links which need to be available on the device to the right as halo links.

7. `cudaMemcpyHostToDevice` of $U_t(t^i_{\max})$

Note that the we need extra memory for the links $U_t(t^i_{\min}-1)$ which belong to node $i-1$ (the $U_t(t^{i-1}_{\max})$ links). This extra memory is called the *halo region*.

We use the memory pattern `GPUPatternTimesliceParityPriority`, introduced in Section 7.4.1. There, the time index is running slowest and the 3-dimensional spatial lattice (in each timeslice) is split into red and black parity. Within each parity the Lorentz index μ is the slowest running index. Thus, the relevant parts for exchange (fixed parity and $\mu = t$) build a continuous block in memory. Therefore, only 1/8-th of the timeslice needs to be exchanged.[9]

In order to hide the data transfer, we overlap the calculations of the inner timeslices with the exchange of the halo region. The weak and strong scaling of our implementation will be presented in Section 7.5.2.

7.5. Results

7.5.1. Numerical Accuracy

During the gauge fixing iterations a numerical round off error will accumulate. Especially for single precision the numerical error needs to be controlled. In the following we investigate the numerical accuracy by studying the violation of unitarity of the SU(3) matrices as a function of the number of gauge fixing steps without reprojection[10]. In Fig. 7.8 we show the average violation

$$\frac{1}{4V}\sum_{x,\mu}|1-\det(U_\mu(x))| \tag{7.21}$$

[9] 1/2 for parity and 1/4 of one parity since we only need to exchange the time links $\mu = t$.

[10] Usually, a projection of the links back to SU(3) is performed after some iterations to deal with the round-off errors and the loss of unitarity.

and the maximal violation

$$\max |1 - \det(U_\mu(x))| \tag{7.22}$$

of unitarity. In addition to single precision (SP) and double precision (DP) we show the accuracy of a *mixed precision* (MP). In the mixed precision algorithm we use single precision to store links in memory but calculate the gauge transformation in double precision. Our intent with mixed precision is to have a fast algorithm with higher numerical accuracy compared to single precision. After 12000 steps of the overrelaxation algorithm the error

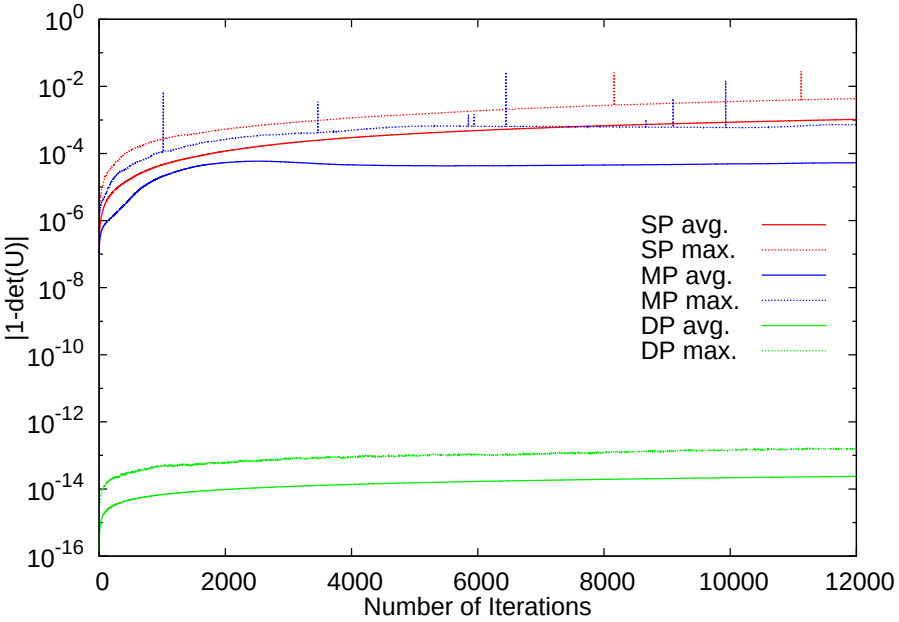

Figure 7.8.: Violation of unitarity as a function of the number of iterations.

in double precision is well below 10^{-12}, whereas in single precision the maximal violation is in the order of 10^{-2}. Mixed precision is more stable by one order of magnitude. The peaks are single outliers that appeared only on one of our devices and might be related to a malfunction of that device.

As it turned out, in Fig. 7.9 the value of the gauge functional $F^U[g]$ (7.2) is very sensitive to the precision. Especially, when no reprojection steps are included, the final single precision value deviates substantially from double precision. Additionally, in single precision it is essential to include reprojection steps since the value $F^U[g]$ even starts to decrease for a large number of steps. On the other hand, the functional value in double precision is monotonically rising even without reprojection[11]. Together with the stable unitarity from Fig. 7.8 we conclude that double precision without reprojection is very accurate. Thus, we use that curve to test the other algorithms in more detail in the inner plot of Fig. 7.9. There, we show the relative deviation of the different algorithms from the final value in double precision

$$\delta(n) = F^{\text{alg}}(n) - F^{\text{DP}}(12000) \tag{7.23}$$

over the number of gauge fixing steps n. After 12000 steps the single precision with reprojection (after every 100 steps) and mixed precision without reprojection stay within a deviation of 2×10^{-5}, mixed precision with reprojection even within 5×10^{-6}. Qualitatively,

[11] In production runs we apply reprojection in all setups, including double precision.

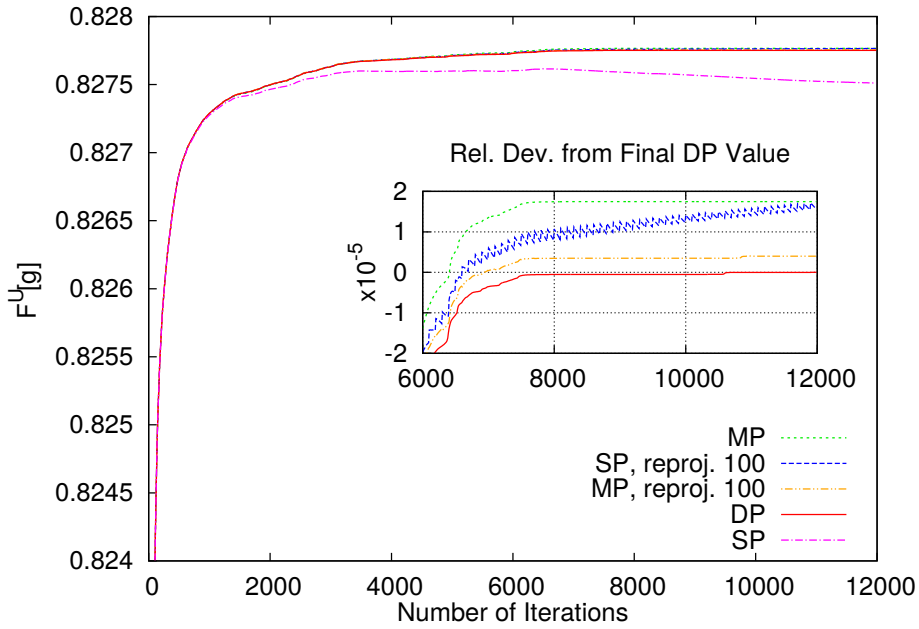

Figure 7.9.: Functional value as a function of the number of iterations with and without reprojection for single, mixed and double precision. Inner plot: deviation from the final double precision value.

the mixed precision algorithms have the same behavior as double precision, they rise monotonically and saturate at a constant value. On the contrary, single precision does not saturate and shows, on the scale of the plot, a clear zigzag from the reprojection steps.

The choice of the algorithm clearly depends on the specific problem. If one wants to select only a random gauge copy from the Gribov region and one does not depend on a high accuracy in the gauge fixing, the single precision algorithm might be enough. If the global maximum is sought, we recommend to use at least mixed precision. Mixed precision is a interesting choice since it achieves nearly the same performance as single precision, see Section 7.5.2.

7.5.2. Performance Results

In the following we will first discuss the performance of the overrelaxation algorithm on a single GPU, then we will analyze the scaling of our multi-GPU implementation.

We use the number of floating point operations per second as a measure of performance. It is based on the calculation as described in Appendix E, intended to serve as a measure to compare the algorithms to other architectures. Note that the actual number of operations that are performed on the device differs for several reasons. First, we did not include the overhead for reconstruction of the third line, in the case of SU(3). Second, we did not account for fused multiply-add operations.

Performance on Single GPUs

In Fig. 7.10 we compare the performance on GPUs from the Fermi and the Kepler generation. The GTX 580 (Fermi) and the GTX 680 (Kepler) are consumer GPUs. They suffer from a limited double precision performance. The Tesla K20 (Kepler) is a general purpose GPU, i.e. specially designed for high performance computing. The ratio of double to single precision performance is 1:3. The high-end consumer card GTX Titan, equipped

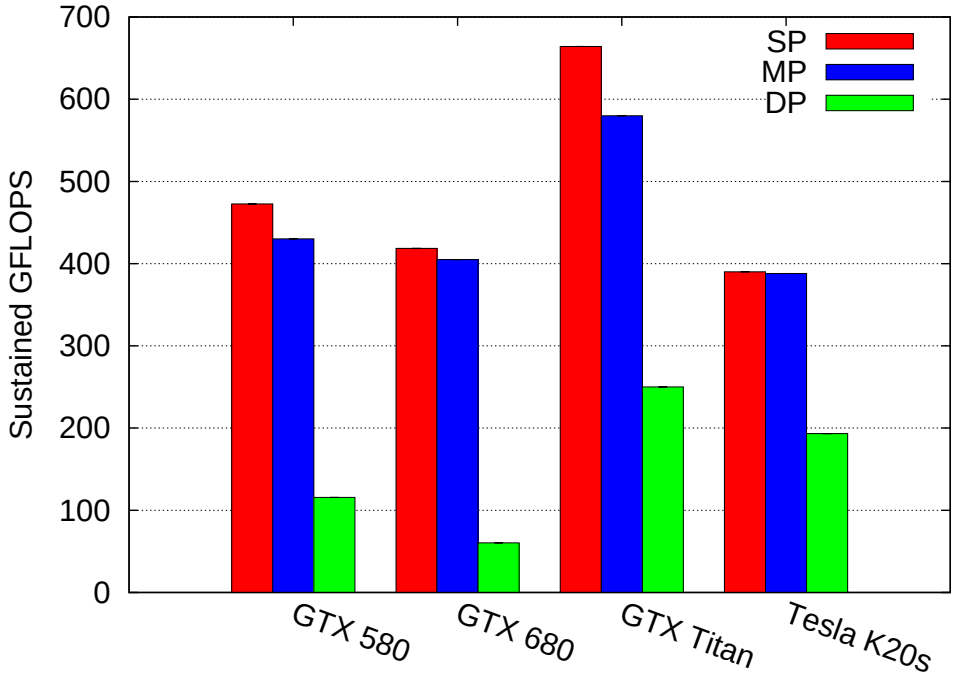

Figure 7.10.: Performance on different GPUs for a lattice of size 32^4.

with the same chip, has the full double precision power of the chip, but lacks features, like ECC memory, compared to the Tesla model. Among these GPUs, the GTX Titan performs best at around 670 GFLOPS and 250 GFLOPS in single and double precision respectively. The main difference to the other GPUs is a significantly higher memory bandwidth. Even though the Tesla K20 is equipped with the same chip, one SMX is disabled (192 CUDA cores less) and, since the Tesla GPUs are designed for continuous operation, the core clock is reduced compared to the GTX Titan. It is worth mentioning the considerable difference in double precision performance. For example, the GTX 580 (a GPU with reduced double precision performance) clearly falls behind the Tesla K20 even though the memory bandwidth is nearly same for both devices. Additionally to the increased compute power for double precision operations, the effect of the relaxed register per thread limit might play a role.

An important result is that on all GPUs the mixed precision code runs nearly at the same speed as the single precision program. This makes mixed precision an attractive option when balancing between numerical accuracy and performance.

A more detailed look on the performance of our top performer, the GTX Titan, is given in Fig. 7.11. We compare three different spatial volumes ($N_t \times 16^3$, $N_t \times 24^3$, $N_t \times 32^3$) as a function of the temporal lattice extent N_t. For each lattice size, the algorithm was tuned, as described in Section 7.4.3. Then, we took the average of 100 individual runs with 1000 overrelaxation steps. For the smallest lattices (up to 32×16^3) the problem size is not big enough to fully utilize the device and therefore the performance lags behind the maximum. For the bigger lattices the performance is more or less stable. Only on the 80×24^3 lattice a surprising dent appears. However we did not try to identify the origin of this behavior.

In Fig. 7.1 we already showed, that the GTX 580 operates at 80 % of the theoretical bandwidth in single precision. For the GTX Titan, with the significantly higher memory bandwidth, the throughput is slightly worse with 75 % of the theoretical peak.

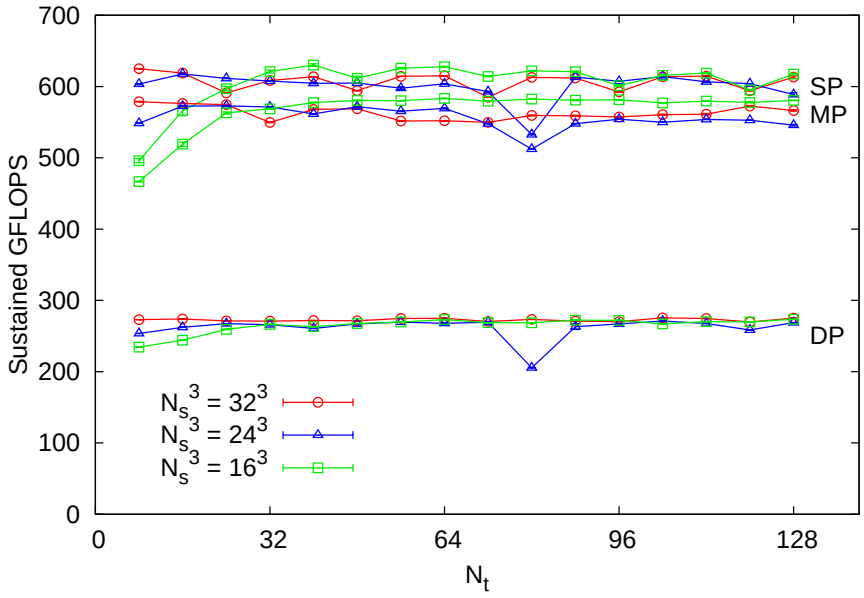

Figure 7.11.: Single GPU performance on a GTX Titan for lattices sizes $N_t \times 16^3$, $N_t \times 24^3$ and $N_t \times 32^3$ with $N_t = 8, \ldots, 128$ in single, mixed and double precision.

Performance on Multi-GPUs

At the time of writing, our multi-GPU code is not yet ported to the improved cuLGT2 design. Therefore, the results in this section are still based on the cuLGT1 code. The performance analysis was carried out on the "mephisto" cluster at the University of Graz. Each node of the cluster is equipped with two Intel Xeon X5650 ("Westmere") CPUs (6 cores) and 4 NVIDIA Tesla C2070. The nodes are connected via InfiniBand. For our study we used up to 16 GPUs (4 nodes) of the cluster.

Fig. 7.12 demonstrates linear weak scaling of our implementation. We used two different lattice sizes: 64×32^3 per GPU and 48^4 per GPU. In both cases we see perfect linear scaling. The better performance of the lattice with the bigger spatial size (48^3) is reasonable. In the multi-GPU implementation we update individual timeslices. The smaller (32^3) lattice is not big enough to fully occupy the device. To improve performance of the smaller lattices one could update several timeslices at one. However, with the multi-GPU code, we focused on very large lattices and did not implement improvement for smaller spatial volumes.

For a given lattice size, the performance, when increasing the number of GPUs, will eventually drop because the computation in a node will not be able to hide data transfer between the nodes. As depicted in Fig. 7.13, linear strong scaling is achieved on up to 16 nodes for a (total) lattice size of 256×64^3. For a smaller lattice of size 128×64^3 linearity is only achieved up to 8 GPUs. Performance drops by 15 % (DP) to 30 % (SP) when all 16 GPUs are used. For the smallest set with time extent 96 the performance is decreased further. At 12 GPUs the performance completely saturates.

Comparison to CPU Code

Finally we compare our GPU code to CPU implementations. In Ref. [29] we compared to the publicly available overrelaxation algorithm of the FermiQCD library [239]. However,

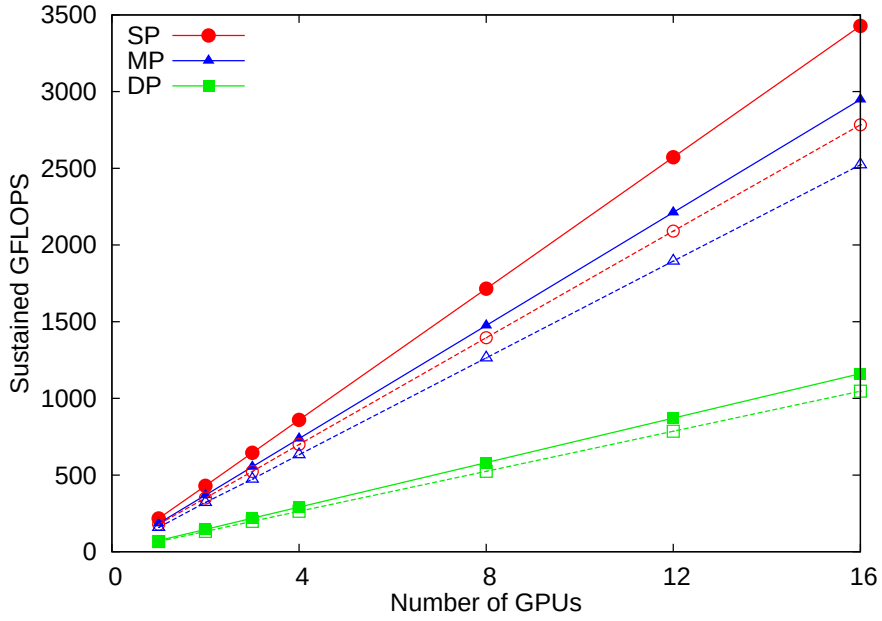

Figure 7.12.: Weak scaling on lattices of size 64×32^3 (open symbols) and 48^4 (filled symbols) per device.

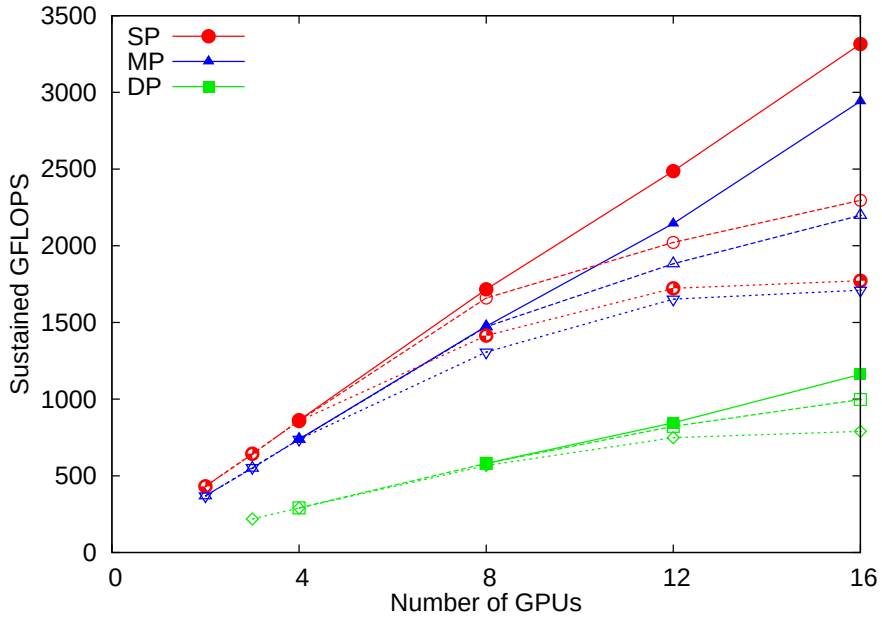

Figure 7.13.: Strong scaling on lattices of total size 256×64^3, 128×64^3 and 96×64^3 (from highest to lowest performance).

it turned out that the implementation is far from optimal, even in the single core setup. Therefore, we present here a performance measurement based on our own code which is faster by a factor of 5-10. We do not want to go in detail since the implementation does not make use of any optimizations for the hardware. For an optimized version several options would have to be considered, foremost, the link operations should explicitly make use of SIMD instructions (SSE, AVX) which would also be an important first step for an efficient implementation on Intel MIC hardware. For a recent approach on implementing flexible SIMD vector types for QCD codes we refer to Ref. [240].

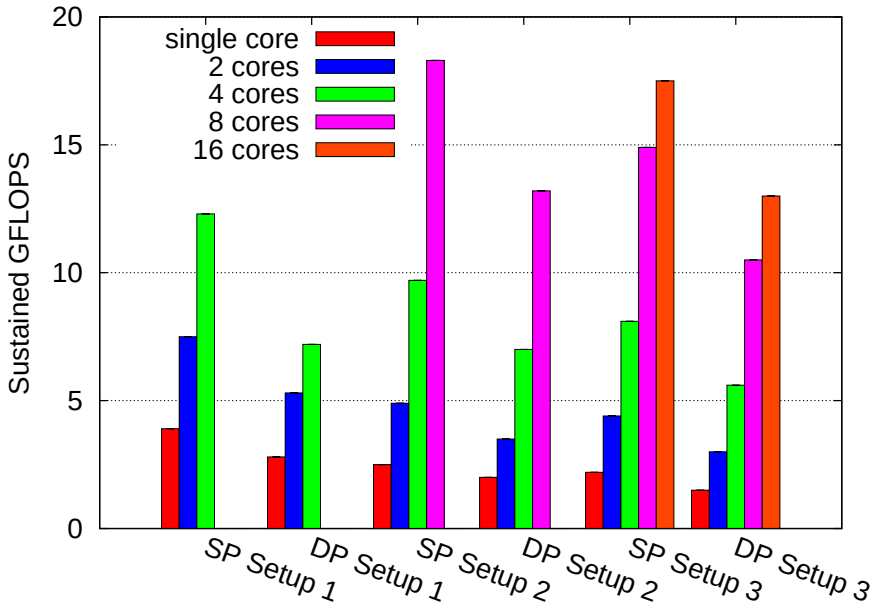

Figure 7.14.: Comparison of different CPU nodes in single and double precision: Setup 1: Intel Core i5-4460 @ 3.20GHz; Setup 2: 2 x Intel Xeon E5-2609 v2 @ 2.50GHz; Setup 3: 2 x Intel Xeon E5530 @ 2.40GHz (8 physical cores, 16 virtual cores with hyper-threading).

In Fig. 7.14 we show the performance of our CPU code on three nodes equipped with different CPUs. For the CPU implementation we used a variant of the `StandardPattern` where the lattice sites are ordered by parity, but the matrices are continuous in memory. Additionally, we did not use the 12 parameter representation of the SU(3) links, but used the full 3×3 complex matrix. We verified that, as expected, the computational overhead of the reconstruction leads to a performance decrease on the CPU.

A significant difference between the GPU and CPU performance is the ratio of double to single precision. While on the GPUs the best ratio is slightly worse than $1 : 2$ for the Tesla K20s, the double precision operates still at 60% of single precision in the worst case on CPUs (Setup 1 with 4 cores).

Setup 3 are the nodes from the CPU cluster of our institute. The GPU cluster is equipped with GTX Titan GPUs. Thus, when switching from a CPU node of the cluster to one of the GPUs we gain a factor of nearly 40 in single precision and still more than a factor of 15 in double precision. Although these numbers show the importance of the GPU implementations for our group, they have to be treated with care for two reasons. As we already stressed in the beginning, we put a lot of effort in the GPU optimizations, while the CPU implementation is basically a straight forward implementation. Secondly,

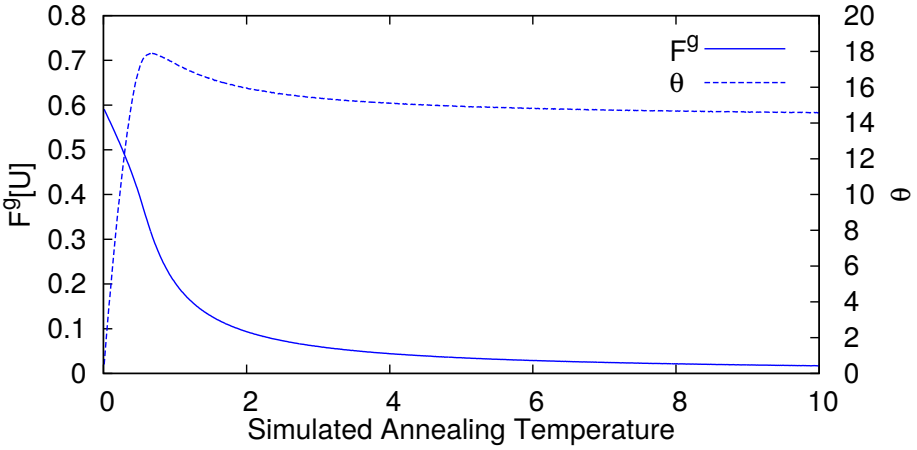

Figure 7.15.: Functional value and gauge precision as a function of the simulated annealing temperature when cooling down from 10 to 10^{-4}.

the GTX Titan GPUs, are at the point of writing, still state of the art, while the CPU cluster is not equipped with the latest hardware. For a detailed comparison of CPU and GPU implementations these issues need to be resolved. Of further interest would be to compare the energy consumption (operational costs) which is usually in favor of GPUs [241] and the acquisition costs.

7.5.3. Towards the Global Maximum

The simulated annealing algorithm, as already discussed, is used to improve the probability to find the global maximum of the functional (7.2), i.e. to locate the Gribov copy in the fundamental modular region. Defining an optimal annealing schedule is important: on the one hand, the temperature steps have to be small enough to be close to equilibrium but, on the other hand, the number of steps should be minimal in order not to waste time in unnecessary iterations. In Fig. 7.15 we investigate the evolution of $F^U[g]$ and the gauge precision θ with temperature for a hot[12] gauge field of size 32^4. We decrease the temperature linearly from 10 to 10^{-4}. We find that for temperatures $T > 4$ it is not very sensitive to the specific value. In this setup the starting temperature should be chosen around $T \in [2, 4]$. The sensitive interval may, of course, depend on the size of the lattice and the inverse gauge coupling β.

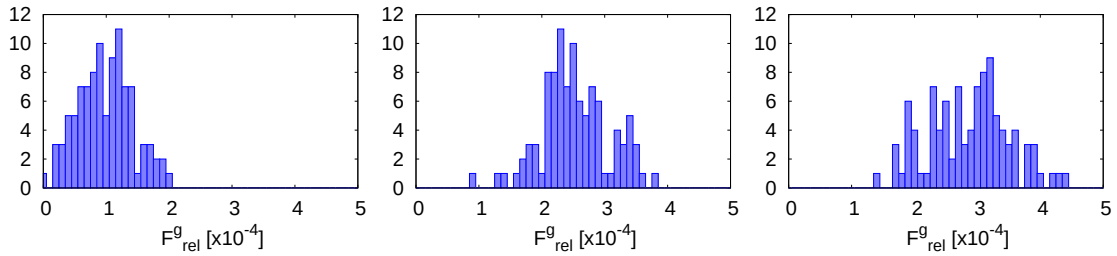

Figure 7.16.: The relative deviation from the maximal gauge functional. From left to right with 10000, 3000 and zero simulated annealing steps.

In Fig. 7.16 we demonstrate the success of the simulated annealing in finding the maximal value with higher probability. We take a 32^4 thermalized configuration at $\beta = 5.7$

[12] All links are chosen randomly in SU(3). This corresponds to an inverse coupling $\beta \to 0$.

and apply $N_{\text{sasteps}} = 10000, 3000$ and zero annealing steps prior to a final overrelaxation gauge fixing. The simulated annealing temperature is now decreased from 4 down to 10^{-4}. Overrelaxation is stopped once the precision $\theta < 10^{-10}$ is reached. For each N_{sasteps} we start gauge fixing from 100 random gauge copies, i.e. we first apply a random gauge transformation at each lattice point. In the figure we show the relative deviation F^g_{rel} from the maximal value that is found in all copies

$$F^g_{\text{rel}} = \frac{F^g_{\text{max}} - F^g}{F^g_{\text{max}}}. \tag{7.24}$$

Firstly, the distribution clearly tends towards the highest value if the number of simulated annealing steps is increased. Secondly, a high number of the costly simulated annealing steps is essential to find the highest value. Note that this result is only a snapshot of a single gauge configuration. Already for this test several hours were needed on two Tesla C2070 GPUs. A more detailed test is beyond the scope of this work.

7.6. Summary

In this chapter we discussed the technical part of gauge fixing in lattice field theory. We first stated the optimization problem and discussed several well-established algorithms for solving it. Then we turned to parallelization of these algorithms. In the main part, after a general introduction to GPU programming with CUDA, we discussed several performance optimization for our GPU implementation, including an implementation for multiple GPUs. Then, we provided a detailed performance analysis for single and double precision algorithms and a version with mixed precision at the example of the overrelaxation code for Landau gauge. The mixed precision calculates the gauge transformation in double precision while the links are stored in single precision leading to a performance boost over double precision at a better numerical accuracy compared to single precision. We achieved a performance of about 670 GFLOPS on a GTX Titan, the best-performing GPU of our study. We also critically discussed the speedup of a factor of 15 (DP) or 40 (SP) compared to a full node of the CPU cluster of our institute. Finally we showed how the simulated annealing algorithm improves the probability of finding the global maximum of the gauge functional.

8. Conclusion and Outlook

For our study of strongly coupled gauge theories in Coulomb gauge we employed the lattice approach, a numerical technique based on the discretization of space-time on a hypercubic lattice. Apart from this numerical approach, Yang–Mills theory and QCD in Coulomb gauge were also studied by means of analytic methods, e.g. the Hamiltonian approach [17–23]. Both the lattice and the Hamiltonian approach find vacuum solutions of the gluon and the ghost propagator in agreement with the confinement scenario developed by Gribov and Zwanziger. While the solutions agree quantitatively very well for the gluon propagator [44], the infrared exponents of the ghost form factor is off by a factor of two [108]. This result is puzzling since the infrared exponents of the gluon propagator are coupled by a sum rule which follows by the well-motivated assumption that the ghost-gluon vertex is bare [125]. However the lattice results violate the sum rule.

A possible source for this disagreements could be the Gribov ambiguity: the choice of gauge does not uniquely identify a single gauge field configuration and one has to further restrict the path integral to resolve the over-counting of gauge equivalent fields. This can be achieved by restricting the field configurations to the first Gribov horizon and even further to the fundamental modular region. While for gauge-independent observables the specific choice to resolve the Gribov problem is not important, gauge-dependent quantities might well depend on the particular choice. In Chapter 3 we review the well-established way, based on finding the global maximum of the gauge functional, the so-called best-copy approach, and compare it to a novel idea put forward in [129] and already successfully applied in Landau gauge [135]. This new approach chooses the Gribov copy where the smallest eigenvalue of the Faddeev–Popov operator is closest to zero, the so-called lowest-copy approach[1]. The best-copy can be thought of the best approximation of the fundamental modular region, while the lowest-copy is closest to the first Gribov horizon. The new choice is motivated by the argument of the Gribov–Zwanziger scenario of confinement, which implies that in the continuum limit the relevant configurations are the ones on the first Gribov horizon for entropic reasons. Within the limitations given by a reasonable computer-time and the lack of an algorithm to drive the gauge fixing towards a small eigenvalue, we could not find a lower bound for the smallest eigenvalue. If the smallest eigenvalue should be unbounded it would be surprising since one would expect a finite distance to the Gribov horizon on a finite lattice. On the ghost propagator which is basically the inverse of the Faddeev–Popov operator and the Coulomb potential where the operator enters twice, the smallness of the lowest eigenvalue has a significant effect. This effect is to some extent positive for the ghost propagator since it brings the infrared exponent close to the one found in continuum studies, however this value is actually overshot and a saturation is not yet observed. Otherwise the Coulomb potential calculated from the Coulomb kernel (2.160) does not allow a physical interpretation at all. Its value, over the whole momentum range, is increased by orders of magnitude. A different definition of the Coulomb potential, based on the correlation of temporal links, (2.173) does not see this dramatic effect. In conclusion, the new gauge fixing scheme does not solve the tension

[1] We use the name "best-copy" because it is common in the literature, however we don't want to imply that the copy with the highest functional value is better than other choices.

between the continuum and the lattice results. Further investigations in this direction would have to focus on a refined gauge fixing scheme, e.g. by applying a condition on the two smallest eigenvalues and the discretization effects related to a near-singular Faddeev–Popov operator. Finally it would be interesting to explicitly calculate the ghost-gluon vertex in Coulomb gauge on the lattice to settle discussions about the validity of the sum rule.

In recent years continuum techniques were extended to study Coulomb gauge correlation functions at finite temperature [20, 155–157], while lattice studies were not available in great detail. In Chapter 4 we fill this gap in search for a manifestation of the deconfinement phase transition in Coulomb gauge correlators. A rather interesting question was how the infrared exponent of the ghost form factor would be above the critical temperature, since the lattice result (in the best-copy approach) at $T = 0$ corresponds to the one found above T_c in the continuum calculations [20]. The results of our lattice study allow a very short summary: around the phase transition, at least up to $T = 1.5T_c$, the propagators do not show any difference to zero temperature. Furthermore the Coulomb string tension, which is an upper bound for the physical Wilson string tension, is further increased, while naively one would expect this string tension to vanish in the deconfined phase as the Wilsonian one does.

The physical string tension, which can be calculated from space-time Wilson loops on the lattice, is an order parameter for the deconfinement phase transition. It is finite in the confined phase and vanishes in the deconfined phase. Closely related is the spatial string tension which measures the correlation of space-space Wilson loops. The spatial string tension, in contrast to the physical string tension, does not vanish at T_c but is known to rise with temperature. This led us to the question if the Coulomb string tension is tied to the spatial string tension instead of the physical one. To explore this question we employed the center vortex picture of confinement in Chapter 5. First we verified that the Gribov–Zwanziger scenario in and the center vortex picture in Coulomb gauge are compatible with each other. On center vortex removal the ghost form factor becomes flat in the infrared and the Coulomb potential acquires a string tension compatible with zero. In a next step we introduced a technique which we called spatial vortex removal. Instead of applying the usual procedure of center gauge fixing, center projection and vortex removal to all four space-time dimensions, we applied the procedure only to spatial links. By this procedure the physical (temporal) Wilson string tension stays intact while the spatial string tension drops to zero. On configuration prepared in this way the Coulomb gauge propagators loose their confining signal as well, which confirms our assumption that the spatial string tension is the relevant one for the Coulomb gauge correlation functions and explains why they do not behave as expected in the deconfined phase.

After these studies, which were carried out for pure SU(2) Yang–Mills theory, we included quarks in our calculations. We chose a theory, which might be a candidate for Walking Technicolor, a possible extension of the Standard Model to improve on the theoretical puzzles associated with the Higgs mechanism. This study was based on numerically expensive lattice configurations, generously provided by the authors of Refs. [59–62]. In Chapter 6, we analyzed the gluonic Coulomb gauge quantities and discussed their lattice artifacts. Within the limits given by the parameters of the available configurations (fixed coupling, mainly small lattice volumes) we may conclude that the theory is conformal or quasi-conformal, the latter would be the required property for a walking technicolor theory. We also discussed the possibility of a glueball representing the Higgs boson of the Standard Model. A much larger parameter set and larger lattices would be needed to allow a stronger conclusion. Due to several technical problems related to the Wilson Dirac

operator, which was used to generate these configurations, see Appendix D, a reliable result for the quark propagator could not be achieved within this work. The analysis of the quark propagator would be of great interest, since it would give access to the mass anomalous dimension, which is an important input for phenomenology in walking technicolor models. For further studies it would be interesting to analyze a larger parameter set of this technicolor candidate. Especially the use of improved discretizations for the Dirac operator will be beneficial.

To approach continuum physics from lattice simulations it is desirable to increase the simulated volume and at the same time reduce the lattice spacing, both changes are leading to an increasing number of lattice points and thus a more demanding numerical work. In recent years GPUs have proven beneficial for many numerically expensive applications because of their high degree of parallelism, their high memory bandwidth and their energy efficiency. In Chapter 7 we explain how lattice gauge fixing algorithms can be implemented on GPUs with CUDA. We emphasize on the important points that have to be taken care of when porting a CPU application to an efficient GPU application. Our implementation achieves an efficiency of more than 80% of the theoretical peak bandwidth ob a GeForce GTX 580. A single GTX Titan GPU beats a full node of our CPU cluster by a factor of 15 in double precision and a factor of 40 in single precision[2].

[2]This factors have to be taken with care, since we did not put as much effort in the CPU implementation as we did for the GPU code.

A. Units

A.1. Natural Units

In this work we used the natural units defined by

$$\hbar = c = k_B = 1, \tag{A.1}$$

where $\hbar$ is Plank's constant divided by 2π, c is the velocity of light and k_B Boltzmann's constant. In these units the following relation of quantities holds

$$[\text{energy}] = [\text{temperature}] = [\text{momentum}] = [\text{length}^{-1}] = [\text{time}^{-1}]. \tag{A.2}$$

The unit of energy (and momentum) or the inverse lattice spacing is typically given in MeV or 1/fm. From (A.1) and the physical values of $\hbar$ and c

$$\hbar \approx 6.582 \times 10^{-16}\text{eVs} \tag{A.3}$$

$$c \approx 2.998 \times 10^{8}\text{m/s} \tag{A.4}$$

we find the relation

$$\frac{1}{\text{fm}} \approx 197.327\text{MeV} \tag{A.5}$$

between fm^{-1} and MeV.

A.2. Lattice Units

With n_μ we denote the lattice indices with $0 < n_\mu < L_\mu$. The distance from the lattice origin in physical units is defined as $x_\mu = a n_\mu$, a is the lattice spacing in units of fm (or 1/GeV).
The discrete lattice momenta for periodic boundary conditions are given by

$$k_\mu = \frac{2\pi}{a L_\mu} n_\mu. \tag{A.6}$$

For antiperiodic boundary conditions (in time direction) they are

$$k_0 = \frac{2\pi}{a L_0}\left(n_0 + \frac{1}{2}\right). \tag{A.7}$$

A.2.1. Tree-level Momentum Corrections

For the gluon and ghost propagator as well as for the Coulomb potential we use the "kinematic momenta", see e.g. Ref. [207],

$$p_\mu = p(k_\mu) = \frac{2}{a}\sin(a k_\mu/2) = \frac{2}{a}\sin\left(\frac{\pi n_\mu}{L_\mu}\right) \tag{A.8}$$

For the Wilson Dirac quark propagator it is convenient to also introduce the momenta [242]

$$\tilde{p}_\mu = \tilde{p}(k_\mu) = \frac{1}{a}\sin(ak_\mu). \tag{A.9}$$

$\hat{k}_\mu = ak_\mu$ and $\hat{p}_\mu = ap_\mu$ are dimensionless momenta.

A.2.2. Momentum Cuts

Rotational invariance of space-time is lost by introducing a hypercubic lattice. Therefore, the propagators in momentum space suffer from such discretization effects in addition to the effects of the finite volume. The authors of Ref. [207] proposed two restrictions on the allowed lattice momenta in the context of the Landau gauge gluon propagator. Later, these cuts were also applied to Coulomb gauge [44, 101, 122]. The first one is the so-called cylinder cut. The allowed lattice momenta are restricted to a cylinder around the lattice diagonal. Usually we use a cylinder with radius of one lattice spacing

$$\boldsymbol{k} = \begin{pmatrix} k \pm 1 \\ k \pm 1 \\ k \pm 1 \end{pmatrix}. \tag{A.10}$$

Additionally, to address finite volume effects, they proposed to restrict the momenta to a cone around the diagonal. The cone cut removes the smallest off-diagonal momenta.

B. Residual gauge fixing

The Coulomb gauge condition does not fix the gauge completely. We are still free to apply space-independent gauge transformations $g(t)$. A possible choice to fix this residual gauge freedom in the continuum is

$$\int \mathrm{d}^3x\ \partial_\mu A_\mu(t,\boldsymbol{x}) = \partial_0 \int \mathrm{d}^3x\ A_0(t,\boldsymbol{x}) = 0. \tag{B.1}$$

By integrating over the 3-dimensional space the gauge condition is space-independent. The lattice analog of (B.1) is the so-called *integrated Polyakov gauge* [44]

$$u(t) = \frac{1}{N_s^3}\sum_{\boldsymbol{x}} U_0(t,\boldsymbol{x}) \to \text{const.} \tag{B.2}$$

B.1. Integrated Polyakov gauge

To implement the integrated Polyakov gauge we need to find the gauge transformations $g(t)$ fulfilling the gauge condition (B.2). Since the sum over the SU(N) links is not itself an SU(N) element, we project $u(t)$ to its closest SU(N) element $\hat{u}(t)$ such that

$$\mathrm{Re}\,\mathrm{tr}\left[\hat{u}u^{-1}\right] = \max. \quad \text{with} \quad \hat{u} \in \mathrm{SU}(N). \tag{B.3}$$

For SU(2) $\hat{u}(t)$ is easily found by normalization of $u(t)$

$$\hat{u}(t) = \frac{u(t)}{\sqrt{\det u(t)}}, \tag{B.4}$$

since the sum of SU(2) is proportional to an SU(2) element. For SU(3) we seek $\hat{u}(t)$ in each SU(2) subgroup iteratively by the Cabibbo-Marinari technique [58]. Now, define the Polyakov loop

$$P = \prod_t \hat{u}(t) \tag{B.5}$$

of the integrated links $u(t)$. By construction $\mathrm{tr}P$ is gauge invariant for periodic boundary conditions. If we choose the gauge transformation $g(t)$ such that

$$g(t)\hat{u}(t)g^\dagger(t+1) = P^{\frac{1}{N_t}} \tag{B.6}$$

the gauge condition (B.2) is satisfied. $P^{\frac{1}{N_t}}$ is the n-th matrix root of P which can be calculated, e.g., by the Schur algorithm [243]. Without loss of generality, we choose $g(0) = \mathbb{1}$. Then $g(t)$ is found via the recursion

$$g^\dagger(t+1) = \hat{u}^\dagger(t)g^\dagger(t). \tag{B.7}$$

C. Maximal Center Gauge in SU(2)

Direct maximal center gauge fixing is achieved by maximizing

$$F^U[g] = \sum_{x,\mu} \left| \mathrm{tr}\left[U^g_\mu(x) \right] \right|^2 \tag{C.1}$$

The maximum of the functional corresponds to the ensemble where the links are closest to center elements[1]. Following [166], we rewrite this expression as a sum of local functionals at site x.

$$F^U[g] = \sum_x F_x[g(x)] \tag{C.2}$$

with

$$F_x[g(x)] = \frac{1}{4} \sum_\mu \left\{ \left| \mathrm{tr}\Big[g(x) U_\mu(x) \Big] \right|^2 + \left| \mathrm{tr}\Big[U_\mu(x-\hat{\mu}) g^\dagger(x) \Big] \right|^2 \right\}. \tag{C.3}$$

We then optimize (C.3) at each site. We parameterize the SU(2) gauge transformation by

$$g = g_0 \mathbb{1} + \mathrm{i} \boldsymbol{g} \boldsymbol{\sigma} \tag{C.4}$$

with the Pauli matrices σ_a. The optimization problem has to be solved with respect to the 4 parameters g_a with the constraint that g is unitary, i.e. $\sum_{a=0}^3 g_a^2 = 1$. F_x takes the form

$$F_x(g) = \sum_{a,b} g_a M_{ab} g_b, \tag{C.5}$$

where M is a 4×4 matrices build from the 8 links $U_\mu(x)$ and $U_\mu(x-\hat{\mu})$. The norm constraint $\sum_a g_a^2 = 1$ can be implemented by a Lagrange multiplier λ

$$F^c_x(g) = F_x + \frac{1}{2} \lambda \left[1 - \sum_a g_a^2 \right]. \tag{C.6}$$

This leads to the coupled system of equations

$$Mg = \lambda g \tag{C.7}$$

$$g \cdot g = 1 \tag{C.8}$$

The first line is an eigenvalue problem for the matrix M, the second line describes the normalization of the eigenvectors. We solve the eigenvalue problem for the dominant eigenvalue numerically with the power iteration method [244]. The (normalized) resulting eigenvector (for the largest eigenvalue) yields the coefficients for the local optimization. Convergence can be improved by the standard overrelaxation prescription as described for Coulomb gauge fixing in Chapter 7.

[1] Taking the complex norm is only necessary for the SU(3) case. For SU(2) the trace of a group element is already real-valued.

D. Remarks on the Quark Sector of Minimal Walking Technicolor in Coulomb gauge

Whereas the calculation of the Coulomb gauge propagators in the gluon sector of minimal walking technicolor are straight forward with the techniques developed in earlier works for pure Yang–Mills theory and QCD, the calculation of the quark propagator is more challenging. Earlier studies of the quark propagator in both Landau, e.g. [242], and Coulomb gauge [122, 123] usually used an improved quark action since the discretization artifacts of the Wilson Dirac propagator are known to be large. Since our studies rely on configurations provided by [59–62]which where produced using the Wilson Dirac operator for the sea quarks, we will also use the same discretization for the valence quarks. The Wilson Dirac operator has also the advantage that it is computationally less demanding compared to other discretizations. In general using a different discretization would be an option, however additional sources for systematic errors might be introduced by such an approach.

During our investigation of the quark propagator we were faced with several numerical problems. Each of them would require a proper systematic analysis on its own. Such a study could not be completed in the available time for this work. Therefore we cannot present any conclusive results here but will give a short overview of the challenges we were faced with, in the hope that they might be useful to someone.

The lattice quark propagator in Coulomb gauge was first studied in [122]. We will summarize their notation and the most important results of their study. The free continuum Dirac operator in momentum space is given by

$$S^{(0)}(p) = \left[\mathrm{i}\not{\boldsymbol{p}} + \mathrm{i}\not{p}_0 + m\right]^{-1} = -\frac{\mathrm{i}\gamma_i p_i + \mathrm{i}\gamma_0 p_0 - m}{\boldsymbol{p}^2 + p_0^2 + m^2}, \tag{D.1}$$

where we split the $\boldsymbol{p}$ and p_0 dependence. For the Euclidean covariant Landau gauge quark propagator two dressing functions, usually denoted as A and B or Z and M [242], are sufficient to parameterize the interacting propagator

$$S^{-1}_{\text{Landau}}(p) = \mathrm{i}\not{p}A(p) + B(p) = \frac{1}{Z(p)}\left(\mathrm{i}\not{p} + M(p)\right). \tag{D.2}$$

Since Coulomb gauge breaks Euclidean covariance, additional dressing functions might be necessary to account for all combinations of γ matrices with the momenta p_μ. Therefore, the authors of Ref. [122] proposed the following parameterization for the interacting Coulomb gauge propagator

$$S^{-1}(p) = \mathrm{i}\not{\boldsymbol{p}}A_s(p_0, \boldsymbol{p}) + \mathrm{i}\not{p}_0 A_t(p_0, \boldsymbol{p}) + \mathrm{i}p_i\gamma_i p_0\gamma_4 A_d(p_0, \boldsymbol{p}) + B(p_0, \boldsymbol{p}). \tag{D.3}$$

Although we do not expect that the mixed component will contribute, since all previous studies of the quark propagator in Coulomb gauge agree that the mixed component $A_d(p_0, \boldsymbol{p})$ vanishes [122, 123], we will still incorporate the dressing function in our parameterization.

In Ref. [122] it was shown that the dressing functions are energy-independent for the Asqtad improved staggered fermions [245] and Kogut–Susskind fermions [246]. This observation allowed the authors to average the p_0 dependency and introduce the energy-independent static dressing functions $A_s(\boldsymbol{p})$, $A_t(\boldsymbol{p})$ and $B(\boldsymbol{p})$. They introduce the static quark propagator as

$$S^{-1}(\boldsymbol{p}) = \mathrm{i}\not{\boldsymbol{p}} a A_s(\boldsymbol{p}) + B(p). \tag{D.4}$$

Additionally, the energy-independence allows for a simple parameterization of the renormalized propagator

$$S_\zeta = \frac{Z_\zeta(\boldsymbol{p})}{\mathrm{i}a\not{\boldsymbol{p}} + \mathrm{i}a\not{p}_0\alpha(\boldsymbol{p}) + M(\boldsymbol{p})}, \tag{D.5}$$

where

$$Z_\zeta(\boldsymbol{p}) = \frac{1}{A_s(\boldsymbol{p})} \tag{D.6}$$

is the renormalization function,

$$M(\boldsymbol{p}) = \frac{B(\boldsymbol{p})}{A_s(\boldsymbol{p})} \tag{D.7}$$

the mass function and

$$\alpha(\boldsymbol{p}) = \frac{A_t(\boldsymbol{p})}{A_s(\boldsymbol{p})} \tag{D.8}$$

a form factor for the energy. For the derivation of the functions we refer to the appendix of the original work [122]. The mass function is expected to reach a finite value in the infrared which would be the constituent quark mass. We will see later that these definitions cannot be applied directly to Wilson quarks due to an additional lattice artifact, see Section D.1. The parameterization (D.4) for the renormalized propagator allows a pleasing physical interpretation proposed in [122].

D.1. The Wilson Dirac Operator

In Section 2.4 we already introduced the free Wilson Dirac operator in momentum space

$$D(p) = m + \frac{\mathrm{i}}{a}\sum_{\mu=0}^{3}\gamma_\mu \sin(ak_\mu) + \frac{1}{a}\sum_{\mu=0}^{3}(1-\cos(ak_\mu)), \tag{D.9}$$

where $k_i = \frac{2\pi}{aL_i}n_i$ and $k_0 = \frac{2\pi}{aL_i}\left(n_0 + \frac{1}{2}\right)$ are the momenta in the first Brillouin zone. Compared to a naive discretization of the operator (2.78), the extra term $\frac{1}{a}\sum_{\mu=0}^{3}(1-\cos(ap_\mu))$ was necessary to solve the doubling problem.

With the following abbreviations for the momenta, see also Appendix A,

$$\tilde{p}_\mu = \frac{1}{a}\sin(ak_\mu) \tag{D.10}$$

$$p_\mu = \frac{2}{a}\sin(ak_\mu/2), \tag{D.11}$$

we can rewrite the free Wilson Dirac operator to take the well-known form of the continuum propagator plus the additional Wilson term which vanishes in the limit $a \to 0$

$$D(p) = m + \frac{\mathrm{i}}{a}\sum_{\mu=0}^{3}\gamma_\mu\tilde{p}_\mu + \frac{a}{4}\sum_{\mu=0}^{3}p_\mu^2. \tag{D.12}$$

D.2. Artifacts due to the Wilson Term

D.2.1. Momentum Definition

For earlier Coulomb gauge studies of the quark propagator with staggered [122] and overlap fermions [123] the kinematic lattice momentum was defined by identifying the term with the Brillouin momenta k_μ which is proportional to the γ structure with its continuum counterpart as proposed in [247]. For this approach the inverse tree-level propagator is written in the form

$$S^{(0)}(k) = \mathrm{i}\left(\sum_\mu C_\mu(k)\gamma_\mu\right) + B(k)\mathbb{1}. \tag{D.13}$$

With the free continuum Dirac operator (D.1) we can then identify the lattice momenta to be

$$p_\mu(k) = C_\mu(k). \tag{D.14}$$

The coefficients $C_\mu(k)$ can be calculated either analytically or numerically by calculating the quark propagator on a *cold* lattice, i.e. in the free case where the interactions are turned of, $A_\mu = 0$. The latter may serve as a numerical check of the implementation.

With the Wilson term, however, such a definition is no longer possible, since the mass term, proportional to the identity, depends on the momentum k_μ, too. The authors of the Landau gauge study [206] did not comment on this issue. They just used the p_μ definition of (D.10) which would be appropriate for the gluon propagator.

Using the unimproved momentum $\tilde{p}_\mu$ (D.11) would pose another problem. If $\tilde{p}_\mu$ is used over the whole Brillouin zone, the momentum would result in a unphysical non-monotonous function, since the sine would be evaluated over a full period.

Here we propose an alternative technique for the momentum definition. The idea is to find a spatial momentum which reproduces the correct lattice quark dispersion relation at tree-level up to order k^2

$$p(k)^2 = \left[\omega_m^2(k) - \omega_m^2(0)\right]\left[\frac{1}{2}\left.\frac{\partial^2\omega_m^2(k)}{\partial k^2}\right|_{k=0}\right]^{-1}. \tag{D.15}$$

The details of the derivation are summarized in the next section.

Derivation of the Improved Momentum Definition for the Wilson Quark Propagator

We will shortly repeat how the dispersion relation is obtained from the quark propagator in the continuum. Then, we will apply the same technique to the lattice Wilson Dirac quark propagator. The tree-level Euclidean (inverse) quark propagator in the continuum is given by

$$S_0^{-1}(p) = \mathrm{i}\not{p}_0 + \mathrm{i}\not{\boldsymbol{p}} + m. \tag{D.16}$$

Inverting (D.16) yields the tree-level quark propagator

$$S_0(p) = \frac{-\mathrm{i}\not{p}_0 - \mathrm{i}\not{\boldsymbol{p}} + m}{p_0^2 + \boldsymbol{p}^2 + m^2}. \tag{D.17}$$

We integrate the quark propagator in p_0 to obtain the dispersion relation of a free quark

$$\int_{-\infty}^{\infty}\frac{dp_0}{2\pi}S_0(\boldsymbol{p}, p_0) = \frac{-\mathrm{i}\not{\boldsymbol{p}} + m}{2\sqrt{\boldsymbol{p}^2 + m^2}} \equiv \frac{-\mathrm{i}\not{\boldsymbol{p}} + m}{2\omega_F}. \tag{D.18}$$

Following the remark in Eq. 13 of [122] we may get the dispersion directly by integrating the *square* of the propagator. Multiplying the propagator (D.17) by

$$S_0^\dagger = \frac{+\mathrm{i}\not{p}_0 + \mathrm{i}\not{\boldsymbol{p}} + m}{p_0^2 + \boldsymbol{p}^2 + m^2} \tag{D.19}$$

yields

$$|S_0(p)|^2 = S_0^\dagger(p) S_0(p) = \frac{1}{p_0^2 + \boldsymbol{p}^2 + m^2} \tag{D.20}$$

using $\gamma_\mu^\dagger = \gamma_\mu$ for the Euclidean gamma matrices. After integration we get directly

$$\omega_F^{-1} = \int_{-\infty}^{\infty} \frac{dp_0}{2\pi} |S(p)|^2 = (\boldsymbol{p}^2 + m^2)^{-\frac{1}{2}}. \tag{D.21}$$

Our proposal is to apply this procedure to the Wilson Dirac operator to obtain a momentum $p = \sqrt{\omega_F^2(k) - m^2}$ that yields exactly the tree-level dispersion relation. The inverse Wilson Dirac quark propagator is given by

$$S_0^{-1}(k) = \frac{\mathrm{i}}{a} \sum_\mu \gamma_\mu \sin(k_\mu a) + m + \frac{1}{a} \sum_\mu (1 - \cos(k_\mu a)) \,. \tag{D.22}$$

In the following we will use $a = 1$. Along the lines of the continuum calculation we get

$$S_0^{\mathrm{lat}}(k) = \frac{-\mathrm{i}\gamma_0 \sin(k_0) - \mathrm{i} \sum_i \gamma_i \sin(k_i) + m + \sum_\mu (1 - \cos(k_\mu))}{\sin^2(k_0) + \sum_i \sin^2(k_i) + \left[m + \sum_\mu (1 - \cos(k_\mu)) \right]^2}. \tag{D.23}$$

Then,

$$\left| S_0^{\mathrm{lat}}(k) \right|^2 = \frac{1}{\sin^2(k_0) + \sum_i \sin^2(k_i) + \left[m + \sum_\mu (1 - \cos(k_\mu)) \right]^2}. \tag{D.24}$$

By replacing the integral in (D.21) by a sum over the discrete lattice momenta

$$\int \frac{dp_0}{2\pi} \to \frac{1}{2\pi} \frac{2\pi}{N_t} \sum_{k_0} \tag{D.25}$$

we get

$$w_F^{-1}(\boldsymbol{p}^2) = \frac{1}{\sqrt{\boldsymbol{p}^2 + m^2}} \equiv \frac{2}{N_t} \sum_{k_0} \left| S_0^{\mathrm{lat}}(k) \right|^2. \tag{D.26}$$

Thus, we find for the momentum

$$|\boldsymbol{p}(\boldsymbol{k})| = \sqrt{\frac{1}{\left(\frac{2}{N_t} \sum_{k_0} \left| S_0^{\mathrm{lat}}(k) \right|^2 \right)^2} - m^2}. \tag{D.27}$$

Note, that the momentum definition is now a function of the mass. For $m = 0$, this definition provides a useful momentum

$$|\boldsymbol{p}|^{-1} = \frac{2}{N_t} \sum_{k_0} \left| S_0^{\mathrm{lat}}(k) \right|^2 \tag{D.28}$$

$$= \frac{2}{N_t} \sum_{n_0 = -L_t/2+1}^{L_t/2} \frac{1}{\sin^2(k_0) + \sum_i \sin^2(k_i) + \left[\sum_\mu (1 - \cos(k_\mu)) \right]^2}. \tag{D.29}$$

However for $m > 0$ the formula (D.27) does not work as it stands. In the integrated propagator the pole is shifted from m to $\frac{1}{2}m^2 + m$, i.e. $\omega_F(\boldsymbol{k} = 0) = \frac{1}{2}m^2 + m$ and thus $\boldsymbol{p}(\boldsymbol{k} = 0) \neq 0$. Additionally, the slope of the momentum from (D.27) is incorrect $\lim_{k\to 0} \frac{\mathrm{d}p}{\mathrm{d}k} \neq 1$ and thus does not provide the correct continuum limit.

We propose to fix the low momentum behavior by expanding $\omega_m^2(k)$ around $k = 0$ up to second order for diagonal momenta $\boldsymbol{k} = (k, k, k)$. Then the momentum can be defined from the expansion with the correct limit for $k \to 0$. The expansion is

$$\omega_m^2(k) = \left[\frac{N_t}{2} \frac{1}{\sum_{k_0} \frac{1}{\sin^2(k_0) + 3\sin^2(k) + \left[m + 2\sin^2\left(\frac{k_0}{2}\right) + 6\sin^2\left(\frac{k}{2}\right)\right]^2}} \right]^2 \tag{D.30}$$

$$= \omega_m^2(0) + \frac{1}{2} \left.\frac{\partial^2 \omega_m^2(k)}{\partial k^2}\right|_{k=0} k^2 + \mathcal{O}(k^4). \tag{D.31}$$

Then, we define

$$\omega_m^2(k) - \omega_m^2(0) =: \frac{1}{2} \left.\frac{\partial^2 \omega_m^2(k)}{\partial k^2}\right|_{k=0} p(k)^2. \tag{D.32}$$

The coefficients are

$$\omega_m^2(0) = \left[\frac{N_t}{2 \sum_{k_0} \frac{1}{S_m(k_0)}} \right]^2, \tag{D.33}$$

$$\left.\frac{\partial^2 \omega_m^2(k)}{\partial k^2}\right|_{k=0} = \frac{N_t^2 \sum_{k_0} \frac{6 + 6\left(m + 2\sin^2\left(\frac{k_0}{2}\right)\right)}{S_m^2(k_0)}}{2\left[\sum_{k_0} \frac{1}{S_m(k_0)}\right]^3} \tag{D.34}$$

where we used the abbreviation

$$S_m(k_0) = \sin^2(k_0) + \left[m + 2\sin^2\left(\frac{k_0}{2}\right)\right]^2 \tag{D.35}$$

$$= m^2 + 4(m+1)\sin^2\left(\frac{k_0}{2}\right). \tag{D.36}$$

The momentum defined in this way is based on a derivation for diagonal momenta $\boldsymbol{k} = (k, k, k)$. Since we always work with a cylinder cut on the momenta, see Section A.2.2, i.e. with momenta close to or at the diagonal, the restriction to diagonal momenta does not introduce a major problem.

D.2.2. Energy-dependency of the Mass Function and Renormalization

The leading lattice artifact for the dressing function B (in Coulomb and Landau gauge) is the Wilson term. This can be read off from the tree-level Wilson Dirac operator in momentum space (D.12). The authors of Ref. [206] proposed to correct the dressing function by

$$B = \frac{B_{\mathrm{lat}}}{B_{\mathrm{lat}}^0}, \tag{D.37}$$

where B_{lat} is the dressing function as obtained from the simulation and B_{lat}^0 is the tree-level dressing function for the Wilson Dirac quark

$$B_{\mathrm{lat}}^0(k_0, \boldsymbol{k}) = m + \frac{a}{4} \sum_{\mu=0}^{3} p_\mu^2 = m + \frac{a}{4} |\boldsymbol{p}|^2 + \frac{a}{4} p_0^2. \tag{D.38}$$

Thus the corrected dressing function obeys $B^0(k_0, \boldsymbol{k}) = 1$. Since $A_s^0(k_0, \boldsymbol{k}) = 0$ by definition, the mass function at tree-level is normalized to unity, as well,

$$M^0(k_0, \boldsymbol{k}) = \frac{B^0(k_0, \boldsymbol{k})}{A_s^0(k_0, \boldsymbol{k})} = 1. \tag{D.39}$$

To restore the meaning of M we have to introduce an additional renormalization to the B function which is not present in the continuum, such that

$$B(\mu) = m. \tag{D.40}$$

In Refs. [122, 123] the authors showed that the dressing function $B(p_0, \boldsymbol{p})$ for staggered and overlap quarks is independent of the energy p_0. With the Wilson term, however, already at tree-level a dependency on the energy is introduced in (D.38). With the help of (D.37) this effect can be canceled exactly only at tree-level. To cancel the energy dependency exactly in the interacting case, the ratio between different energies k_0^1, k_0^2

$$\frac{B_{\text{lat}}(k_0^1, \boldsymbol{k})}{B_{\text{lat}}(k_0^2, \boldsymbol{k})} \tag{D.41}$$

would have to match exactly the ratios at tree-level. However, this is not the case, as

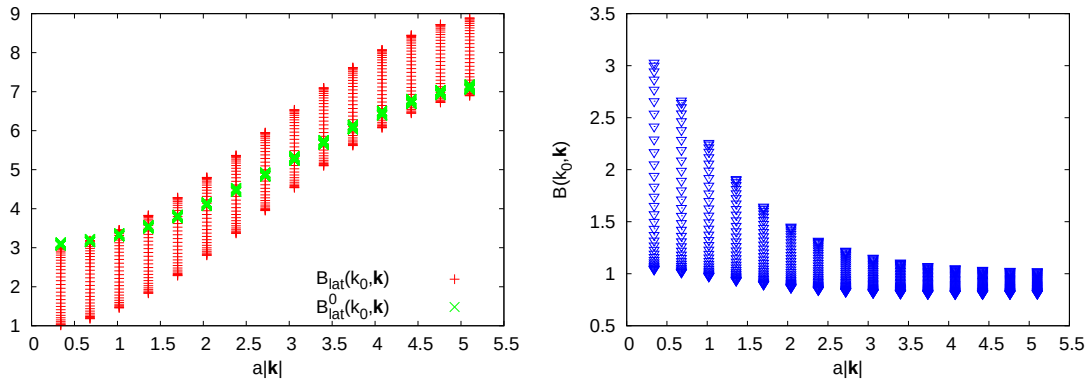

Figure D.1.: Bare lattice dressing function in the interacting case B_{lat}, at tree-level B_{lat}^0 (l.h.s.) and after tree-level correction according to (D.37) (r.h.s).

can be seen on the l.h.s. of Fig. D.1. Therefore the corrected B dressing function still has an artificial energy dependency, see r.h.s. of Fig. D.1. From the observation in the earlier Coulomb gauge studies [122, 123], we assume that the energy dependency in the interacting case is only an artifact of the Wilson term and thus this ambiguity has to be resolved to define the static dressing function, e.g. by taking the k_0 average

$$B(\boldsymbol{k}) = \frac{1}{N_t} \sum_{k_0} B(k_0, \boldsymbol{k}) \tag{D.42}$$

or by selecting B at fixed $\tilde{k}_0$

$$B(\boldsymbol{k}) = B(\tilde{k}_0, \boldsymbol{k}) \tag{D.43}$$

Without further theoretical input this choice is arbitrary and may introduce a large bias in the study.

D.2.3. Negative Bare Mass

As already noted we are interested in the theory of massless quarks. For the adjoint Wilson Dirac operator massless quarks at $\beta = 2.25$ are approached for a negative bare mass $-am_0 \approx 1.20$. The negative bare mass further complicates matters: it is neither a meaningful choice in the renormalization prescription (D.40) nor does it provide a reasonable tree-level correction of the B function as was already pointed out in the Landau gauge studies [206]. Additionally a negative mass does not work in our momentum definition, Section D.2.1. The authors of Ref. [206] proposed to use the PCAC mass instead which should be a good choice in the continuum limit but can still be the source of another uncertainty.

D.3. Summary

The three main problems described in the previous section prevent an unambiguous calculation of the Quark propagator. For each of them we (or the authors of Ref. [206] for the negative bare mass) proposed a possible solution, however each of these solution requires an involved analysis of possible artifacts which was out of reach for this work. Note that the problem with the momentum definition (where it was ignored) and the negative bare mass was also present in the Landau gauge studies of Ref. [206]. The problem of how to correct for the Wilson term in the dressing function for the mass, however, is a problem genuine to Coulomb gauge further complicating the matter.

E. Counting FLOPs

In this section we will explain how we calculated the number of floating point operations (FLOPs) for the SU(3) overrelaxation algorithm for Landau gauge. The algorithm is summarized in listing Alg. 1 as pseudocode. We will calculate the number of FLOPs per

Algorithm 1

```
while precision θ not reached do
  for parity = red, black do
    for all x of sublattice(parity) do
      for all SU(2) subgroups do
        local optimization: find g(x) ∈ SU(2)                    Step 1.
        which is a function of U_μ(x), U_μ(x − μ̂)
        for all μ do
          apply g(x) to U_μ(x), U_μ(x − μ̂)                       Step 2.
        end for
      end for
    end for
  end for
end while
```

site, i.e. the operations within the sublattice loop. Only the calculation of the new gauge transformation (Step 1 of Alg. 1) differs for the different algorithms. The update of the links (Step 2) is same for all algorithms. The number of FLOPs for the update of a single site is 2274. The detailed calculation is given in the next sections.

Step 1

The first step consists of the calculation of the matrix $K(x)$ from (7.10). Since we do not store the gauge transformation $g(x)$, but directly apply them to the links $U_\mu(x)$, the equation simplifies to a sum over 2×2 matrices for each of the three subgroups

$$K(x) = \sum_\mu \left[U_\mu(x) + U_\mu^\dagger(x - \hat{\mu}) \right]. \tag{E.1}$$

The matrix $K(x)$, as a sum over SU(2) elements, can be parameterized by a quaternion (Cayley-Klein four parameter representation). The extraction of the quaternion costs 4 additions (4 FLOPs) per link. Additionally, 4 FLOPs per link are used to sum these four elements. Thus, we have a total of

$$8 \text{ link} \times 2 \times 4 \frac{\text{FLOP}}{\text{link}} = 64 \text{ FLOP} \tag{E.2}$$

per subgroup or 192 FLOPs per site for SU(3). From (E.1) the overrelaxation update g^ω is calculated. Here we use a first order approximation of g^ω. The algorithm is presented in listing Alg. 2. It needs 22 FLOPs per subgroup, where we counted the inverse square root operation `rsqrt()` as two operations. In total we need **258 FLOPs for Step 1** per lattice site.

Algorithm 2

```
template<typename T>
void OrUpdate<T>::calculateUpdate( Quaternion<T>& K, T omega )
{
        T ai_sq = K[1]*K[1]+K[2]*K[2]+K[3]*K[3];
        T a0_sq = K[0]*K[0];

        T b=(omega*a0_sq+ai_sq)/(a0_sq+ai_sq);
        T c=rsqrt(a0_sq+b*b*ai_sq);

        K[0]*=c;
        K[1]*=b*c;
        K[2]*=b*c;
        K[3]*=b*c;
}
```

Step 2

The update operation of the links by multiplication with the gauge transformation

$$U_\mu(x) \to g(x)U_\mu(x) \tag{E.3}$$

$$U_\mu(x-\hat{\mu}) \to U_\mu(x-\hat{\mu})g^\dagger(x) \tag{E.4}$$

needs much more FLOPs compared to finding the gauge transformation in Step 1. The algorithm of multiplying the link U by a gauge transformation $g(x)$, which is represented as a quaternion, from the left is given in Alg. 3. The operation in mathematical notation

Algorithm 3

```
template<typename T>
void leftSubgroupMult( SU3<T>& U, const Quaternion<T>& g, int i, int j )
{
        for( int k = 0; k < 3; k++ )
        {
                Complex<T> IK = Complex<T>( g[0], g[1] ) * U[i][k];
                IK += Complex<T>( g[2], g[3] ) * U[j][k];

                Complex<T> JK = Complex<T>( -g[2], g[3] ) * U[i][k];
                JK += Complex<T>( g[0], -g[1] ) * U[j][k];

                U[i][k] = IK;
                U[j][k] = JK;
        }
}
```

is given in (E.5) for the subgroup which corresponds to $i = 0$, $j = 1$ in Alg. 3.

$$U \to \begin{pmatrix} g_0 + \mathrm{i}g_1 & g_2 + \mathrm{i}g_3 & 0 \\ -g_2 + \mathrm{i}g_3 & g_0 - \mathrm{i}g_1 & 0 \\ 0 & 0 & 1 \end{pmatrix} U \tag{E.5}$$

In each loop over k in Alg. 3 we have 4 complex multiplications (six FLOPs each) and 2 complex additions (two FLOPs each). Thus, we have 84 FLOPs for each of the four $U_\mu(x)$. Equivalently, we have the same number for each of the four links $U_\mu(x-\hat{\mu})$ (for a multiplication with $g^\dagger$ from the right). The total number of FLOPs for each subgroup is

$$2 \times 4 \times 84 \ \frac{\text{FLOP}}{\text{subgroup}} = 672 \frac{\text{FLOP}}{\text{subgroup}}. \tag{E.6}$$

Thus, the total number for **Step 2 is 2016 FLOPs**.

F. Maximally Abelian Gauge

In this chapter we present an application of our gauge fixing code for maximally Abelian gauge which is included in cuLGT [29]. The text already appeared in exactly this form in [248] and therefore has a small overlap with introductions given earlier.

F.1. Introduction

Despite the long standing acceptance of quantum chromodynamics (QCD) as the correct theory to describe the strong interactions of quarks and gluons, a basic understanding of its main characteristic features, the dynamical breaking of the chiral symmetry and confinement, is still lacking. Several scenarios for the underlying mechanism of confinement have been suggested over the decades. Under the most popular ones are the Kugo–Ojima [249] and the Gribov–Zwanziger scenarios [35, 250], as well as the dual superconductor picture [87, 251, 252]. Some common aspects of the different confinement criteria have been investigated in [106, 253–256].

The dual superconductor picture of confinement is especially appealing since it offers a rather intuitive approach to confinement. Type II superconductors in their superconducting phase are known to repel external magnetic fields below a critical value of the external field strength. If the magnetic field exceeds that value, tubes of magnetic flux (Abrikosov vortices) begin to penetrate the superconductor. The flux tubes are encircled by Cooper pairs which squeeze the latter. Identifying the penetrating magnetic flux tubes with the color electric field of the Yang–Mills vacuum, and moreover the condensed electric monopoles (Cooper pairs) with color magnetic monopoles, one finds a dual picture where hypothetical magnetic monopoles at the beginning and end of the Abrikosov vortices correspond to the confined quarks of QCD. Therefore, it is suggested that confinement is due to the condensation of color magnetic monopoles which squeeze the color electric flux tube between quarks and antiquarks. The dual superconductor picture has a far reaching consequence: the Abelian parts of the gauge fields should dominate the nonperturbative infrared (IR) dynamics [72].

While confinement is the reason why individual quarks and gluons have never been observed in experiment, the theory still allows to investigate correlation functions of single quark and gluon entities: the QCD Green's functions. QCD is a gauge theory and therefore the gauge has to be fixed in order to study the fundamental two-point functions. The maximally Abelian gauge, as the name suggests, rotates the gauge fields such that the diagonal, i.e., Abelian parts of the gauge fields are enhanced over the off-diagonal parts. This renders the maximally Abelian gauge particularly suitable to study IR Abelian dominance.

Lattice QCD provides an approximation to the continuum formulation with a finite number of degrees of freedom which allows to perform numerical simulations. Various attempts of investigating the dual superconductor picture in lattice QCD have been carried out, see, e.g., [257, 258]. IR Abelian dominance has been demonstrated in lattice gauge field theory in SU(2) [74, 75, 79] and more recently in SU(3) [77, 78] by studying the infrared behavior of the gluon propagator in the maximally Abelian gauge. In the recent

study [80] almost perfect Abelian dominance of the string tension on large physical volumes in quenched SU(3) has been found. Additionally, IR Abelian dominance has been found in an alternative lattice formulation [76] which does not rely on the maximally Abelian gauge. Complementary to the lattice approach several continuum investigations of Abelian dominance were performed. In [259] the authors showed that the off-diagonal gluon and ghost contributions become massive, a necessary condition for the effective model described in [81]. Furthermore, Abelian dominance has been analyzed perturbatively [82, 83] and in Dyson–Schwinger and renormalization group equation studies [84–86].

It is interesting to study the influence of Abelian dominance on chiral symmetry breaking and the hadron spectrum; in [260] it has been found that SU(2) Abelian projected fields give a chiral condensate which closely resembles the results of strongly coupled gauge theory. In [261] quenched hadron spectra in Abelian gauge fields, extracted by maximal Abelian projection have been studied: the ratios of the hadron mass to the square root of the string tension of the Abelian fields are similar to those of the full SU(3) theory. The authors concluded that they have found Abelian dominance (and monopole dominance) for the hadron spectra.

In the current paper we advance previous investigations of the gluon propagator in maximally Abelian gauge from pure Yang–Mills theory [77, 78] to full dynamical QCD by adopting $N_f = 2 + 1$ gauge field configurations. Furthermore, we analyze for the first time the maximally Abelian gauge quark propagator. In order to obtain insights in the dependence of chiral symmetry breaking and the dynamic mass generation of quarks on the type of gluon background, we invert the Dirac matrix separately on the diagonal and off-diagonal gluon fields.

The remainder of this work is structured as follows. In Sec. F.2 we introduce the maximally Abelian gauge and discuss some aspects of its implementation on the lattice. After reviewing the methods to extract the QCD Green's functions on the lattice in Sec. F.3, we list details of our lattice setup in Sec. F.4 and present our results.

F.2. The maximally Abelian gauge on the lattice

The continuum gauge fields are given by

$$A_\mu(x) = \frac{1}{2} \sum_{i=1}^{8} \lambda_i A_\mu^{(i)}(x) \,, \tag{F.1}$$

where the λ_i are the Gell-Mann matrices and $A_\mu^{(i)}(x)$ are real. On the lattice, the latter translate to the lattice link variables $U_\mu(x) \in \mathrm{SU}(3)$. The continuum and lattice fields are related via

$$U_\mu(x) = e^{iag_0 A_\mu(x)} \tag{F.2}$$

with a being the lattice spacing and g_0 the bare coupling constant. A gauge transformation in the language of lattice QCD reads

$$U_\mu(x) \to g(x)\, U_\mu(x)\, g(x+\hat{\mu})^\dagger \tag{F.3}$$

with local gauge transformations $g(x) \in \mathrm{SU}(3)$.

The maximally Abelian gauge (MAG) aims at minimizing the off-diagonal part of the gauge fields, i.e., $A_\mu^{(i)}(x)$ with $i \neq 3, 8$. This is equivalent to maximizing the following

functional of the link variables,

$$F^g_{\mathrm{MAG3}}[U] = \sum_{x,\mu} \mathrm{tr}\lambda_3 U_\mu(x)\lambda_3 U_\mu(x)^\dagger \tag{F.4}$$

$$+\,\mathrm{tr}\lambda_8 U_\mu(x)\lambda_8 U_\mu(x)^\dagger \tag{F.5}$$

where λ_3 and λ_8 build the Cartan subalgebra of SU(3). Once the functional Eq. (F.4) resides in a local maximum, the gauge condition

$$\theta = \frac{1}{VN_d}\sum_{x,j}\Big(\sum_\mu u^{(j)}_\mu(x)\,\sigma_3\,u^{(j)}_\mu(x)^\dagger \tag{F.6}$$

$$+u^{(j)}_\mu(x-\hat{\mu})^\dagger\,\sigma_3\,u^{(j)}_\mu(x-\hat{\mu})\Big)^2 \tag{F.7}$$

becomes small. Here N_d is the number of Euclidean spacetime indices, V the number of lattice sites and the $u^{(j)}_\mu(x)$, $j = 1,2,3$ are the SU(2) subgroup elements of the link variables $U_\mu(x)$.[1] In practice we reach a gauge precision of $\theta < 10^{-13}$. More details of the implementation can be found in Refs. [29, 262].

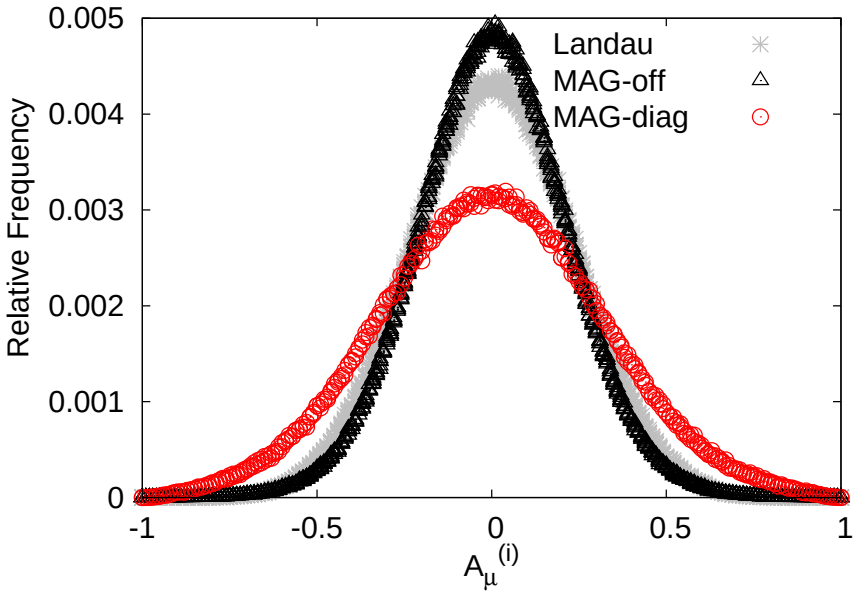

Figure F.1.: The relative frequency of the gluon field components $A^{(i)}_\mu(x)$ (in lattice units) from a single gauge field configuration in Landau gauge and MAG. In Landau gauge the eight field components follow the same normal distribution while in MAG a trend of the off-diagonal components (MAG-*off*) towards smaller values compared to the diagonal components (MAG-*diag*) is manifest.

Once a maximum of Eq. (F.4) has been reached, the diagonal gluon fields, $A^{(i)}_\mu(x)$ with $i = 3, 8$ are favored over the off-diagonal gluons. In Fig. F.1 we show the distribution of the gluon fields $A^{(i)}_\mu(x)$ from a single lattice gauge field configuration. While in Landau gauge none of the gauge fields is favored and thus their distribution lies on top of each

[1] Two SU(2) matrices overlap on the diagonal of $U_\mu(x)$ and the third one consists of the corners of $U_\mu(x)$.

other, the distribution of the MAG fields shows a clear shift of the diagonal fields towards larger values and correspondingly a shift towards smaller values for the off-diagonal parts.

The MAG functional Eq. (F.4) is invariant under gauge transformations of the form

$$g_d(x) = \exp\left(i\omega^{(3)}\lambda_3 + i\omega^{(8)}\lambda_8\right) \tag{F.8}$$

and therefore the MAG is an incomplete gauge condition; it leaves a remaining $U(1)_3 \times U(1)_8$ gauge freedom. The latter we remove by enforcing that $U_\mu(x)$ fulfills in addition to the MAG the Landau gauge condition

$$F^g_{\text{Landau}}[U] = \text{Re}\sum_{\mu,x} \text{tr} g(x)\, U_\mu(x)\, g(x+\hat{\mu})^\dagger \xrightarrow{!} \text{max.}\,, \tag{F.9}$$

with respect to diagonal gauge transformations $g(x) = g_d(x)$.

Lastly, in order to study the diagonal and off-diagonal parts of the gluon fields separately, we extract the fields $A_\mu(x)$ from the link variables Eq. (F.2) via the first order approximation

$$A_\mu(x) = \frac{1}{2iag_0}\left(U_\mu(x) - U_\mu(x)^\dagger\right)\Big|_{\text{traceless}}. \tag{F.10}$$

Note that we do not make use of the "exact" logarithmic definition of the lattice gluon fields in order to stay consistent with the definition of the gluon fields in the Landau gauge condition [29].[2]

F.3. QCD propagators

F.3.1. Gluon propagator

In Landau gauge the gluon propagator in momentum space is transverse and diagonal in color space

$$D_{\mu\nu}(k^2) = \frac{1}{8}\sum_{i=1}^{8}\left\langle A^{(i)}_\mu(k) A^{(i)}_\nu(-k)\right\rangle \tag{F.11}$$

$$= \left(\delta_{\mu\nu} - \frac{k_\mu k_\nu}{p^2}\right) D(k^2), \tag{F.12}$$

where $A^{(i)}_\mu(k)$ are the Fourier transformed gauge fields extracted from the links by Eq. (F.10). Appropriate for the Symanzik-improved Lüscher–Weisz gauge action [263], we define the momentum variable as

$$k_\mu = \frac{2}{a}\sqrt{\sin^2\left(\frac{p_\mu a}{2}\right) + \frac{1}{3}\sin^4\left(\frac{p_\mu a}{2}\right)}, \tag{F.13}$$

where

$$p_\mu = \frac{2\pi n_\mu}{aL_\mu} \tag{F.14}$$

are the discrete lattice momenta. The transversality of the momentum space propagator is a direct consequence of the Landau gauge condition $\partial_\mu A_\mu(x) = 0$.

[2] We performed some checks using the logarithmic definition: the qualitative behavior of the gluon propagator is the same, as it was also found in Ref. [231]. The main difference here is, as expected, that the diagonal part of the longitudinal gluon propagator from the logarithmic definition does not vanish.

For the MAG case we split the propagator in a diagonal

$$D^{\text{diag}}_{\mu\nu}(k^2) = \frac{1}{2}\sum_{i=3,8}\left\langle A^{(i)}_{\mu}(k)A^{(i)}_{\nu}(-k)\right\rangle \tag{F.15}$$

and an off-diagonal part

$$D^{\text{off}}_{\mu\nu}(k^2) = \frac{1}{6}\sum_{i\neq 3,8}\left\langle A^{(i)}_{\mu}(k)A^{(i)}_{\nu}(-k)\right\rangle . \tag{F.16}$$

Due to the residual $U(1)_3 \times U(1)_8$ Landau gauge fixing, the diagonal propagator is transverse, whereas the off-diagonal propagator has a longitudinal and a transverse component

$$D^{\text{off}}_{\mu\nu}(k^2) = \left(\delta_{\mu\nu} - \frac{k_\mu k_\nu}{k^2}\right) D^{\text{off}}_{\text{T}}(k^2) + \frac{k_\mu k_\nu}{k^2} D^{\text{off}}_{\text{L}}(k^2). \tag{F.17}$$

F.3.2. Quark propagator

In manifestly covariant gauges, the interacting quark propagator $S(\mu; p^2)$, renormalized at the renormalization point μ, can be decomposed into Dirac scalar and vector parts

$$S(\mu; p^2) = \left(i\not{p}_A(\mu; p^2) + B(\mu; p^2)\right)^{-1} \tag{F.18}$$

or equivalently as

$$S(\mu; p^2) = Z(\mu; p^2)\left(i\not{p}_+ M(p^2)\right)^{-1}. \tag{F.19}$$

In the last equation the wave-function renormalization function $Z(\mu; p^2) = 1/A(\mu; p^2)$ carries all the information about the renormalization scale and the mass function $M(p^2) = B(\mu; p^2)/A(\mu; p^2)$ is a renormalization group invariant.

The lattice regularized quark propagator $S_L(p^2; a)$, which depends on the lattice spacing a, can then be renormalized at renormalization scale μ with the momentum independent quark wave-function renormalization constant $Z_2(\mu; a)$,

$$S_L(p^2; a) = Z_2(\mu; a)S(\mu; p^2). \tag{F.20}$$

The momentum subtraction scheme (MOM) has the renormalization point boundary conditions $Z(\mu; \mu^2) = 1$ and $M(\mu^2) = m(\mu)$ where $m(\mu)$ is the running mass.

The nonperturbative functions $M(p^2)$ and $Z(p^2) \equiv Z_2(\mu; a)Z(\mu; p^2)$ can be extracted directly from the lattice. To this end we invert the Asqtad fermion matrix [245] in order to obtain the quark propagator which we subsequently Fourier transform to momentum space. Taking basic Clifford algebra properties into account we can extract the dressing functions. For details we refer to [264, 265]. Note that the lattice dressing functions will be functions of the lattice quark momenta (which differ from the gluon momenta (F.13)) and for the Asqtad action these are defined by

$$k_\mu = \sin(p_\mu)\left(1 + \frac{1}{6}\sin^2(p_\mu)\right). \tag{F.21}$$

We perform a cylinder-cut [242] on all our data and average over the discrete rotational and parity symmetries of $S_L(p^2; a)$ to increase statistics.

F.4. Results

F.4.1. Gauge configurations

For our simulation we adopted two sets of gauge field configurations generated by the MILC collaboration [266–269]: a "coarse" set of size $20^3 \times 64$ with lattice spacing $a = 0.12\,\text{fm}$, which consists of five dynamical plus a quenched ensemble, and furthermore a "fine" set consisting of a single ensemble of size $40^3 \times 96$ with lattice spacing $a = 0.09\,\text{fm}$. The configurations were generated with the Symanzik-improved Lüscher–Weisz gauge action [270] and have been made available to the lattice community via the Gauge Connection [271]. Both sets include two light degenerate (l) and one heavier quark flavor (s) (except the quenched ensemble), implemented with the Asqtad improved action [245]. The parameters of the lattices are summarized in Table F.1; for the reported lattice scales and quark masses we refer to the original work [266–269].

$N_s^3 \times N_t$	a [fm]	m_l [MeV]	m_s [MeV]	# configs.
$20^3 \times 64$	0.12	11.5	82.2	976
		16.4		573
		32.9		391
		49.3		432
		65.8		350
		∞	∞	408
$40^3 \times 96$	0.09	6.8	68.0	187

Table F.1.: Overview of the gaugefield parameters: the lattice size $N_s^3 \times N_t$, lattice spacing a, dynamical quark masses m_l and m_s (∞ indicating quenched gauge fields) and the number of configurations that enter our analysis.

F.4.2. Gluon propagator

The gluon propagator in the maximally Abelian gauge has already been studied both in SU(2) [74, 75] and SU(3) [77, 78] for pure Yang–Mills theory. Here we extend those studies to full QCD with $2 + 1$ flavors of dynamical quarks. In Fig. F.2 we show the propagators of the coarse ensemble for the different quark masses including the quenched dataset. In addition to the three MAG propagators (diagonal transverse, off-diagonal longitudinal and off-diagonal transverse) we include the Landau gauge propagator for comparison. The Landau gauge propagator has been studied on the same dataset in [272]. Following their setup we use the same renormalization condition

$$D(k^2 = \mu^2) = \frac{1}{\mu^2} \tag{F.22}$$

at $\mu = 4\,\text{GeV}$. In the IR we find suppression of the propagator with dynamical quarks due to screening effects. Compared to Landau gauge, this effect is more pronounced in the maximally Abelian gauge. Decreasing the quark mass leads to a further suppression in the IR, however the dependence on the quark mass is small.

In Fig. F.3 we present the gluon form factors of the fine ensemble. It is very important to note that in both Figs. F.2 and F.3, it is obvious that the diagonal parts of the MAG gluon propagator are pronounced as compared to the Landau gauge counterparts, and,

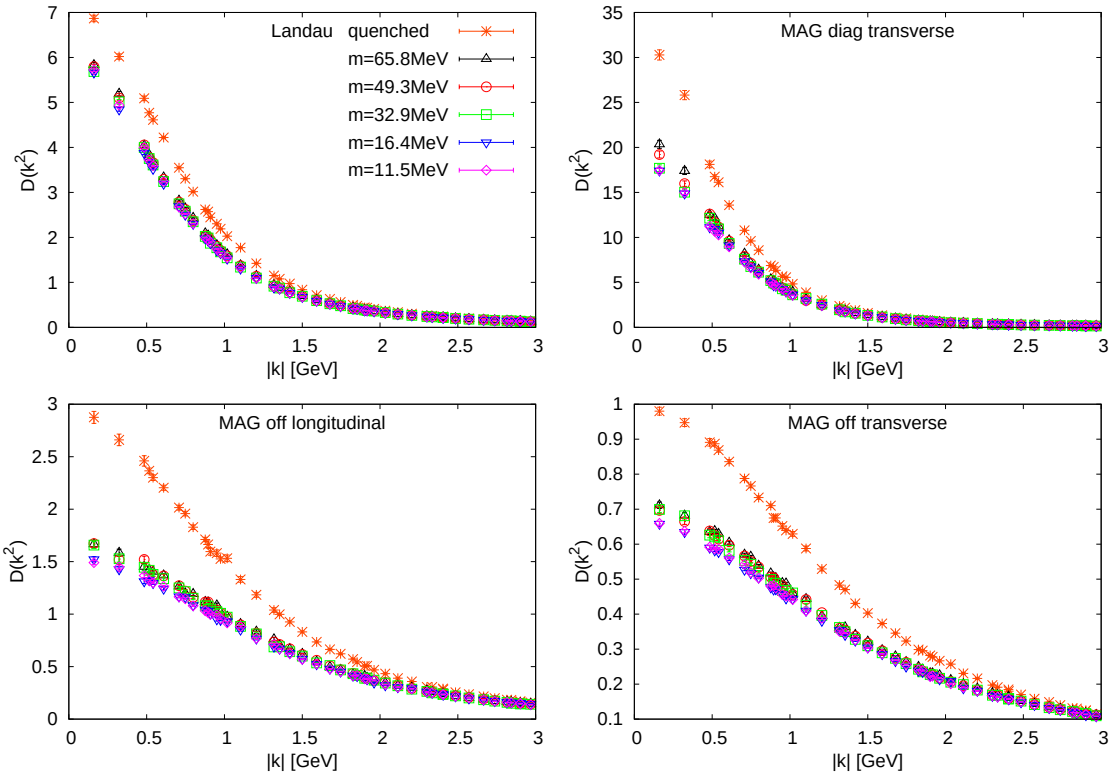

Figure F.2.: The gluon propagator of the coarse ensembles of Table F.1 renormalized at $\mu = 4\,\mathrm{GeV}$.

respectively, the off-diagonal parts are suppressed. This extends previous findings of IR Abelian dominance from pure Yang–Mills theory to full QCD.

Our findings for the fine ensemble in Fig. F.3 are in very good agreement with the SU(2) results of [75] considering the fact that we study the SU(3) propagator and included dynamical quarks. There the authors found a wide maximum of the dressing function $k^2 D_{\mathrm{L}}^{\mathrm{off}}(k^2)$ at around 2 GeV and a sharp peak of $k^2 D^{\mathrm{diag}}(k^2)$ around 0.7 GeV. To compare our results with the quenched SU(3) results of [78] we applied a fit to our data with the their function

$$D(k^2) = \frac{Z}{(k^2 + m^2)^{\nu}} \tag{F.23}$$

in the same momentum regime $k < 3\,\mathrm{GeV}$. Qualitatively, the results compare well to the quenched results from Ref. [78].

	m [GeV]	ν	Z	χ^2/n.d.f.
$D_{\mathrm{T}}^{\mathrm{off}}$	1.47(2)	1.18(2)	14.9(6)	0.9
$D_{\mathrm{L}}^{\mathrm{off}}$	1.66(3)	1.77(4)	36.2(36)	1.0
D^{diag}	0.78(1)	1.85(1)	181.6(54)	1.7

Table F.2.: Results of a fit of the maximally Abelian gluon propagators to (F.23).

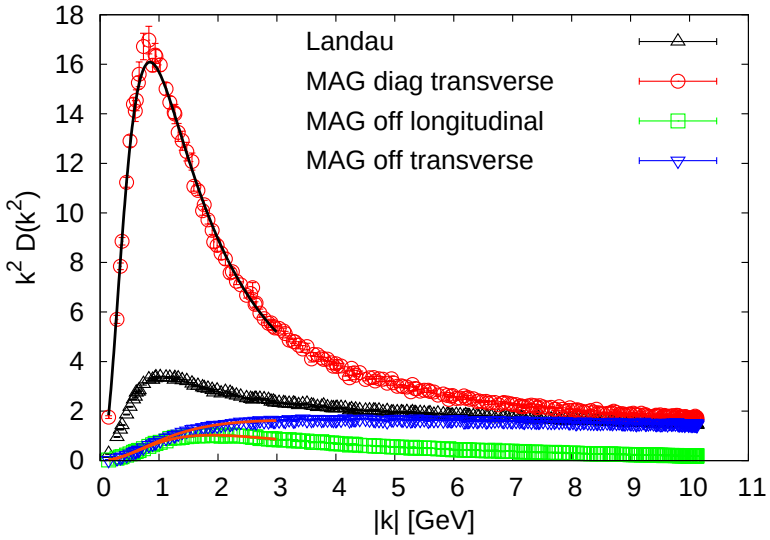

Figure F.3.: The gluon form factors of the fine ensemble. The solid lines illustrate the fit to Eq. (F.23).

F.4.3. Quark propagator

We obtain the quark propagator in the standard way by inverting the (Asqtad) Dirac operator for a point source on a gauge field background. This is performed in Landau gauge and in the maximally Abelian gauge with $U(1)_3 \times U(1)_8$ Landau residual gauge fixing. Additionally, we split the maximally Abelian gauge gluon fields in their diagonal and off-diagonal components and invert the Dirac operator on the two parts separately. Thus, we obtain four "kinds" of quark propagators from each ensemble.

Quark mass dependence

On the five dynamical coarse ensembles of Table F.1, we calculate the quark propagator in Landau gauge, in maximally Abelian gauge (MAG), on a pure diagonal MAG background (MAG-*diag*) and a pure off-diagonal MAG background (MAG-*off*). The mass parameter of the valence quark propagator has been set to the value of the corresponding light sea quark mass for these five ensembles. This will allow for a systematic extrapolation to the chiral limit.

In Fig. F.4 the quark mass function $M(k^2)$ is shown for the four types of gluon backgrounds (Landau gauge, MAG, MAG-*diag* and MAG-*off*) from all coarse ensembles, including a linear extrapolation to the chiral limit. In analog, Fig. F.5 shows the corresponding quark wave-function renormalization functions $Z(k^2)$.

When comparing the Landau gauge quark propagator to the quark propagator in MAG, the first observation is that the MAG data, with the same statistics, results in more gauge noise from the Monte Carlo integration. Moreover, the running masses of the MAG data lie higher than the corresponding Landau gauge masses, which holds from the largest mass of $m_l = 65.8\,\mathrm{MeV}$ down to the chiral limit. The dynamically generated infrared masses, on the other hand, appear compatible within the error bars.

It is evident that $M(k^2)$ from the MAG-*diag* gluon background nicely resembles the Landau gauge analog (despite being more noisy), whereas $M(k^2)$ from MAG-*off* gluons is constant, lying roughly 40% higher than the corresponding bare quark mass. In the chiral limit it is compatible with zero. Similarly, the wave-function renormalization function

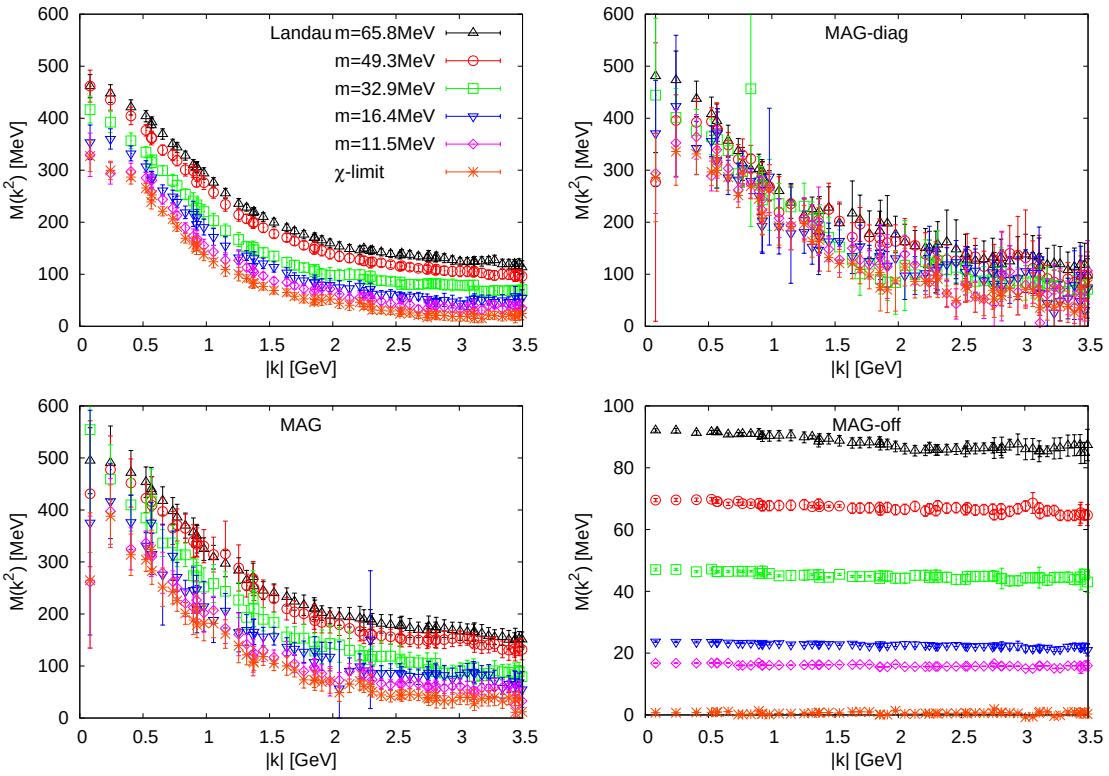

Figure F.4.: The quark mass function from the coarse ensembles of Table F.1. The bare quark masses are set to the values of the dynamical light quark masses. Additionally, a linear extrapolation to the chiral limit is shown.

from MAG-*off* gluons comes out close to its tree-level value, $Z(k^2) \approx 1$, independent of the quark mass.

Infrared behavior

The coarse ensembles cannot provide a clear picture of the infrared behavior of the quark propagators. To improve thereon we adopt the fine MILC ensemble of Table F.1. In order to keep the gauge noise and the simulation costs at an acceptable level, we use a valence quark with the mass of the heavier dynamical strange quark, $m_s = 68.0\,\mathrm{MeV}$, instead of setting it to the light quark mass of $m_s = 6.8\,\mathrm{MeV}$.

In Fig. F.6 we compare $M(k^2)$ and $Z(k^2)$ in MAG, MAG-*diag* and MAG-*off*, respectively, directly to the Landau gauge counterparts. While the MAG and Landau gauge mass functions agree within the error bars over the whole momentum range, $Z(k^2)$ appears to be stronger IR suppressed in MAG as compared to Landau gauge.

Similarly, the MAG-*diag* mass function agrees over the whole momentum range within the error bars with its Landau gauge counterpart. The renormalization function exhibits qualitatively the same IR behavior as in Landau gauge. In contrast, the MAG-*off* quark dressing functions hardly show any non-trivial dynamics. This is the main finding of this study: it shows that the Abelian parts of the gluon fields not only dominate the purely gluonic interactions, but also the infrared interactions of quarks.

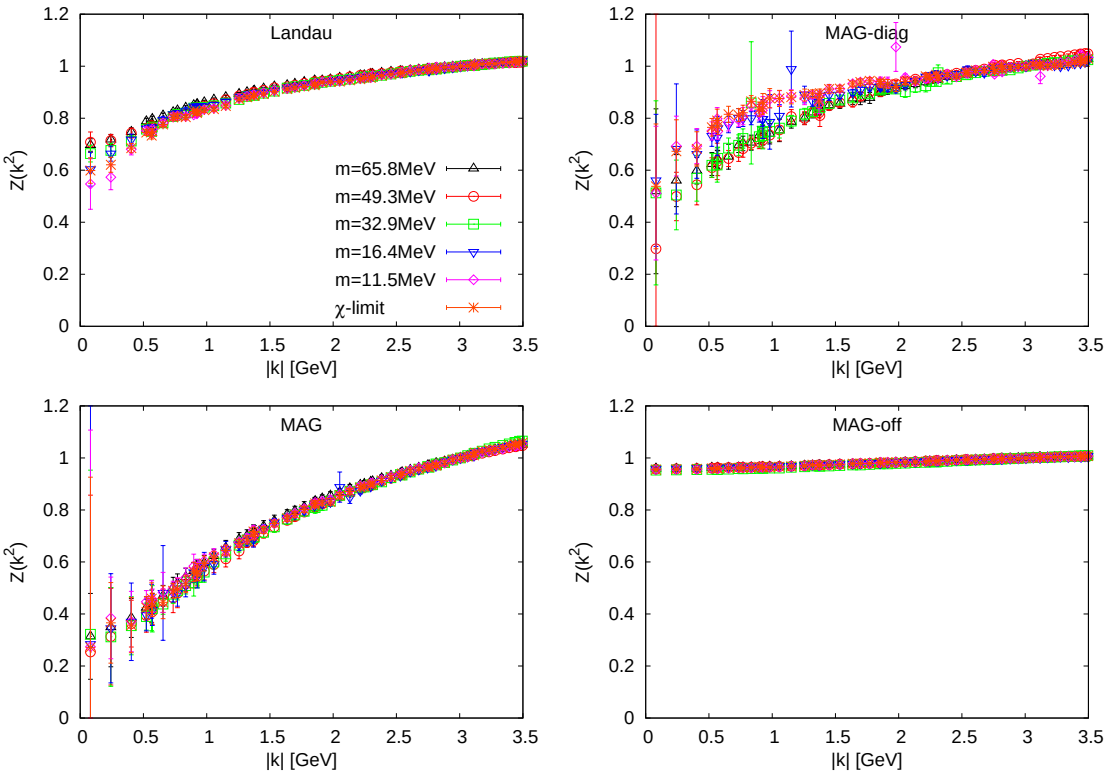

Figure F.5.: The quark function renormalization function from the coarse ensembles of Table F.1. The bare quark masses are set to the values of the dynamical light quark masses. A linear extrapolation to the chiral limit is shown. All data have been been renormalized at $\mu = 3\,\mathrm{GeV}$.

F.5. Summary

We have fixed dynamical SU(3) lattice gauge fields to the combined maximally Abelian gauge and $U(1)_3 \times U(1)_8$ Landau gauge. From the lattice link variables we have extracted the continuum gluon fields which we subsequently separated into purely diagonal (Abelian) and off-diagonal components.

We investigated the gluon propagator from diagonal and off-diagonal gluon fields. Dynamical quarks lead to an IR suppression compared to the quenched case. The suppression becomes stronger when decreasing the quark mass. The screening is more pronounced in the MAG propagators compared to the Landau gauge propagator. Our findings confirm the manifestation of infrared Abelian dominance in the gluon propagator as found in earlier studies on quenched lattices.

Finally, for the first time the maximally Abelian gauge quark propagator has been analyzed on a background of purely diagonal gluons as well as on the remaining, off-diagonal gluon background. The hypothesis of Abelian dominance implies that the non-Abelian gluon field does not propagate at a long-distance scale and hence that only the Abelian component is relevant at a long-distance scale. In accordance therewith, we have demonstrated that the quark propagator from a non-Abelian gluon background hardly shows any effects while the quark propagator from an Abelian gluon background closely resembles its Landau gauge counterpart.

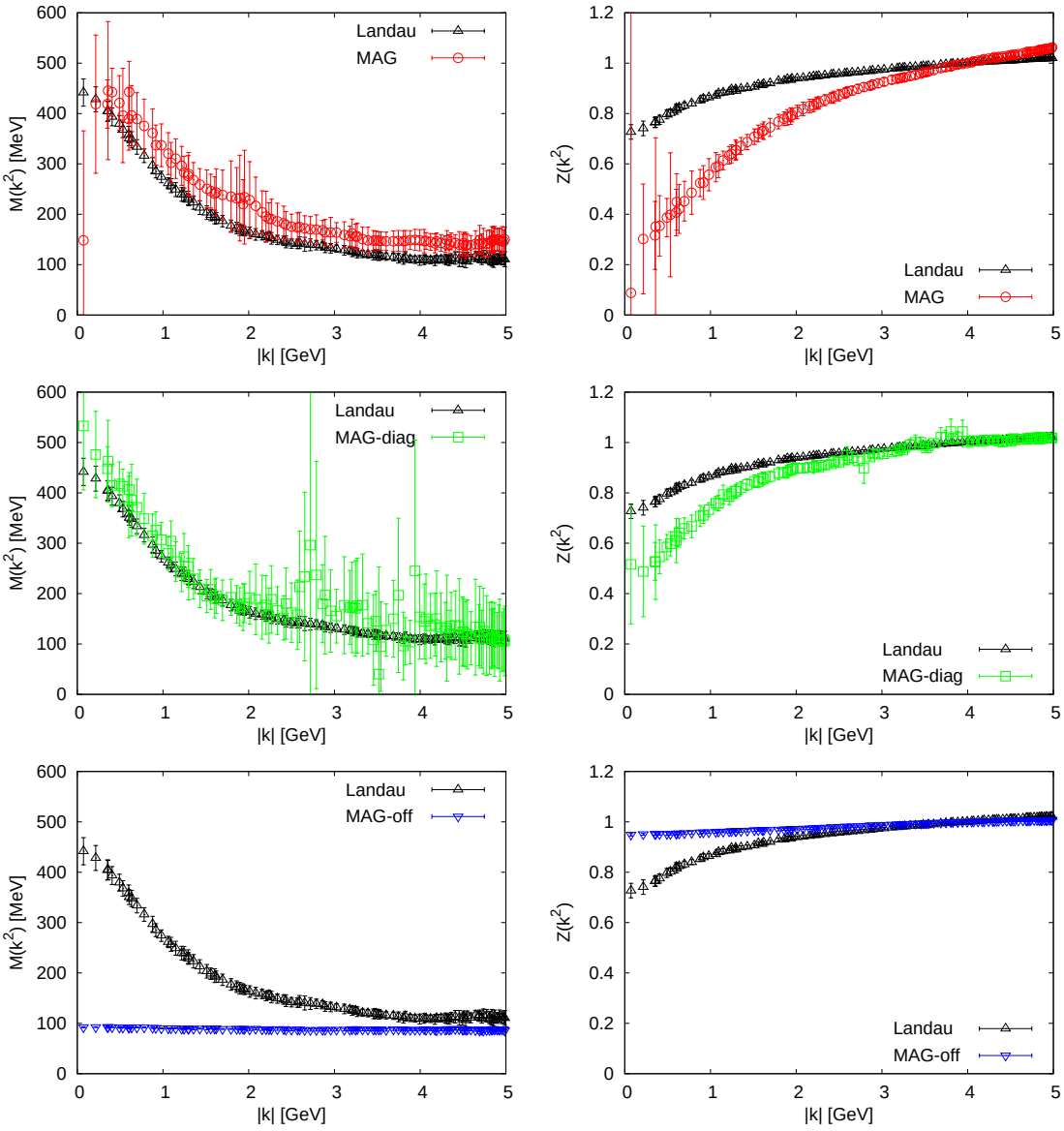

Figure F.6.: The quark mass function (left column) and renormalization function (right column) from the fine ensemble of Table F.1. The MAG (top row), MAG diagonal part (middle row) and MAG off-diagonal part (bottom row) are shown. Each of the three rows of plots includes additionally the Landau gauge quark propagator for direct comparison. The quark mass is equal to the dynamical strange quark mass ($m_s = 68.0\,\mathrm{MeV}$). $Z(k^2)$ has been renormalized at $\mu = 4\,\mathrm{GeV}$.

G. Bibliography

[1] S. Abachi et al. Observation of the top quark. *Phys. Rev. Lett.*, 74:2632–2637, 1995.

[2] F. Abe et al. Observation of top quark production in $\bar{p}p$ collisions. *Phys. Rev. Lett.*, 74:2626–2631, 1995.

[3] Georges Aad et al. Observation of a new particle in the search for the Standard Model Higgs boson with the ATLAS detector at the LHC. *Phys. Lett.*, B716:1–29, 2012.

[4] Serguei Chatrchyan et al. Observation of a new boson at a mass of 125 GeV with the CMS experiment at the LHC. *Phys. Lett.*, B716:30–61, 2012.

[5] Y. Fukuda et al. Evidence for oscillation of atmospheric neutrinos. *Phys. Rev. Lett.*, 81:1562–1567, 1998.

[6] Q. R. Ahmad et al. Measurement of the rate of $\nu_e + d \rightarrow p + p + e^-$ interactions produced by ^8B solar neutrinos at the Sudbury Neutrino Observatory. *Phys. Rev. Lett.*, 87:071301, 2001.

[7] P. A. R. Ade et al. Planck 2013 results. XVI. Cosmological parameters. *Astron. Astrophys.*, 571:A16, 2014.

[8] Chen-Ning Yang and Robert L. Mills. Conservation of Isotopic Spin and Isotopic Gauge Invariance. *Phys. Rev.*, 96:191–195, 1954.

[9] Peter Watson and Hugo Reinhardt. Propagator Dyson-Schwinger Equations of Coulomb Gauge Yang-Mills Theory Within the First Order Formalism. *Phys. Rev.*, D75:045021, 2007.

[10] Peter Watson and Hugo Reinhardt. Two-point functions of Coulomb gauge Yang-Mills theory. *Phys. Rev.*, D77:025030, 2008.

[11] C. Popovici, P. Watson, and H. Reinhardt. Quarks in Coulomb gauge perturbation theory. *Phys. Rev.*, D79:045006, 2009.

[12] Hugo Reinhardt and Peter Watson. Resolving temporal Gribov copies in Coulomb gauge Yang-Mills theory. *Phys. Rev.*, D79:045013, 2009.

[13] Peter Watson and Hugo Reinhardt. The Coulomb gauge ghost Dyson-Schwinger equation. *Phys. Rev.*, D82:125010, 2010.

[14] Craig D. Roberts and Anthony G. Williams. Dyson-Schwinger equations and their application to hadronic physics. *Prog. Part. Nucl. Phys.*, 33:477–575, 1994.

[15] Reinhard Alkofer and Lorenz von Smekal. The Infrared behavior of QCD Green's functions: Confinement dynamical symmetry breaking, and hadrons as relativistic bound states. *Phys. Rept.*, 353:281, 2001.

[16] Christian S. Fischer. Infrared properties of QCD from Dyson-Schwinger equations. *J. Phys.*, G32:R253–R291, 2006.

[17] C. Feuchter and H. Reinhardt. Variational solution of the Yang-Mills Schrodinger equation in Coulomb gauge. *Phys. Rev.*, D70:105021, 2004.

[18] D. Epple, H. Reinhardt, and W. Schleifenbaum. Confining Solution of the Dyson-Schwinger Equations in Coulomb Gauge. *Phys. Rev.*, D75:045011, 2007.

[19] Davide R. Campagnari and Hugo Reinhardt. Non-Gaussian wave functionals in Coulomb gauge Yang–Mills theory. *Phys. Rev.*, D82:105021, 2010.

[20] Jan Heffner, Hugo Reinhardt, and Davide R. Campagnari. The deconfinement phase transition in the Hamiltonian approach to Yang–Mills theory in Coulomb gauge. *Phys. Rev.*, D85:125029, 2012.

[21] M. Pak and H. Reinhardt. Quark Sector of the QCD Groundstate in Coulomb Gauge. *Phys. Rev.*, D88:125021, 2013.

[22] Davide R. Campagnari and Hugo Reinhardt. Dyson–Schwinger approach to Hamiltonian Quantum Chromodynamics. *Phys. Rev.*, D92(6):065021, 2015.

[23] P. Vastag, H. Reinhardt, and D. Campagnari. Improved variational approach to QCD in Coulomb gauge. *Phys. Rev.*, D93(6):065003, 2016.

[24] Kenneth G. Wilson. Confinement of Quarks. *Phys. Rev.*, D10:2445–2459, 1974.

[25] M. Creutz. Monte Carlo Study of Quantized SU(2) Gauge Theory. *Phys. Rev.*, D21:2308–2315, 1980.

[26] S. Durr, Z. Fodor, C. Hoelbling, S. D. Katz, S. Krieg, T. Kurth, L. Lellouch, T. Lippert, K. K. Szabo, and G. Vulvert. Lattice QCD at the physical point: Simulation and analysis details. *JHEP*, 08:148, 2011.

[27] M. A. Clark, R. Babich, K. Barros, R. C. Brower, and C. Rebbi. Solving Lattice QCD systems of equations using mixed precision solvers on GPUs. *Comput. Phys. Commun.*, 181:1517–1528, 2010.

[28] R. Babich, M. A. Clark, B. Joo, G. Shi, R. C. Brower, and S. Gottlieb. Scaling Lattice QCD beyond 100 GPUs. In *SC11 International Conference for High Performance Computing, Networking, Storage and Analysis Seattle, Washington, November 12-18, 2011*, 2011.

[29] Mario Schröck and Hannes Vogt. Coulomb, Landau and Maximally Abelian Gauge Fixing in Lattice QCD with Multi-GPUs. *Comput. Phys. Commun.*, 184:1907–1919, 2013.

[30] S. Pokorski. *Gauge Field Theories.* Cambridge Monographs on Mathematical Physics. Cambridge University Press, 2000.

[31] C. Gattringer and C. Lang. *Quantum Chromodynamics on the Lattice: An Introductory Presentation.* Lecture Notes in Physics. Springer Berlin Heidelberg, 2009.

[32] M.E. Peskin and D.V. Schroeder. *An Introduction to Quantum Field Theory.* Advanced book program. Levant Books, 2005.

[33] L. D. Faddeev and V. N. Popov. Feynman Diagrams for the Yang-Mills Field. *Phys. Lett.*, B25:29–30, 1967.

[34] H. Reinhardt, D. Campagnari, J. Heffner, M. Quandt, and P. Vastag. Hamiltonian approach to QCD in Coulomb gauge: From the vacuum to finite temperatures. In *4th International Conference on New Frontiers in Physics (ICNFP 2015) Kolymbari, Greece, August 23-30, 2015*, 2015.

[35] V. N. Gribov. Quantization of Nonabelian Gauge Theories. *Nucl. Phys.*, B139:1, 1978.

[36] Daniel Zwanziger. Fundamental modular region, Boltzmann factor and area law in lattice gauge theory. *Nucl. Phys.*, B412:657–730, 1994.

[37] G. Dell'Antonio and D. Zwanziger. Every gauge orbit passes inside the Gribov horizon. *Commun. Math. Phys.*, 138:291–299, 1991.

[38] Pierre van Baal. More (thoughts on) Gribov copies. *Nucl. Phys.*, B369:259–275, 1992.

[39] Daniel Zwanziger. Nonperturbative Faddeev-Popov formula and infrared limit of QCD. *Phys. Rev.*, D69:016002, 2004.

[40] R. Jackiw. Functional Representations for Quantized Fields. In *1st Asia Pacific Conference on High-energy Physics: Superstrings, Anomalies and Field Theory Singapore, Singapore, June 21-28, 1987*, 1987.

[41] Claus Feuchter. *Yang-Mills-Theorie in Coulombeichung (in German)*. PhD thesis, 2006.

[42] Davide R. Campagnari. *The Yang-Mills vacuum wave functional in Coulomb gauge*. PhD thesis, 2011.

[43] N. H. Christ and T. D. Lee. Operator Ordering and Feynman Rules in Gauge Theories. *Phys. Rev.*, D22:939, 1980. [Phys. Scripta23,970(1981)].

[44] G. Burgio, M. Quandt, and H. Reinhardt. Coulomb gauge gluon propagator and the Gribov formula. *Phys. Rev. Lett.*, 102:032002, 2009.

[45] Michael Creutz. *Quarks, Gluons and Lattices*. Cambridge Monographs on Mathematical Physics. Cambridge University Press, 1983.

[46] H. J. Rothe. Lattice gauge theories: An Introduction. *World Sci. Lect. Notes Phys.*, 43:1–381, 1992. [World Sci. Lect. Notes Phys.82,1(2012)].

[47] István Montvay and Gernot Münster. *Quantum fields on a lattice*. Cambridge monographs on mathematical physics. Cambridge Univ. Press, Cambridge, 1994.

[48] Holger Bech Nielsen and M. Ninomiya. No Go Theorem for Regularizing Chiral Fermions. *Phys. Lett.*, B105:219–223, 1981.

[49] Holger Bech Nielsen and M. Ninomiya. Absence of Neutrinos on a Lattice. 1. Proof by Homotopy Theory. *Nucl. Phys.*, B185:20, 1981. [,533(1980)].

[50] Holger Bech Nielsen and M. Ninomiya. Absence of Neutrinos on a Lattice. 2. Intuitive Topological Proof. *Nucl. Phys.*, B193:173–194, 1981.

[51] F. Karsch. SU(N) Gauge Theory Couplings on Asymmetric Lattices. *Nucl. Phys.*, B205:285–300, 1982.

[52] Timothy R. Klassen. The Anisotropic Wilson gauge action. *Nucl. Phys.*, B533:557–575, 1998.

[53] A. Sokal. *Functional Integration: Basics and Applications*, chapter Monte Carlo Methods in Statistical Mechanics: Foundations and New Algorithms, pages 131–192. Springer US, Boston, MA, 1997.

[54] Ulli Wolff. Monte Carlo errors with less errors. *Comput. Phys. Commun.*, 156:143–153, 2004. [Erratum: Comput. Phys. Commun.176,383(2007)].

[55] N. Metropolis, A. W. Rosenbluth, M. N. Rosenbluth, A. H. Teller, and E. Teller. Equation of state calculations by fast computing machines. *J. Chem. Phys.*, 21:1087–1092, 1953.

[56] Stephen L. Adler. An Overrelaxation Method for the Monte Carlo Evaluation of the Partition Function for Multiquadratic Actions. *Phys. Rev.*, D23:2901, 1981.

[57] C. Whitmer. Overrelaxation Methods for Monte Carlo Simulations of Quadratic and Multiquadratic Actions. *Phys. Rev.*, D29:306–311, 1984.

[58] N. Cabibbo and E. Marinari. A New Method for Updating SU(N) Matrices in Computer Simulations of Gauge Theories. *Phys. Lett.*, B119:387–390, 1982.

[59] Luigi Del Debbio, Biagio Lucini, Agostino Patella, Claudio Pica, and Antonio Rago. Mesonic spectroscopy of Minimal Walking Technicolor. *Phys. Rev.*, D82:014509, 2010.

[60] Luigi Del Debbio, Biagio Lucini, Agostino Patella, Claudio Pica, and Antonio Rago. The infrared dynamics of Minimal Walking Technicolor. *Phys. Rev.*, D82:014510, 2010.

[61] Agostino Patella. A precise determination of the psibar-psi anomalous dimension in conformal gauge theories. *Phys. Rev.*, D86:025006, 2012.

[62] L. Del Debbio, B. Lucini, A. Patella, C. Pica, and A. Rago. Large volumes and spectroscopy of walking theories. *Phys. Rev.*, D93(5):054505, 2016.

[63] Christof Gattringer and Kurt Langfeld. Approaches to the sign problem in lattice field theory. *Int. J. Mod. Phys.*, A31(22):1643007, 2016.

[64] M. Luscher. Symmetry Breaking Aspects of the Roughening Transition in Gauge Theories. *Nucl. Phys.*, B180:317–329, 1981.

[65] G. Marchesini and E. Onofri. An Elementary Derivation of Wilson's and Polyakov's Confinement Tests From the Hamiltonian Formulation. *Nuovo Cim.*, A65:298, 1981.

[66] Michael Creutz. Asymptotic Freedom Scales. *Phys. Rev. Lett.*, 45:313, 1980. [,266(1980)].

[67] Antonio Gonzalez-Arroyo and Masanori Okawa. The string tension from smeared Wilson loops at large N. *Phys. Lett.*, B718:1524–1528, 2013.

[68] Steven Weinberg. *The quantum theory of fields. Vol. 2: Modern applications.* Cambridge University Press, 2013.

[69] S. Mandelstam. Vortices and quark confinement in non-Abelian gauge theories. *Phys. Lett.*, B53:476–478, 1975.

[70] Gerard 't Hooft. Gauge Fields with Unified Weak, Electromagnetic, and Strong Interactions. In *Palermo Conf.1975:1225*, page 1225, 1975.

[71] Gerard 't Hooft. Topology of the Gauge Condition and New Confinement Phases in Nonabelian Gauge Theories. *Nucl. Phys.*, B190:455, 1981.

[72] Z. F. Ezawa and A. Iwazaki. Abelian Dominance and Quark Confinement in Yang-Mills Theories. *Phys. Rev.*, D25:2681, 1982.

[73] G. S. Bali, V. Bornyakov, M. Muller-Preussker, and K. Schilling. Dual superconductor scenario of confinement: A Systematic study of Gribov copy effects. *Phys. Rev.*, D54:2863–2875, 1996.

[74] Kazuhisa Amemiya and Hideo Suganuma. Off diagonal gluon mass generation and infrared Abelian dominance in the maximally Abelian gauge in lattice QCD. *Phys.Rev.*, D60:114509, 1999.

[75] V.G. Bornyakov, M.N. Chernodub, F.V. Gubarev, S.M. Morozov, and M.I. Polikarpov. Abelian dominance and gluon propagators in the maximally Abelian gauge of SU(2) lattice gauge theory. *Phys.Lett.*, B559:214–222, 2003.

[76] A. Shibata, S. Kato, K. I. Kondo, T. Murakami, T. Shinohara, and S. Ito. Compact lattice formulation of Cho-Faddeev-Niemi decomposition: Gluon mass generation and infrared Abelian dominance. *Phys. Lett.*, B653:101–108, 2007.

[77] Shinya Gongyo, Takumi Iritani, and Hideo Suganuma. Off-diagonal Gluon Mass Generation and Infrared Abelian Dominance in Maximally Abelian Gauge in SU(3) Lattice QCD. *Phys. Rev.*, D86:094018, 2012.

[78] Shinya Gongyo and Hideo Suganuma. Gluon Propagators in Maximally Abelian Gauge in SU(3) Lattice QCD. *Phys.Rev.*, D87:074506, 2013.

[79] Shinya Gongyo. Two-dimensional gluon propagators in maximally Abelian gauge in SU(2) Lattice QCD. *arXiv:1410.8572*, 2014.

[80] Naoyuki Sakumichi and Hideo Suganuma. Perfect Abelian dominance of quark confinement in SU(3) QCD. *Phys.Rev.*, D90:111501, 2014.

[81] Kei-Ichi Kondo. Abelian projected effective gauge theory of QCD with asymptotic freedom and quark confinement. *Phys. Rev.*, D57:7467–7487, 1998.

[82] M. Quandt and H. Reinhardt. Field strength formulation of SU(2) Yang-Mills theory in the maximal Abelian gauge: Perturbation theory. *Int.J.Mod.Phys.*, A13:4049–4076, 1998.

[83] M. Quandt and H. Reinhardt. Ward identities for Yang-Mills theory in Abelian gauges: Abelian dominance at high-energies. *Phys.Lett.*, B424:115–124, 1998.

[84] Markus Q. Huber, Kai Schwenzer, and Reinhard Alkofer. On the infrared scaling solution of SU(N) Yang-Mills theories in the maximally Abelian gauge. *Eur.Phys.J.*, C68:581–600, 2010.

[85] Markus Q. Huber. *On gauge fixing aspects of the infrared behavior of Yang-Mills Green functions*. PhD thesis, 2010.

[86] Markus Q. Huber, Reinhard Alkofer, and Kai Schwenzer. Infrared scaling solutions beyond the Landau gauge: The maximally Abelian gauge and Abelian infrared dominance. *PoS*, FACESQCD:001, 2010.

[87] Gerard 't Hooft. On the Phase Transition Towards Permanent Quark Confinement. *Nucl. Phys.*, B138:1, 1978.

[88] G. Mack and V. B. Petkova. Sufficient Condition for Confinement of Static Quarks by a Vortex Condensation Mechanism. *Annals Phys.*, 125:117, 1980.

[89] M. Engelhardt and H. Reinhardt. Center projection vortices in continuum Yang-Mills theory. *Nucl. Phys.*, B567:249, 2000.

[90] H. Reinhardt and M. Engelhardt. Center vortices in continuum Yang-Mills theory. In *Quark confinement and the hadron spectrum. Proceedings, 4th International Conference, Vienna, Austria, July 3-8, 2000*, pages 150–162, 2000.

[91] D. Zwanziger. Vanishing of zero momentum lattice gluon propagator and color confinement. *Nucl. Phys.*, B364:127–161, 1991.

[92] D. Zwanziger. Renormalization in the Coulomb gauge and order parameter for confinement in QCD. *Nucl. Phys.*, B518:237–272, 1998.

[93] Daniel Zwanziger. No confinement without Coulomb confinement. *Phys. Rev. Lett.*, 90:102001, 2003.

[94] J. E. Mandula and M. Ogilvie. The Gluon Is Massive: A Lattice Calculation of the Gluon Propagator in the Landau Gauge. *Phys. Lett.*, B185:127–132, 1987.

[95] Attilio Cucchieri and Daniel Zwanziger. Numerical study of gluon propagator and confinement scenario in minimal Coulomb gauge. *Phys. Rev.*, D65:014001, 2001.

[96] Attilio Cucchieri and Daniel Zwanziger. Fit to gluon propagator and Gribov formula. *Phys. Lett.*, B524:123–128, 2002.

[97] Y. Nakagawa, A. Nakamura, T. Saito, and H. Toki. Scaling study of the gluon propagator in Coulomb gauge QCD on isotropic and anisotropic lattices. *Phys. Rev.*, D83:114503, 2011.

[98] Kurt Langfeld and Laurent Moyaerts. Propagators in Coulomb gauge from SU(2) lattice gauge theory. *Phys. Rev.*, D70:074507, 2004.

[99] Markus Quandt, Giuseppe Burgio, Songvudhi Chimchinda, and Hugo Reinhardt. Coulomb gauge Green functions and Gribov copies in SU(2) lattice gauge theory. *PoS*, LAT2007:325, 2007.

[100] Yoshiyuki Nakagawa, Hiroshi Toki, Atsushi Nakamura, and Takuya Saito. Color confinement and the Faddeev-Popov ghosts in Coulomb gauge QCD. *PoS*, LAT2007:319, 2007.

[101] Aiko Voigt, Ernst-Michael Ilgenfritz, Michael Muller-Preussker, and Andre Sternbeck. Coulomb gauge studies of SU(3) Yang-Mills theory on the lattice. *PoS*, LAT2007:338, 2007.

[102] Y. Nakagawa, A. Voigt, E. M. Ilgenfritz, M. Muller-Preussker, A. Nakamura, T. Saito, A. Sternbeck, and H. Toki. Coulomb-gauge ghost and gluon propagators in SU(3) lattice Yang-Mills theory. *Phys. Rev.*, D79:114504, 2009.

[103] Yoshiyuki Nakagawa, Atsushi Nakamura, Takuya Saito, and Hiroshi Toki. Coulomb gauge gluon propagator on anisotropic lattices. *PoS*, LAT2009:230, 2009.

[104] A. Sternbeck, E. M. Ilgenfritz, M. Muller-Preussker, and A. Schiller. Towards the infrared limit in SU(3) Landau gauge lattice gluodynamics. *Phys. Rev.*, D72:014507, 2005.

[105] Attilio Cucchieri. Gribov copies in the minimal Landau gauge: The Influence on gluon and ghost propagators. *Nucl. Phys.*, B508:353–370, 1997.

[106] H. Reinhardt. The Dielectric function of the QCD vacuum. *Phys. Rev. Lett.*, 101:061602, 2008.

[107] Markus Quandt, Giuseppe Burgio, Songvudhi Chimchinda, and Hugo Reinhardt. Coulomb gauge ghost propagator and the Coulomb potential. *PoS*, CONFINEMENT8:066, 2008.

[108] G. Burgio, M. Quandt, and H. Reinhardt. Ghost propagator and the Coulomb form factor from the lattice. *Phys. Rev.*, D86:045029, 2012.

[109] Jeff Greensite, Stefan Olejnik, and Daniel Zwanziger. Center vortices and the Gribov horizon. *JHEP*, 05:070, 2005.

[110] Y. Nakagawa, A. Nakamura, T. Saito, and H. Toki. Infrared behavior of the Faddeev-Popov operator in Coulomb gauge QCD. *Phys. Rev.*, D75:014508, 2007.

[111] Attilio Cucchieri and Daniel Zwanziger. Renormalization group calculation of color Coulomb potential. *Phys. Rev.*, D65:014002, 2001.

[112] Enzo Marinari, Maria Luigia Paciello, Giorgio Parisi, and Bruno Taglienti. The String tension in gauge theories: A Suggestion for a new measurement method. *Phys. Lett.*, B298:400–404, 1993.

[113] Jeff Greensite and Stefan Olejnik. Coulomb energy, vortices, and confinement. *Phys. Rev.*, D67:094503, 2003.

[114] Jeff Greensite. An introduction to the confinement problem. *Lect. Notes Phys.*, 821:1–211, 2011.

[115] Jeff Greensite, Stefan Olejnik, and Daniel Zwanziger. Coulomb energy, remnant symmetry, and the phases of nonAbelian gauge theories. *Phys. Rev.*, D69:074506, 2004.

[116] A. Voigt, E. M. Ilgenfritz, M. Muller-Preussker, and A. Sternbeck. The Effective Coulomb potential in SU(3) lattice Yang-Mills theory. *Phys. Rev.*, D78:014501, 2008.

[117] Y. Nakagawa, A. Nakamura, T. Saito, H. Toki, and D. Zwanziger. Properties of color-Coulomb string tension. *Phys. Rev.*, D73:094504, 2006.

[118] Takumi Iritani and Hideo Suganuma. Instantaneous interquark potential in generalized Landau gauge in SU(3) lattice QCD: a possible gauge for the quark potential model. *Phys. Rev.*, D83:054502, 2011.

[119] Takumi Iritani and Hideo Suganuma. Lattice QCD analysis for Faddeev-Popov eigenmodes in terms of gluonic momentum components in the Coulomb gauge. *Phys. Rev.*, D86:074034, 2012.

[120] Jeff Greensite and Adam P. Szczepaniak. Coulomb string tension, asymptotic string tension, and the gluon chain. *Phys. Rev.*, D91(3):034503, 2015.

[121] J. Greensite. Gauge Orbits and the Coulomb Potential. *Phys. Rev.*, D80:045003, 2009.

[122] G. Burgio, M. Schrock, H. Reinhardt, and M. Quandt. Running mass, effective energy and confinement: the lattice quark propagator in Coulomb gauge. *Phys. Rev.*, D86:014506, 2012.

[123] M. Pak and M. Schröck. Overlap Quark Propagator in Coulomb Gauge QCD and the Interrelation of Confinement and Chiral Symmetry Breaking. *Phys. Rev.*, D91(7):074515, 2015.

[124] D. Epple, H. Reinhardt, W. Schleifenbaum, and A. P. Szczepaniak. Subcritical solution of the Yang-Mills Schroedinger equation in the Coulomb gauge. *Phys. Rev.*, D77:085007, 2008.

[125] W. Schleifenbaum, M. Leder, and H. Reinhardt. Infrared analysis of propagators and vertices of Yang-Mills theory in Landau and Coulomb gauge. *Phys. Rev.*, D73:125019, 2006.

[126] A. Cucchieri, T. Mendes, and A. Mihara. Numerical study of the ghost-gluon vertex in Landau gauge. *JHEP*, 12:012, 2004.

[127] A. Sternbeck, E. M. Ilgenfritz, M. Muller-Preussker, and A. Schiller. Landau gauge ghost and gluon propagators and the Faddeev-Popov operator spectrum. *Nucl. Phys. Proc. Suppl.*, 153:185–190, 2006.

[128] Markus Leder, Jan M. Pawlowski, Hugo Reinhardt, and Axel Weber. Hamiltonian Flow in Coulomb Gauge Yang-Mills Theory. *Phys. Rev.*, D83:025010, 2011.

[129] Patrick Cooper and Daniel Zwanziger. Origin of Confining Force. *Phys. Rev. D 93, 105024*, 2016.

[130] Giuseppe Burgio, Markus Quandt, Hugo Reinhardt, and Hannes Vogt. Gribov horizon and Gribov copies effect in lattice Coulomb gauge. arXiv:1608.05795, 2016.

[131] Enzo Marinari, Claudio Parrinello, and Roberto Ricci. Evidence for the existence of Gribov copies in Landau gauge lattice QCD. *Nucl. Phys.*, B362:487–497, 1991.

[132] F Barahona. On the computational complexity of ising spin glass models. *Journal of Physics A: Mathematical and General*, 15(10):3241, 1982.

[133] Axel Maas. More on Gribov copies and propagators in Landau-gauge Yang-Mills theory. *Phys. Rev.*, D79:014505, 2009.

[134] Philippe de Forcrand and James E. Hetrick. The Continuum limit of the lattice Gribov problem, and a solution based on Hodge decomposition. *Nucl. Phys. Proc. Suppl.*, 42:861–866, 1995.

[135] André Sternbeck and Michael Müller-Preussker. Lattice evidence for the family of decoupling solutions of Landau gauge Yang-Mills theory. *Phys. Lett.*, B726:396–403, 2013.

[136] André Sternbeck and Michael Müller-Preussker. Another look at the Landau-gauge gluon and ghost propagators at low momentum. *PoS*, ConfinementX:074, 2012.

[137] Axel Maas. Constructing non-perturbative gauges using correlation functions. *Phys. Lett.*, B689:107–111, 2010.

[138] Axel Maas. More on the properties of the first Gribov region in Landau gauge. *Phys. Rev. D 93, 054504*, 2016.

[139] G. Burgio, Markus Quandt, Hugo Reinhardt, Mario Schröck, and H. Vogt. Confinement in Coulomb gauge. *PoS*, LATTICE2013:365, 2014.

[140] Giuseppe Burgio, Markus Quandt, Hugo Reinhardt, and Hannes Vogt. Coulomb versus physical string tension on the lattice. *Phys. Rev.*, D92(3):034518, 2015.

[141] Ciaran Hughes, Dhagash Mehta, and Jon-Ivar Skullerud. Enumerating Gribov copies on the lattice. *Annals Phys.*, 331:188–215, 2013.

[142] Dhagash Mehta and Mario Schröck. Enumerating Copies in the First Gribov Region on the Lattice in up to four Dimensions. *Phys. Rev.*, D89(9):094512, 2014.

[143] Hannes Vogt, Giuseppe Burgio, Markus Quandt, and Hugo Reinhardt. Coulomb gauge on the lattice: From zero to finite temperature. *PoS*, LATTICE2013:363, 2014.

[144] Umberto Villa and Santiago Akle. https://code.google.com/archive/p/tminres/, 2012.

[145] C. C. Paige and M. A. Saunders. Solution of sparse indefinite systems of linear equations. 12(4):617–629, September 1975.

[146] A. Barresi, G. Burgio, Massimo D'Elia, and M. Muller-Preussker. A Finite temperature investigation of dual superconductivity in the modified SO(3) lattice gauge theory. *Phys. Lett.*, B599:278–284, 2004.

[147] G. Burgio, M. Fuhrmann, W. Kerler, and M. Muller-Preussker. Vortex free energy and deconfinement in center-blind discretizations of Yang-Mills theories. *Phys. Rev.*, D74:071502, 2006.

[148] G. Burgio, M. Fuhrmann, W. Kerler, and M. Muller-Preussker. Modified SO(3) lattice gauge theory at T <> 0 with parallel tempering: Monopole and vortex condensation. *Phys. Rev.*, D75:014504, 2007.

[149] Giuseppe Burgio and Hugo Reinhardt. Topological order and the vacuum of Yang-Mills theories. *Phys. Rev.*, D91(2):025021, 2015.

[150] A. Barresi, G. Burgio, and M. Muller-Preussker. Universality, vortices and confinement: Modified SO(3) lattice gauge theory at nonzero temperature. *Phys. Rev.*, D69:094503, 2004.

[151] A. Barresi and G. Burgio. Fixed twist dynamics of SO(3) gauge theory. *Eur. Phys. J.*, C49:973–981, 2007.

[152] Cian O'Luanaigh. LHC collides ions at new record energy, http://cds.cern.ch/record/2114669. Nov 2015.

[153] A. Das. *Finite Temperature Field Theory*. World scientific lecture notes in physics. World Scientific, 1997.

[154] J.I. Kapusta and C. Gale. *Finite-Temperature Field Theory: Principles and Applications*. Cambridge Monographs on Mathematical Physics. Cambridge University Press, 2006.

[155] H. Reinhardt, D. R. Campagnari, and A. P. Szczepaniak. Variational approach to Yang-Mills theory at finite temperatures. *Phys. Rev.*, D84:045006, 2011.

[156] Hugo Reinhardt and Jan Heffner. Effective potential of the confinement order parameter in the Hamiltonian approach. *Phys. Rev.*, D88:045024, 2013.

[157] J. Heffner and H. Reinhardt. Finite-temperature Yang-Mills theory in the Hamiltonian approach in Coulomb gauge from a compactified spatial dimension. *Phys. Rev.*, D91(8):085022, 2015.

[158] J. Fingberg, Urs M. Heller, and F. Karsch. Scaling and asymptotic scaling in the SU(2) gauge theory. *Nucl. Phys.*, B392:493–517, 1993.

[159] G. S. Bali, J. Fingberg, Urs M. Heller, F. Karsch, and K. Schilling. The Spatial string tension in the deconfined phase of the (3+1)-dimensional SU(2) gauge theory. *Phys. Rev. Lett.*, 71:3059–3062, 1993.

[160] G. Boyd, J. Engels, F. Karsch, E. Laermann, C. Legeland, M. Lutgemeier, and B. Petersson. Thermodynamics of SU(3) lattice gauge theory. *Nucl. Phys.*, B469:419–444, 1996.

[161] F. J. Wegner. Duality in Generalized Ising Models and Phase Transitions Without Local Order Parameters. *J. Math. Phys.*, 12:2259–2272, 1971.

[162] M. Engelhardt, K. Langfeld, H. Reinhardt, and O. Tennert. Interaction of confining vortices in SU(2) lattice gauge theory. *Phys. Lett.*, B431:141–146, 1998.

[163] M. Engelhardt, K. Langfeld, H. Reinhardt, and O. Tennert. Deconfinement in SU(2) Yang-Mills theory as a center vortex percolation transition. *Phys. Rev.*, D61:054504, 2000.

[164] Oliver Tennert. *Vortex condensation and confinement in centre-projected lattice Yang-Mills theory*. PhD thesis, 2000.

[165] K. Langfeld, O. Tennert, M. Engelhardt, and H. Reinhardt. Center vortices of Yang-Mills theory at finite temperatures. *Phys. Lett.*, B452:301, 1999.

[166] L. Del Debbio, Manfried Faber, J. Giedt, J. Greensite, and S. Olejnik. Detection of center vortices in the lattice Yang-Mills vacuum. *Phys. Rev.*, D58:094501, 1998.

[167] Philippe de Forcrand and Massimo D'Elia. On the relevance of center vortices to QCD. *Phys. Rev. Lett.*, 82:4582–4585, 1999.

[168] Manfried Faber, J. Greensite, and S. Olejnik. Center projection with and without gauge fixing. *JHEP*, 01:008, 1999.

[169] Kurt Langfeld. Vortex structures in pure SU(3) lattice gauge theory. *Phys. Rev.*, D69:014503, 2004.

[170] Kurt Langfeld, Hugo Reinhardt, and Oliver Tennert. Confinement and scaling of the vortex vacuum of SU(2) lattice gauge theory. *Phys. Lett.*, B419:317–321, 1998.

[171] V. G. Bornyakov, D. A. Komarov, and M. I. Polikarpov. P vortices and drama of Gribov copies. *Phys. Lett.*, B497:151–158, 2001.

[172] Tamas G. Kovacs and E. T. Tomboulis. On P vortices and the Gribov problem. *Phys. Lett.*, B463:104–108, 1999.

[173] Manfried Faber, Jeff Greensite, and Stefan Olejnik. Remarks on the Gribov problem in direct maximal center gauge. *Phys. Rev.*, D64:034511, 2001.

[174] M. Quandt, H. Reinhardt, and G. Burgio. The role of center vortices in Gribov's confinement scenario. *Phys. Rev.*, D81:065016, 2010.

[175] M. Albanese et al. Glueball Masses and String Tension in Lattice QCD. *Phys. Lett.*, B192:163–169, 1987.

[176] Jacques C. R. Bloch, Attilio Cucchieri, Kurt Langfeld, and Tereza Mendes. Propagators and running coupling from SU(2) lattice gauge theory. *Nucl. Phys.*, B687:76–100, 2004.

[177] Jochen Gattnar, Kurt Langfeld, and Hugo Reinhardt. Signals of confinement in Green functions of SU(2) Yang-Mills theory. *Phys. Rev. Lett.*, 93:061601, 2004.

[178] A. Sternbeck, E. M. Ilgenfritz, and M. Muller-Preussker. Spectral properties of the Landau gauge Faddeev-Popov operator in lattice gluodynamics. *Phys. Rev.*, D73:014502, 2006.

[179] T.P. Cheng and L.F. Li. *Gauge Theory of Elementary Particle Physics.* Oxford science publications. Clarendon Press, 1984.

[180] Christopher T. Hill and Elizabeth H. Simmons. Strong dynamics and electroweak symmetry breaking. *Phys. Rept.*, 381:235–402, 2003. [Erratum: Phys. Rept.390,553(2004)].

[181] Francesco Sannino. Conformal Dynamics for TeV Physics and Cosmology. *Acta Phys. Polon.*, B40:3533–3743, 2009.

[182] Gerard 't Hooft. Renormalizable Lagrangians for Massive Yang-Mills Fields. *Nucl. Phys.*, B35:167–188, 1971.

[183] Gerard 't Hooft and M. J. G. Veltman. Regularization and Renormalization of Gauge Fields. *Nucl. Phys.*, B44:189–213, 1972.

[184] Kenneth D. Lane. Technicolor 2000. In *Nuclear, subnuclear and astroparticle physics. Proceedings, 5th LNF Spring School, Frascati, Italy, May 15-20, 2000*, pages 235–280, 2000.

[185] Sally Dawson, Howard E Haber, James L Siegrist, and Timothy L Barklow. *Electroweak symmetry breaking and new physics at the TeV scale*. Adv. Ser. Direct. High Energ. Phys. World Scientific, Singapore, 1997.

[186] Porter Williams. Naturalness, the autonomy of scales, and the 125 GeV Higgs. *Stud. Hist. Phil. Sci.*, B51:82–96, 2015.

[187] David E. Morrissey, Tilman Plehn, and Tim M. P. Tait. Physics searches at the LHC. *Phys. Rept.*, 515:1–113, 2012.

[188] Leonard Susskind. Dynamics of Spontaneous Symmetry Breaking in the Weinberg-Salam Theory. *Phys. Rev.*, D20:2619–2625, 1979.

[189] Steven Weinberg. Implications of Dynamical Symmetry Breaking: An Addendum. *Phys. Rev.*, D19:1277–1280, 1979.

[190] Estia Eichten and Kenneth D. Lane. Dynamical Breaking of Weak Interaction Symmetries. *Phys. Lett.*, B90:125–130, 1980.

[191] Savas Dimopoulos and Leonard Susskind. Mass Without Scalars. *Nucl. Phys.*, B155:237–252, 1979.

[192] E. Farhi and Leonard Susskind. A Technicolored G.U.T. *Phys. Rev.*, D20:3404–3411, 1979.

[193] K. A. Olive et al. (Particle Data Group). Review of Particle Physics. *Chin. Phys.*, C38:090001, (2014) and 2015 update.

[194] Thomas A. Ryttov and Francesco Sannino. Supersymmetry inspired QCD beta function. *Phys. Rev.*, D78:065001, 2008.

[195] Dennis D. Dietrich and Francesco Sannino. Conformal window of SU(N) gauge theories with fermions in higher dimensional representations. *Phys. Rev.*, D75:085018, 2007.

[196] Simon Catterall and Francesco Sannino. Minimal walking on the lattice. *Phys. Rev.*, D76:034504, 2007.

[197] Simon Catterall, Joel Giedt, Francesco Sannino, and Joe Schneible. Phase diagram of SU(2) with 2 flavors of dynamical adjoint quarks. *JHEP*, 11:009, 2008.

[198] Ari J. Hietanen, Jarno Rantaharju, Kari Rummukainen, and Kimmo Tuominen. Spectrum of SU(2) lattice gauge theory with two adjoint Dirac flavours. *JHEP*, 05:025, 2009.

[199] Jarno Rantaharju. Gradient Flow Coupling in the SU(2) gauge theory with two adjoint fermions. *Phys. Rev. D 93, 094516*, 2016.

[200] Jarno Rantaharju, Teemu Rantalaiho, Kari Rummukainen, and Kimmo Tuominen. Running coupling in SU(2) with two adjoint fermions. *Phys. Rev. D 93, 094509*, 2016.

[201] Howard Georgi. Another odd thing about unparticle physics. *Phys. Lett.*, B650:275–278, 2007.

[202] Howard Georgi. Unparticle physics. *Phys. Rev. Lett.*, 98:221601, 2007.

[203] Biagio Lucini. Glueballs from the Lattice. *PoS*, QCD-TNT-III:023, 2013.

[204] Luigi Del Debbio, Agostino Patella, and Claudio Pica. Higher representations on the lattice: Numerical simulations. SU(2) with adjoint fermions. *Phys. Rev.*, D81:094503, 2010.

[205] Axel Maas. On the gauge boson's properties in a candidate technicolor theory. *JHEP*, 05:077, 2011.

[206] Daniel August and Axel Maas. On the Landau-gauge adjoint quark propagator. *JHEP*, 07:001, 2013.

[207] Derek B. Leinweber, Jon Ivar Skullerud, Anthony G. Williams, and Claudio Parrinello. Asymptotic scaling and infrared behavior of the gluon propagator. *Phys. Rev.*, D60:094507, 1999. [Erratum: Phys. Rev.D61,079901(2000)].

[208] Mario Schröck and Hannes Vogt. Gauge fixing using overrelaxation and simulated annealing on GPUs. *PoS*, LATTICE2012:187, 2012.

[209] Mario Schröck and Hannes Vogt. Gauge fixing in lattice QCD with multi-GPUs. *Acta Phys. Polon. Supp.*, 6(3):763–768, 2013.

[210] Hannes Vogt and Mario Schröck. cuLGT: Lattice Gauge Fixing on GPUs. In *Proceedings, GPU Computing in High-Energy Physics (GPUHEP2014)*, 2014.

[211] E. Scott Larsen and David McAllister. Fast matrix multiplies using graphics hardware. In *Proceedings of the 2001 ACM/IEEE Conference on Supercomputing*, SC '01, pages 55–55, New York, NY, USA, 2001. ACM.

[212] Peng Du, Rick Weber, Piotr Luszczek, Stanimire Tomov, Gregory Peterson, and Jack Dongarra. From cuda to opencl: Towards a performance-portable solution for multi-platform gpu programming. *Parallel Computing*, 38(8):391 – 407, 2012.

[213] Nico Galoppo, Naga K. Govindaraju, Michael Henson, and Dinesh Manocha. Lu-gpu: Efficient algorithms for solving dense linear systems on graphics hardware. In *Proceedings of the 2005 ACM/IEEE Conference on Supercomputing*, SC '05, pages 3–, Washington, DC, USA, 2005. IEEE Computer Society.

[214] Gyozo I. Egri, Zoltan Fodor, Christian Hoelbling, Sandor D. Katz, Daniel Nogradi, and Kalman K. Szabo. Lattice QCD as a video game. *Comput. Phys. Commun.*, 177:631–639, 2007.

[215] TOP500. Top 500 list of supercomputers, http://top500.org/, 11 2015.

[216] Matthias Bach, Volker Lindenstruth, Owe Philipsen, and Christopher Pinke. Lattice QCD based on OpenCL. *Comput. Phys. Commun.*, 184:2042–2052, 2013.

[217] Pushan Majumdar. Lattice Simulations using OpenACC compilers. *PoS*, LATTICE2013:031, 2014.

[218] Mario Schröck. The chirally improved quark propagator and restoration of chiral symmetry. *Phys. Lett.*, B711:217–224, 2012.

[219] Nuno Cardoso and Pedro Bicudo. SU(2) Lattice Gauge Theory Simulations on Fermi GPUs. *J. Comput. Phys.*, 230:3998–4010, 2011.

[220] Nuno Cardoso and Pedro Bicudo. Generating SU(Nc) pure gauge lattice QCD configurations on GPUs with CUDA and OpenMP. *Comput. Phys. Commun.*, 184:509–518, 2013.

[221] Nuno Cardoso, Paulo J. Silva, Pedro Bicudo, and Orlando Oliveira. Landau Gauge Fixing on GPUs. *Comput. Phys. Commun.*, 184:124–129, 2013.

[222] Nuno Cardoso. Coulomb and Landau Gauge Fixing in GPUs using CUDA and MILC. *PoS*, LATTICE2014:033, 2015.

[223] Attilio Cucchieri and Tereza Mendes. Critical slowing down in SU(2) Landau gauge fixing algorithms. *Nucl. Phys.*, B471:263–292, 1996.

[224] Jeffrey E. Mandula and Michael Ogilvie. Efficient gauge fixing via overrelaxation. *Phys. Lett.*, B248:156–158, 1990.

[225] J.H. Holland. *Adaptation in natural and artificial systems: an introductory analysis with applications to biology, control, and artificial intelligence*. University of Michigan Press, 1975.

[226] J. Kennedy and R. Eberhart. Particle swarm optimization. In *Neural Networks, 1995. Proceedings., IEEE International Conference on*, volume 4, pages 1942–1948 vol.4, Nov 1995.

[227] S. Kirkpatrick, C. D. Gelatt, and M. P. Vecchi. Optimization by Simulated Annealing. *Science*, 220:671–680, 1983.

[228] Scott Kirkpatrick. Optimization by simulated annealing: Quantitative studies. *Journal of Statistical Physics*, 34(5-6):975–986, 1984.

[229] G. S. Bali, V. Bornyakov, M. Muller-Preussker, and F. Pahl. New algorithm for gauge fixing in SU(2) lattice gauge theory. *Nucl. Phys. Proc. Suppl.*, 42:852–854, 1995.

[230] Sadataka Furui and Hideo Nakajima. Infrared features of the Landau gauge QCD. *Phys. Rev.*, D69:074505, 2004.

[231] Ernst-Michael Ilgenfritz, Christoph Menz, Michael Muller-Preussker, Arwed Schiller, and Andre Sternbeck. SU(3) Landau gauge gluon and ghost propagators using the logarithmic lattice gluon field definition. *Phys.Rev.*, D83:054506, 2011.

[232] NVIDIA. Cuda c programming guide, http://docs.nvidia.com/cuda/cuda-c-programming-guide.

[233] J. Sanders and E. Kandrot. *CUDA by Example: An Introduction to General-Purpose GPU Programming, Portable Documents*. Pearson Education, 2010.

[234] D.B. Kirk and W.W. Hwu. *Programming Massively Parallel Processors: A Hands-on Approach*. Elsevier Science, 2012.

[235] Xinxin Mei and Xiaowen Chu. Dissecting GPU memory hierarchy through microbenchmarking. *CoRR*, abs/1509.02308, 2015.

[236] P. de Forcrand, D. Lellouch, and C. Roiesnel. OPTIMIZING A LATTICE QCD SIMULATION PROGRAM. *J. Comput. Phys.*, 59:324–330, 1985.

[237] NVIDIA. Cuda c best practices guide, https://docs.nvidia.com/cuda/cuda-c-best-practices-guide.

[238] David Abrahams and Aleksey Gurtovoy. *C++ Template Metaprogramming: Concepts, Tools, and Techniques from Boost and Beyond (C++ in Depth Series)*. Addison-Wesley Professional, 2004.

[239] Massimo Di Pierro, Aida X. El-Khadra, Steven A. Gottlieb, Andreas S. Kronfeld, Paul B. Mackenzie, Masataka Okamoto, Mehmet B. Oktay, and James N. Simone. www.fermiqcd.net. *Nucl. Phys. Proc. Suppl.*, 129:832–834, 2004. [,832(2003)].

[240] Peter Boyle, Azusa Yamaguchi, Guido Cossu, and Antonin Portelli. Grid: A next generation data parallel C++ QCD library. *arXiv:1512.03487*, 2015.

[241] GREEN500. The green500 list, http://green500.org/, 11 2015.

[242] Jon Ivar Skullerud and Anthony G. Williams. Quark propagator in Landau gauge. *Phys. Rev.*, D63:054508, 2001.

[243] Matthew I. Smith. A Schur algorithm for computing matrix pth roots. *Siam J. Matrix Anal. Appl*, 24(4):971–989, 2003.

[244] R. V. Mises and H. Pollaczek-Geiringer. Praktische Verfahren der Gleichungsauflösung. *ZAMM - Journal of Applied Mathematics and Mechanics / Zeitschrift für Angewandte Mathematik und Mechanik*, 9(1):58–77, 1929.

[245] Kostas Orginos, Doug Toussaint, and R. L. Sugar. Variants of fattening and flavor symmetry restoration. *Phys. Rev.*, D60:054503, 1999.

[246] John B. Kogut and Leonard Susskind. Hamiltonian Formulation of Wilson's Lattice Gauge Theories. *Phys. Rev.*, D11:395–408, 1975.

[247] Frederic D. R. Bonnet, Patrick O. Bowman, Derek B. Leinweber, Anthony G. Williams, and Jian-bo Zhang. Overlap quark propagator in Landau gauge. *Phys. Rev.*, D65:114503, 2002.

[248] Mario Schröck and Hannes Vogt. Lattice QCD Green's functions in maximally Abelian gauge: Infrared Abelian dominance and the quark sector. *Phys. Rev.*, D93(1):014501, 2016.

[249] Taichiro Kugo and Izumi Ojima. Local Covariant Operator Formalism of Nonabelian Gauge Theories and Quark Confinement Problem. *Prog.Theor.Phys.Suppl.*, 66:1–130, 1979.

[250] Daniel Zwanziger. Renormalizability of the critical limit of lattice gauge theory by BRS invariance. *Nucl. Phys.*, B399:477–513, 1993.

[251] Yoichiro Nambu. Strings, Monopoles and Gauge Fields. *Phys.Rev.*, D10:4262, 1974.

[252] S. Mandelstam. Vortices and Quark Confinement in Nonabelian Gauge Theories. *Phys.Rept.*, 23:245–249, 1976.

[253] D. Dudal, S.P. Sorella, N. Vandersickel, and H. Verschelde. Gribov no-pole condition, Zwanziger horizon function, Kugo-Ojima confinement criterion, boundary conditions, BRST breaking and all that. *Phys.Rev.*, D79:121701, 2009.

[254] Tsuneo Suzuki. Color Confinement and Asymptotic Completeness. *Prog.Theor.Phys.*, 69:1827, 1983.

[255] Hiroyuki Hata and Ikki Niigata. Color confinement, Abelian gauge and renormalization group flow. *Nucl.Phys.*, B389:133–152, 1993.

[256] Valentin Mader, Martin Schaden, Daniel Zwanziger, and Reinhard Alkofer. Infrared Saturation and Phases of Gauge Theories with BRST Symmetry. *Eur.Phys.J.*, C74:2881, 2014.

[257] L. Del Debbio, A. Di Giacomo, and G. Paffuti. Detecting dual superconductivity in the ground state of gauge theory. *Phys.Lett.*, B349:513–518, 1995.

[258] J.M. Carmona, Massimo D'Elia, L. Del Debbio, A. Di Giacomo, B. Lucini, et al. Color confinement and dual superconductivity in full QCD. *Phys.Rev.*, D66:011503, 2002.

[259] Kei-Ichi Kondo and Toru Shinohara. Abelian dominance in low-energy gluodynamics due to dynamical mass generation. *Phys. Lett.*, B491:263–274, 2000.

[260] R.M. Woloshyn. Chiral symmetry breaking in Abelian projected SU(2) lattice gauge theory. *Phys.Rev.*, D51:6411–6416, 1995.

[261] S. Kitahara, O. Miyamura, T. Okude, F. Shoji, and Tsuneo Suzuki. Monopoles and hadron spectrum in quenched QCD. *Nucl.Phys.*, B533:576–590, 1998.

[262] J.D. Stack, W.W. Tucker, and R.J. Wensley. The maximal abelian gauge, monopoles, and vortices in SU(3) lattice gauge theory. *Nucl. Phys. B*, 639:203–222, 2002.

[263] Frederic D.R. Bonnet, Patrick O. Bowman, Derek B. Leinweber, Anthony G. Williams, and James M. Zanotti. Infinite volume and continuum limits of the Landau gauge gluon propagator. *Phys.Rev.*, D64:034501, 2001.

[264] Patrick O. Bowman, Urs M. Heller, and Anthony G. Williams. Lattice quark propagator in Landau and Laplacian gauges. *Nucl.Phys.Proc.Suppl.*, 106:820–822, 2002.

[265] Patrick O. Bowman, Urs M. Heller, and Anthony G. Williams. Lattice quark propagator with staggered quarks in Landau and Laplacian gauges. *Phys. Rev. D*, 66:014505, 2002.

[266] Claude W. Bernard, Tom Burch, Kostas Orginos, Doug Toussaint, Thomas A. DeGrand, et al. The QCD spectrum with three quark flavors. *Phys. Rev. D*, 64:054506, 2001.

[267] C. Aubin, C. Bernard, C. DeTar, J. Osborn, Steven Gottlieb, et al. Light hadrons with improved staggered quarks: Approaching the continuum limit. *Phys. Rev. D*, 70:094505, 2004.

[268] C. Aubin, Jack Laiho, and Ruth S. Van de Water. The Neutral kaon mixing parameter B(K) from unquenched mixed-action lattice QCD. *Phys.Rev.*, D81:014507, 2010.

[269] A. Bazavov, C. Bernard, C. DeTar, Steven Gottlieb, U. M. Heller, J. E. Hetrick, J. Laiho, L. Levkova, P. B. Mackenzie, M. B. Oktay, R. Sugar, D. Toussaint, and R. S. Van de Water. Full nonperturbative QCD simulations with 2+1 flavors of improved staggered quarks. *Rev. Mod. Phys.*, 82:1349–1417, 2010.

[270] M. Lüscher and P. Weisz. On-shell improved lattice gauge theories. *Commun. Math. Phys.*, 97:59, 1985.

[271] Massimo Di Pierro, James Hetrick, Shreyas Cholia, and David Skinner. Making QCD Lattice Data Accessible and Organized through Advanced Web Interfaces. *PoS*, LATTICE2011:305, 2011.

[272] Patrick O. Bowman, Urs M. Heller, Derek B. Leinweber, Maria B. Parappilly, and Anthony G. Williams. Unquenched gluon propagator in Landau gauge. *Phys.Rev.*, D70:034509, 2004.

Danksagung

Zuallererst möchte ich mich bei Prof. Dr. Hugo Reinhardt für die Betreuung meiner Promotion bedanken, sowie für die Bereitstellung der finanziellen Mittel zur Anschaffung eines GPU-Rechners, was mir den Weg in meinen heutigen Beruf ermöglicht hat. Mein ganz besonderer Dank gilt Dr. Giuseppe Burgio für seine hervorragende Hilfe bei allen physikalischen Problemen, von der Diplomarbeit bis zum Ende meiner Promotionszeit. Dieser Dank gilt ebenfalls Dr. Markus Quandt, der mich darüber hinaus bei der Lösung technischer Probleme unterstützte.

Bedanken möchte ich mich auch bei meinem langjährigen Bürokollegen Jan für die angenehme Zeit, bei Davide, Ehsan, Peter und der ganzen Kaffeerunde des 7. Stocks für viele interessante Gespräche, auch außerhalb der Universität, bei Mario für die gute Zusammenarbeit in verschiedenen Projekten und bei Martin für lange Diskussionen über C++, CUDA und das Programmieren im Allgemeinen.

Für die Unterstützung mit einem Promotionsstipendium gilt mein Dank dem Evangelischen Studienwerk Villigst, ganz besonders auch für die ideele Förderung in Form der freitäglichen Mittagessensrunde.

Dankbar bin ich meinen Eltern, die mir neben so vielem auch das Physikstudium ermöglicht haben. Zu guter Letzt möchte ich mich bei meiner Frau Kathrin bedanken, die mich schon so viele schöne Jahre lang erträgt.